Pipeline Monitoring Using Radar Sensors for the Detection of Oil Leaks

by

Elijah Uche

A thesis submitted to the University of Birmingham

for the degree of

DOCTOR OF PHILOSOPHY

Microwave Integrated Systems Laboratory

School of Electronic, Electrical and Systems Engineering

College of Engineering and Physical Sciences

University of Birmingham

June 2024

Abstract

This research explores the use of radar sensors for real-time remote monitoring of oil and gas pipeline infrastructure, enabling the detection of oil leaks, spills and unusual activities while ensuring prompt escalation to authorities for early response. This helped to evade a flooding or spillage occurrence and thereby curtailed the wastage attributed to issues of pipeline spillage/leaks. The research also focused on the theoretical development and simulation of rough surface models with a view to understanding and analysing the reflectivity of various rough surfaces and how this reflectivity varies, when the dielectric properties of these rough surfaces are modified. The modification amongst other parameters can be due to oil spills and leaks. In particular, the radar cross section (RCS) of various soil samples (with oil and without oil) was analysed. The varied reflectivity results from these soil samples enabled us to understand and appreciate the difference between a soil that is soaked with oil and another that is not. The oil in the soil sample soaked with oil could be due to spills and leaks from oil pipelines, so an understanding of these differences in reflectivities was utilised in improving the detection and identification of oil spills/leaks in pipeline infrastructure which is the major question this research addresses. The radar parameters modified in this project for the RCS analysis of varied soil samples include frequency, aspect angle, polarisation as well as the dielectric properties of the material with the obtained results extensively analysed and discussed. After showing and analysing the simulation results of the rough surface model, an experimental investigation of this RCS analysis was also conducted as means of validation of the theoretical / analytical results. For the theoretical and analytical phase, rough surface models which can be likened to various soil surfaces on which these pipeline networks are laid upon were developed in MATLAB and imported into CST for the simulation of the radar cross section (RCS) / reflectivity analyses under various dielectric properties and parameters. The validity of the rough surface models was tested through simulations with varied soil samples and dielectric properties. In the simulations, the impact of oil as well as other dielectrics on the reflectivity or RCS analysis of various soil samples was presented for the first time. Furthermore, an in-depth analysis was conducted on the measurement parameters, their relationships with dielectric constants, and their impact on the reflectivity of various soil samples. This has given us an idea of what the reflectivity of oil, emanating from the pipelines because of oil spills / leaks, could be when, for example, the pipeline infrastructure is laid on a dry or wet soil, such that my radar sensor is able to discriminate between these oil spills/leaks from other obscurants like water etc which might have seeped into or floats on the soil under investigation. In addition, the results of the rough surface models have been compared with literature. The validity of the developed theoretical rough surface models was tested and applied to experimental, proof-of-concept data in a controlled environment using radar instruments and the experimental results, which were thoroughly analysed and extensively presented for the first time, agreed with the analytical or theoretical results. The results of the theoretical or analytical RCS of the rough surface models were compared with the experimental results and the results have been presented. The results show that there is 10 dB difference in RCS from a 14 cm rough surface without oil and a similar surface that has been soaked with at least 7.5 L of oil. This implies that a litre of oil results in at least 1 dB change in RCS from a rough surface of 14 cm rms height. In addition, there is about a 4 dB difference for that of 7 cm surface roughness for a 9L oil that leaks onto the rough surface. This also implies that 2 L of oil results in a dB change in reflectivity from a rough surface of 7 cm rms height. This 4 dB difference is significant because it is about half the difference obtained for the 14cm rough surface profile and the 14 cm rough surface profile is double the 7 cm rough surface profile. The results obtained via experiment were also verified via simulations and both results tally and align with each other as have been extensively discussed and analysed. Distributed and back scattering as well as back reflections from the sandy soil was also investigated during the experiments and the results have been thoroughly analysed. Finally, the rough surface model was integrated with the radar system and the parameters measured from this system were thoroughly examined and extensively analysed. In addition, the performance of the developed theoretical and experimental models and systems was compared to specific requirements by the oil and gas industry, successfully meeting expectations in line with global best practices. The methods used, theoretical and experimental results obtained as well as the key findings and research output have been analysed, validated and presented as appropriate.

In summary, this research successfully developed and validated a radar-based remote monitoring system for oil and gas pipeline infrastructure, enabling real-time detection of leaks, spills, and anomalous activities. A key achievement was the theoretical development and experimental validation of rough surface models to analyse radar cross-section (RCS) variations in soil samples with and without oil contamination. The study demonstrated, for the first time, the impact of dielectric properties on soil reflectivity, showing a measurable correlation between oil volume and RCS variation – such as a 10 dB difference for a 14 cm rough surface soaked with 7.5 L of oil. These findings enhance the ability to discriminate oil spills from other environmental factors, improving detection accuracy. The results, validated through simulations and experiments, align with industry standards, positioning this work as a novel contribution towards enhancing oil spill detection and response in pipeline monitoring systems.

Dedication

I would like to specially dedicate this thesis to the two most beautiful sets of parents anyone on this planet could ever wish for

- ✓ *My Parents – Patrick & Janet Uche Oko for their unalloyed support, commitment, and training towards me right from when I came into this world right up till this moment. Their prayers and effort as well as their constant show of love have been mind-blowing to say the least.*

- ✓ *My Parents-In-law – Elder Anthony & Mrs Edith Ogbuagu for their unrivalled and immense support towards me for the past dozen years. Their prayers and consistent show of love towards me as well as my endeavours have swept me off my feet and blown me out of the waters.*

This thesis is dedicated to them as a token of my love and loyalty.

Acknowledgement

The PhD journey has been a wonderful experience, full of challenges, sleepless nights, silent screams, stress, joy, patience and digging deeper into research materials. The motivation behind all was a great support system. I have finally come to the end of the successful completion of my PhD which has included the most important years of my life thus far.

First and foremost, I want to appreciate God Almighty, the Giver and Keeper of life and knowledge for the grace to see me thru this sojourn. I would not have successfully completed this PhD without His help, guidance, direction, and support and for this I remain eternally grateful Lord. I would like to also appreciate the PTDF Nigeria for their support of this PhD.

Second, I would like to appreciate my supervisor – Dr. Michail Antoniou, for his doggedness and tenacity in seeing that this dream becomes a reality today. I have learnt a lot from you, and I sincerely appreciate you sir for your immense support during the most difficult times as well as your words of motivation to “keep going” always. This has helped me get through this dynamic research process with relative ease. Also, I would like to specially thank Prof. Mikhail Cherniakov whose patient and thorough research style always amazed me and pushed me to do more and go the extra mile. This was evident in the plethora of meetings held monthly and the insights drawn from these meetings can never be over emphasised. I would like to state at this juncture that most of the achievements in this presented work were only possible thru the insightful comments and professional support received from both Dr. Antoniou and Prof. Cherniakov. I must confess that their excellent supervision and support inspired my research interests, motivation, and passion in the field of radio frequency (RF) sensors.

I would not forget to thank every member of the MISL team for their support and guidance all these years. Special thanks must go to Dr. Anum Pirkani whose words of encouragement and constant checking up always kept me sane. Anum was always happy to help whenever I was stuck with an idea, a script or even a sub-chapter. I also appreciate Jared for his help and assistance with some of my measurements towards the tail end of my PhD. How can I forget Mr Alan Yates – our Senior technician for his immense support with my experimental setups as well as Risks assessments and SOPs. Thank you so very much Alan for all your huge sacrifices and availability even when your health was challenged, you ensured that I did not lose a lot of time in my measurements. I would like to also appreciate Dr Furkan Korkmaz, Dr. Ali Bekar, Muge, Bilge, Nuoshi, Xiaofei, Dillon, Daniel White and Darren for their helpful ideas.

In addition, I would like to appreciate the members and leaders of Winners Chapel International, Birmingham, UK for their prayers and fellowship all these years, especially every member of the Choir / Band. Permit me to say a big God bless you for all your encouragement.

Finally, I would like to thank my wife – Chioma Uche, and our two beautiful children – Chimamaka and Naetochim, for putting up with me all through these years of turmoil as well as sweat and blood. I can never forget your love, support and understanding. Your sacrifices are immense and for that I remain forever grateful. Thank you once again for being a part of this success story. I think it is fair to say that this would not have been possible without your invaluable contributions. I love you all deeply and trust that we shall all live to enjoy the fruits and benefits emanating from the huge sacrifices sown towards this PhD success story.

Table of Contents

List of Figures

List of Tables

Chapter 1. INTRODUCTION AND OVERVIEW

Pipelines are commonly utilised globally for the conveyance of hydrocarbon fluids over several kilometres. The usage of pipelines is regarded as one of the foremost ways in transporting products of petroleum which include gases, chemicals, fossil fuels as well as other necessary hydrocarbon fluids which serve as valuable resources to a nation's economy [1], [2]. Oil and gas pipeline networks have been shown to be the safest and most economical means if conveying crude oil as they fulfil a great demand for reliability and efficiency [3], [4]. For instance, the accidents per ton-mile which led to deaths as a result of transporting products of petroleum were generally higher when using rail (3%), ship (4%) and trucks (87%) compared to when pipelines were used [5]. The pipelines structures have been generally built to resist numerous environmental loading conditions in order to guarantee reliable and safe delivery of petroleum products from the production point to the distribution depot or the shore.

Conversely, as carrying precarious substances using very extended pipelines have become common across the world in recent years, the probability of dangerous mishaps as a result of pipeline disasters rises [6]. The roots of these failures are either deliberate damages – for example vandalism, or unintended damages – for example device/material failure and corrosion [7], [8]. These damages lead to pipeline disasters and therefore result in irretrievable reparations which comprise economic losses & extreme ecological contamination, especially when the leakage is discovered in an untimely manner [9], [10]. Leakages in pipeline infrastructure are among the main sources of numerous losses in the operation of pipelines. Issues of oil spillage have developed into grave sources of pollution both in the rural and urban areas, with resulting damage to the ecosystem & massive impact on livelihoods. Instances of pipeline failure can result in severe environmental catastrophes and human & financial losses.

1.1. Background

In the oil and gas sector, principally in Nigeria, there have remained countless occurrences of the wreckage of oil and gas pipelines ensuing in colossal discharge and depletion of crude oil with significant destruction to the environment as well as the means of livelihood for the rural settlers whose foremost occupation is agriculture (fishing and farming) [7]. These ugly activities also result in huge economic breakdown to the country, amidst loss of human lives, severe environmental pollution, and destruction of aquatic life. Pipelines are subject to numerous threats including third party damage, corrosion, mechanical failure of pumps and valves, land movement, and illegal tapping. These threats may lead to uncontrolled releases of products and the impact on human life as well as the environment can be significant.

Nigeria is one of the biggest producers of oil in the world and the first in Africa. Crude oil mining is regarded as the main source of income in Nigeria while agriculture and manufacturing industries as well as other income generation sectors are supportive. Crude oil is largely used by automobile companies across the world and the same can be said of other facets of the world economy [11]. The world consumes about 88 million barrels of petrol daily, while the US alone consumes about 44% of this on fuel for cars. Oil theft in Nigeria which is extremely on the rise as well as pipeline vandalism pose serious threats to the country’s national economy as the highest source of income [7]. Varied approaches using technology as countermeasures to pipeline vandalism have recorded little or no success. In addition, deployment of security agents such as the police, para-military and other non-governmental agencies has yielded very poor results due to the difficult terrain of the location of the oil and gas pipeline networks coupled with other criminal strategies adopted by the vandals of these pipelines.

Nigeria has lost roughly $14bn in the past twelve years as a consequence of crude oil spillage due to rupture of pipelines. In this period, a total of about 16,000 leakages of pipelines were logged. About 500 of these occurrences were due to rupture while vandalism contributed to the rest [12]. Nigeria loses nearly 850,200 barrels of crude oil every day due to vandalism by criminals and rupture of pipelines. This accounts for over 95% of these incidences, resulting in over $56bn in losses of the product and pipeline repairs in the past twelve years [12]. Moreover, the destruction meted on the environment, the outcome on the socio-economic wellbeing of the community as well as the price for environmental clean-up is immeasurable.

The resultant boomerang outcome on the nation's economy has led the country into crisis because of these wastages, which have also deteriorated with the nefarious actions of the criminals. Numerous efforts have been made to overcome this challenge, but a more enduring resolution is yet to be arrived at. Extensive interference has made the protection of the concerned areas against pipeline vandalism by the armed forces ineffective. Drones have also been suggested for monitoring pipeline networks, but they are quite costly and are not the ideal answer as they could be brought down by these same criminals and vandals [12].

Globally, the incidents of pipeline leakages have also led to huge economic losses [13]. For the past thirty years, pipeline accidents in the USA smashed properties that amounted to almost $7bn, killed over 500 people, besides thousands who were also injured [14]. For instance, on the 6th of Sept, 2010, a pipeline explosion incident in San Bruno community in California, killed over 7 persons besides over 50 persons who were also injured [14]. On July 26, 2010, a similar event occurred in Michigan, USA where over 800,500 gallons of crude oil leaked into River Kalamazoo with assessed charge of $800m [14] due to pipeline failure.

There are various reasons for pipeline damage. A column chart that shows the data (in percentages) of the foremost causes of pipeline disasters is shown in Figure 1.1. They comprise human negligence, pipeline corrosion, installation and erection process defects, defects arising from the manufacturing process as well as external causes [15]. External factors contributing to pipeline disasters include natural disasters (like earthquakes, landslides, floods, hurricanes), soil erosion and land subsidence, extreme weather conditions, accidental third-party damage, vandalism & sabotage, animal & plant interference, as well as marine hazards (for offshore pipelines). These external factors combined with other technical failures make continuous monitoring essential for pipeline integrity and safety.

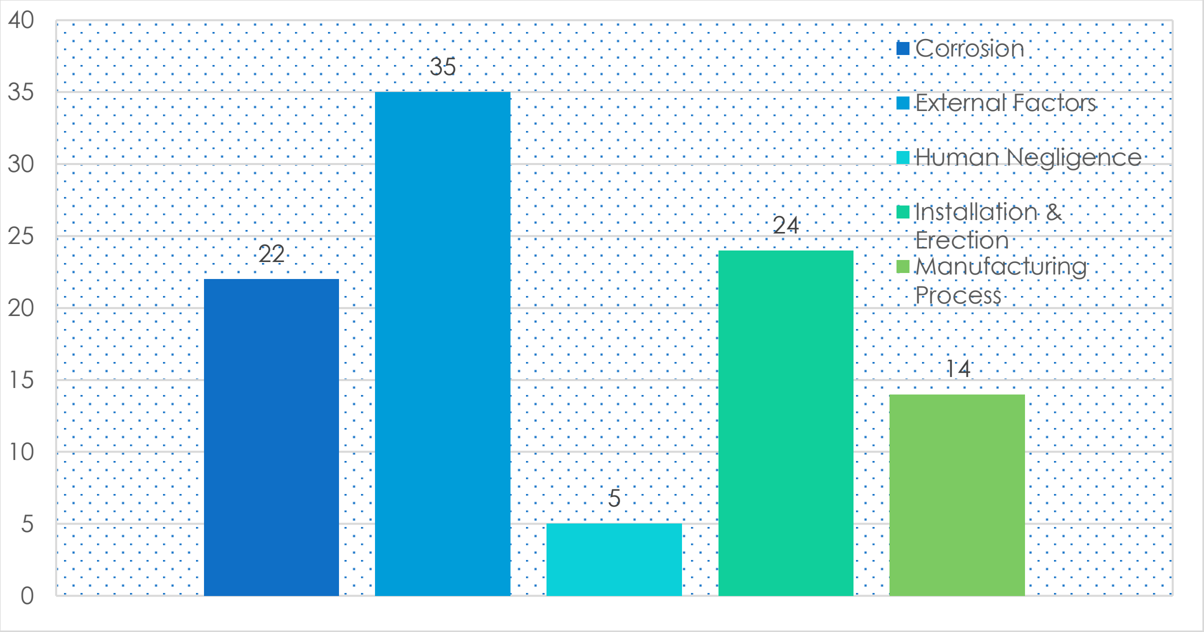

Figure 1.1: A column chart of the statistics of the causes of pipeline failures (adapted from [15])

From this data, it can be seen that the reasons for leakages in pipelines are difficult to avoid in its entirety as the causes of failures vary. Nonetheless, in order to lessen the effects of oil spills, it is essential to monitor pipeline networks for the real-time leakage detection or even prediction of leaks, since timely leak detection enables fast reactions to halt further oil discharge and proper maintenance of pipelines [15]. As a result, the rate of loss, injuries and other grave environmental and societal concerns due to pipeline failures are reduced. It thus becomes pertinent to cultivate suitable methods and techniques to alleviate these challenges.

Furthermore, considerable efforts in research have been developed and dedicated towards implementing leak detection and localisation technologies for pipeline networks as well as pipeline monitoring using different techniques. This is done to circumvent hazards and maintain a reliable and safe pipeline infrastructure. These efforts will be elucidated upon in the literature review segment. However, not much work has been done in the use of radio frequency sensors particularly radar sensors for remote monitoring of oil and gas pipeline networks, hence, the nitty-gritty of this project. Radar sensors have some distinctive merits over other sensors. They include operating at day or night, being operational in all weather conditions, etc.

This project therefore aims to discuss, analyse, and propose a more effective way of resolving these challenges. An efficient approach for solving these challenges will be by setting up some instrument to remotely monitor these oil and gas pipeline networks in real time and at each point in time as well as escalate strange movement to the appropriate authorities for prompt action and early response in order to evade a flooding or spillage occurrence and thereby curtail the wastage attributed to issues of pipeline spillage.

1.2. Literature Review

This section discusses and analyses a plethora of pipeline leakage detection technologies as well as a thorough review on remote monitoring of pipeline infrastructure [2].

Several pipeline monitoring schemes utilising varied working principles and techniques have been discussed and implemented in previous years. Current pipeline leakage detection techniques include: acoustic emission [16]–[19], optical fibre sensors [20]–[22], ground penetration radar [23], [24], negative pressure wave [25]–[27], analysis of pressure point [28]–[30], dynamic modelling [31], [32], infrared thermography, vapour sampling, digital signal processing as well as mass-volume balance [33]–[37]. These technologies have been categorised utilising different contexts. Some authors have categorised them into two (2) broad groups of ***hardware*** and ***software-based*** methods [38], [39]. Further research efforts [40]–[45] have also led to the organisation of obtainable leak detection schemes into three (3) main categories. They are *internal*, *external* and *non-technical* technologies [3], [5]. Internal leak detection technologies use pipeline instrumentation to monitor internal parameters such as flow rate, pressure, temperature and mass balance to detect leaks. The external leak detection technologies monitor the area surrounding the pipeline to detect leaks, rather than analysing internal pipeline parameters. Non-technical leak detection methods involve manual inspections and administrative measures to detect pipeline leaks. While internal and external methods have advantages, they also suffer from false alarms, environmental interference and difficulties in detecting small leaks. The radar-based system developed in this research overcomes these limitations by using RCS analysis to differentiate oil leaks from water or environmental noise, provide real-time remote monitoring without requiring extensive sensor networks, operating effectively in all weather and terrain conditions as well as reducing false positives by focusing on dielectric property variations in leaked substances. This novel approach ensures higher accuracy and reliability in pipeline leak detection while addressing the key weaknesses of existing methods. The remote monitoring of pipelines has also been accomplished by deploying sensing techniques to selected points by intelligent pigging, drones / autonomous underwater vehicles (AUVs) or utilising sensor systems as detailed in [3].

In [46], pipeline installations were monitored by deploying a low cost energy efficient liquid level monitoring system which used radio frequency identification (RFID) technique. The installations were monitored at each point in time using passive ultra-high frequency (UHF) RFID tag sensors operating between 865 – 868 MHz. The pipeline installations were monitored and any unusual liquid activity, detected by the RFID reader, is immediately reported to the related authorities for swift action in order to curb depletion attributed to issues of pipeline spillage. The passive UHF RFID tag sensors were also deployed to offer timely caution signals in the indication and control of engineering installations as well as in monitoring. The distinctive information on the chip of the tag sensor is conveyed through a wireless interface to a database for referencing. One of the advantages of this RFID based monitoring is that it reduces the need for manual inspection. Other merits include the fact that this monitoring technique provides continuous tracking at predefined checkpoints and capable of covering large pipeline networks. The demerits of this technique include high initial cost for deployment and maintenance as well as the fact that RFID sensors only monitor fixed points and may miss intermediate leaks. While mobile monitoring solutions provide flexibility, they lack real-time continuous tracking over the entire pipeline. The proposed radar-based solution which this thesis addresses ensures continuous and autonomous remote monitoring, thereby overcoming the intermittent nature of existing technologies.

The usage of acoustic emission techniques for pipeline leak detection have been described in a plethora of studies [47]–[49]. In [50], a reference standard for setting up and assessing acoustic emissions sensors installed for the detection of leaks in pipelines was designed and constructed. The reference standard comprised a short span of 2-inch diameter tubing with facilities for hosting numerous types of controlled leaks. The developed reference standard was very valuable not just for monitoring the infrastructure at a given threshold, but for also characterising source mechanisms as part of a combined method to numerical acoustic emission leak detection and location technology. By introducing numerous kinds of organised leakages, the effects of air injection and pressure were measured for thread leaks on the order of 0.1 gal/hr, a ratio that is significant in the framework of ecological protection guidelines.

In [51], leakages in a pipeline which was subjected to failure of a socket joint using acoustic emission technique and pattern recognition was suggested and experimentally investigated. The acoustic characteristics of leak signals in the socket and spigot pipe segments were also investigated. After feature extraction and selection, a classifier based on artificial neural network was established and good estimation accuracy of at least 96.9% was achieved. The study revealed that the major frequency of environmental noise was not up to 2 kHz whereas the major frequency of the acoustic signals as a result of the socket joint failure was focused on the range of 0 – 10 kHz. This indicates that over long distances, high sensitivity can be exhibited by acoustic emission-based methods. Nevertheless, there may be a requirement to increase the leak noise as an extra strategy for sensitive leak detection.

An experiment to detect gas leaks on a gas pipeline of length 3.13 km utilising measured acoustic waves was conducted by Jia et. al. in [22]. The sensors were situated at various positions along the gas pipeline. Acoustic waves produced as a result of the transmitted leakage from the point of rupture to every side of the pipeline at the velocity rate of the gas was observed throughout the experiment. However, the high frequency counterpart of the acoustic signal decayed considerably quicker than the low-frequency components. It was thus resolved that it was appropriate to detect leaks in gas pipelines utilising signals of low frequency. Localisation of leak points, assessment of the size of leaks, as well as early detection of leaks can be achieved by applying acoustic emission technique for leak detection in pipeline infrastructure [42]. However, the real sound of a leak can be masked by the effect of background noise. Numerous signal analyses schemes to overcome this problem have been proposed. They include interrogation techniques [16], wavelet transform techniques and the blend of acoustic sensors with other kinds of sensors [17], [48], [52]. These techniques have improved leak detection accuracy and helped mitigate noise interference. However, environmental noise, high computational requirements, and cost remain significant challenges. The radar-based system proposed in this research overcomes these issues by detecting leaks through dielectric property variations, making it more resilient to noise and environmental factors.

In summary, the acoustic emission techniques described earlier generally rely on the detection of sound waves generated by leaks in pipelines, and these methods have been extensively studied and implemented in real-world pipeline monitoring. The merits of this technique include high sensitivity to leak signals, also non-intrusive and does not require pipeline shutdown. However, the background noise interference can mask actual leak signals, especially at high flow velocities. It also requires additional signal processing techniques to improve accuracy and high frequency acoustic waves decay faster, limiting their detection range. While acoustic methods provide real-time leak detection, they suffer from significant interference due to background noise, limiting their effectiveness. This research therefore advances leak detection by using radar sensors that are unaffected by acoustic noise, thereby improving detection accuracy and reliability.

In [53], the usage of a cross-correlation technique for detecting numerous leak locations in buried pipelines was examined. Two vibration signals emanating from two detectors located at the ends of the buried pipe were measured and this technique was now used to detect various leaks simultaneously. The delay of the signals related to the leaks were also properly estimated using this technique. The results reveal the effectiveness of the technique in detecting several leak locations as the position of each detected leak was digitally calculated. The limitation of this technique is that it requires precise synchronisation of sensors and is sensitive to external vibrations and environmental noise. These factors can introduce errors in signal delay estimation, affecting the accuracy of leak localisation. In addition, the method may struggle with distinguishing weak leak signals from background noise in complex pipeline networks.

Furthermore, Oh et. al. [48] suggested an acoustic data condensation technique to improve pipeline leak detection. The results obtained revealed that the proposed technique effectively enabled abridged data sets in characterising the signature of the acoustic data. Normally, the benefits of utilising acoustic emission for pipeline monitoring include easy use of interrogation and ease of installation since it does not necessitate a halt of the system, in terms of shutdown, for purposes of calibration or installation. However, critical leakage might not be reliably detected as the leakage sound at a high flow velocity could be concealed by background noise.

Numerous studies have also been suggested for achieving localisation and detection of pipeline leaks by use of accelerometers [54], [55]. In [54], a model for an instantaneous monitoring system with the capacity to identify the presence of distinct incident leaks in pressurised pipelines was proposed. To achieve this, wireless accelerometers were located inside the pipeline network on the external of the valves linking the pipelines. Experiments were implemented on one-inch cast iron pipelines, one-inch and two-inch PVC pipelines using distinct event leaks in order to test the viability of the proposal. The vibration signal derived from each accelerometer was evaluated and analysed to classify the monitoring index at each sensor. The results from the developed model showed an accuracy of 98.25% in differentiating between leak and non-leak states. Furthermore, in [56], [57], the usage of hydrophones and accelerometers for monitoring pipeline networks was proposed. Leaks were artificially induced on a plastic pipe of a buried experimental facility. The obtained results also showed a false positive rate of 2 - 5% which defined the reliability of the system.

Several pipeline monitoring schemes based on optical fibre techniques have been suggested in literature [6], [58]–[60]. The efficiency in utilising distributed optical fibre sensors for detection of leaks in pipeline networks have been reported in [61]. The position of the leak was obtained utilising the time order of the anti-Stoke light received at the measuring station. Amongst the advantages of pipeline monitoring using optical fibre techniques is the ability to detect small leaks as well as monitor pipeline networks for intrusion [62] thereby safeguarding the pipelines from vandals/intruders. In [62], an optical fibre distributed acoustic sensing (DAS) system used for monitoring pipelines against third party interference and a fibre optic leak detection sensor was demonstrated and applied to provide monitoring along the entire length of a pipeline using the same fibre optic cable. The results showed that leaks within 1 – 5m along the pipeline were accurately located within 10 seconds of detection time, while the fibre optic DAS accurately detected threats within 1 -10 m of the pipeline. Moreover, perceived threats, say of a few metres up to 250m away from the pipeline network could also be detected.

Furthermore, another merit of the optical fibre-based techniques is the potential of monitoring pipeline networks as well as the capacity to correctly function in both surface and subsea pipeline networks [5]. In addition to these benefits, the fibre optic sensors are non-intrusive, hence, do not necessitate total closure and shut down of plant operations all through the period of installation. However, its demerits comprise short lifecycle as well as the incapability to estimate the leakage rate. In addition, the deployment of optical fibre system over an enormous and intricate network of pipeline infrastructure is challenging as optical fibres are brittle.

A related study centred on a macro-bend coated single mode fibre (SMF-28) optic sensor for pipeline leakage detection was proposed and developed in [63]. The fibre optic sensor comprised of a bending structure and the macro-bending loss was utilised as the sensing mechanism for the detection of pipeline leakage at low frequency. Through this system, the fibre optic sensor was characterised by measuring the power loss corresponding to the vibration at various bending radius as well as the number of wrapping turns. The results obtained showed that the fibre optic sensor scheme was capable of detecting leakages between the range of 20 Hz – 2500 Hz when implemented in a field test.

In [21], a Loop integrated Mach-Zehnder Interferometer (LMZI) fibre optic vibrational sensor was suggested to be implemented for monitoring pipelines as well as leakage localisation and detection. The vibration sensing was based on method of power demodulation utilising the torsion sensitive LMZI sensor. The system was verified in a 40m steel pipeline field. The outcome showed that at a pressure of 2 bar, the LMZI sensor detected a significant leak-induced at ~100 Hz, while at a pressure of 3 bar, a further ~288 Hz peak was detected during the leak. Both leaks detected at those frequencies had percentage errors below 3%.

In [6], a distributed fibre Bragg grating (DFBG) hoop strain sensor in cooperation with a support vector regression (SVR) for detection and localisation of leakages as well as the continuous monitoring of pipeline networks was designed and reported [6]. Several hoop strain signals were removed from the DFBG hoop strain sensors placed alongside the pipeline to reveal the leakage route. The study demonstrated the usage of various, distributed FBG hoop strain sensors in combination with a support vector machine algorithm to localise a leak point along a typical pipeline. A sequence of variations of strain on the terminal hoop were removed as the input variables to realise multi regression analysis as to localise the leak point. The factors of various kernel functions were optimised via 5-fold cross confirmation to achieve the peak accuracy in localisation of leakages. The results reveal the viability and robustness of the SVR method utilising measurements of multi-hoop strain signal for localisation of leaks in pipelines.

In summary, the optical fibre sensing techniques described earlier detect leaks and monitor pipeline integrity by detecting changes in light transmission caused by vibrations or environmental disturbances. Despite their high sensitivity, optical fibre sensors have deployment challenges and are prone to physical damage. The proposed radar-based system offers a more robust and scalable alternative, with higher durability and adaptability for various terrains.

In [64], a novel hybrid method for localisation and detection of leaks in straight pipelines was recommended. The performance of the proposed hybrid system was assessed using an experimental bench for straight pipelines. Also, equivalent experimental test programs for the localisation and detection of gas leaks were designed and conducted. The leak occurrence was preliminarily evaluated by the variance between the measured data and the value projected from the model as well as the fluctuating patterns of parameters in the leak condition. The leak point was located using the stimulus-response method. Results showed that the hybrid technique was successful in detecting and locating gas pipeline leaks.

In [65], an innovative sensor system was established for leak detection in supply pipes. The proposed system used a Continuous Wave (CW) Doppler sensing element which operated at 2.45 GHz and comprised a low power transmitter, a homodyne receiver as well as a digital signal processing unit. The results show that the leaks out of the pipe were detected via the Doppler frequency shifts of the reflected electromagnetic wave. Even though GPR technology has proved to be an operative non-destructive instrument for detection of buried objects [66], signals of GPR can easily be masked by other noises from the environment [23]. Several signal processing schemes have been reported in literature [67], [68] as a way of overcoming this shortcoming and enhancing the profile features of GPR signals. These enhancements include noise reduction & signal filtering, improved leak localisation, feature extraction & enhancement as well as higher signal-to-noise ratio (SNR).

Furthermore, the potential to detect oil spills resulting from a pipeline leak or rupture in and underneath snow utilising airborne GPR was assessed in [69]. It was found that the oil placed underneath the snow tend to decrease the impedance disparity through ice and resulted in inconsistent radar echoes with small amplitude. The results show that a thick oil film of 2 cm stuck between snow and ocean ice could be detected with a 50% drop in force of reflection by utilising 1 GHz GPR technique. The approach also showed improved performance despite the existence of weak SNR. The improved performance of airborne GPR in detecting oil spills under snow, despite weak SNR was achieved using lower frequency (1 GHz) GPR, impedance disparity analysis, as well as advanced signal processing techniques. For underground pipelines, synthetic aperture radar (SAR) could also be combined with GPR technology for pipeline monitoring and leak detection systems as they are reliable and better suited. SAR combined with GPR enhances pipeline monitoring and leak detection due to their complementary strengths as SAR provides wide-area coverage while GPR offers high resolution sub-surface imaging. However, GPRs suffer from high environmental noise interference and low penetration in wet conditions, whereas SARs require advanced signal processing for accurate leak identification as well as limited penetration depth in certain soil types. The radar-based system developed in this research significantly improves leak detection by using RCS analysis to differentiate oil spills from other substances, overcoming GPR's shortcomings.

The operational aspects of the most popular offline detection technologies (like GPRs, IR cameras and acoustic detectors) were compared to a novel offline detector proposed in [70]. The novel offline detector aimed to improve leak detection in underground pipelines by integrating acoustic sensors with a digital communication system. This hybrid approach significantly improves leak localisation accuracy and ensures continuous data collection even in complex underground pipeline networks. The authors also studied the potential of using the recent Terahertz imaging technology for the same application. The study concluded that Terahertz imaging technology has strong potential for detecting pipeline leaks due to its ability to penetrate non-metallic materials and provide high-resolution imaging of leak-induced anomalies. However, its practical application remains limited by certain challenges. While THz imaging shows promise, its limitations currently restrict widespread adoption in pipeline leak detection, particularly for underground and metallic pipelines. Further advancements in penetration depth and cost reduction would be required for broader implementation. Acoustic detectors were found the most suitable technology for the atmosphere in UAE, where the levels of humidity and consequently, soil moisture are high, because both of GPRs and IR cameras operational capability to detect leaks tend to decrease sharply as soil moisture increases. Conversely, a conventional acoustic detector has very limited scope of detection. The authors therefore proposed a method of expanding the sensing component of acoustic detectors by connecting acoustic sensors through a digital communications system using the 3G/4G networks to a monitoring centre with an acoustic spectrum analyser. The system was able to provide offline detection of leakages in underground pipelines remotely without deforming the surrounding environment or adjusting the acoustic detector’s analysing system. Simulation results showed the ability of the system to reconstruct the input noise signal at the end of the proposed network which is connected to the acoustic analyser [70]. The major limitation of the described technique is that conventional acoustic detectors have a very limited detection range. While the proposed system enhances sensing capabilities by using digital communication and remote acoustic spectrum analysis, it still relies on acoustic sensors, which may struggle with background noise, signal attenuation, and interference in real-world conditions. Additionally, factors like pipeline material, depth, and external environmental noise could affect the accuracy and reliability of leak detection.

Finally, a novel solution for leak detection based on soil moisture sensors based on the technologies of Internet of Things was proposed in [71]. Varieties of different leak scenarios were performed during the experimental trials and leaks in different places were examined. The results showed that the proposed solution provided great advantages in terms of leak detection and localisation.

Having considered these pipeline monitoring as well as leak detection techniques, this thesis aims to advance the frontiers of research in this area by deploying RADAR sensors for the detection, identification and localisation of oil leaks in pipelines without suffering from the effects of background and other noises which may mask the actual signal. Radar sensors are deployed for the real-time monitoring of pipeline networks against third party interference, thereby safeguarding the pipelines from vandals/intruders; and help in the detection and identification of oil leaks/spills in pipelines with a view to increasing pipeline productivity and integrity as well as offering protection of the environment.

Furthermore, existing pipeline monitoring technologies, while effective, have critical limitations, including environmental interference, deployment challenges, and difficulties in detecting small leaks. This research bridges these gaps by developing a radar-based remote monitoring system that:

- ✓ Provides real-time continuous pipeline surveillance
- ✓ Is immune to environmental noise (unlike acoustic and optical fibre methods)
- ✓ Accurately detects oil leaks using RCS variations, thereby offering early-stage identification.
- ✓ Can operate in both surface and underground pipeline networks
- ✓ Eliminates the need for predefined sensor placements, ensuring comprehensive coverage.

The integration of radar sensing with dielectric property analysis has demonstrated unprecedented accuracy in leak detection, setting a new benchmark in pipeline monitoring and leak detection technologies.

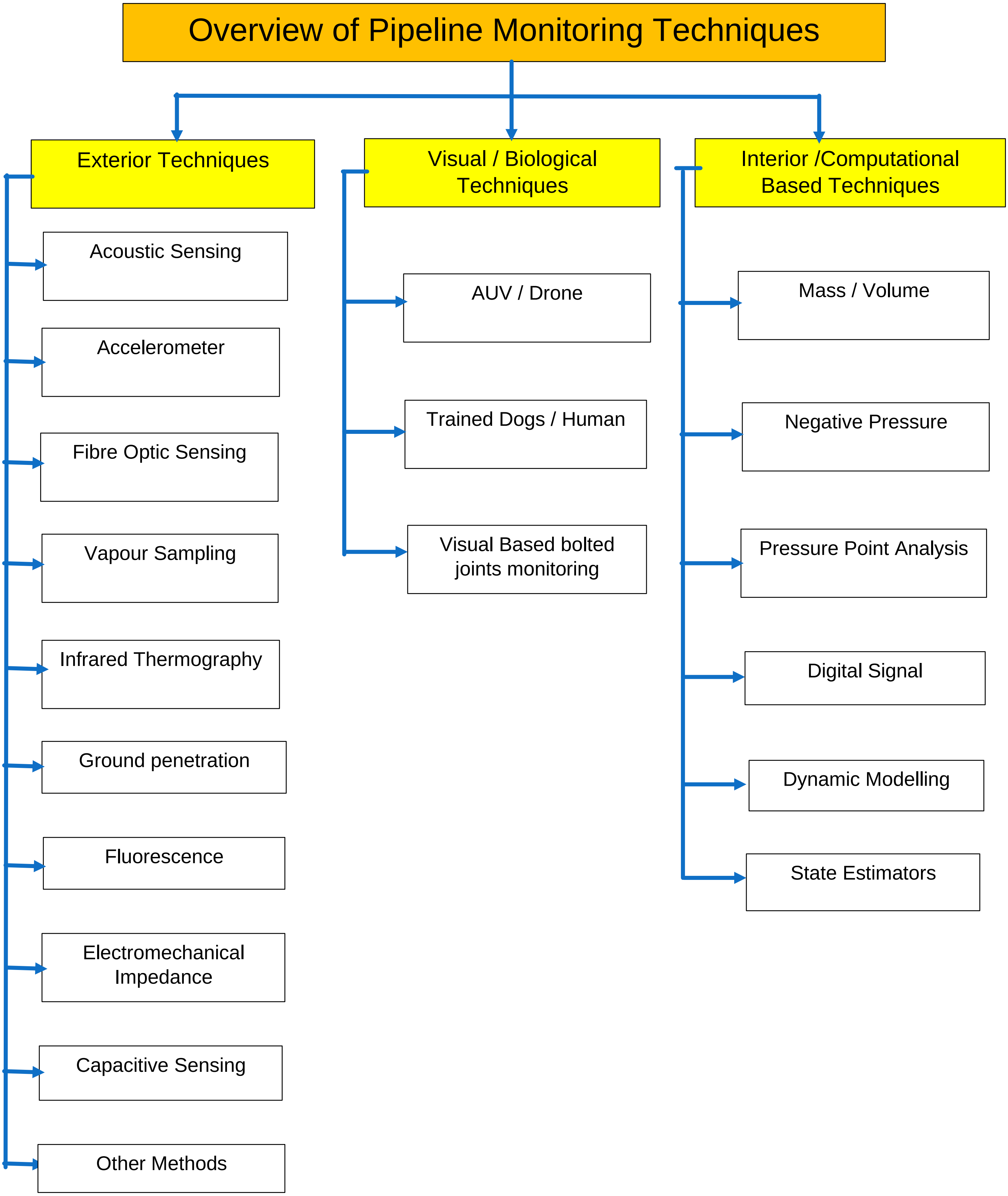

Figure 1.2: An Overview of Existing Pipeline Monitoring Techniques

Table 1.1 presents a structured comparison of the existing pipeline monitoring techniques, highlighting the advantages and limitations of these techniques as well as helping to understand their suitability, effectiveness and limitations in pipeline monitoring.

Table 1.1: Comparison of the various existing pipeline monitoring technologies

Pipeline Monitoring Technique	**Advantages**	**Limitations**
Exterior Techniques		
Acoustic Sensing	Can detect leaks by analysing sound patterns Works well for pressurised pipelines	Limited effectiveness in noisy environments Performance decreases in low-pressure pipelines
Accelerometer	Detects pipeline vibrations and structural changes Can identify sudden impacts or stress	May not differentiate between external disturbances and internal issues Requires regular calibration
Fibre optic Sensing	Provides continuous, real-time monitoring Can detect temperature and strain variations over long distances	High installation and maintenance costs Requires specialised interpretation
Vapour Sampling	Detects leaks by sensing escaped gases or chemicals Effective for detecting volatile substance leaks	Limited to detecting specific gases May not work well in high-wind environments
Infrared Thermography	Detects leaks based on temperature differences Non-invasive and works from a distance	Less effective in varying environmental conditions Cannot detect underground leaks effectively
Ground Penetration	Can detect underground leaks and anomalies Works in different soil types	Expensive and time-consuming Limited depth penetration
Fluorescence	Highly sensitive to detecting specific chemical compounds Effective in dark or underwater environments	Limited to certain types of leaks Requires specific fluorescence-inducing agents
Electromechanical Impedance	Effective for detecting structural integrity issues Can be applied to various materials	Needs direct sensor contact with the pipeline Requires complex signal analysis
Capacitive Sensing	Can detect changes in material properties near the pipeline Works in real-time	Sensitive to environmental changes May not be effective for all pipeline materials
Other Methods	Can be customised based on specific needs	May require integration with other techniques

Table 1.1 continued

Visual / Biological Techniques		
AUV / Drone	Provides aerial or underwater monitoring Can access remote or hazardous areas	Limited battery life and range Requires skilled operators
Trained Dogs / Human	Can detect leaks based on scent or direct observation Useful in hard-to-access areas	Not practical for continuous monitoring Subject to human error or fatigue
Visual-Based Bolted Joints Monitoring	Allows direct assessment of potential weak points Can identify corrosion or mechanical failures	Requires frequent manual inspection Limited to accessible areas
Interior / Computational-Based Techniques		
Mass / Volume	Measures fluid loss to detect leaks Works well for closed systems	Less effective for small leaks Requires highly accurate sensors
Negative Pressure	Detects pressure drops associated with leaks Effective for detecting sudden ruptures	Limited sensitivity to slow leaks False alarms may occur due to pressure fluctuations
Pressure Point Analysis	Identifies leak locations based on pressure variations Can detect internal anomalies	Requires multiple sensors Complex data interpretation
Digital signal processing	Uses advanced algorithms for leak detection Can process large amounts of data quickly	Requires sophisticated hardware and software May generate false positives
Dynamic modelling	Predicts potential failures before they occur Enhances proactive maintenance	Relies on accurate input data Requires continuous updating
State Estimators	Provides real-time monitoring and analysis Helps in predictive maintenance	Computationally intensive Requires integration with other systems

1.3. Problem Statement / Research Statement

Pipeline monitoring techniques for the detection and localisation of oil leaks have gained a lot of interest in literature as seen in the previous section. Recent studies have paid particular attention to what we call ‘non-radar’ techniques to circumvent hazards and maintain a reliable and safe pipeline infrastructure. However, not much work has been done in the use of radio frequency (RF) sensors particularly radar sensors for the remote monitoring of oil and gas pipeline networks. By using RF sensors, particularly radar sensors, for remote monitoring of oil and gas pipelines, several advantages can be achieved that other techniques cannot provide effectively which serves as a strong motivation for this work. They include:

- ✓ ***Penetration through different materials*** – unlike acoustic or infrared-based methods, RF sensors can penetrate soil, concrete and pipeline coatings, making them effective for detecting leaks without direct contact or invasive procedures.
- ✓ ***Long – range, remote monitoring*** – RF sensors especially radar-based systems, allow for wide-area coverage and real-time remote monitoring of pipelines over long distances, reducing the need for frequent manual inspections.
- ✓ ***Resilience to environmental conditions*** – unlike acoustic detectors which suffer in noisy or wet environments, and infrared cameras, which struggle with humidity, RF sensors perform consistently under various weather conditions, including fog, rain and high humidity.
- ✓ ***Enhanced leak localisation and classification*** – advanced signal processing techniques can enable precise leak localisation and even classification of leak types based on RF signal reflections, improving maintenance efficiency and reducing false alarms.
- ✓ ***Detection through buried and subsea pipelines*** – RF technology can be used for monitoring underground and underwater pipelines, where other methods like GPR or IR cameras become ineffective due to signal attenuation or scattering.
- ✓ ***Integration with wireless networks and Internet of Things (IoT)*** – RF sensors can be easily integrated with IoT-based pipeline monitoring systems, allowing for automated alerts, predictive maintenance and real-time data analytics.

This work therefore explores how RF sensors can provide a non-invasive, weather resistant and scalable solution for remote leak detection. By developing and optimising RF-based methods, we can contribute to safer, more reliable, and cost-effective pipeline infrastructure management. Radar sensors have some distinctive merits over other sensors which have just been extensively discussed. In addition, we are not using SAR technique due to the increased complexity, as well as because SAR technique requires more advanced signal processing amongst other reasons.

Furthermore, most pipeline monitoring techniques are not well grounded either in real-time or remote monitoring of pipeline infrastructure. This project therefore aims to discuss, analyse and propose a more effective way of resolving these challenges. One of the efficient ways to solve these challenges is what this project will be considering and that is by setting up some instrument to remotely monitor these oil and gas pipeline installations in real time and at each point in time. Furthermore, this approach will help in soliciting for prompt action as well as early response in order to evade a flooding or spillage occurrence. By so doing, we can now curtail the wastage attributed to the issues of pipeline spillage.

This concept of using radar sensors for the real time remote monitoring of pipeline infrastructure for the detection of oil leaks is a new concept which would be explored in greater depth in this thesis. To the best of the author's knowledge, there is little, or no work done in this regard in the literature, but some inspiration will definitely be taken from previous or current methods in order to contribute to solving these anomalies.

1.4. Objectives and Novel Contributions

The aim of this research is to investigate the methods and potential in using radar sensors as enabling technologies to remotely monitor oil and gas pipeline networks in real time. As oil pipeline networks span hundreds of thousands of kilometres, it is imperative to have a system with reduced complexity and which also rely on minimal signal processing to be able to be used efficiently and at scale.

Specifically, the research will seek to assess the feasibility and performance of using radar sensors to detect temporal changes in an area at large scale. These temporal changes could be as a result of change in the roughness parameters, or the dielectric properties of the area due to oil leaks from pipeline infrastructure etc.

Since we are trying to build an efficient system with reduced complexity, the simplest measurable parameter in that regard is surface reflectivity. In particular, the RCS of various soil samples (with oil and without oil) will be analysed. The varied reflectivity results from that soil sample will enable us to understand a soil that is soaked with oil and another that is not. The oil in the soil sample soaked with oil could be due to spills and leaks from oil pipelines, so an understanding of these differences in reflectivities will be utilised in improving the detection and identification of oil spills/leaks in pipeline infrastructure which is the major question this project addresses. There will be a marked difference in the reflectivity between the soil sample soaked with oil and the other soil sample not soaked with oil because of the gradient when it moves from ‘dry’ soil to the soil soaked with oil. The common denominator in this instance will be the roughness which should be ‘constant’ all through and the difference will just be the oil reflectivity. The radar parameters that will be modified or varied in the RCS analysis of the soil samples include the frequency, aspect angle, polarisation as well as the dielectric properties of the different soil types. Since various soils have different dielectric constants, these variations will influence their reflectivity and consequently the ability to distinguish between oil-soaked and dry soil.

The actual objectives and novel contributions of this project are thus highlighted below:

i. To investigate surface reflectivity from surfaces with or without oil contamination, as a function of surface roughness, aspect angle, frequency etc.
ii. To create an experimental setup that allows us to understand how oil affects the reflectivity of rough soil surfaces and at different levels based on some distinct parameters or features like surface roughness, aspect angle as well as the varied frequencies of our system.

iii. To conduct an experimental campaign in a proof-of-concept environment to validate findings obtained through electromagnetic wave simulations of soil surfaces considering different parameters and assess practical performance limits.
iv. To understand in specific terms what the RCS of different dielectric materials with varied roughness parameters are when they are contaminated with varying quantities of oil as well as their implications in the remote monitoring of pipeline infrastructure for the detection of oil leaks.
v. To investigate and understand the differences between electrically smooth and electrically rough surfaces and their implications in radar measurements

Finally, signal processing algorithms to verify analytical modelling in MATLAB will be applied to experimental, proof-of-concept data in a controlled environment using radar instruments. The measured performance of these models (both analytical and experimental) will be compared to specific requirements by the oil and gas industry.

The process objectives revolve around detecting oil-induced changes in soil/ground characteristics using RCS measurements. Below is a breakdown of how each step in the process contributes to achieving these objectives:

1. Detecting changes in soil reflectivity due to oil contamination

   Objective: is to differentiate between soil that is soaked with oil and soil that is not by measuring how radar waves interact with these surfaces.

   Process: use radar sensors to measure the RCS of soil samples. RCS is measure of how much radar signal is reflected back from a surface. Oil contamination changes the dielectric properties and surface roughness of soil, which affects its reflectivity.

   Goal: identify specific changes in RCS values that indicate the presence of oil, providing a reliable method for detecting oil leaks.
2. Large scale temporal change detection

Objective: to monitor large areas for changes over time that may indicate oil leaks, using temporal analysis of surface reflectivity.

Process: collect radar data at regular intervals from the same area; analyse differences in reflectivity over time; then focus on large-scale changes in surface roughness and dielectric properties caused by oil contamination.

Goal: detect potential oil leaks early by identifying significant temporal changes in the radar data.

3. Small-scale experimental validation in controlled environments

   Objective: to simulate real-world conditions in a controlled lab environment and validate my findings through experiments.

   Process: create a setup with soil samples that are both clean and contaminated with different quantities of oil and measure the RCS for each sample under various conditions like frequency, aspect angle and polarisation.

   Goal: understand how these parameters impact the ability to detect oil in soil and determine the optimal conditions for real-time monitoring.

4. Surface roughness analysis (Electrically Smooth vs. Electrically Rough Surfaces)

   Objective: study how radar signals behave on different types of surfaces (smooth vs rough) and determine their implications for oil spill detection.

   Process: classify surfaces into electrically smooth (small irregularities compared to the radar wavelength) and electrically rough (larger irregularities); then measure how these differences influence RCS values, especially when oil is present.

   Goal: develop a robust understanding of how surface roughness affects radar detection, ensuring accurate measurements in diverse environments.

5. Signal Processing and Analytical Modelling

   Objective: combine experimental data with mathematical models to improve accuracy and reliability of oil spill detection.

Process: use MATLAB to simulate radar wave interaction with soil and compare it with experimental results; then apply signal processing algorithms to reduce noise and improve detection sensitivity.

Goal: validate the analytical models with real-world data and refine them to meet the performance requirements of the oil and gas industry.

Figure 1.3 shows a graphical representation of the process objectives for detecting oil-induced changes in soil using radar sensors. The flow illustrates each step, from large-scale temporal change detection to small-scale experimental validation, surface roughness analysis, and finally signal processing and analytical modelling. These stages culminate in optimal detection and industry validation.

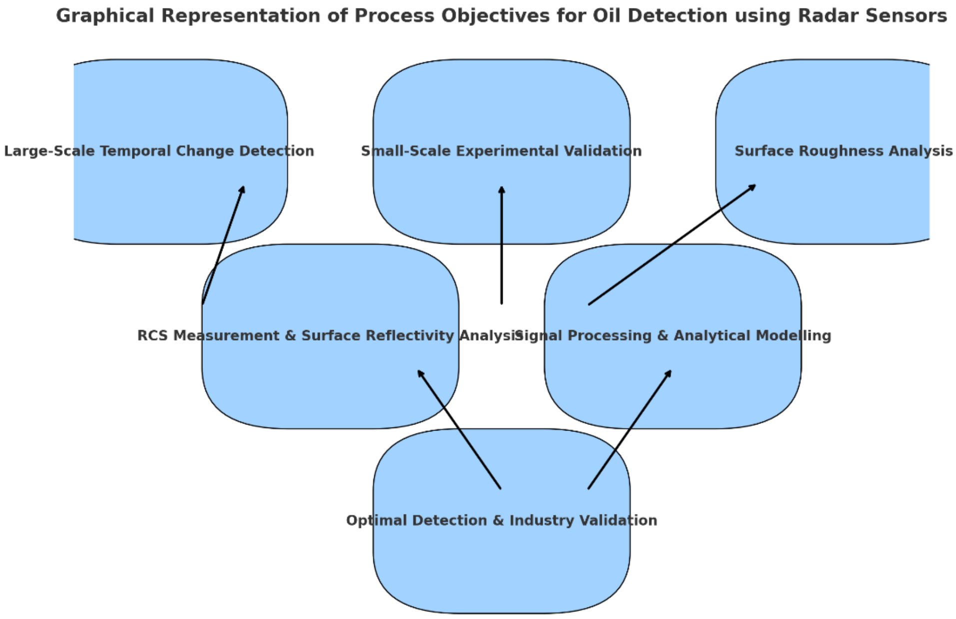

Figure 1.3: Graphical Representation of Process Objectives for Oil Detection using radar sensors

So, a summary of the process objectives earlier elucidated on are now highlighted below:

- **Measure RCS** of soil to detect oil-induced changes in dielectric properties and surface roughness

- **Monitor temporal changes** to detect oil spills at large scale in real time
- **Optimise radar parameters** (frequency, aspect angle, polarisation) for better performance.
- **Validate findings** in a controlled environment and integrate them with analytical models for practical deployment.

In summary, the novel contributions of this research are highlighted and re-emphasised below:

- Development of a simplified, low-complexity radar-based monitoring system
- Investigation of surface reflectivity and RCS for oil-contaminated surfaces
- Experimental validation through proof-of-concept setup
- Analysis of electromagnetic response of varying dielectric properties and roughness parameters
- Identification of electromagnetic differences between electrically smooth and rough surfaces
- Integration of analytical modelling and signal processing algorithms in MATLAB
- Industry-relevant solutions for oil spill detection

1.5. Thesis Outline / Organisation

This thesis consists of eight chapters and a section for appendices and bibliography. The outline of the thesis can be presented as follows:

In ***Chapter 2***, the fundamentals of RADAR is presented and discussed, including a brief history of RADAR as well as types of RADAR. The chapter will provide a thorough analysis of key concepts such as the radar equation, radar waveforms and pulsed continuous wave radar, ensuring a detailed and in-depth exploration of these topics. Radar sensors will also be discussed in greater detail and some simulations performed to buttress the fundamentals and applications of radars. The results from the computational modelling will also be discussed in addition to the implications and relevance of the results.

In ***Chapter 3***, a rough surface model is developed and presented including a thorough analysis of the properties of dielectric materials as well as the propagation of electromagnetic waves in dielectric materials. The mechanism of reflection and transmission from surfaces is also discussed extensively and the propagation over a reflecting surface is thoroughly analysed. In addition, the Rayleigh roughness criterion is x-rayed and its implication in the reflection from a rough earth as well as the reflection coefficient for a flat smooth earth. We shall also look at how our rough surface model reflects electromagnetic wave and its implication in terms of determining the difference between a surface with oil and another surface without oil. It will conclude with a thorough analysis of the scattering problems and electromagnetic fields as well as the generation of randomly rough isotropic surfaces.

In ***Chapter 4***, the results of the electromagnetic wave simulation of a rough surface model using CST are discussed and thoroughly analysed. The RCS of common objects like flat plate and sphere is extensively discussed and thoroughly analysed. Furthermore, the RCS of a lossless material such as a perfect electric conductor (PEC) is x-rayed, and the properties of this rough surface model is discussed. For lossy materials such as sandy soil, the RCS is also analysed as well as the results thoroughly explained. The implications of the varied dielectric materials as well as their relationship with surface reflectivity is also discussed and analysed in deeper detail. The interpretation and implications of these results are also x-rayed and discussed. Finally, the reflectivity of the developed rough surface model which is periodically ‘filled’ with oil as a result of the reduced surface roughness is also thoroughly analysed and discussed. We will also consider the experimental verification of theoretical results.

In ***Chapter 5***, the experimental plan / set up is discussed in greater depth. The methodology for carrying out experimental measurements is discussed in more detail. In this chapter, we also talk about the calibration of the experimental set up as well as the measurements of the three rough surface profiles in oil. The implications and interpretation of these results will be x-rayed and discussed in greater detail. In addition, the theoretical verification of the results of the experimental rough surface model will also be carried out and both sets of results will be compared and analysed with salient conclusions drawn from them as well as the implications of these results. We shall also consider in greater depth, how the surface reflectivity changes when varied quantities of oil is introduced onto the rough surface. The impact of oil on these modified rough surfaces will be analysed and measurements using the 3 rough surface profiles in oil will be extensively discussed and analysed. the rough surface model is integrated with a radar system. Finally, the measurement parameters from both the developed rough surface and experimental models are verified and compared with each other as well as against industry benchmarks in the oil and gas industry.

In ***Chapter 6***, the conclusions of the study overall including findings and outcomes from the research are presented. In addition, the limitations encountered are x-rayed and the section on future work shows possible further studies based on this thesis.

1.6. Publications

E.Uche, M.Cherniakov, M. Antoniou, “Oil leak detection using X-band radar”, IEEE Sensors Journal, *in preparation*

E. Uche, M.Cherniakov, M. Antoniou, “Surface reflectivity analysis for oil leak detection – simulation results”, IET Radar, *in preparation*

Chapter 2. FUNDAMENTALS OF RADAR

Radar has been a hugely significant technology in terms of its military applications during World War II [72]. RADAR which is an acronym based on the phrase “***RA****dio* ***D****etection* ***A****nd* ***R****anging*”, is an electromagnetic based detection system that works by radiating electromagnetic waves outwards in space to illuminate an area and then studying the reflected back waves otherwise known as echoes emanating from a target(s) within the illuminated area in order to detect this target(s) as well as determine its location(s) [73], [74]. Detection refers to whether the target (which can be stationary or non-stationary) is present or not. Ranging refers to the distance between the radar and the target. A radar system can therefore be used to determine the ranges, velocities, and angles of targets. In a computational environment, the information acquired by radar is processed. As a result, it is possible to now retrieve information about targets [73].

Despite the fact that radar systems were created for military purposes, they have been implemented in a variety of fields, including air traffic control, weather forecasting, astronomy and navigation [75]. In addition, there are a number of types of radar employed for a range of purposes and employing a number of techniques, such as monostatic and bistatic radars, pulsed radars, continuous wave radars, secondary surveillance radars as well as Synthetic Aperture Radar (SAR) [73], [74]. Further details about these types of radars will be explored in greater depth as we progress in this thesis.

2.1. Introduction

A radar system [76] therefore comprises of at least a transmitter, a target and a receiver as shown in Figure 2.1 which also contains a pictorial description of its basic principle.

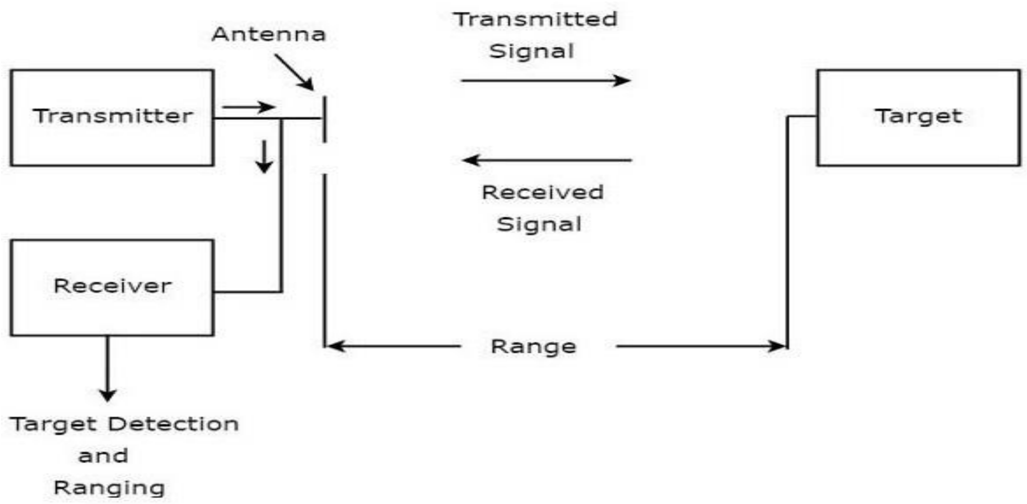

Figure 2.1: A radar system and a pictorial description of its working principle

Radar signals radiated from the transmitter antenna propagate in space and illuminate an area that depends on the antenna beam pattern. The target within this area scatters the incoming energy of the signal. A small amount of scattered energy reaches the receiver antenna as the received signal. The received signal is a delayed version of the transmit signal. By using this delay, the distance between the radar and the target can be calculated easily. Radar is a significant instrument in remote sensing because it can operate under extreme weather conditions, whether it is day or night, and over long distances. As a result, radars can be used for various applications on ground, on sea and in space. In addition, radars can discriminate moving targets, even with undesired reflections emanating from the illuminated area, and other objects. Radars can thus measure the comparative speed of these targets as well as estimate the radial velocity with the aid of the Doppler effect [77].

Radar systems can be classified into different categories based on various criteria. The criteria could be in terms of the separation between the transmitting and the receiving antennas or in terms of the application of the radar system [73]. If the phases of the transmit signals are the same with each other, the radar is referred to as a coherent radar. This kind of radar enables velocity and angle estimation by using the phase difference of the incoming signals. When two consecutive coherent signals are transmitted towards a moving target, a phase difference occurs between two received signals due to the movement of the target. By exploiting this phase difference, velocity can be estimated. Two receivers are also needed to estimate the angle. If the scattered signal is received by multiple antennas which are separated by a small distance, a phase difference depending on the target's angle occurs between received signals. By using this phase difference, relative angle estimation can be easily realised.

2.2. Brief History of RADAR

The basic concept of radar, which is the detection and location of reflecting objects, was first demonstrated through the experiments conducted by the German physicist between 1885 and 1888. Following this other evidence on the radar method appeared and was examined by scientists from many other countries, for example Britain and the USA. This method did not become truly useful until the transmitter and receiver were collocated at a single site and pulse waveforms were used. From the 1930s to World War II, radar was rediscovered and many radar systems were developed almost simultaneously and independently in many countries [78]. The original systems measured the range to a target via time delay, and the direction of a target via antenna directivity. It was not long before Doppler shifts were used to measure target speed. Then in 1951, it was discovered that the Doppler shifts could be processed to obtain fine resolution in a direction that was perpendicular to the range or beam direction. This method was termed Synthetic Aperture Radar (SAR), which referred to the concept of achieving high resolution in the cross-range dimension by taking advantage of the motion of the platform carrying the radar to synthesize the effect of a large antenna aperture through signal processing [79]. This concept of SAR will be x-rayed in greater depth as we progress in this thesis.

The phenomenology of radar goes back to the 1800s when Heinrich Hertz demonstrated radio wave reflection by metallic objects at 455 MHz [80]. Nicola Tesla, in 1900 suggested that the reflection of EM waves could be used to detect metallic objects. The first patent on radar was acquired in 1904 by Christian Hulsmeyer, who called this a 'Remote Object Viewing Device' for obstacle detection and ship navigation. Hulsmeyer developed a prototype device to locate nearby ships in thick fog that were otherwise invisible to the human eye.

However, the late nineteenth and early twentieth century saw the emergence of technologies that eventually led to contemporary radar systems. At that time, radar applications were primarily focused on military and commercial use. Modern radar was rapidly developed during World War II for its use in air defence, such as long-range air surveillance and short-range low altitude target identification. In 1939, the US Navy created the acronym, ‘RADAR’. The invention of the cavity magnetron by British Physicists John Randall and Harry Boot marked a significant advancement in the use of radar. Cavity magnetron shortened the radio wave pulse and allowed for compact radar systems.

In the post war period, improvements were made in developing continuous wave (CW) and pulsed radar systems for military and civilian applications. Notable civilian applications of radar were the weather radar and the air-traffic control radar for air traffic safety in airports. The radar gun was later developed during the 1950s and 1960s and was used by police officers to ensure the speed limits of vehicles.

Since the 1970s, digital technology has undergone incredible development, making the signal processing requirements for contemporary radar achievable. Significant advances were made in the airborne pulse-Doppler radar, which enhanced its ability to detect aircraft amid dense ground clutter. Over the next decade, technology further evolved, and radars could distinguish between different types of targets. As computer technology advanced, more information about the characteristics of targets and the surroundings in which radar functions became available.

2.3. Types of RADAR

Broadly, radar can be classified into two types, as indicated in Figure 2.2.

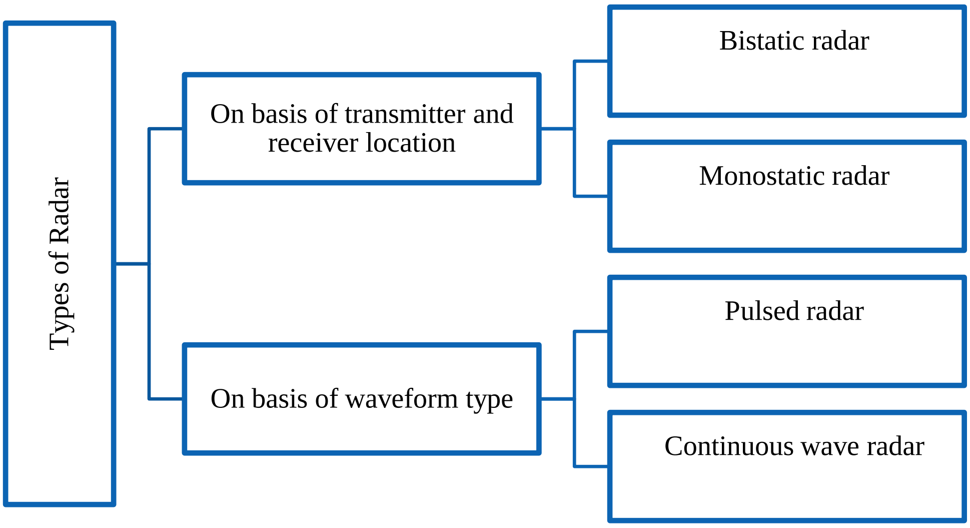

Figure 2.2: Major Types of Radars

These types of radars will be briefly discussed in the following subsections as we progress in this thesis.

2.3.1. Monostatic RADAR

A monostatic radar has a collocated transmitter and receiver. As a result, the radar can transmit or receive at a specific instant of time [81]. The radar configuration for a monostatic radar is shown in Figure 2.3.

Figure 2.3: Configuration of a Monostatic Radar

2.3.2. Bistatic RADAR

In a bistatic radar, the transmitter and the receiver are at separate locations if observed from the target’s perspective. Therefore, they can operate simultaneously [81]. The radar configuration for a bistatic radar is shown in Figure 2.4.

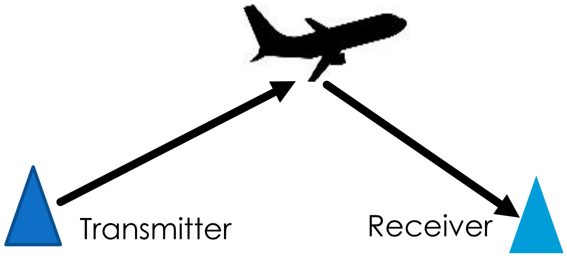

Figure 2.4: Configuration of a Bistatic Radar

Radar sensors that are a subject of discussion in the presented work are monostatic.

2.3.3. Pulsed and Continuous Wave RADAR

Pulsed radars transmit a short-duration pulse and then go into listening mode. During this time, they receive and process the echo signal before the new transmission. These radars are commonly used for longer ranges. A typical example of pulsed radar is airborne radar [82].

Continuous wave radars operate continuously and therefore have lower average power than pulse radars. Therefore, they are more suitable for comparatively short-range operations. The continuous wave radars are further divided into the unmodulated continuous wave radars and the modulated continuous wave radars. The unmodulated continuous wave radars transmit continuous wave signal of specific frequency and are used to measure the speed of targets, such as radar guns used to monitor the speed of vehicles. While for the modulated continuous wave radars, the continuous wave is modulated with either frequency modulation – frequency modulated continuous wave radars (FMCW) or phase modulation – phase modulated continuous wave radars (PMCW). These radars are used to estimate the range of the targets as well as the relative speed.

In this project, a stepped frequency waveform is used. A stepped frequency waveform is a type of waveform that consists of a series of discrete frequency steps, each with a constant frequency and amplitude for a specific duration of time. This type of waveform is often used in radar systems, where it allows for the precise measurement of distance and velocity of targets.

2.4. RADAR Sensors

A radar sensor is any device that can convert radio or microwaves into an electrical signal. Radar sensors make use of radio waves to determine the relative distance and position of an object to the sensor. Radar sensors are a key technology that is rapidly evolving and have become a popular choice in many machine vision and automation applications. In relation to this project, there are a lot of advantages of radar over other sensors. Radar sensors are able to operate in all weather conditions and have the capability of sensing either in the day or night. Radar sensors are also sensitive to the roughness of a surface as well as the dielectric materials they are sensing. In many areas, we are benefitting from innovative sensor solutions. A radar sensor works on the detection of transmitted and reflected electromagnetic radiation. Some of the other characteristics of the technology of radar sensors include the following –

- ✓ Contactless – The radar detection measuring principle involves no contact at all. The sensor does not have to have direct contact with a material or object being detected as radar sensors reliably measure and detect even at a long distance.
- ✓ Anonymous – Radar sensors are used for industrial and automotive applications and don’t produce images. They merely form a sort of cloud of dots, which gives a rough indication of the contours of objects as well as the infrastructure of the surroundings. Contrary to a camera, people are not identifiable.
- ✓ Comprehensive data – Radar sensors detect movements and stationary objects. After signal processing, the data received through reflection provides a variety of information about the detected objects, vehicles, animals, or persons. In addition, data such as direction of movement, speed, distance and angular position in relation to the sensor are available.

- ✓ Multi-dimensional detection – Depending on its modulation, radar collects extensive data about its environment. This enables sensors to also record the environment in three dimensions, like a human eye.
- ✓ Wide range variability – Radar waves spread freely in space or in the air. Depending on the sensor’s technical development and purpose, extreme ranges can be achieved if necessary. For commercial applications, the coverage range usually varies from one centimetre to a few hundred metres.
- ✓ Material penetration – The electromagnetic waves of radar sensors penetrate various materials. Plastics are very well suited for covering or designing a radome (antenna cover). It allows the sensors to be integrated discreetly into a product design.

Radar sensing relies on the principle of reflection of electromagnetic waves by surfaces and Table 2.1 provides a rough overview of what makes radar sensors different from other sensor technologies.

Table 2.1: Comparison of radar sensors to other sensor technologies.

	PERFORMANCE LEVEL			
FEATURES	RADAR	INFRARED	ULTRASONIC	LASER
Application flexibility	BEST	BAD	BAD	BAD
Resistance to moisture, dirt and temperature	BEST	BAD	BAD	BAD
Speed detection	BEST	BAD	GOOD	BEST
Accuracy sensitivity	BEST	BAD	BEST	BEST
Resolution (separability)	BEST	BAD	BEST	BEST
Direction capability	BEST	GOOD	GOOD	BAD
Distance measurement	BEST	GOOD	BAD	BEST
Penetration of materials	BEST	BAD	BAD	BAD
Size of solutions	BEST	BEST	BEST	BAD
Cost	GOOD	BEST	BEST	BAD

Not all radar is the same. The radar sensors often differ in terms of functions and properties. This is because, depending on the application, different configurations are required to conduct the desired measurement. The differences between different radar types are defined via two basic parameters which are the frequency band used and the modulation.

In terms of the structure of a radar sensor, in addition to its front end, a complete radar sensor consists of units for signal conditioning as well as signal processing. Signal conditioning and processing analyse and interpret the signals provided by the front end. Most radar sensors also incorporate a number of signal processing electronics to process phase information about the detected waves that can be converted into information about object distance and angle. These elementary components may be supplemented with a radome, housing, lens and a component carrier.

2.5. RADAR Equation

In an ideal free-space environment, radar waves travel in straight lines without attenuation or distortion. The radar equation indicates trade-offs among radar parameters, and it can be used to calculate the maximum detectable range, sensitivity and signal to noise ratio (SNR) [73], [77]. The first part of the equation (2.1) shows the power loss of the transmitted signal in free space until reaching the target. The second part is responsible for the power loss of the back-scattered signal towards the radar receiver in free space. The last term of the equation is related to the size of the receiver antenna.

$$P_r = \frac{P_t G_t}{4\pi R^2} * \frac{\sigma}{4\pi R^2} * A_e \tag{2.1}$$

where P_r is the received signal power, P_t is the transmit signal power, G_t is the transmitter antenna gain, *R* is the range i.e. the distance between the radar and the target, σ is radar cross section, A_e is the effective aperture of the receiver antenna. This effective aperture of the antenna is given by equation (2.2), where G_r is the receiver antenna gain.

$$A_e = \frac{\lambda^2 G_r}{4\pi} \tag{2.2}$$

The maximum detectable range can be calculated by using equations (2.1) and (2.2). When the received signal power P_r is equal to the minimum received power P_{rmin} which is required to detect a target, range R can be expressed as maximum detectable range R_{max} . As seen from equation (2.3), if the transmit power P_t is increased by a given factor, R_{max} will increase only to the fourth root of that factor. Equation (2.3) therefore illustrates that:

$$R_{max} = \sqrt[4]{\frac{P_t G_t G_r \sigma \lambda^2}{(4\pi)^3 P_{rmin}}} \tag{2.3}$$

The minimum required received power P_{rmin} represents the sensitivity of the radar receiver and it is limited by the thermal noise of the receiver. Noise power is expressed by equation (2.4)

$$P_n = k.T.B.F \tag{2.4}$$

where P_n is the Noise Power, *k* is the Boltzmann's constant, *T* is the Noise Temperature, *B* is the Bandwidth, and *F* is the Noise Figure.

In equation (2.4), *k* is a constant and *T* is not an adjustable parameter. Therefore, there are only two parameters which can be altered to adjust the noise power. High bandwidth is desired to have a better resolution. Hence, there should be a trade-off between high bandwidth and noise power. On the other hand, the noise figure can be reduced as much as possible to keep the noise power at a certain level.

Noise figure is a measure which shows how much the signal is degraded by the receiver. Each component in the receiver chain contributes to the noise figure. However, it can be said that the first component in the chain dominates the system noise figure if it has more than 10 dB gain. Therefore, a low noise amplifier is always used after the antenna as the first component in the receiver chain. The noise figure of a system is given in equation (2.5) as

$$F_{system} = F_{LNA} + \frac{F_{second-1}}{Gain_{LNA}} + \frac{F_{third-1}}{Gain_{LNA} * Gain_{second}} + \cdots \tag{2.5}$$

Signal to noise ratio (SNR) is one of the most important parameters. It must always be higher than a specific value depending on the sensitivity of the receiver. SNR can be calculated with the ratio of equation (2.1) to equation (2.4). However, until that point, the radar equation has been presented without considering losses. As mentioned in [73], there are five different losses namely: system loss, transmit loss, the atmospheric loss, the receiver loss, and the signal processing loss. If the sum of all the losses is represented by L_S, SNR can thus be represented by equation (2.6) as

$$SNR = \frac{P_r}{P_n} = \frac{P_t G_t G_r \sigma \lambda^2}{(4\pi)^3 R^4 kTBFL_s} \tag{2.6}$$

2.6. RADAR Waveform – Stepped Frequency Waveform

Radars are critical systems used for detecting and ranging objects. Traditional radar waveforms such as continuous wave (CW) and pulse waveforms have limitations in range resolution and penetration capabilities. Stepped Frequency Waveform (SFW) addresses these limitations by combining the benefits of both pulse and frequency modulated signals.

SFW offers several advantages over traditional radar waveforms:

1. **High Range Resolution**: By using multiple frequencies, SFW can achieve finer range resolution than single-frequency pulse waveforms.
2. **Improved Penetration**: The varying frequencies can penetrate through different materials better than a single frequency, enhancing detection capabilities in cluttered environments.

3. **Reduced Ambiguity**: The stepped frequency approach reduces range and Doppler ambiguities compared to CW radars.
4. **Flexibility**: SFW allows for flexible waveform design to adapt to various operational requirements and constraints.

Consider a radar system that transmits a sequence of *N* pulses, each with a different frequency. The parameters are defined as follows:

- Initial frequency f_o
- Frequency step Δf
- Number of steps *N*
- Pulse width *T*

The n-th transmitted pulse can be expressed mathematically in equation 2.7 as:

$$Acos\left(2\pi\left(f_o + \frac{n}{\Delta f}\right)t\right) \qquad 0 \leq t < T \tag{2.7}$$

Where n = 0, 1, 2, ……. N – 1 and A is the amplitude.

Assuming a single target at range R with reflectivity σ, the received signal for the n-th pulse can be modelled as equation 2.8:

$$r_n(t) = \sigma Acos\left(2\pi(f_o + n\Delta f)\left(t - \frac{2R}{c}\right)\right) \tag{2.8}$$

Where c is the speed of light.

The received signals are sampled and stored in a matrix *R* of size *N x M*, where *M* is the number of samples per pulse given in equation 2.9 as:

$$R_{n,m} = r_n(m\Delta t) \tag{2.9}$$

with Δt being the sampling interval.

In the time domain, each transmitted pulse has a duration of *T* seconds and is separated from the next by the same duration. The sequence of pulses with different frequencies forms the stepped frequency waveform.

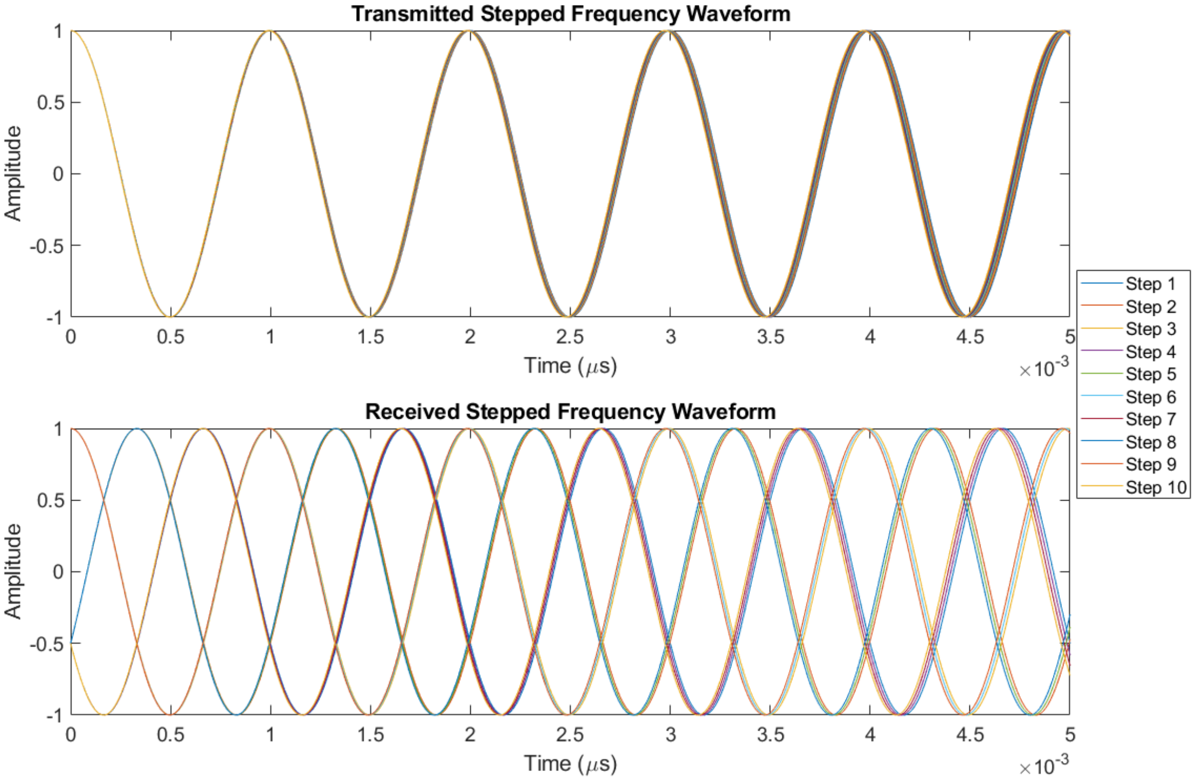

Figure 2.5: Transmitted and received stepped frequency waveforms

Figure 2.5 illustrates the transmitted and received stepped frequency waveforms. The transmitted waveforms consist of a series of pulses with increasing frequency. The received waveform is a delayed and attenuated version of the transmitted waveform depending on the target’s range and reflectivity.

To analyse the waveform in the frequency domain, a fast Fourier Transform (FFT) is applied on the received signal for each pulse as shown in equation 2.10:

$$R_n(f) = \sum_{m=0}^{M-1} r_n(m\Delta t)e^{-j2\pi f_m \Delta t} \tag{2.10}$$

The frequency domain representation shows the discrete frequency components corresponding to each pulse. The spectrum consists of spikes at the transmitted frequencies. Each spike in the spectrum corresponds to a specific transmitted frequency, providing a clear view of the frequency components. The results are shown in Figure 2.6.

2.7. Propagation and Target RCS

Radar systems rely on the transmission and reflection of electromagnetic waves to detect, locate, and characterise objects. However, the propagation environment, including atmospheric conditions, terrain, and obstacles, significantly affects the behaviour of these waves, thereby influencing overall radar performance. Several factors play critical roles in shaping the propagation characteristics of radar signals. These include the frequency and wavelength of the radar signal, atmospheric conditions such as humidity, temperature, pressure, the nature of the terrain and surface features, and the presence of obstacles and clutter in the environment.

2.7.1. Atmospheric Effects on Radar Propagation

The atmosphere impacts radar wave propagation through various mechanisms, including attenuation, refraction, and scattering. These effects are highly frequency-dependent and vary with the prevailing atmospheric conditions.

2.7.1.1. Attenuation

Atmospheric attenuation arises from absorption by atmospheric gases and scattering by particles such as rain and fog. This results in signal degradation and limits the radar's effective range. The total attenuation A (dB/km) is the sum of molecular absorption and scattering losses, as represented by Equation 2.11 as:

$$A = A_{abs} + A_{scat} \tag{2.11}$$

Molecular Absorption occurs due to the interaction of radar waves with atmospheric gases such as oxygen and water vapour. This effect becomes more pronounced at higher frequencies, particularly in mmWave radar systems.

Scattering losses result from the interaction of radar waves with particles like raindrops, fog, and dust. The extent of scattering depends on the size of these particles relative to the wavelength of the radar signal, with larger particles causing greater scattering and attenuation.

2.7.1.2. Refraction

Refraction occurs when radar waves bend due to variations in the refractive index of the atmosphere. The refractive index is influenced by temperature, pressure, and humidity. Refraction can lead to three key effects:

- Sub-refraction: Radar waves bend away from the Earth’s surface, reducing the detection range.
- Super-refraction: Radar waves bend towards the Earth, increasing the detection range.
- Ducting: Under specific conditions, radar waves can become trapped in a duct, significantly extending the radar range beyond normal limits.

2.7.1.3. Scattering and Clutter

Scattering from the ground, vegetation, and man-made structures introduces clutter, which can obscure target returns and reduce radar performance. The characteristics of clutter depend on the radar frequency, polarisation, and incidence angle, with different environments exhibiting unique clutter signatures.

2.7.2. Terrain and Surface Effects

The nature of the terrain and surface features further influences radar wave propagation through reflection, diffraction, and shadowing. These effects can affect detection accuracy and create blind spots in radar coverage.

2.7.2.1. Surface Reflection

Radar waves reflect off surfaces such as water, soil, and concrete with the reflection behaviour depending on the surface material and incidence angle. Smooth surfaces result in specular reflections, while rough surfaces scatter the radar waves in multiple directions, leading to diffuse reflections.

2.7.2.2. Diffraction

Diffraction allows radar waves to bend around obstacles, a phenomenon particularly significant in hilly or urban environments. This effect enables waves to propagate beyond physical obstructions such as buildings and terrain features, albeit with reduced strength.

2.7.2.3. Shadowing

Obstacles such as buildings and mountains create shadow regions, where radar waves cannot penetrate. These shadow zones result in blind spots in radar coverage, reducing situational awareness and target detection capability.

2.7.3. Multipath Propagation

Multipath propagation occurs when radar waves reflect off multiple surfaces before reaching the target or returning to the radar receiver. This phenomenon can have both constructive and destructive effects on radar performance:

- Ghost targets: False detections caused by delayed reflections from multiple paths.
- Signal fading: Reduction in signal strength due to destructive interference between multiple signal paths.
- Phase shifting: Alteration in the phase of the received signal, which affects coherent processing and degrades signal quality.

Figure 2.6 shows the effect of propagation on radar returns for free space as well as when the electromagnetic wave undergoes attenuation, refraction and reflection. The plot demonstrates how radar signal strength degrades with distance and additional environmental losses. Free space loss is the baseline, while atmospheric attenuation and refractive bending compound energy loss. Reflection introduces further degradation, often simulating worst-case propagation paths. The analysis helps contextualise how real-world factors influence radar signal strength. The radar range equation forms the baseline for all conditions where a monostatic radar is used, and a standard atmospheric model is assumed for a flat terrain with line-of-sight propagation

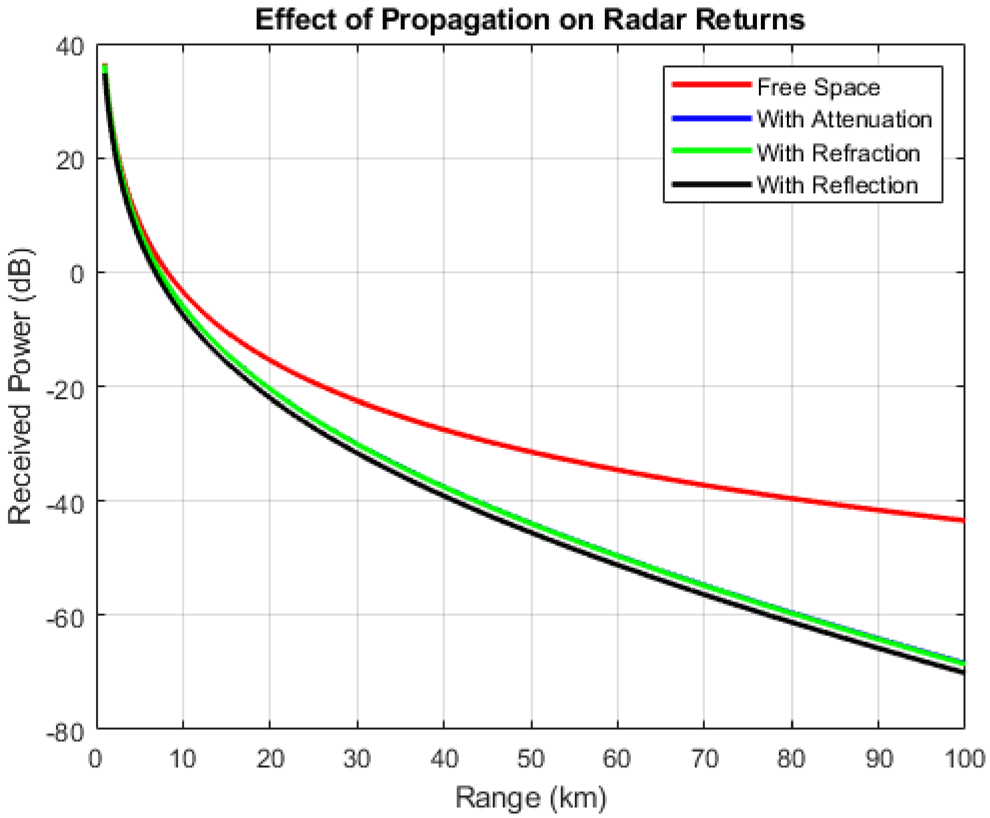

Figure 2.6: Effect of Propagation on Radar Returns

2.8. RCS vs Aspect Angle

Radar Cross Section (RCS) is a measure of a target's ability to reflect radar signals in the direction of the radar receiver. It is a crucial parameter in radar system design and target detection, identification and tracking. The RCS of a target is not a fixed value but varies with the aspect angle, frequency of the radar signal, polarisation and the physical characteristics of the target.

RCS, denoted as σ is defined in Equation 2.12 as:

$$\sigma = \lim_{R\to\infty} 4\pi R^2 \frac{|E_s|^2}{|E_i|^2} \tag{2.12}$$

Where *R* is the distance from the radar to the target, E_s is the scattered electric field strength, E_i is the incident electric field strength.

The RCS of a target depends on several factors:

- **Frequency of the incident radar wave**: Higher frequencies tend to reveal more detailed features of the target.
- **Polarisation of the radar wave**: Different polarisations (horizontal, vertical, circular) interact differently with the target.
- **Aspect Angle**: The orientation of the target relative to the radar affects the RCS significantly.
- **Target Shape and Material**: The geometry and composition of the target influence how it reflects radar waves.

2.8.1. Aspect Angle and Its Impact on RCS

The aspect angle is the angle between the line of sight of the radar and a reference axis on the target, typically the longitudinal axis. It describes the target’s orientation relative to the radar. The RCS can vary dramatically with aspect angle due to:

- **Specular Reflection**: When the radar wave reflects directly back to the radar, the RCS is high. This typically occurs at certain angles, like nose-on or tail-on for simple shapes.
- **Diffraction**: Waves bending around the edges of the target contribute to RCS, more noticeable at side-on aspects.
- **Multipath Reflection**: Complex targets with multiple surfaces can cause multipath reflections, creating constructive or destructive interference patterns.

The variation of RCS with aspect angle can be modelled using different methods depending on the complexity and shape of the target:

2.8.1.1. Simple Geometric Shapes:

For simple shapes like spheres, cylinders or flat plates, analytical expressions can describe the RCS. For example:

- **Sphere**: The RCS of a sphere is constant and independent of the aspect angle.

- **Cylinder**: The RCS of a cylinder varies with the angle θ as shown in Equation 2.13 below:

$$\sigma(\theta) = \frac{2\pi R^2 L^2}{\lambda^2}\sin^2(\theta) \tag{2.13}$$

  where *R* is the radius, *L* is the length, and λ is the wavelength of the incident radar wave.

- **Flat Plate**: The RCS of a flat plat also varies with angle and is defined in Equation 2.14 as:

$$\sigma(\theta) = 4\pi\frac{A^2}{\lambda^2}\cos^2(\theta) \tag{2.14}$$

  where *A* is the area of the plate.

2.8.1.2. Complex Targets:

For complex targets, numerical methods such as the Method of Moments (MoM), Finite Element Method (FEM), and Physical Optics (PO) are used to calculate the RCS. These methods consider the intricate interactions of electromagnetic waves with the target's surface.

Empirical models and experimental measurements often complement theoretical models, especially for complex targets. Anechoic chambers and outdoor radar ranges are used to measure the RCS at various aspect angles.

Figure 2.7 shows how the RCS varies with aspect angles for a Sphere and a flat plate. The figure visually captures the difference between isotropic and anisotropic radar scatterers. The sphere is ideal for omnidirectional reflection modelling (like calibration targets) while the flat plate demonstrates aspect-dependent reflectivity, which is crucial in stealth design, where minimising radar return is desired at certain angles. For the sphere, due to its symmetrical shape, the radar sees the same cross-section at all angles. The RCS remains flat across 0° to 180°. For the flat plate, the maximum RCS at broadside (0° to 180°) drops sharply to a null at 90° (edge-on). This is where the radar wave reflects away from the transmitter.

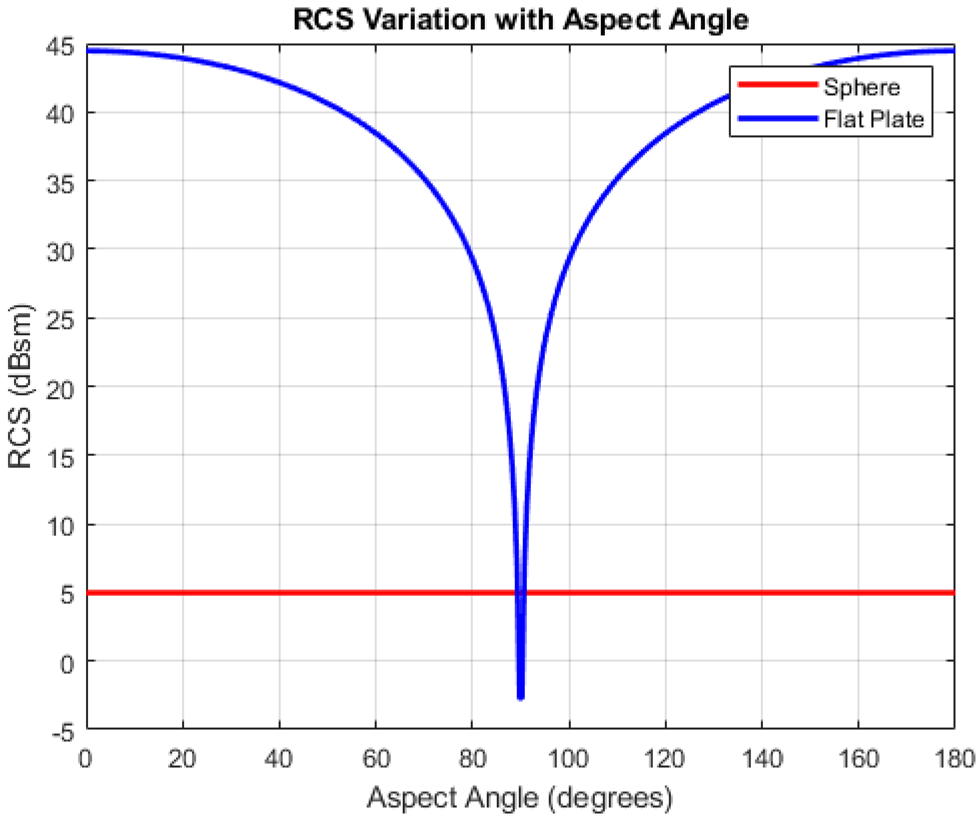

Figure 2.7: RCS variation with Aspect Angle

2.9. Summary

The fundamentals of RADAR as well as a brief history of RADAR have been presented. The types of RADAR as well as their modes of operation were investigated. The RADAR equation as well as the RADAR waveform especially in terms of the Stepped Frequency Waveforms were also x-rayed in greater detail and implemented. MATLAB simulations were also performed to validate the radar waveform and the Stepped Frequency Waveforms both in the time and frequency domains. The findings demonstrated that it performed as predicted. The effect of propagation on radar returns was discussed and extensively analysed for a free space as well as other scenarios. The atmospheric effects (which include attenuation, refraction and reflection) on radar propagation was also investigated. Furthermore, the variation of RCS with the aspect angle was also discussed and extensively analysed for a flat plate and a sphere. The complexity and shape of the target also has an impact on the RCS.

Chapter 3. DEVELOPMENT OF A ROUGH SURFACE MODEL

In this chapter, we shall consider the development of a rough surface model, but before we consider the simulation of a rough surface it is important to consider the properties of some materials and the propagation of electromagnetic waves in such materials. The materials in this instant will involve looking at soils and the dielectric properties of various types of soils. Soils are being investigated in this research because pipeline networks are typically laid on or buried beneath them, making their properties crucial for understanding electromagnetic wave propagation and leak detection [83]. While soils often exhibit rough surface characteristics, their primary relevance here lies in their role as the medium surrounding the pipelines. So, the detection and identification of oil spills and leaks from pipeline networks on these soil surfaces is the reason behind the simulation of a rough surface model. A rough surface model is simulated so as to understand how reflections occur from these rough surfaces and in turn extrapolate it to a soil surface to know how oil reflects from a soil surface that is smooth and another that is rough [84]. This will ultimately help with the effective remote monitoring of pipeline networks using radar sensors in detecting oil leaks and spills. As a result, the radar reflectivity of oil in various soil types and varied materials will be thoroughly considered [85], [86]. X-band radars which offer high resolution but less penetration, making it ideal for detailed surface imaging, will be used for the model unlike the P-band radars applied in SAR systems.

3.1. Properties of Materials

In looking at the properties of materials, it is expedient to note that the attenuation of electromagnetic (EM) radiation rises with frequency and at a given frequency, wet materials exhibit a higher loss than dry ones. It is therefore important to understand the characteristics of materials which affect both the velocity of propagation and attenuation [87], [88]. The velocity of propagation is governed by the relative permittivity of a material which is influenced by multiple factors, including moisture content, material composition, density and temperature. The velocity Ʋ of an electromagnetic wave in a material is given by Equation 3.1 as

$$\mathrm{Ʋ} = \frac{c}{\sqrt{\in_r}} \tag{3.1}$$

where c is the speed of light in a vacuum (≈ 3.0 x 10^8 m/s), and $\in_r$ is the relative permittivity (also called the dielectric constant) of the material.

At low microwave frequencies, the relative permittivity ($\in_r$) of most dry soils and man-made materials typically ranges between 2 and 9. However, due to moisture content and other compositional factors, the measured relative permittivity of soils can vary between 4 and 40 [88], [89]. The absolute permittivity $\in$ which is the product of relative permittivity and the permittivity of free space $\in_0$ also varies with frequency. However, for most materials, it remains approximately constant over the range of frequencies used in ground penetrating radar (GPR) applications [70], [90], [91]. Permittivity is a fundamental property of a material that describes its ability to store electrical energy in an electric field and is very essential in understanding electromagnetic wave propagation, reflection and attenuation in different materials. Relative permittivity $\in_r$ which is also known as the dielectric constant is the ratio of a material's absolute permittivity $\in$ to the permittivity of free space $\in_0$ which is given in Equation 3.2. The attenuation of EM wave in a material is a much more complex relationship and will be looked at in more detail later.

$$\in_r = \frac{\in}{\in_0} \tag{3.2}$$

The physical models that will be used to predict the propagation of EM waves in dielectric materials are the EM wave theory and other relevant wave propagation models [83], [85], [88], [92]. Geometrical optics is generally applicable when the wavelength of EM radiation is much smaller than the dimensions of the object or medium being illuminated. It is particularly relevant in materials with low dielectric losses, such as dry materials because it assumes that EM waves travel as rays and do not undergo significant absorption or scattering. However, optical theory applies to both dry and wet materials, as it encompasses wave-based and ray-based models depending on the medium's properties. Since wet materials introduce significant absorption and scattering, wave-based approaches like the full-wave EM theory are suitable for modelling wave interactions rather than geometrical optics. Furthermore, geometrical optics assumes well-defined refractive boundaries, which are more common in dry, solid materials than in highly conductive or lossy wet materials. Materials containing appreciable amounts of moisture will behave as conducting dielectrics especially if the moisture contains ions. The variability of both material parameters and local geological conditions is such as to cause great difficulty in accurate prediction of propagation behaviour. Based on the crux of this project, we are not really too interested in how EM wave propagates in a material but more interested in the reflectivity of EM waves from such materials and this will be investigated in more detail as this research progresses. We are more interested in the reflectivity of radar signals because this will make us understand in detail how EM waves interact with oil spills on a soil surface emanating from leaks on pipeline networks so as to facilitate the early detection of leaks in the remote monitoring of pipeline infrastructure. Table 3.1 highlights the typical range of dielectric characteristics of various materials at 100MHz [86], [93].

Table 3.1: Typical range of dielectric characteristics of various materials measured at 100MHz [93], [94]

Material	Conductivity (S/m)	Rel. Permeability
Air	0	1
Asphalt dry	0.01 – 0.1	2 – 4
Asphalt wet	0.001 – 0.1	6 – 12
Soil clay dry	0.01 – 0.1	4 – 10
Soil clay wet	0.001 – 1	10 – 30
Soil loamy dry	0.0001 – 0.001	4 – 10
Soil loamy wet	0.01 – 0.1	10 – 30
Soil sandy dry	0.0001 – 0.01	4 – 10
Soil sandy wet	0.01 – 0.1	10 – 30
Sea water	100	81
Sea water ice	0.01 – 0.1	4 – 8

3.2. Propagation of Electromagnetic Waves in Dielectric Materials

Now let’s briefly consider the propagation of EM waves in dielectric materials. Maxwell’s equations are the foundation for the consideration of EM waves [83], [85], [90]. In free space, the magnetic susceptibility and electric permittivity are constants which implies they are independent of frequency and the medium is not dispersive. In a perfect dielectric, no propagation losses are encountered, hence, there is no consideration of the attenuation which occurs in real dielectric media. Plane waves are good approximations to real waves in practical situations particularly in low loss and resistive media e.g. sands and dry limestone. More complicated EM wavefronts can be considered as a superimposition of plane waves, and this may be used to gain insight into complex situations. The most important microwave characteristics of soils are the relative dielectric constants and attenuation. These values as a function of frequency can be used to predict the performance of radar signals in typical soils with known moisture contents. A table of dielectric constants (like conductivity, permittivity, permeability values etc.) for various land and soil types and at various frequencies has been worked upon and populated despite difficult efforts to obtain most of these constants in literature [86], [95]. As a result, the reflectivity of radar signals and at very high frequencies for various soil types with oil and without oil have been successfully modelled utilising these parameters. By so doing, some of the parameters of the reflected signal like the reflectivity, amplitude, phase, frequency etc. have been obtained and correctly interpreted. The actual performance of radars can vary quite considerably due to the wide variations that may be encountered in local soil and material conditions.

3.3. Mechanism of Reflection and Transmission from Surfaces

Reflection occurs when light (EM wave) moves from a medium of one index of refraction into a second medium with a different index of refraction. The reflectance of the surface of a material is its effectiveness in reflecting radiant energy. It is the fraction of incident power that is reflected at an interface. When an EM wave encounters a boundary between two materials with different impedances, some of the energy in the wave will be reflected at the boundary, while some of the energy will be transmitted through the boundary. The amplitude of the reflected wave is predicted by multiplying the amplitude of the incident wave by the reflection coefficient ***R*** [91]. The impedance contrast ***Z*** is determined by the wave velocity ***V*** and the density ***ρ*** of the material. For a wave that hits a boundary at normal incidence, Equation 3.3 is thus:

$$R = \frac{Z_2 - Z_1}{Z_2 + Z_1} \tag{3.3}$$

where Z_1 and Z_2 are the impedances of the first and second medium. The amplitude of the transmitted wave is predicted by multiplying the amplitude of the incident wave by the transmission coefficient ***T*** given by Equation 3.4 below as:

$$T = 1 - R = \frac{2Z_1}{Z_2 + Z_1} \tag{3.4}$$

As the sum of the squares of amplitudes of the reflected and transmitted waves must be equal to the square of the amplitude of the incident wave, then Equation 3.5 below is given:

$$Z_1(1 - R^2) = \frac{Z_1(Z_2 + Z_1)^2 - Z_1(Z_2 - Z_1)^2}{(Z_2 + Z_1)^2} = \frac{4Z_2Z_1^2}{(Z_2 + Z_1)^2} = Z_2T^2 \tag{3.5}$$

Figure 3.1a shows the reflection of a P-wave off an interface at normal incidence, while Figure 3.1b shows the mode conversions that occur when a P-wave reflects off an interface at non-normal incidence. The P-wave is one of the linear polarisation components of the incident wave, while the other linear polarisation component is the S-wave.

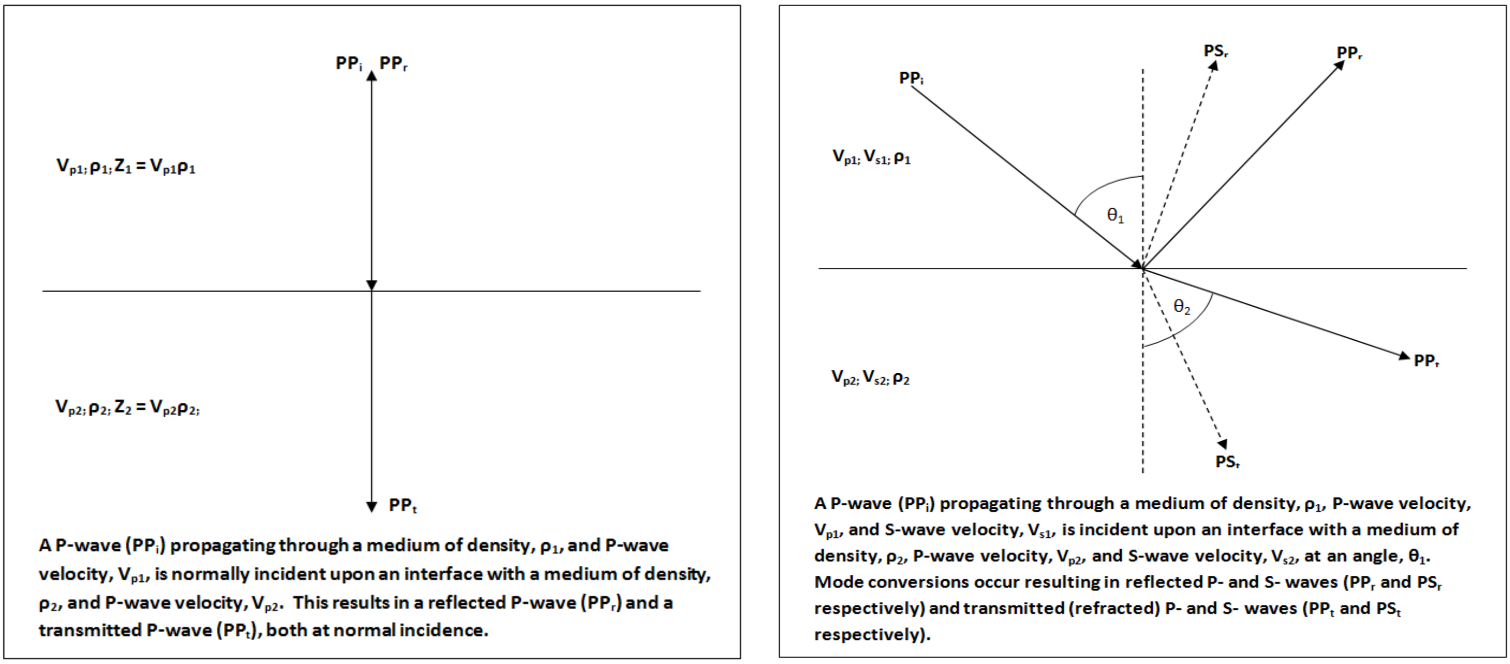

A P-wave (PP$_i$) propagating through a medium of density, ρ$_1$, and P-wave velocity, V$_{p1}$, is normally incident upon an interface with a medium of density, ρ$_2$, and P-wave velocity, V$_{p2}$. This results in a reflected P-wave (PP$_r$) and a transmitted P-wave (PP$_t$), both at normal incidence.

A P-wave (PP$_i$) propagating through a medium of density, ρ$_1$, P-wave velocity, V$_{p1}$, and S-wave velocity, V$_{s1}$, is incident upon an interface with a medium of density, ρ$_2$, P-wave velocity, V$_{p2}$, and S-wave velocity, V$_{s2}$, at an angle, θ$_1$. Mode conversions occur resulting in reflected P- and S- waves (PP$_r$ and PS$_r$ respectively) and transmitted (refracted) P- and S- waves (PP$_t$ and PS$_t$ respectively).

(a)Reflection at normal incidence (b)mode conversions at non-normal incidence

Figure 3.1: a) Reflection of a P-wave off an interface at normal incidence b)mode conversions when a P-wave reflects off an interface at non-normal incidence [86], [92], [96]

The situation becomes much more complicated in the case of non-normal incidence (as shown in Figure 3.1b due to mode conversion between ***P***-waves and ***S***-waves. The P-wave and the S-wave are the two different linear polarisation components of the incident wave and are orthogonal to each other. The ***s*** polarisation refers to the polarisation of a wave's electric field normal to the plane of incidence, and the magnetic field is in the plane of incidence, while the ***p*** polarisation refers to the polarisation of the electric field in the plane of incidence with the magnetic field normal to the plane of incidence. Although the reflectivity and transmission are dependent on polarisation, at normal incidence, there is no distinction and so all polarisation states are governed by Fresnel equations or coefficients.

Fresnel equations describe the ratios of the electric fields of the transmitted and reflected waves to the electric fields of the incident wave. The equations also assume the interface between the media is flat and the media are homogenous and isotropic. Fresnel equations for reflection and transmission for both s – polarised (electric field perpendicular to the plane of incidence) and p – polarised (electric field parallel to the plane of incidence) light are highlighted in Equations 3.6 to 3.9.

$$reflection\ coeff\ s-polarised = r_s = \frac{n_1 \cos\theta_i - n_2 \cos\theta_t}{n_1 \cos\theta_i + n_2 \cos\theta_t} \tag{3.6}$$

$$transmisson\ coeff\ s-polarised = t_s = \frac{2n_1 \cos\theta_i}{n_1 \cos\theta_i + n_2 \cos\theta_t} \tag{3.7}$$

$$reflection\ coeff\ p-polarised = r_p = \frac{n_2 \cos\theta_i - n_1 \cos\theta_t}{n_2 \cos\theta_i + n_1 \cos\theta_t} \tag{3.8}$$

$$transmisson\ coeff\ p-polarised = t_p = \frac{2n_1 \cos\theta_i}{n_2 \cos\theta_i + n_1 \cos\theta_t} \tag{3.9}$$

where n_1 and n_2 are the refractive indices of medium 1 and medium 2 respectively,

θ_i is the angle of incidence and θ_t is the angle of transmission, determined by Snell's Law

$n_1 \sin\theta_i = n_2 \sin\theta_t$

It is important to note at this juncture that the direction of reflection considered thus far is for a bistatic radar case where the reflected signal travels in a different direction from the transmitted signal. For this research, a monostatic radar system will be employed in the analysis. It is crucial to also note that in addition to reflections off interfaces, there are several other responses that might be detected by the receiver and are unwanted or not needed. They include air wave such as coherent noise, Rayleigh wave which propagates along the surface of the earth, refraction as well as multiple reflections off these surfaces. How to reduce the impact of some of these sources of noise have been investigated and will be discussed as we progress.

3.4. Propagation Over a Reflecting Surface

The free space propagation equations apply only under restricted conditions. However, in practical situations, there are almost always obstructions in or near the propagation path or surfaces from which the radio waves can be reflected. The received signal to our monostatic radar will just be the ground-reflected wave (and back-scatter), while it will be a combination of both direct and ground reflected waves as well as back-scatter for a bistatic radar. To determine the resultant in this case, the reflection coefficient must be obtained. The amplitude and phase of the ground reflected wave depends on the reflection coefficient of the earth at the point of reflection and differs for both horizontal and vertical polarisations [86].

Free space propagation can occur for some remote sensing systems under ideal conditions. However, for most remote sensing applications, signal propagation is influenced by environmental factors such as the earth's surface, atmospheric conditions, the ionosphere and hydrometeors like rain, snow, and hail. These factors modify the propagation of electromagnetic waves and can introduce signal degradation, attenuation and scattering effects. The impact of the natural environment on signal propagation is highly dependent on the frequency band used (e.g. L-band, C-band, X-band), the spatial resolution and geometry of the sensing system, and the altitude of the platform. Evaluating a proposed radar remote sensing system must consider these propagation effects to ensure accurate data acquisition and reliable performance under diverse environmental conditions. The goal is to maintain an adequate signal-to-noise ratio (SNR) and minimise data loss or errors due to adverse propagation. By accounting for atmospheric attenuation, ionospheric dispersion, and surface reflectivity, remote sensing systems can reduce outages and ensure continuous monitoring with minimal disruption. The performance of a radar system can generally be predicted on the basis of the assumed typical characteristics for the propagation path [86]. At very high frequencies (≥ GHz range), attenuation and scatter by rain and atmospheric gases, predominantly water vapour, should also be considered. In addition, the scattering and diffraction of radio waves by hills, buildings and trees is also much more pronounced at these higher frequencies. The propagation phenomena of importance at very high frequencies are those associated with interference effects from back reflections.

We will now look at the reflection coefficient of the earth for both horizontally and vertically polarised waves incident on the earth's surface. Since the earth is neither a perfect conductor nor a perfect dielectric, the reflection coefficient therefore depends on the ground constants [86] which include the dielectric constant $\in$ and the conductivity σ. For a horizontally polarised wave incident on the surface of the earth (assumed to be perfectly smooth), the reflection coefficient is given by Equation 3.10 below as [86]:

$$p_h = \frac{\sin\varphi - \sqrt{\left({\in}/{\in_0} - {j\sigma}/{\omega\in_0}\right) - cos^2\varphi}}{\sin\varphi + \sqrt{\left({\in}/{\in_0} - {j\sigma}/{\omega\in_0}\right) - cos^2\varphi}} \tag{3.10}$$

where ω is the angular frequency of the transmission and $\in_0$ is the dielectric constant of free space. Writing $\in_r$ as the relative dielectric constant of the earth yields Equation 3.11 below:

$$p_h = \frac{\sin\varphi - \sqrt{(\in_r - jx) - cos^2\varphi}}{\sin\varphi + \sqrt{(\in_r - jx) - cos^2\varphi}} \tag{3.11}$$

where $x = \frac{\sigma}{\omega\in_0} = \frac{18\ x\ 10^9\sigma}{f}$

For vertical polarisation, the corresponding expression is given by Equation 3.12 below as:

$$p_v = \frac{(\in_r - jx)\sin\varphi - \sqrt{(\in_r - jx) - cos^2\varphi}}{(\in_r - jx)\sin\varphi + \sqrt{(\in_r - jx) - cos^2\varphi}} \tag{3.12}$$

The reflection coefficients p_h and p_v are complex, so the reflected wave will differ from the incident wave in both magnitude and phase. For p_h, the relative phase of the incident and reflected waves is nearly 180° for all angles of incidence. For very small angles of φ (near grazing incidence), the equation for p_h also shows that the reflected wave is equal in magnitude and 180° out of phase with the incident wave for all frequencies and all ground conductivities [86] as shown in Equation 3.13 below:

$$p_h = p_h e^{j\theta} = 1e^{j\pi} = -1 \tag{3.13}$$

As angle of incidence is increased, then p_h and θ change by small amounts. The change is greatest at higher frequencies and when ground conductivity σ is poor. For vertical polarisation, Equation 3.14 still applies at grazing incidence.

$$p_v = p_v e^{j\theta} = 1e^{j\pi} = -1 \tag{3.14}$$

However, as φ is increased, substantial differences appear. The magnitude and relative phase of the reflected wave decrease rapidly as φ increases. At pseudo-Brewster angle, the magnitude becomes a minimum and the phase reaches -90°. At values of φ greater than the Brewster's angle, p_v increases again and the phase tends towards zero. The conductivity σ and dielectric constant ∈ is much higher for flat good ground as compared to poorer and dry grounds found in mountainous areas [86]. For instance, the conductivity for a flat prairie land is around 0.01 S/m with the conductivity values much lower for mountainous regions [86]. The dielectric constant $\in_r$ is smaller around 6 or 7 for soil with poor conductivity, while it increases up to about 30 for soil with high conductivity. The behaviour of the reflection coefficient as a function of the grazing angle φ has been modelled for both vertical and horizontal polarisations using $\in_r$ as 15 and φ as 0.01 S/m and at various frequencies. For a perfectly conducting surface, the reflection coefficient will be equal to 1 for vertical polarisation. As the frequency increases, the effect of a finite ground conductivity decreases. Therefore, for microwave and millimetre wave frequencies where my radar operates, the ground will behave very nearly like a dielectric medium. Whenever the point of reflection occurs over a rough surface, the field is scattered in a more diffuse manner. Operating at microwave and millimetre wave frequencies is ideal because it provides high-resolution detection, improved surface and subsurface interaction, reduced ground conductivity effects, and enhanced scattering properties – all of which are essential for accurately characterising soil conditions and detecting pipeline leaks or other anomalies in the research. The specular reflected component as well as the reflection coefficient is reduced in value. A measure of the height of the surface irregularities that constitutes a "rough surface" may be obtained by considering the effective wavelength of the incident wave in the direction perpendicular to the surface. At longer wavelengths, most surfaces appear smooth, while at microwave frequencies, most surfaces will be rough and the reflection coefficient will be smaller than that given by Fresnel formula [86]. In addition to the above, it is also pertinent to note the effect of the decrease in the index of refraction of the atmosphere with height above the surface. During this research, we have considered how the reflection characteristics of our radar signal varies with frequency, conductivity, permittivity, incidence angle and other dielectric constants in varied degrees of rough surfaces and this shall be elucidated upon as we progress.

3.5. Rayleigh Roughness Criterion

At this juncture, we will look at the Rayleigh roughness criterion which theoretically gives a guideline about what constitutes a smooth or rough surface. The radar equation for free space obtained in Equation 2.1 must obviously be modified to include propagation losses caused by the atmosphere and the earth. When an EM wave encounters a surface, the nature of reflection depends on the surface roughness relative to the wavelength of the incident wave.

The EM waves that bounce from perfectly smooth flat surface are said to be specularly reflected and the angles of incidence and reflection are the same. The magnitude and phase changes due to specular reflections are governed by the dielectric properties of the interface surface and the incidence angle and are determined by Fresnel equations. Specular reflections can also occur even if surface irregularities exist. This means that a surface does not need to be perfectly smooth for specular reflection to occur. The practical implication of this is that in real-world scenarios, surfaces such as wet soil may still produce strong specular reflections even if they have some minor texture or irregularities. This means that Fresnel equations can still be used to describe the reflection behaviour if the surface roughness does not exceed a critical threshold relative to the wavelength. The Rayleigh roughness criterion is a guideline for deciding whether or not a surface is sufficiently smooth for providing specular reflections [86]. Surfaces can be classified as ***smooth (specular reflection)*** where the wave reflects in a single direction, preserving phase and coherence; they can also be classified as ***rough (diffuse scattering)*** where the wave is scattered in multiple directions, leading to phase randomness; and they can also be classified as ***intermediate (mixed reflection and scattering)*** which is a combination of specular reflection and diffuse scattering. The transition between these categories is governed by the Rayleigh Roughness Criterion which provides a theoretical guidance for defining whether a surface behaves as smooth or rough in the EM sense.

To provide a qualitative indication of surface roughness, i.e. how smooth or rough in the EM sense a surface is, Lord Rayleigh [85], [86] considered a surface to be smooth if, according to Equation 3.15

$$\Delta h \sin\theta < \frac{\lambda}{8} \tag{3.15}$$

where θ is the grazing angle between the incident EM waves and a plane surface representing the average of the irregularities, Δh is the range of height differences on a reflecting surface, and λ is the wavelength.

Obviously, most surfaces are neither perfectly smooth nor rough. Whether a surface is smooth or rough depends on the incidence angle and the radar wavelength as well as its physical features. For a rough surface, it is generally agreed [85], [86] as shown in Equation 3.16 that,

$$\sigma_h \sin\theta \geq \frac{\lambda}{8} \tag{3.16}$$

where σ_h is the standard deviation of the surface height distribution.

3.6. Reflection Coefficient for a Flat Smooth Earth

The reflections from a smooth earth can be determined from Fresnel's equations [86]. The magnitude and phase of the reflection coefficient depends on frequency, polarisation, angle of incidence and the electromagnetic properties of the earth such as complex permittivity, conductivity and permeability. The dielectric constant of a material is represented by its complex permittivity $\in_c$ which accounts for both energy storage and energy loss in an electromagnetic field. It is expressed as $\in_c = \in' - j \in''$ where $\in'$ which is the real part represents the permittivity and $\in''$ which is the imaginary part is related to the conductivity of the material. Thus, the complex permittivity governs both the reflection and attenuation of EM waves, influencing how signals interact with the earth's surface.

The reflection coefficients for vertical and horizontal polarisations are given by Fresnel's equations and written as Equations 3.17 and 3.18 below for both vertical and horizontal polarisations as:

$$\Gamma_v = \frac{\in \sin\varphi - \sqrt{\in - cos^2\varphi}}{\in \sin\varphi + \sqrt{\in - cos^2\varphi}} = \rho_v e^{-j\emptyset_V} \tag{3.17}$$

$$\Gamma_h = \frac{\sin\varphi - \sqrt{\in - cos^2\varphi}}{\sin\varphi + \sqrt{\in - cos^2\varphi}} = \rho_h e^{-j\emptyset_H} \tag{3.18}$$

where φ is the grazing angle, $\in = \in' - j \in''$, $\in' = \frac{k}{\in_0}$, $\boldsymbol{k}$ is the permittivity and $\in'' = \frac{\sigma}{\omega \in_0} = \frac{18*10^9 \sigma}{f}$ At normal incidence, $\varphi = \frac{\pi}{2}$ and the two polarisations thus become identical as shown in Equations 3.19 and 3.20 thus:

$$\Gamma_h = \frac{1-\sqrt{\in}}{1+\sqrt{\in}} \tag{3.19}$$

$$\Gamma_v = \frac{\in - \sqrt{\in}}{\in + \sqrt{\in}} = -\Gamma_h \tag{3.20}$$

A minus sign is an indication that the true field is reversed compared to the assumed field, Γ_h and Γ_v must differ in sign if the reflected fields have the same phase. As this thesis progresses, plots of magnitude and phase of the reflection coefficient versus the wavelength and grazing angle have been analysed and will be discussed. In addition, the reflecting properties for horizontal and vertical polarisations have also been thoroughly investigated.

Now, we will look at the magnitude and phase of the reflection coefficient for moist soil, dry soil, average land, and sea water just to understand and analyse the radar reflectivity in those media. Average land generally refers to a typical or representative soil type that falls between dry soil and moist soil in terms of its dielectric properties, conductivity, and permittivity. In most applications, the exact dielectric values for this land vary depending on location, climate and soil composition. The parameters for the model of the radar reflectivity for these different soil types are given in Table 3.2 [77], [85], [86], [97], [98] and reproduced from this textbook [86].

Table 3.2: Parameters for radar reflectivity model for varied ground types

Medium	**λ(m)**	**σ (S/m)**	$\in'$	$\in''$	**Freq (GHz)**
Sea water	0.01 – 10	3.9 - 9.5	76	5.7 – 2340	0.03 – 30
Average land	0.1	0.0016	10	0.0094	3.0
Moist ground	0.1	0.01	30	0.06	3.0
Dry ground	0.1	0.0001	4	0.0006	3.0

Figure 3.2 shows the magnitude of the reflection coefficient for seawater (at 10°C) as a function of grazing angle.

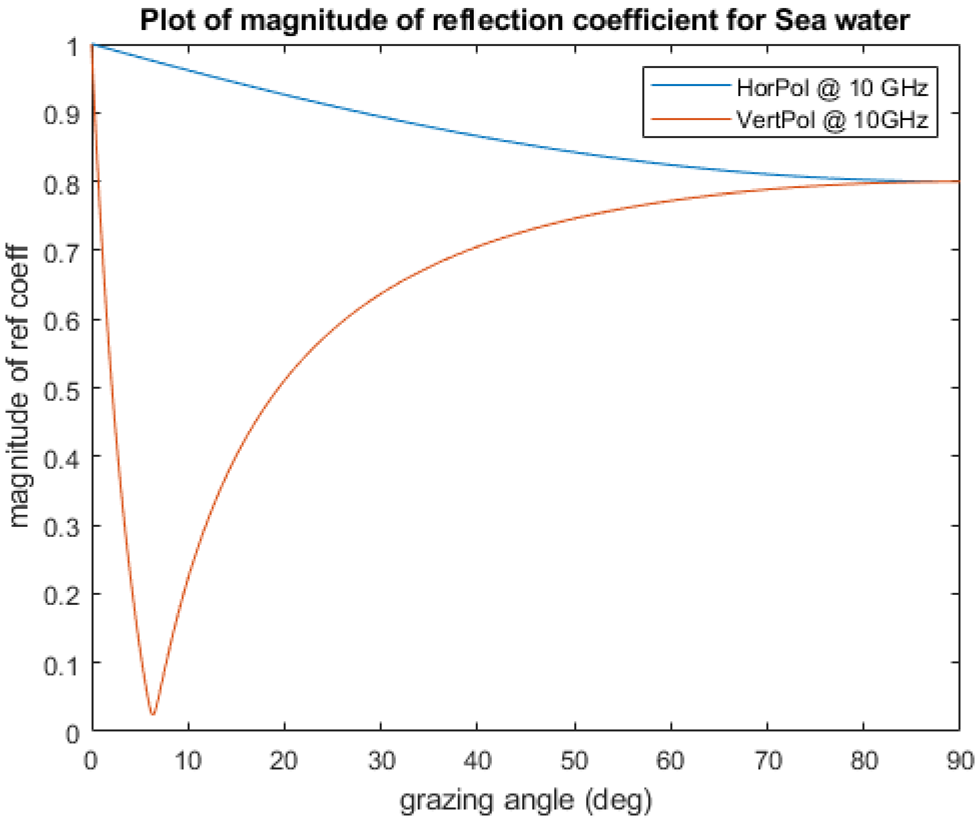

Figure 3.2: Magnitude of the reflection coefficient for sea water

The graph depicts major differences between the reflecting properties for horizontal and vertical polarisations. The lower the frequency of the radar signal, the higher the reflectivity and vice versa for the magnitude of the reflection coefficient. For horizontal polarisation, there is only a slight variation in magnitude with grazing angle, while there is a huge variation in magnitude with grazing angle for the vertical polarisation. In addition, for vertical polarisation, ρ_v reaches its maximum value and the phase lag is 90° at the incidence angle which is sometimes called the pseudo-Brewster angle. The Brewster angle is where ρ_v would be zero for a lossless dielectric [86].

Figure 3.3 shows the magnitude of the reflection coefficient for average land as a function of grazing angle with the parameters highlighted in Table 4.2 [86], [97], [98].

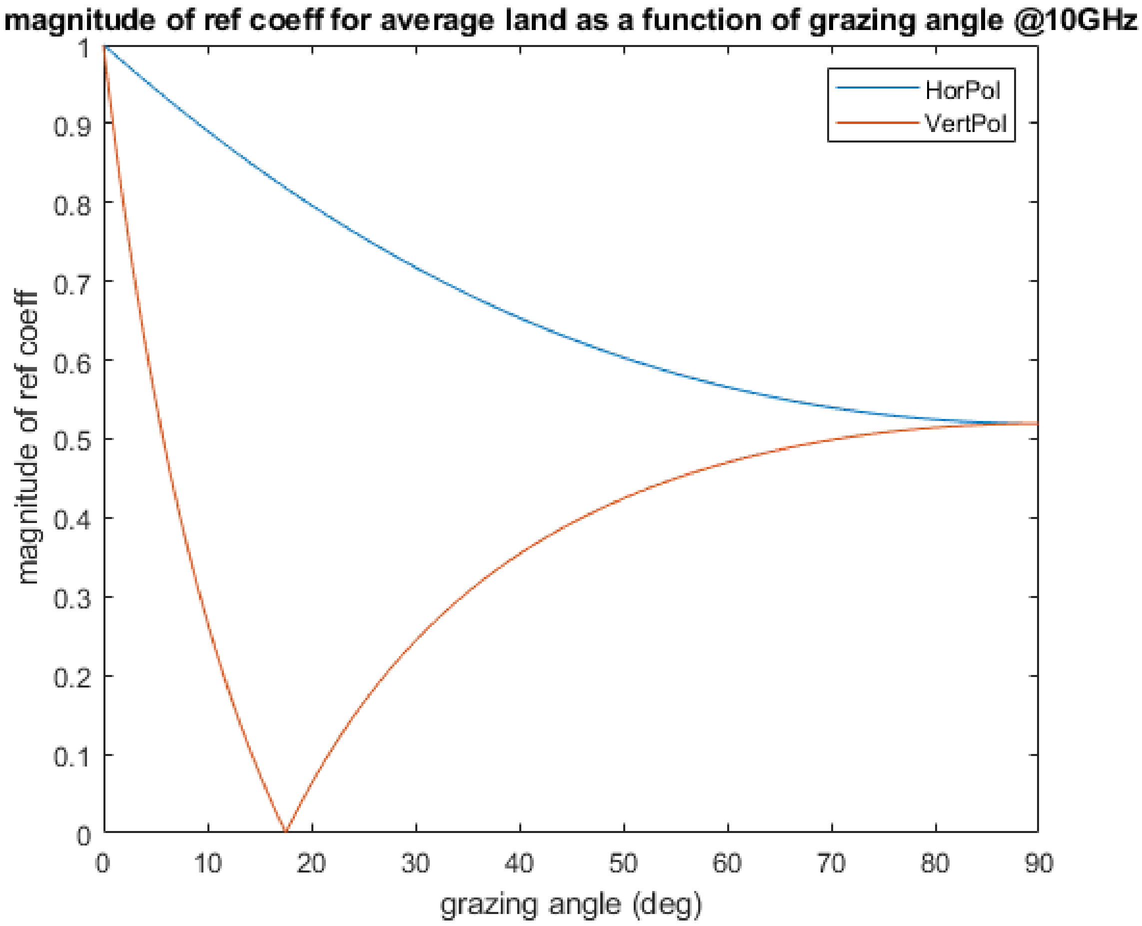

Figure 3.3: Magnitude of the reflection coefficient for average land

Although the dielectric properties of water and land depend on incidence angle and wavelength, for many purposes, the magnitude and phase of the horizontal polarisation can be approximated by unity and pi respectively. For very small grazing angles, the magnitude and phase for the vertical polarisation are also nearly unity and pi respectively. For large grazing angles, the $\emptyset_V$ approaches zero. These characteristic behaviours for smooth surfaces play significant roles in the echo strengths from radar targets for cases of small grazing angles, even under conditions for which the land or water surface is physically rough. Figures 3.4 and 3.5 show the magnitude for moist and dry soil respectively.

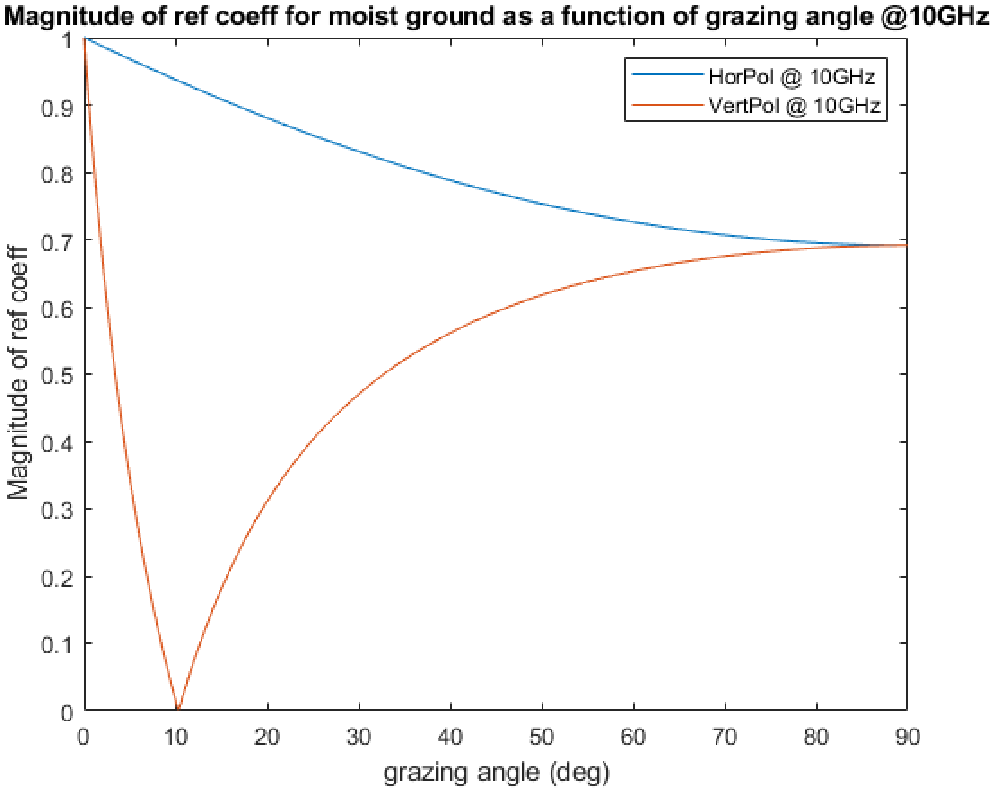

Figure 3.4: Magnitude of the reflection coefficient for moist ground

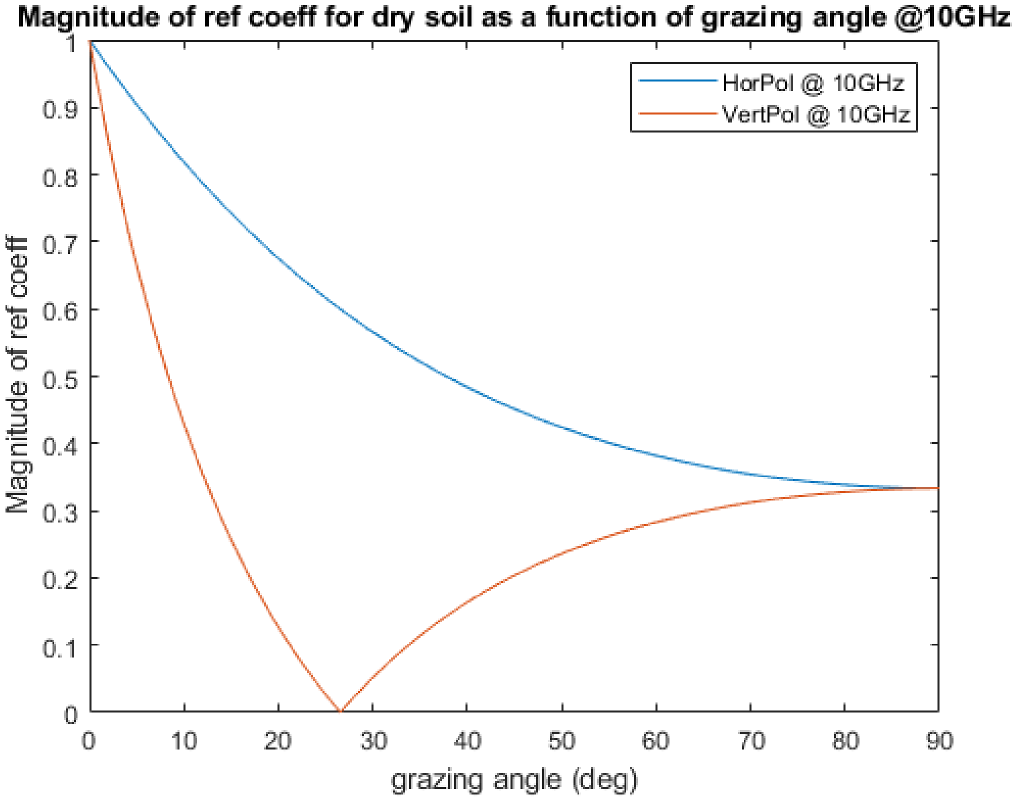

Figure 3.5: Magnitude of the reflection coefficient for dry soil

3.7. Reflections from a Rough Earth

Now to analyse the reflections from a rough earth, it is expedient to note that the EM field scattered by a rough surface is the sum of two components. The two components are the specular (reflected) component and the diffuse (scatter) component [85], [86]. For specular reflections, the angle of incidence and the angle of reflection are equal, however, diffuse scattering can occur in any direction relative to the incident EM field. A specularly reflected component is a coherent field having amplitude and phase that can be described as a function of position. Conversely, the amplitude and phase of a diffusely scattered field are unpredictable and are random functions of position. A diffusely scattered field added to a coherent field will produce a total field that varies randomly as a function of position.

The magnitude R_s which is a specular reflection coefficient of the earth is a product of three factors – $R_s = \rho D_f Y_s$ where the magnitude ρ is the reflection coefficient of a smooth, flat surface, the divergence factor D_f describes the reduction in reflection caused by the earth's curvature and the specular scattering coefficient Y_s expresses the fractional reduction in field strength caused by surface roughness [86]. Both D_f and Y_s can be between 1 and 0. D_f is 1 for the radar geometry is such that the earth can be assumed to be flat. Y_s is 1 for a perfectly smooth surface and decreases with increases in surface roughness [85], [86], [97], [98].

From the foregoing, there are practical implications for the radar system. At microwave and millimetre-wave frequencies, most natural surfaces are rough, leading to a combination of specular and diffuse scattering. Wet soil may still behave as a specular reflector despite minor roughness due to high dielectric contrast. Radar performance is affected by roughness since increased scattering can lead to signal dispersion and reduced coherence. In terms of motivation behind the frequency used, operating at microwave and mmWave frequencies provides high-resolution detection as well as improved surface and subsurface interaction which is essential for accurately detecting leaks and spills from pipeline networks

3.8. Model of a Rough Surface

To start to consider a rough surface model, it is important to also understand some features about soil moisture and surface roughness. Theoretical data indicate that the reflectivity of a radar signal is dependent on soil roughness and radar parameters in various complex ways [85], [86]. Within certain terrain and operational constraints, radar images can be strongly dependent on soil moisture [87], [92], [99]. In some instances, because of the permittivity of oil, soil with oil would have a higher reflectivity than soil without oil. However, in some other instances, the reverse could be the case. The ability to fully appreciate and understand radar reflectivity in varied soil types that have oil content and some that do not have oil content has been explored and fully investigated in this research. This will go a long way in the effective remote monitoring of pipeline infrastructure in the detection of oil leaks and spills. Meanwhile, as this research progresses, the effects of various surface characteristics, terrain structure and emerging techniques have also been thoroughly investigated and would be discussed.

Before we look at the model of a random surface with average height deviations, it is pertinent to understand that models for scattering from rough surfaces can be broadly categorised into empirical models, theoretical models and a combination of the two [83], [85], [88]. Theoretical models though complex can yield a significant understanding of the interaction between the EM waves and the soil. Analytical models include the Kirchhoff Approximation (KA), Small Perturbation Method (SPM), and the Integral Equation Method (IEM) [87], [88], [99].

The basic laws of electromagnetism are given by Maxwell's equations (Equations 3.16 – 3.19) which for a linear, homogenous, isotropic, stationary and non-dispersive media [83] are written below as:

$$\nabla * E = -\frac{\partial B}{\partial t} \tag{3.16}$$

$$\nabla * H = \frac{\partial B}{\partial t} + J_c + J_i \tag{3.17}$$

$$\nabla * D = \rho \tag{3.18}$$

$$\nabla * B = 0 \tag{3.19}$$

where *E* is the electric field vector, *D* is the electric flux density, *H* is the magnetic field vector, *B* is the magnetic flux density, J_c is the conduction electric current density, J_i is the impressed electric current density and ρ is the electric charge density.

In rough surface scattering, the surface enters in the boundary conditions which must be supplied at infinity. If we consider time-harmonic variation of the EM field, the instantaneous field vectors can be related to their complex forms, therefore Maxwell's equations in Equations 3.16 - 3.19 now become Equations 3.20 – 3.23 as highlighted below:

$$\nabla * E = -j\omega\mu H \tag{3.20}$$

$$\nabla * H = (\sigma + j\omega\varepsilon)E + J_i \equiv j\omega\varepsilon_c E + J_i \tag{3.21}$$

$$\nabla . \varepsilon E = \rho \tag{3.22}$$

$$\nabla . \mu H = 0 \tag{3.23}$$

where we assumed the region characterised by permeability μ, permittivity ε, and conductivity σ for a lossy medium. To obtain the governing equation for the electric field, we take the curl of Equation 3.20 and then replace Equation 3.21, which results in Equation 3.24 below:

$$\nabla * \nabla * E + \omega^2 \mu \varepsilon_c E = j\omega\mu J_i H \tag{3.24}$$

which is known as the inhomogenous Helmholtz vector wave equation. In a free source region, $\nabla . E = 0$ and Equation 3.24 above simplifies to $\nabla^2 E + \omega^2 \mu \varepsilon_c E = 0.$ The generation and modelling of the rough surface would be extensively discussed in Section 3.10.

3.9. Scattering Problems and EM Fields

Consider an EM plane wave incident on a rough soil surface as shown in Figure 3.6.

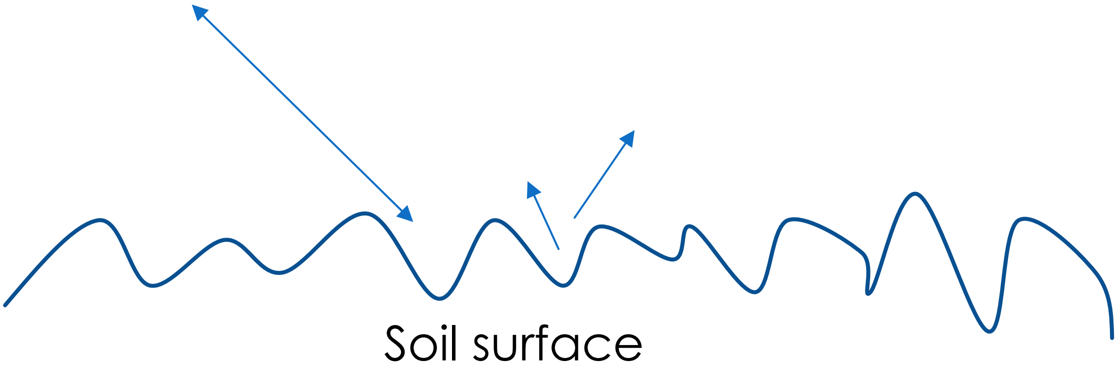

Figure 3.6: Scattering of EM field on Soil Surface

Across any surface interface, the EM field should satisfy continuity conditions given by Equations 3.25 – 3.28 below:

$$\hat{n} * (E - E_1) = 0 \tag{3.25}$$

$$\hat{n} * (H - H_1) = J_s \tag{3.26}$$

$$\hat{n} * (\varepsilon E - \varepsilon_1 E_1) = \rho_s \tag{3.27}$$

$$\hat{n} * (\varepsilon H - \varepsilon_1 H_1) = 0 \tag{3.28}$$

where $\hat{n}$ is unit normal vector of the rough surface. The electric surface current density J_s and the charge surface density ρ_s, at the rough interface are zero unless the scattering surface is a perfect conductor.

When an EM wave encounters a boundary between two homogenous media, surface scattering occurs at the interface. This scenario is classified as a surface scattering problem [84], [87], [88], [92], [100]. In contrast, for inhomogeneous media, volume scattering must also be considered. Since bare soil is assumed to be a homogenous medium, only surface scattering is analysed. If the boundary surface is perfectly smooth, reflection occurs in the specular direction as described by Fresnel equations. However, when the surface is rough, the incident wave is partially reflected in the specular direction and partially scattered in multiple directions. Qualitatively, the relationship between surface roughness and surface scattering is illustrated in Figure 3.7 below.

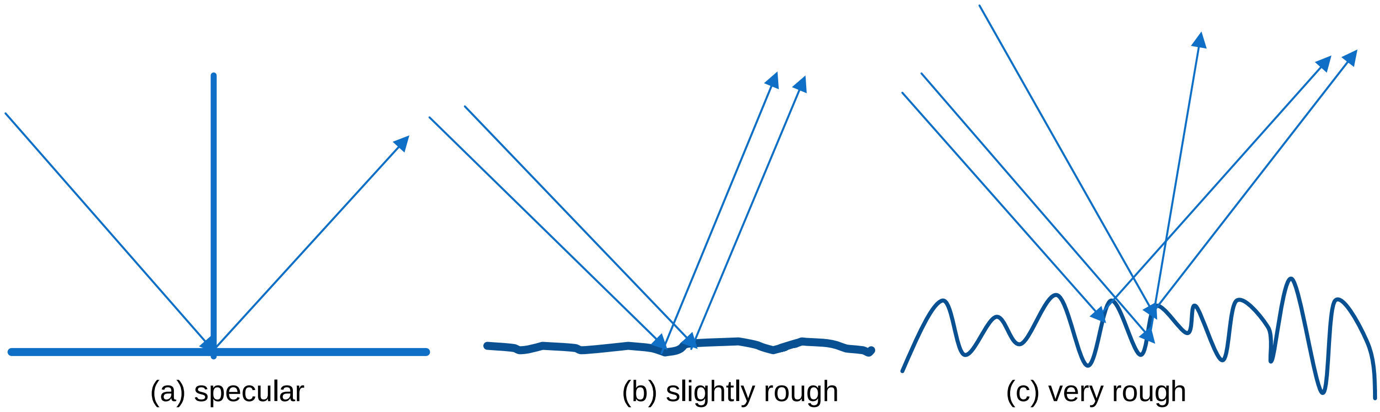
(a) specular (b) slightly rough (c) very rough

Figure 3.7: Relative contributions of coherent and diffuse scattering components for different surface roughness conditions (a) specular (b) slightly rough (c) very rough

For a perfectly smooth surface, the reflected wave's angular radiation pattern is a delta function centred around the specular direction as shown in Fig. 3.7a. When the surface is slightly rough surface, the reflection consists of two components: a ***coherent (specular)*** component and a ***diffuse (incoherent)*** component which is a scattered field distributed in various directions as shown in Fig. 3.7b. As surface roughness increases, the coherent component weakens and the diffuse component dominates, making the surface appear fully rough as shown in Fig. 3.7c. The coherent component represents the mean scattered field, while the diffuse component has a stochastic nature due to surface randomness [83].

Surface roughness is measured using two approaches: ***experimental methods*** which utilise contact or laser probes to reproduce surface profiles and ***theoretical estimation*** which derives roughness by relating scattering measurements to surface features. Scattering studies rely on random rough surface models where surface elevation is treated as a stationary random process with a Gaussian height distribution [100], [101]. The degree of roughness depends on the wavelength, meaning a surface that appears rough at optical frequencies may appear smooth at microwave frequencies. The two key statistical parameters used in rough surface modelling are: ***Root Mean Square (RMS) height*** which represents surface height variations and the ***Surface correlation length*** which defines the spatial extent of roughness. These parameters are fundamental in 1D and 2D rough surface modelling and will be further analysed and discussed in latter sections.

3.10. Generation of Randomly Rough Isotropic Surfaces

Surface roughness is a measure of the topographic height variations of a surface. Random rough surfaces in 1D and 2D have been generated with the rough surfaces having the distribution and auto-correlation functions as either Gaussian or exponential. The parameters for generation of these rough surfaces are highlighted in Table 3.3 and the plots shown thereafter.

Table 3.3: Parameters for the generation of random rough surfaces

Parameter	**1 D surface**	**2 D surface**
Number of surface points (N)	1500	1500
Length of surface (rL)	1 m, 10 m	1 m, 10 m
rms height (h)	1 cm, 14 cm	1 cm, 14 cm
Correlation length (cl)	1 cm, 12.5 cm	-
Correlation length in x & y	-	1 cm, 12.5 cm

Figures 3.8 – 3.10 show the plots for the generation of the 1D random rough surface including the height distribution function as well as the Gaussian and exponential auto correlation functions.

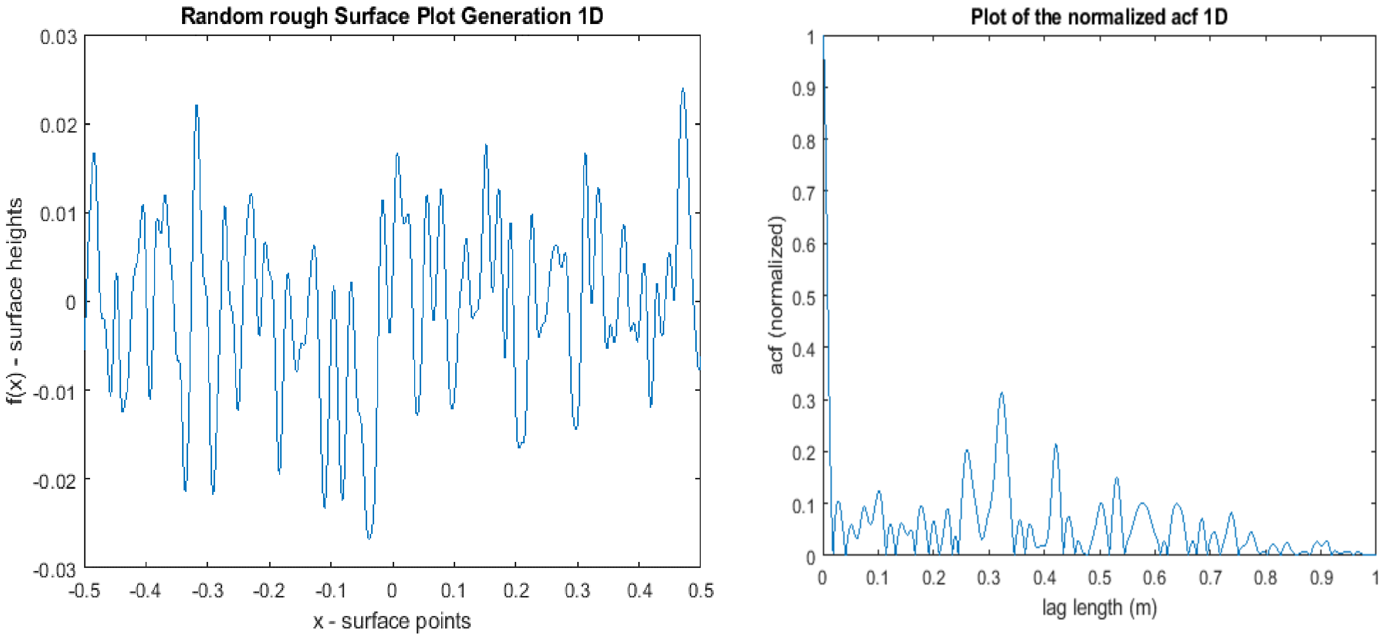
Random rough Surface Plot Generation 1D

Plot of the normalized acf 1D

(a) Plot Generation

(b) Auto Correlation Function (ACF)

Figure 3.8: 1D random rough surface (a) Plot (b)Auto Correlation Function

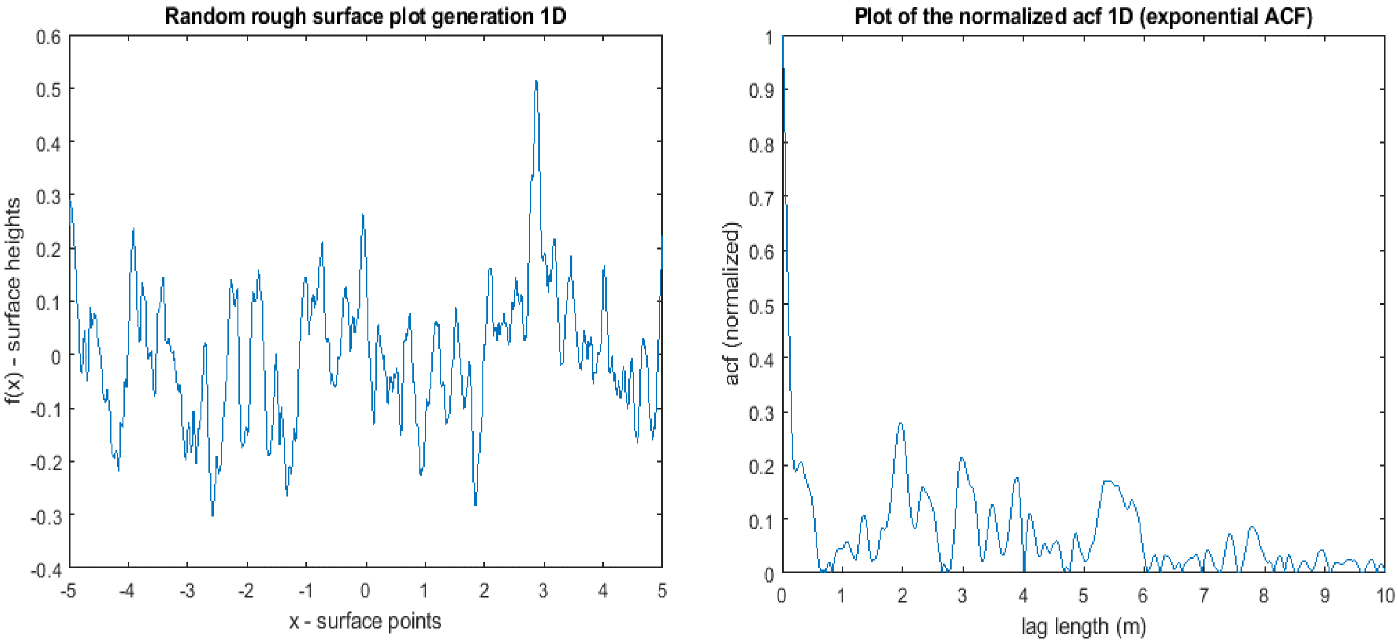

(a). 1D rough surface generation (b) Normalised auto correlation function

Figure 3.9: 1D random rough surface (a) Generation (b)Normalised ACF

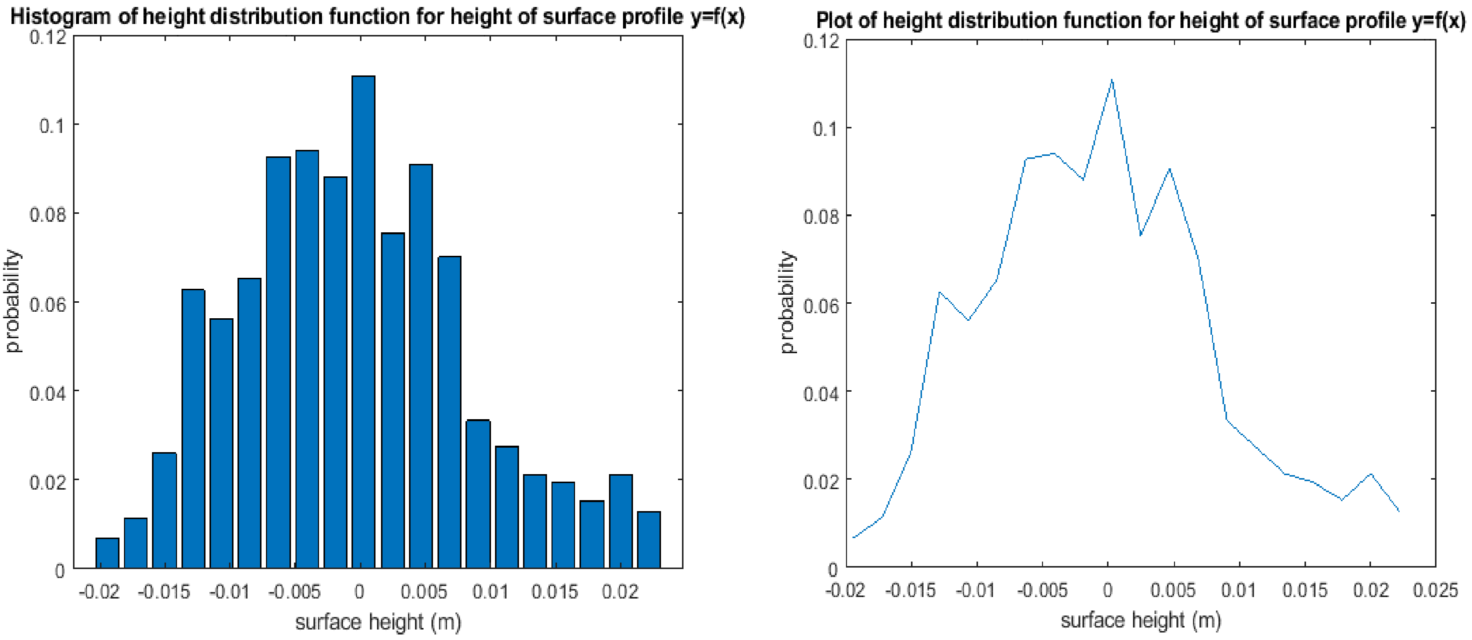

(a) Histogram of the 1D height dist. Func. (b) Plot of the 1D Gaussian height dist. Fun

Figure 3.10: a) Histogram of the height distribution function (b) Plot of the height distribution function

In Figure 3.8, the rough surface shows a faster decay in autocorrelation, meaning height variations are more random and less predictable over distance as a result of the Gaussian auto correlation function applied in the simulation and analysis. In Figure 3.9 where the exponential auto correlation function is applied, the rough surface has a slower decay in autocorrelation, suggesting that surface variations have more extended correlation and continuity. The implications for EM wave scattering are that surfaces with rapidly varying roughness (Fig. 3.8) will cause more diffuse scattering and less coherent reflection while surfaces with longer correlated roughness (Fig. 3.9) will retain more coherent reflection at certain incident angles. For pipeline monitoring, understanding roughness helps optimise radar frequency selection and signal processing techniques to distinguish between different soil conditions (e.g. dry soil vs oil-contaminated soil)

Figures 3.11 – 3.13 show the plots for the generation of the 2D random rough surface including the height distribution function as well as the Gaussian and exponential auto correlation functions.

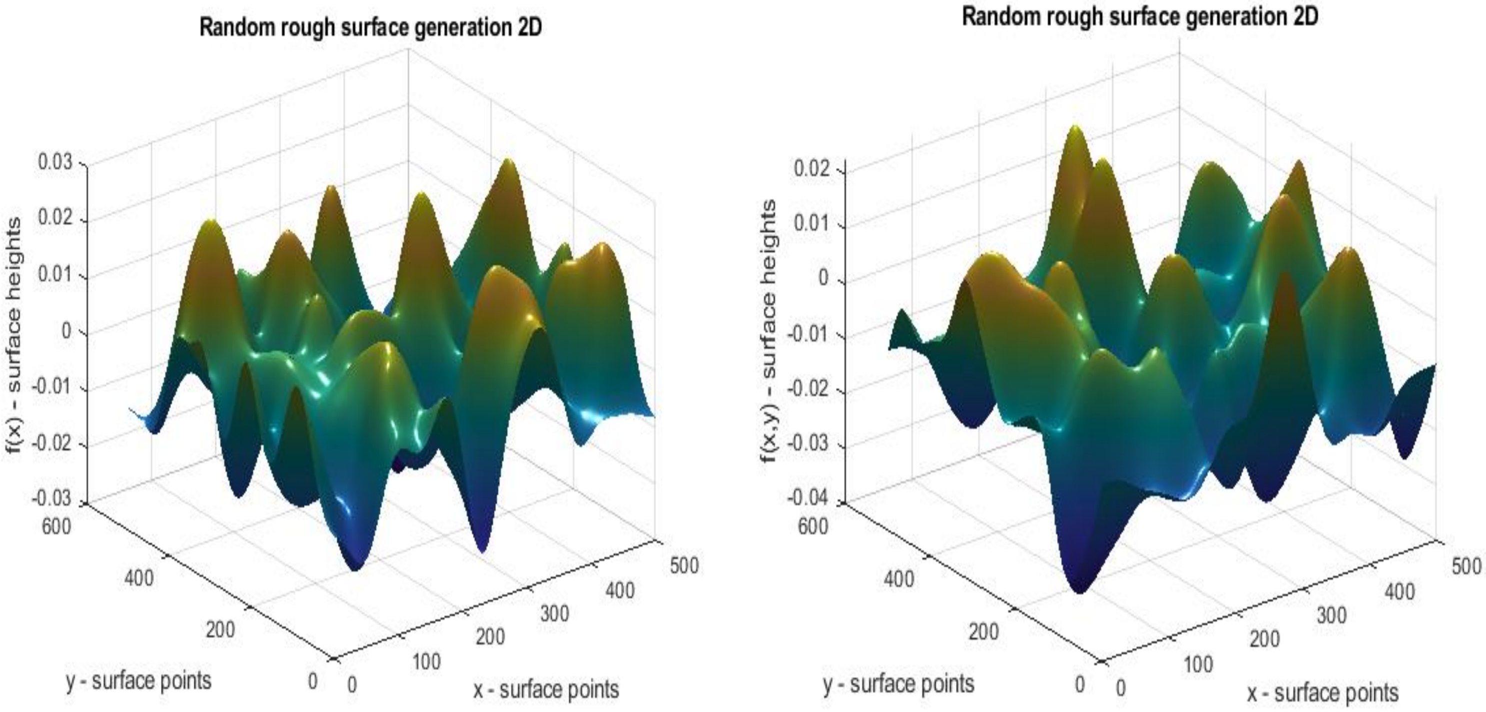

(a) 2D surface with Gaussian auto corr. Func (b) 2D surface with Exp. auto corr. Func

Figure 3.11: 2D rough surface with (a) Gaussian autocorrelation function (b) Exponential autocorrelation function

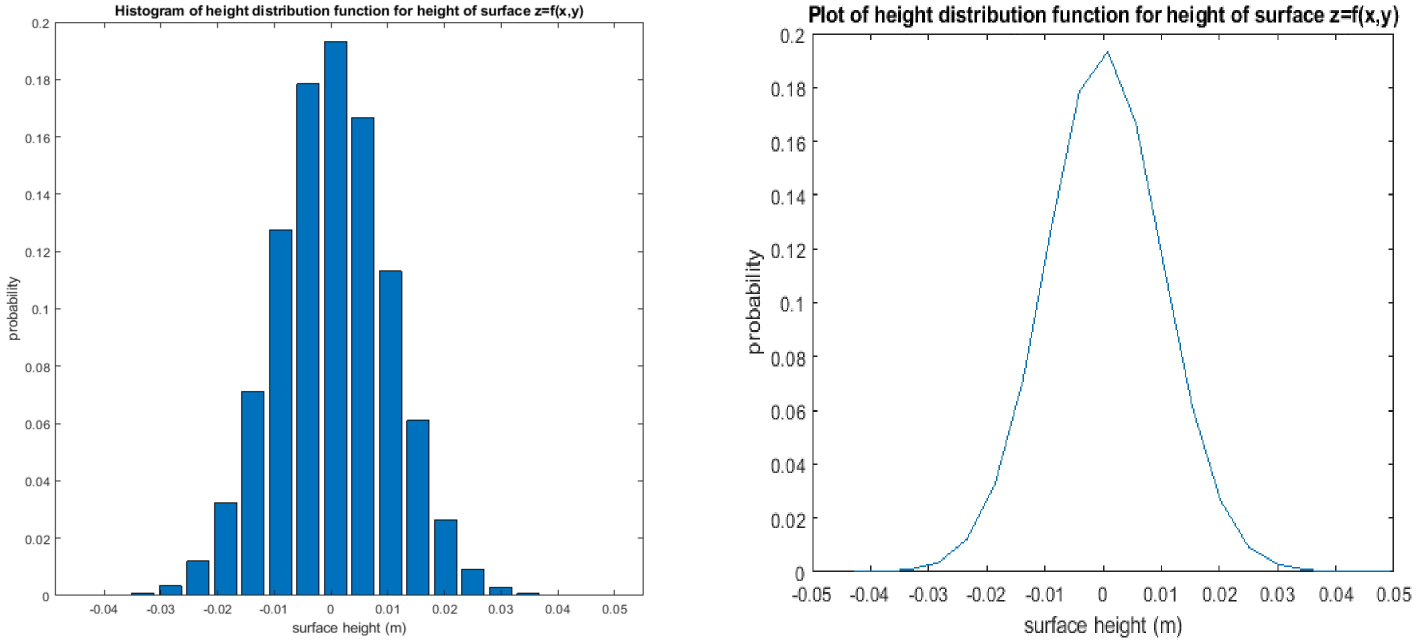

(a) Histogram of the height distribution Func. (b) Plot of the 2D height distribution func.

Figure 3.12: 2D rough surface with (a) histogram of the height distribution function (b) plot of the height distribution function

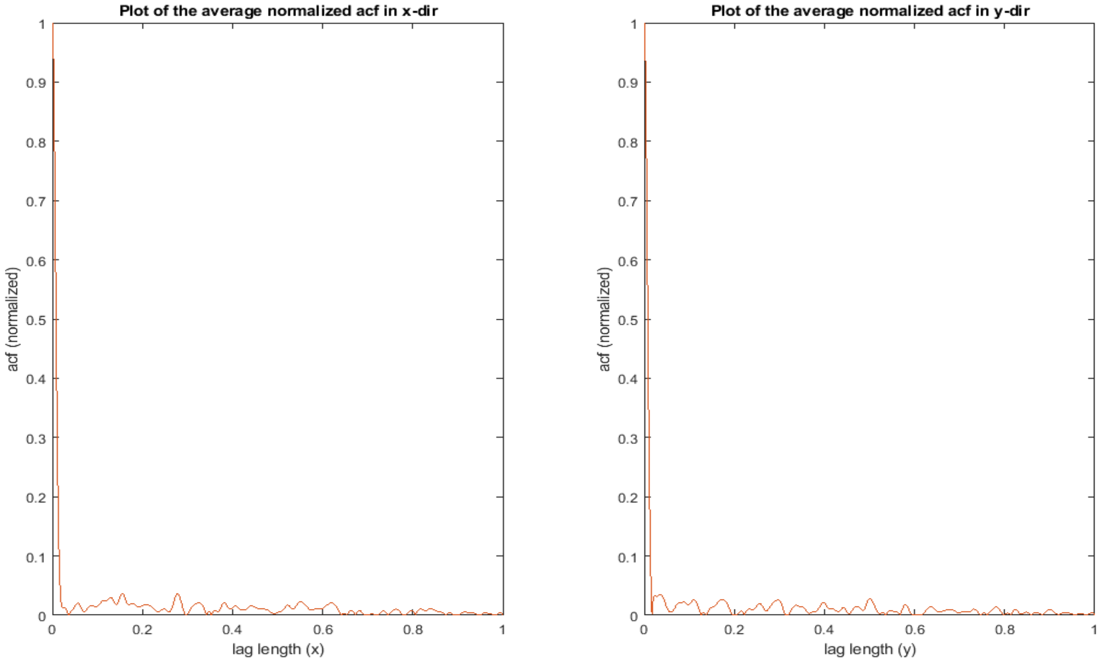

(a) Average normalised 2D Gaussian autocorrelation function in x and y direction

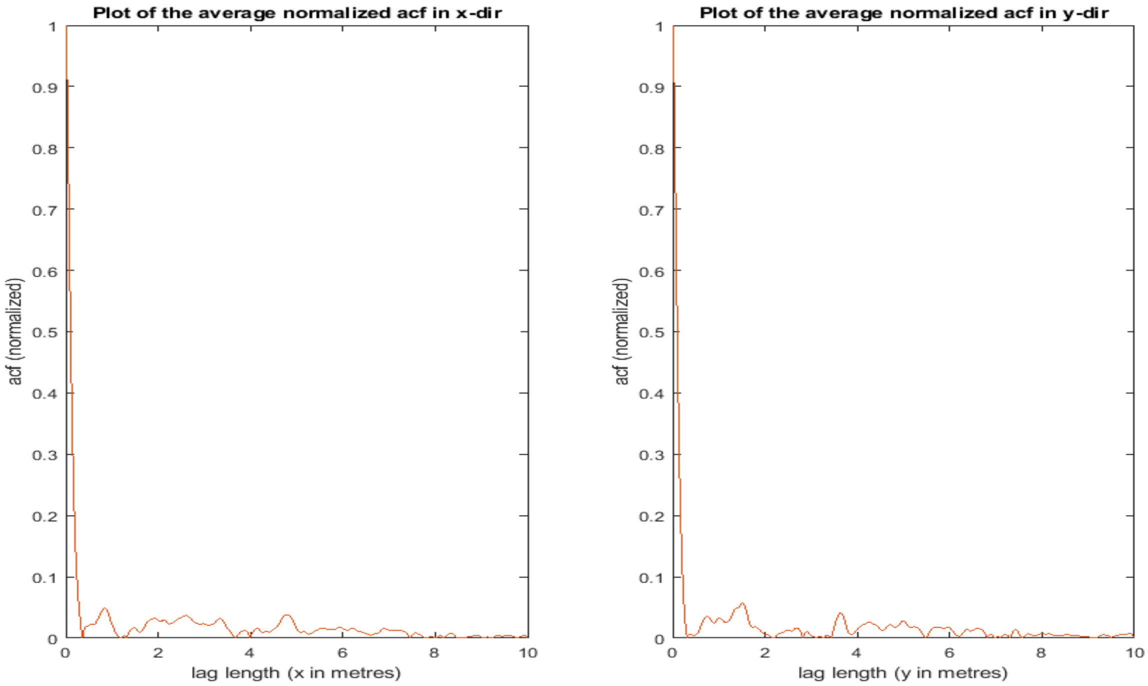

(b) Average normalised 2D exponential autocorrelation function in x and y direction

Figure 3.13: (a) average normalised 2D Gaussian autocorrelation function (b)average normalised 2D exponential autocorrelation function

Figure 3.14 shows the graphs for artificial randomly rough isotropic surfaces with different levels of roughness. The roughness exponent for Fig. 3.14a is 0.8 which makes it rougher than that of Fig. 3.14b. which is 0.7. The roughness exponent is a statistical parameter that quantifies the smoothness or roughness of a surface in relation to its spatial variations. It describes how surface height fluctuations correlate over distance and typically varies between 0 and 1. It basically helps in understanding how a surface will scatter EM waves. Figure 3.14 also shows the generated surface height profile of the randomly rough surface.

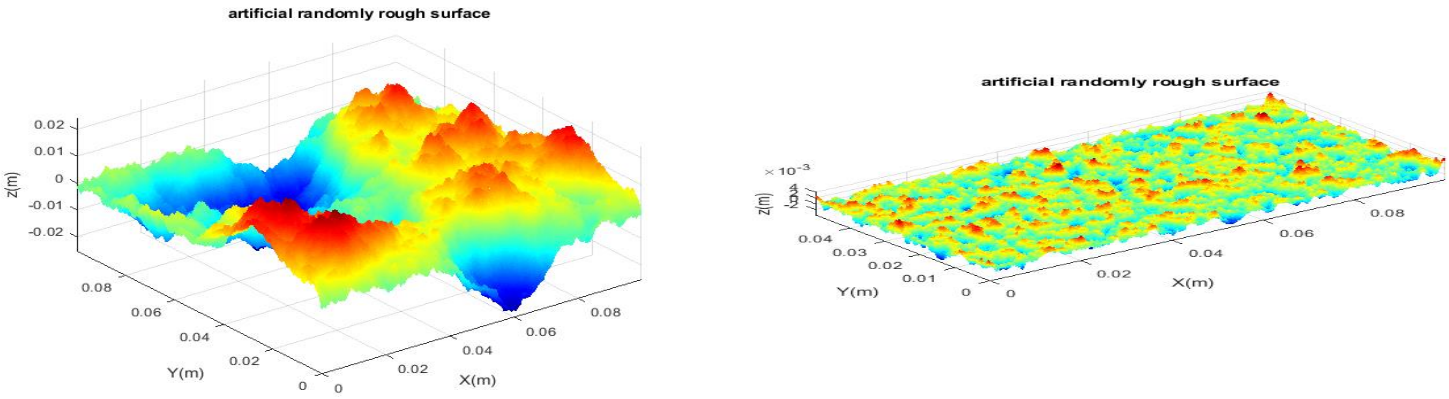

(a) Hurst exponent of 0.8 (b) Hurst exponent of 0.7

Figure 3.14: Rough surface (a) Hurst exponent of 0.8 (b) Hurst exponent of 0.7

The statistical constants for the generated 1D and 2D rough surface models were investigated to ensure the accuracy and correctness of the model. Some of these statistical constants include the rms height, correlation lengths etc. Table 3.4 shows that on comparison with the statistical constants earlier provided in Table 3.3, the values obtained from simulation closely match the predefined values in Table 3.3. This consistency confirms that the simulation results align with the expected statistical parameters, indicating that the model is accurate and reliable. Furthermore, the autocorrelation function derived from the power spectral density confirms that the correlation length and other statistical parameters align with expectations, reinforcing the model's reliability and correctness. However, it was not possible to increase the number of surface points beyond 5000 due to computational challenges. But for all the number of surface points considered, the values of the statistical constants were like the predicted values for both 1D and 2D rough surfaces and both auto correlation functions.

Table 3.4: showing the correct comparison of values of the predicted statistical constants earlier described in Table 3.3

N (no.)	h (m) 1D	h(m) 2D	clx & cly (m)	Cor len. (1D)
1500	0.0101	0.1418	0.1234	0.0097
3000	0.0098	0.1407	0.1301	0.0108
4500	0.0102	0.1390	0.1234	0.0110
5000	0.0100	0.1415	0.1230	0.0111

To further investigate that the rough surface model does what it says it does, the autocorrelation has been generated from the power spectral density (PSD) for the 1D and 2D surfaces, from which the correlation length and the statistical parameters have been obtained. Various dielectric constants have been introduced into our rough surface models and these and many more will be extensively discussed in the next chapters of this thesis. Furthermore, the rough surface has been modelled in CST software. Much later, the model will be incorporated with a chirp signal as part of a radar signal processing system. Distributed and back scattering from the rough surface model has also been investigated and this will be intensively analysed in this thesis. Finally, how the correlation length also varies in literature for various soil types has been analysed as well as investigated and this has also been applied to the rough surface model. All these and more would be addressed in subsequent chapters.

3.11. Summary

In this chapter, the model of a randomly rough surface was first extensively discussed and then generated in MATLAB. To achieve and understand this, the properties of EM waves in various dielectric materials were thoroughly investigated and analysed. The mechanism of reflection and transmission from surfaces was also analysed extensively and thoroughly investigated. How electromagnetic waves propagate over a reflecting surface was also discussed as well as its implications for a rough surface. By so doing, the Rayleigh roughness criterion was examined and further analysed as well as the criteria in determining or ascertaining the differences between a smooth and a rough surface. Some simulations were also conducted to investigate the reflection coefficient for different earth surfaces ranging from a rough earth to a flat smooth earth. The results were also analysed and thoroughly discussed in addition to the implications for the detection of oil leaks in rough surfaces like soil surfaces. Finally, after the rough model was created, the predicted statistical constants such as the correlation lengths, rms height of the rough surface model etc, tallied with the same parameters defined prior to the model being created.

Chapter 4. SIMULATION RESULTS AND ANALYSIS OF A ROUGH SURFACE MODEL

A rough surface model, representative of various soil surfaces where pipeline networks are typically laid was developed using MATLAB and subsequently imported into CST for RCS and reflectivity analysis under different dielectric properties and parameters. The validity of this model was evaluated through simulations involving diverse soil samples with varying dielectric properties. These simulations examined the influence of oil and other dielectric materials (like PEC, and the varied soil types - dry sandy soil, wet sandy soil – since each of these materials has a distinct dielectric constant that influences how EM waves interact with the surface) on the reflectivity and RCS characteristics of different soil types, presenting these effects for the first time.

A detailed analysis of key measurement parameters, their implications and their relationships with dielectric constants is conducted. Following this, an experimental investigation and verification of the RCS analysis were carried out, with the results discussed in latter sections of this thesis. The study involves an in-depth discussion of the simulation results of the rough surface model in CST, evaluating both lossless and lossy materials with different dielectric properties.

To validate the model further, an experimental equivalent of the rough surface model will be developed and tested in a controlled environment using radar instruments. The results from these experiments will be analysed and compared with the simulation outcomes to assess the accuracy and reliability of the model. The measured performance of the developed model is then compared with the specific requirements of the oil and gas industry, ensuring its applicability in remote pipeline monitoring for oil leak and spill detection. The key findings and results from this research are currently undergoing intensive reviews and will be presented and published once the evaluation process is complete.

4.1. Theoretical and Analytical Development of a Rough Surface Model

Surface roughness quantifies the topographic height variations of a surface. To develop a robust rough surface model, it is essential to understand the interaction between soil moisture and surface roughness. Under certain operational and terrain conditions, radar images can be significantly influenced by soil moisture [87], [92], [99].

This thesis explores and thoroughly investigates radar reflectivity across different soil types, distinguishing between oil-contaminated and non-contaminated soils. These insights contribute significantly to the effective remote monitoring of pipeline infrastructure for detecting oil leaks and spills. Furthermore, this research examines the effects of soil surface characteristics, terrain structure, and emerging techniques, providing a comprehensive understanding of their impact on radar-based detection systems. These findings will be detailed in subsequent sections of this thesis.

Now let us delve deeper into the mathematical models of a random rough surface with average height deviations. Random rough surfaces are usually characterised using terms from probability theory such as the height distribution function (hdf), or the statistical moments of mean, variance (or rms height) etc. The surface variation in the lateral directions is described by the autocorrelation function (acf) which describes the correlation of the surface with traditionally shifted versions, where the correlation length is the typical distance between two similar features (e.g. hills or valleys) [84]. These essential parameters, amongst others have been utilised in the rough surface model that has been developed for both 1D and 2D surfaces.

For the generation of a 1D random rough surface with Gaussian height distribution function (hdf), a Gaussian or an exponential autocorrelation function (acf) could be applied to the 1D rough surface model. The input parameters to the model are the number of surface points or number of samples denoted by ***N***, length of surface denoted by ***rL***, the rms height denoted by ***h***, and the correlation length denoted by ***cl***. The uncorrelated Gaussian random rough surface distribution with a mean of 0 and standard deviation or rms height ***h*** is denoted by ***Z*** and given by Equation 4.1 as:

$$Z = h * randn(1, N) \tag{4.1}$$

The Gaussian filter applied to the model is denoted by ***GauF*** and given by Equation 4.2 as:

$$GauF = e^{\left(-x^2 / {cl^2 / 2} \right)} \tag{4.2}$$

where $x \in [0, rL, N]$ is the output of the surface points.

To obtain the output of the surface heights denoted by ***f(x)***, the fast Fourier transforms (FFTs) of the uncorrelated Gaussian random rough surface (Z) and the Gaussian filter must be obtained at first. Therefore, applying FFT to Equation 4.1 and Equation 4.2 results in Equation 4.3 and Equation 4.4 respectively as:

$$Z_k = \sum_{n=1}^{N} Z_n \, e^{-j2\pi kn / N} \ , \ \ k = 1, \dots N \tag{4.3}$$

$$F_k = \sum_{n=1}^{N} F_n \, e^{-j2\pi kn / N}, \qquad k = 1, \dots N \tag{4.4}$$

Now, when the Inverse Fast Fourier transform (IFFT) is applied to a convolution of the filter and the surface, in addition to other normalising prefactors, the output of the correlation of the surface is therefore given by Equation 4.5 below as:

$$f(x) = \sqrt{2 / \sqrt{\pi}} * \sqrt{rL / N * cl} * F^{-1}\{Z_k .* F_k\} \tag{4.5}$$

The plots for the Gaussian 1D filter, the uncorrelated 1D rough surface, the convolution of the filter and the surface, the IFFT of this convolution of the filter and the surface as well as the subsequent generation of the correlated 1D random rough surface are shown in Figure 4.1.

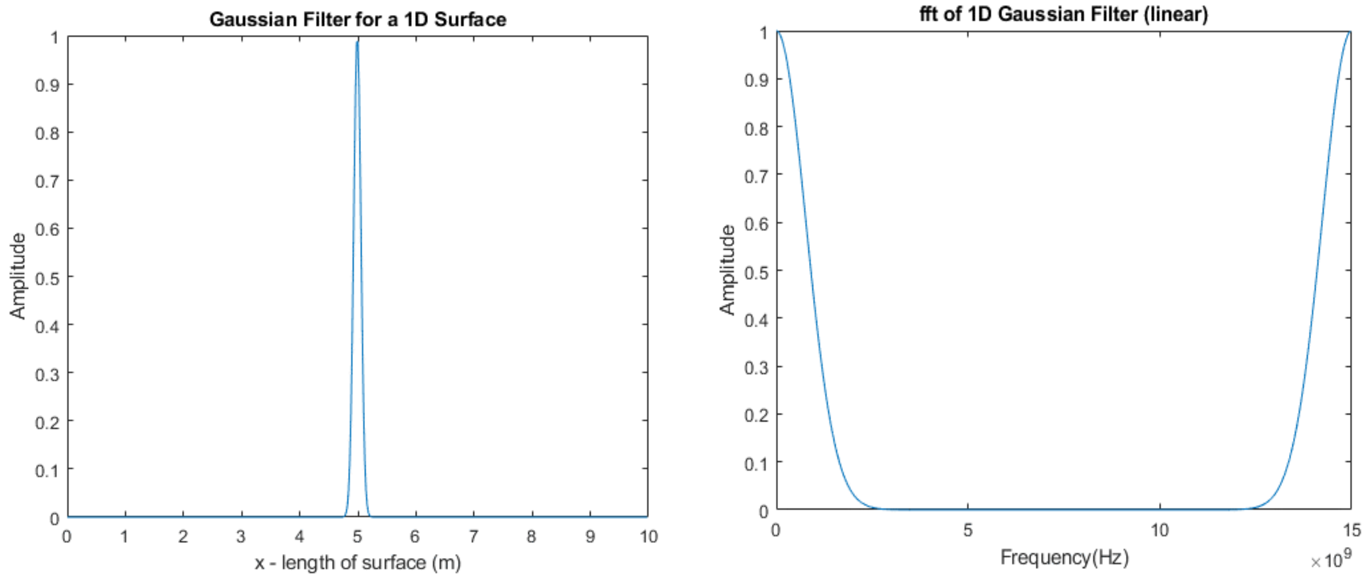

(a) Gaussian Filter for a 1D surface (b) FFT of 1D Gaussian filter - linear

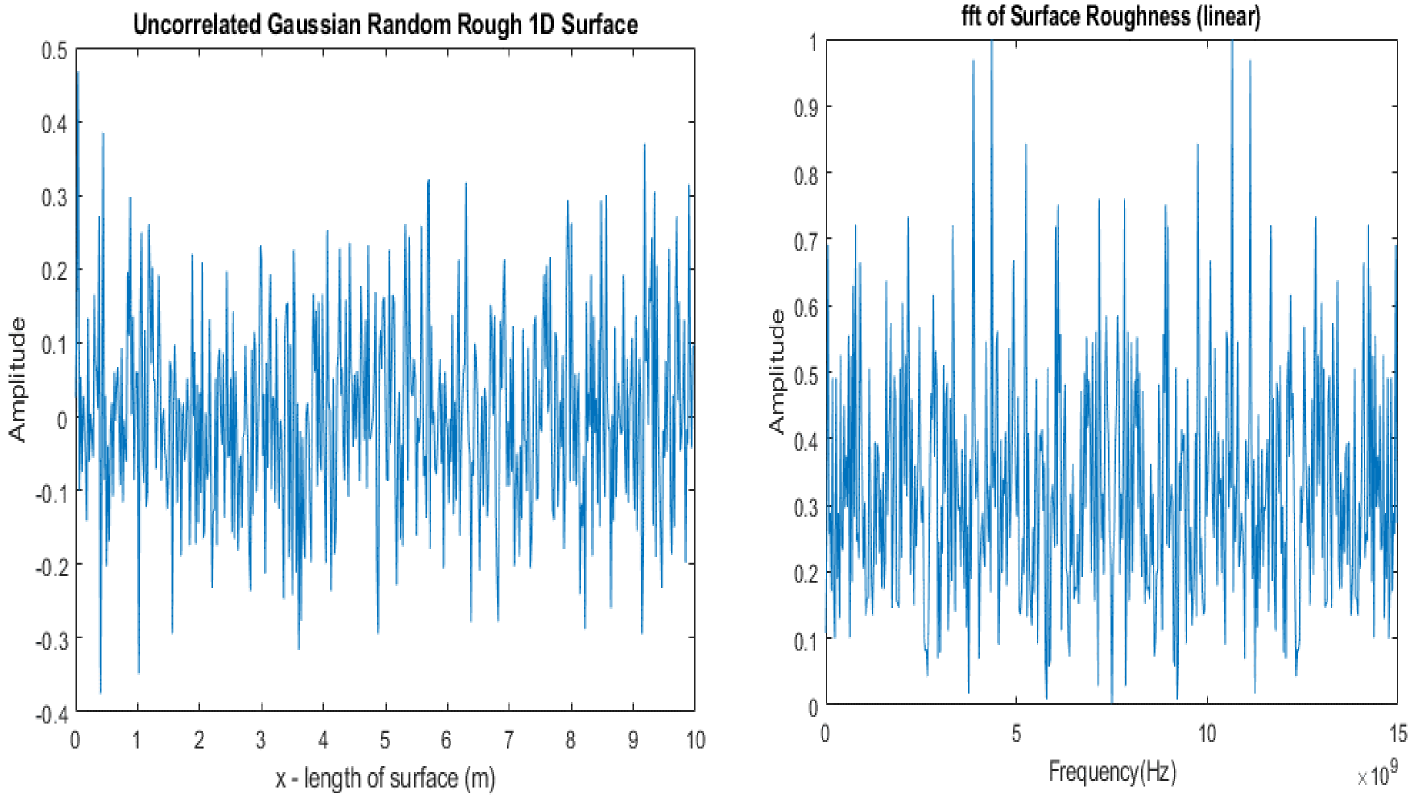

(c) Uncorrelated Gaussian 1D surface (d) FFT of Uncorrelated 1D surface

Please note that the parameters for the generation of these plots as well as the subsequent rough surfaces are highlighted in Table 4.1 and these parameters will be used for all plots (both 1D and 2D rough surfaces) going forward unless otherwise stated.

Table 4.1: Parameters for the generation of random rough surfaces

Parameter	1 D surface	2 D surface
Number of surface points (N)	1500	1500
Length of surface (rL)	10 m	10 m
rms height (h)	1cm, 14 cm	1cm, 14 cm
Correlation length (cl)	1cm, 12.5 cm	-
Correlation length in x & y	-	12.5 cm

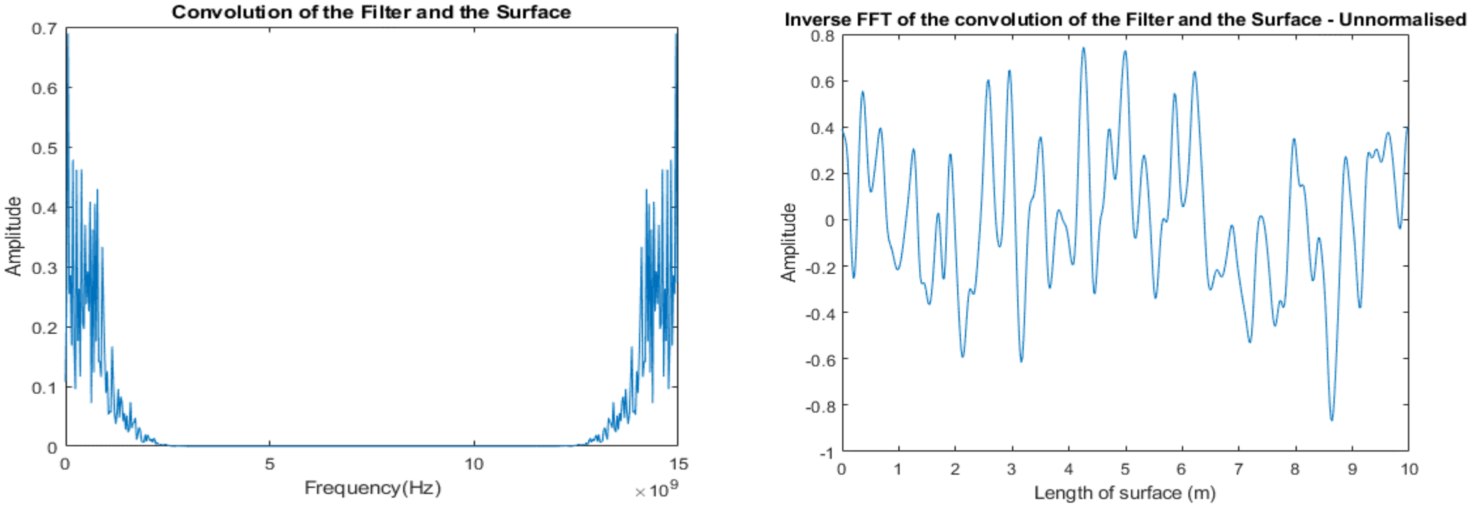

(e) Convolution of the filter & surface

(f) IFFT of Convolution filter & surface

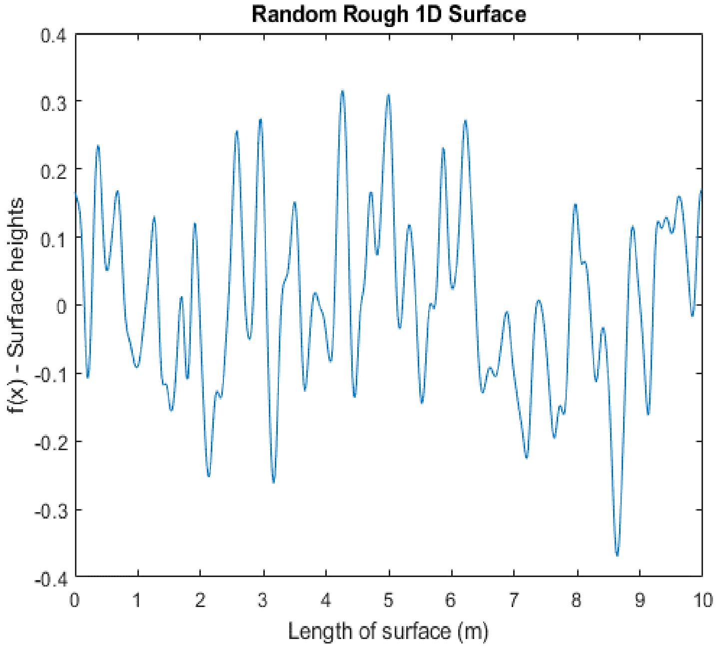

(g) Generated 1D random rough surface.

Figure 4.1: (a) Gaussian filter for a 1D surface (b) FFT of 1D Gaussian filter (c) Uncorrelated Gaussian 1D surface (d) FFT of Uncorrelated 1 D surface (e)Convolution of the filter and surface (f) IFFT of the convolution of the filter and surface (g) Generated 1D random rough surface

In figure 4.1a, the Gaussian filter smoothens the roughness profile, thereby reducing high-frequency variations. The FFT in figure 4.1b confirms that low frequencies are preserved while high frequencies are attenuated. Figure 4.1c is an uncorrelated gaussian rough surface with random height variations which closely models the surfaces pipelines are laid with irregular height variations. The FFT of the uncorrelated rough surface in Figure 4.1d shows a wide range of frequency components highlighting high-frequency roughness which has implications for RCS and reflectivity. The convolution in frequency domain which is shown in Figure 4.1e shows how the surface roughness interacts with the radar system's filter, which invariably represents what happens when EM waves encounter dielectric interfaces or layered terrain. Figure 4.1f is the IFFT of the filtered surface profile which is the resulting terrain after applying radar system characteristics. Compared to the raw surface, this one is spectrally limited, meaning only certain roughness features will contribute to the observed RCS. Figure 4.1g is the random rough 1D surface which has been modelled to simulate scattering behaviour for the various dielectrics. The surface represents a spatial roughness spectrum that impacts RCS

Please note that there is no marked difference in the generation of the plots for a 1D random rough surface when the surface has a Gaussian height distribution function and an exponential autocorrelation function. The major difference is in the exponential filter applied to the model, denoted by ***ExpF*** and given by Equation 4.6 as [102]

$$ExpF = e^{\left(-abs(x) \big/ {cl}/_{2}\right)} \tag{4.6}$$

where $x \in [0, rL, N]$ is the output of the surface points.

For the generation of a square 2-dimensional (2D) random rough surface *f (x, y)* with *N x N* surface points and the surface has a Gaussian height distribution function, a Gaussian or an exponential autocorrelation function in both *x* and *y* (i.e. acfx and acfy) could be applied to the 2D rough surface model. The input parameters to the 2D model are the number of surface points (along square side) denoted by ***N***, length of the surface side denoted by ***rL***, the rms height denoted by ***h***, and the correlation lengths in x and y denoted by ***clx*** and ***cly*** respectively.

Omitting *cly* makes the surface isotropic. A Cartesian grid in 2D space of *x, y* called *[X, Y]* is formed where $x \in [0, rL, N]$ is the output of the surface points in *x* and $y \in [0, rL, N]$ is the output of the surface points in *y* respectively.

The uncorrelated Gaussian random rough surface distribution with a mean of 0 and rms height ***h*** for a 2D surface is denoted by ***Z*** and given by Equation 4.7 below as:

$$Z = h * randn(N, N) \tag{4.7}$$

The Gaussian filter applied to the model is denoted by ***F*** and given by Equation 4.8 as:

$$F = e^{\left\{-\left({X^2}/{{clx^2}/{2}} + {Y^2}/{{cly^2}/{2}}\right)\right\}} \tag{4.8}$$

To obtain the output of the surface heights denoted by ***f (x, y)***, the FFTs of the uncorrelated Gaussian random rough surface (Z) (in x and y axes) as well as the Gaussian filter (in both x and y axes) must be obtained at first. Therefore, applying FFT (in both dimensions i.e. fft2) to Equation 4.7 and Equation 4.8 results in Equation 4.9 and Equation 4.10 respectively as:

$$Z_{x,y} = \sum_{n=1}^{N} \sum_{n=1}^{N} Z_{n,n}\, e^{{-j2\pi(x,y)n,n}/{N,N}}, \quad x, y = 1, \ldots N \tag{4.9}$$

$$F_{x,y} = \sum_{n=1}^{N} \sum_{n=1}^{N} F_{n,n}\, e^{{-j2\pi(x,y)n,n}/{N,N}}, \quad x, y = 1, \ldots N \tag{4.10}$$

Now, when the Inverse Fast Fourier transform is applied to a convolution of the filter and the surface in both axes i.e. x and y, in addition to other normalising prefactors, the output of the correlated generated surface is therefore given by Equation 4.11 below as:

$$f(x, y) = {2}/{\sqrt{\pi}} * {rL}/{\left(N * \sqrt{clx * cly}\right)} * F^{-1}\{Z_{x,y} .* F_{x,y}\} \tag{4.11}$$

The plots for the Gaussian filter for a 2D surface, the uncorrelated 2D rough surface, the convolution of the 2D filter and the surface, the IFFT of this convolution of the 2D filter and the surface as well as the subsequent generation of the correlated 2D random rough surface are shown in Figure 4.2.

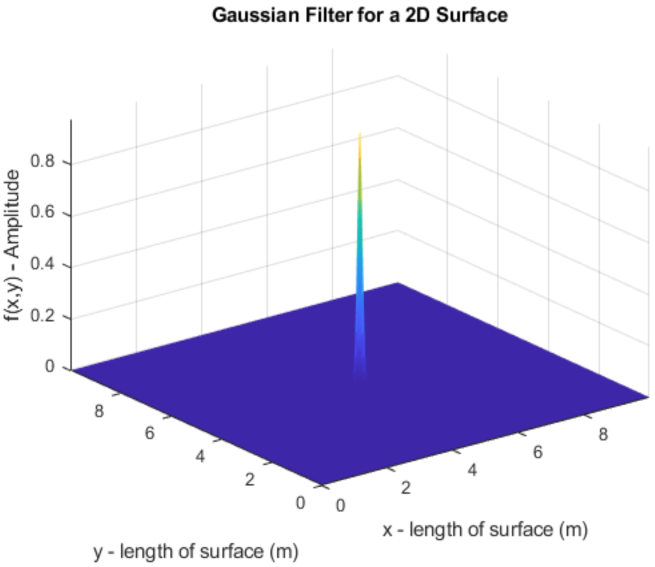

(a) Gaussian filter for a 2D Surface

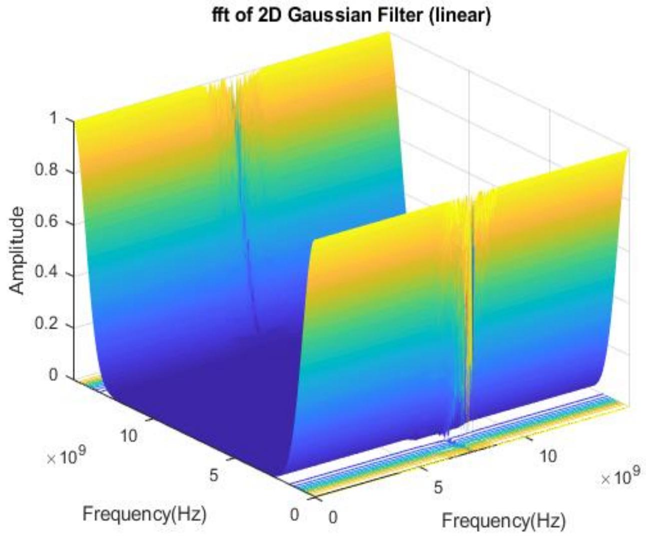

(b) FFT of 2D Gaussian Filter (linear)

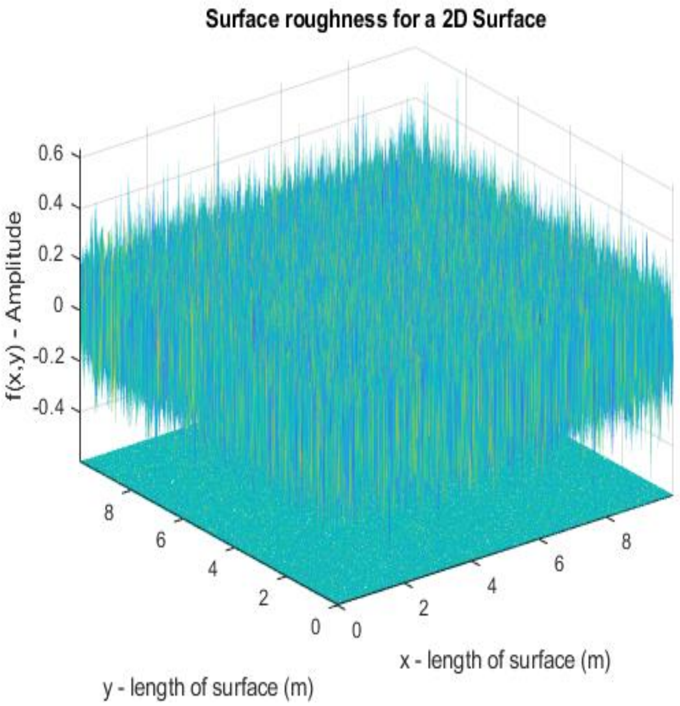

(c) Surface roughness for a 2D Surface

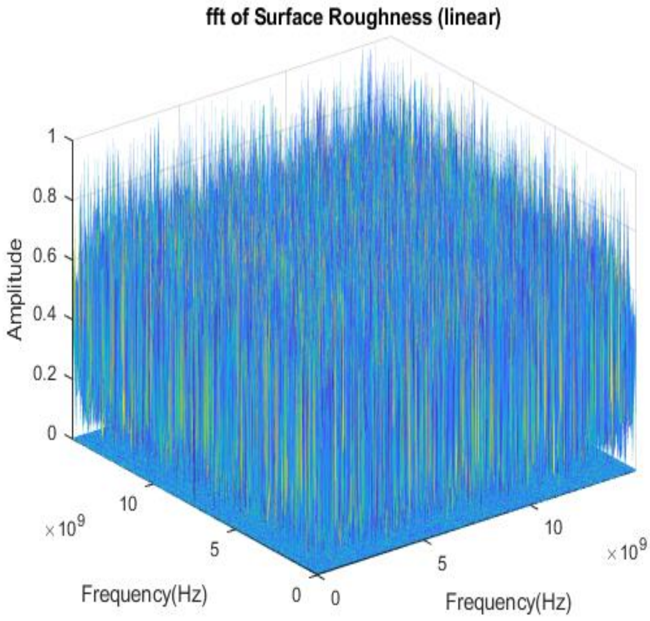

(d) FFT of Surface roughness

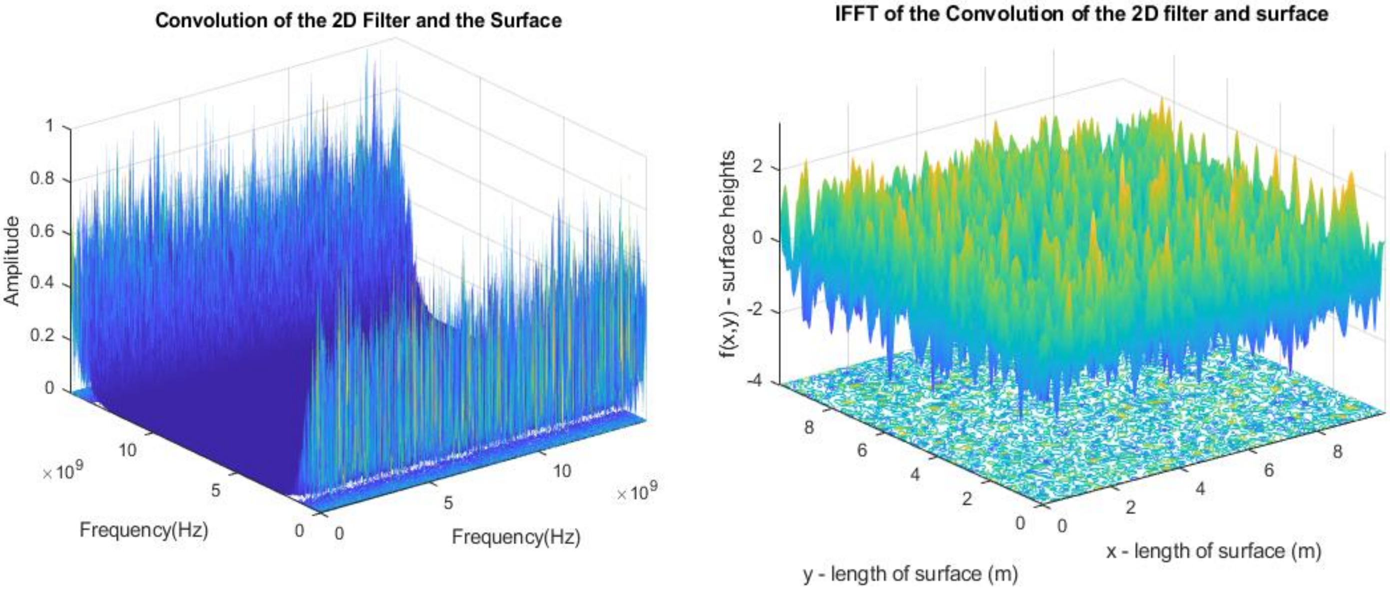

(e) Convolution of the filter & surface

(f) IFFT of convolution of filter & surface

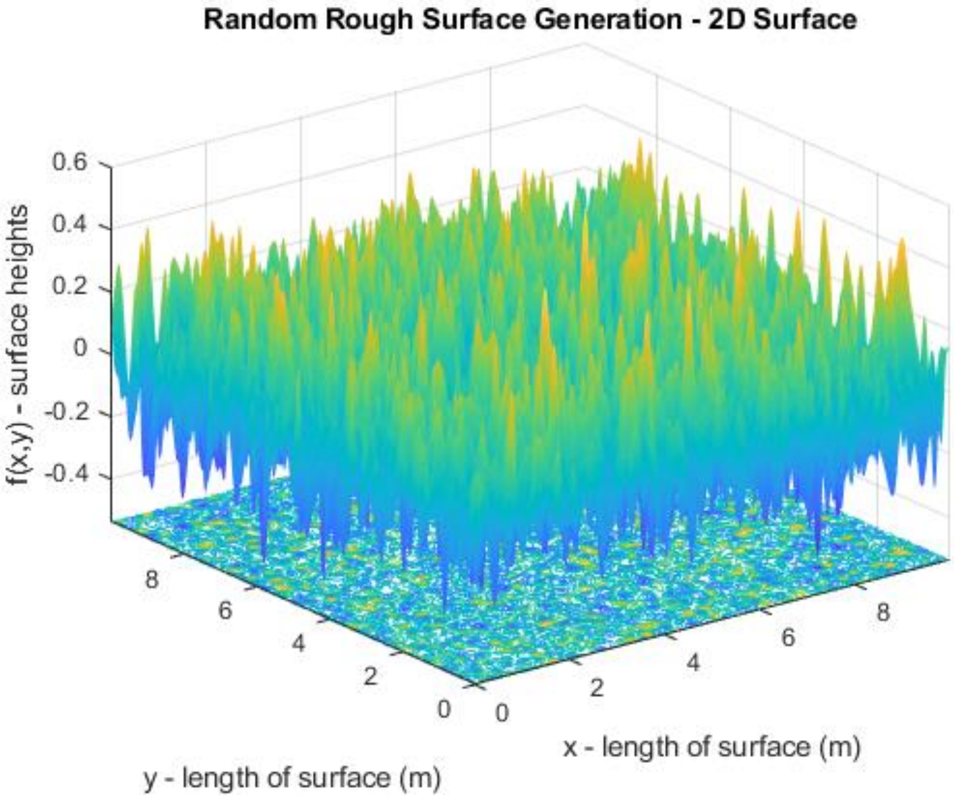

(g) Generated 2D random rough surface

Figure 4.2: (a) Gaussian filter for a 2D surface (b) FFT of 2D Gaussian filter (c) Surface roughness for a 2D surface (d) FFT of surface roughness (e)Convolution of the filter and surface (f) IFFT of the convolution of the filter and surface (g) Generated 2D random rough surface

In figure 4.2(b), the frequency response of the 2D Gaussian filter shows peaks at 0Hz and 15GHz. A peak at 0 Hz is expected because a Gaussian function in the spatial domain is a low-pass filter, meaning most of its energy is concentrated at low frequencies. The peak at 15 GHz likely corresponds to the highest frequency component retained before the signal attenuates. This suggests that 15 GHz represents the cutoff frequency or the highest frequency where the filter allows significant components to pass. Therefore, the peak at 0 Hz and 15 GHz suggest that the filter preserves low-frequency components while suppressing high frequencies beyond 15 GHz. The figure also suggests two frequency dimensions likely corresponding to the x- and y- directions in 2D space. In 2D Fourier Transform, we obtain a 2D frequency spectrum with two independent frequency axes (e.g. fx and fy in Hz). Since the image shows symmetry, it indicates that the Gaussian filter was applied equally in both x and y spatial directions, resulting in identical frequency distributions along both axes. The two frequency axes represent spatial frequency components in the x- and y- directions, reflecting the filtering effect in both dimensions.

Furthermore, the low height values (≈ - 0.4 and below) in figures 4.2(c) and 4.2(g) represent areas of minimal elevation in the random rough surface models. They indicate surface depressions in the roughness model. These values correspond to points where the simulated surface has valleys or depressions relative to the generated roughness profile. The negative height values represent depressions in the rough surface, akin to lower terrain points or dips in a real-world soil surface. Despite the Gaussian filtering process, some of these depressions persist, meaning that certain fine-scale roughness elements remain significant. The FFT transformation and filtering influence the final height distribution but retain the general roughness profile with both peaks and valleys

To achieve adequate Gaussian statistics, it is important to use a ratio of ${}^{rL}\!/_{cl} \geq 500$ for a 1D surface and a ratio of ${}^{rL}\!/_{cl} \geq 70$ for a 2D surface, where 500 and 70 are the surface points.

Similarly, like in the case of the 1D rough surface model, note that there is no marked difference in the generation of the plots for a 2D random rough surface when the surface has a Gaussian height distribution function and an exponential autocorrelation function. The major difference is in the exponential filter ***E*** applied to the model, and given by Equation 4.12 as:

$$F = e^{\left\{-\left({abs(X)}/{{clx}/{2}}+{abs(Y)}/{{cly}/{2}}\right)\right\}} \tag{4.12}$$

The statistical constants for the generated 1D and 2D rough surface models were also investigated to ensure the right results were obtained and the generated models for both 1D and 2D surfaces are correct. Some of these statistical constants include the rms height, correlation lengths etc. Table 4.2 shows that on comparison with the statistical constants earlier provided in Table 4.1, the values obtained from the simulation closely match the predefined values earlier provided in Table 4.1. This consistency confirms that the simulation results align with the expected statistical parameters further indicating that the model is accurate and reliable. However, it was not possible to increase the number of surface points beyond 5000 due to computational challenges. But for all the number of surface points considered, the values of the statistical constants obtained from both models were like the predicted values for both 1D and 2D rough surfaces and both auto correlation functions. This therefore implies the developed or generated rough surface models does what it says it does and can be relied upon for further analysis.

Table 4.2: showing the correct comparison of values of the predicted statistical constants earlier shown in Table 4.1.

N (no.)	h (m) 1D	h(m) 2D	clx & cly (m)	Cor len. (1D)
1500	0.0101	0.1418	0.1234	0.0097
3000	0.0098	0.1407	0.1301	0.0108
4500	0.0102	0.1390	0.1234	0.0110
5000	0.0100	0.1415	0.1230	0.0111

Furthermore, the bandwidth of our 1D and 2D rough surface models can be estimated from the correlation length which is the width of the autocorrelation function of the 1D and 2D rough surfaces. From the analysis and Table 4.2 above, this width of the autocorrelation function is obtained to be about 11cm which tallies with the correlation length as shown in Table 4.2. Therefore, the bandwidth of about 9 Hz is obtained from the reciprocal of the width of the autocorrelation function and this is given in Equation 4.13 as:

$$Bandwidth = \frac{1}{width\, of\, acf} = 9.1\ Hz \tag{4.13}$$

4.2. CST Simulations / Modelling

In the subsequent subsections, the generated rough surface model is imported into CST Studio Suite - a specialist 3D simulation software for electromagnetic wave simulations. This was done in CST to enable us to introduce various dielectric constants into our rough surface model with the special capability to also adjust or change or replace the materials with various soil types like sandy, clay or loamy soil and the added advantage of changing the dielectric properties and related parameters, as this is hardly achievable in MATLAB. This is because while MATLAB is a powerful tool for generating rough surface models and numerical calculations, it lacks a dedicated 3D electromagnetic simulation environment with advanced solvers and material handling capabilities. CST Studio Suite is specifically designed for electromagnetic wave propagation analysis and makes it significantly easier to introduce and modify different dielectric materials in the simulation. How the correlation length also varies in literature for various soil types is investigated and applied to the rough surface model.

Before we consider the calculation and analysis of the RCS of rough surfaces in CST as well as the reflectivity analysis of the rough surface model [103], there is a need to first analyse the RCS of common objects (like a metal plate and sphere) in CST and then compare their results with the theoretical calculation and analysis of these same objects. This is done to enable us to rely on the results we obtain from the RCS analysis of rough surfaces as the theoretical calculation and analysis of the RCS of rough surfaces is unavailable in literature. Besides, the calculation of the RCS is most times possible for just simple objects and extending this calculation and analysis to complex objects or surfaces like a rough surface is not easily achievable with common mathematical tools like MATLAB hence the use of CST software for this RCS analysis of rough surface models.

RCS is the measure of a target’s ability to reflect radar signals in the direction of the radar receiver. RCS is a specific parameter of a reflective object and depends on many factors like the transmitting frequency of the radar, physical geometry of object, type of material, surface roughness, polarisation of the radar wave, angle of incidence, as well as target orientation. The surface area of simple geometric bodies depends on the ratio of the structural dimensions of the object to the wavelength. If absolutely all the incident radar energy on the target were reflected equally in all directions, then the RCS would be equal to the cross-sectional area of the target as seen by the transmitter. In reality, some energy is absorbed, and the reflected energy is not distributed equally in all directions. This therefore makes the RCS quite difficult to estimate and is normally determined by measurement. Thus, a measure of the ratio of backscatter density in the direction of the radar (from the target) to the power density that is intercepted by the target is defined as the RCS and given in Equation 4.14 as:

$$RCS = \frac{4\pi r^2 S_r}{S_t} \tag{4.14}$$

where S_t is the power density that is intercepted by the target,

S_r is the scattered power density in the range r

4.3. RCS Analysis of Common Objects (Flat Plate and Sphere)

The RCS calculation of a geometrical body like a metal plate is given by Equation 4.15 [73], [78], [104], [105] as:

$$RCS = \frac{4\pi b^2 l^2 f^2}{c^2} \tag{4.15}$$

where l is the length of the metal plate, b is the breadth of the metal plate, f is the transmitting frequency of the radar and c is the speed of light.

So for a metal plate of $l = 2m$, $b = 1m$, and radar's transmitting frequency of $10\ GHz$, the RCS is calculated to be about $47.5\ dB(m^2)$ which is in agreement with the results of the CST simulation of the RCS of a flat plate shown in Figure 4.3. The equation is correct for the RCS of a large, flat metal plate in the high-frequency limit where the plate dimensions are much larger than the radar wavelength. For both figures, the simulated RCS values remained the same despite the orientation of the plane wave.

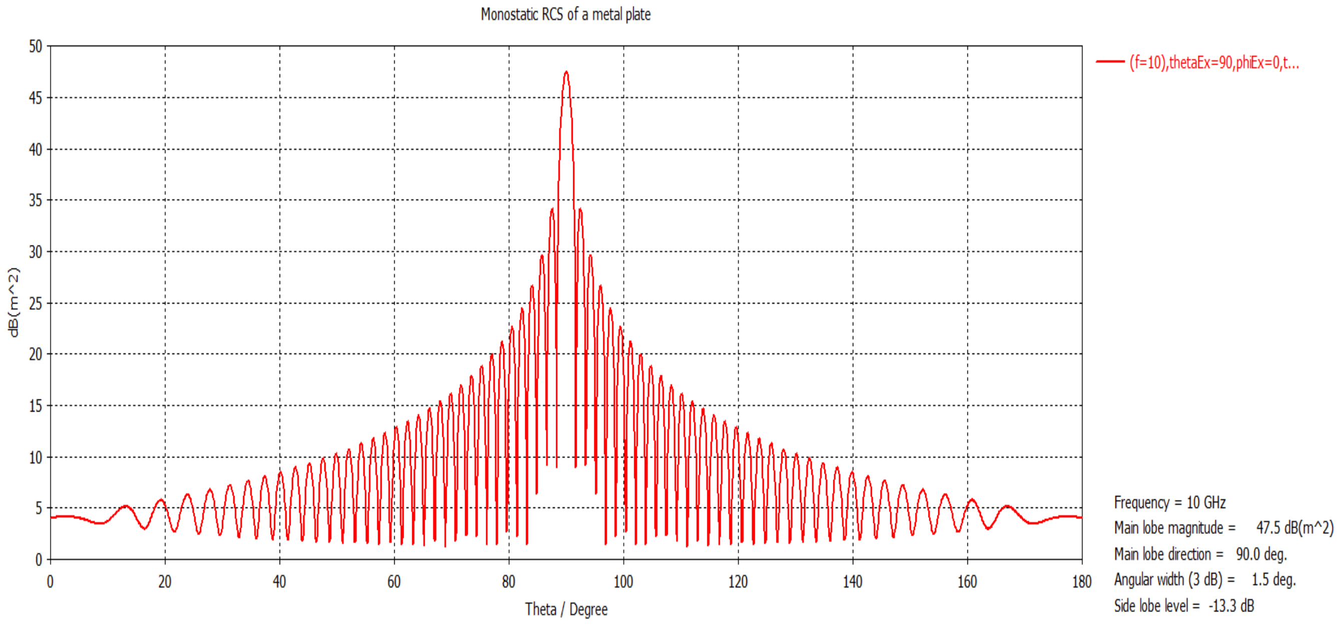

(a) RCS analysis of a metal (flat) plate simulated in CST (0° to 180°)

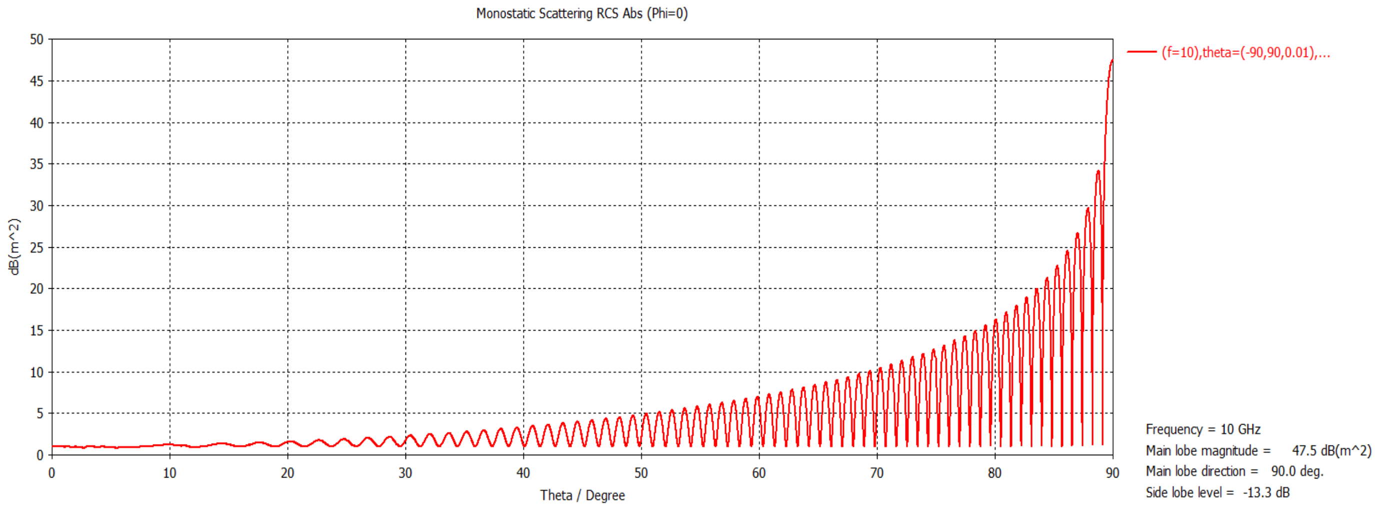

(b) RCS analysis of a metal (flat) plate simulated in CST (-90° to 90°)

Figure 4.3: RCS analysis of a metal (flat) plate simulated in CST (a) 0° to 180° (b) -90° to 90°

The RCS calculation for a sphere where $\lambda \ll size\ of\ sphere$ is given by Equation 4.16 as

$$RCS = \pi R^2 \tag{4.16}$$

where R is the radius of the sphere and λ is the wavelength.

So, for a sphere of $radius = 0.5m$, and radar's transmitting frequency of $6\ GHz$, the RCS is calculated to be about $-1.04\ dB(m^2)$ which is in tandem with the result of the CST simulation of the RCS of a sphere shown in Figure 4.4 below. The choice of 6 GHz is deliberate because the wavelength (5 cm) is much smaller than the sphere diameter (1m), ensuring the object is in the geometric scattering region where the RCS equation is valid. However, when the wavelength is much larger than the size of the sphere (Rayleigh scattering region), the sphere does not reflect the wave effectively like a large object. Instead, it acts like a weak scatterer. The RCS is thus given by Equation 4.17 as:

$$RCS = \frac{9\pi R^6}{\lambda^4} \tag{4.17}$$

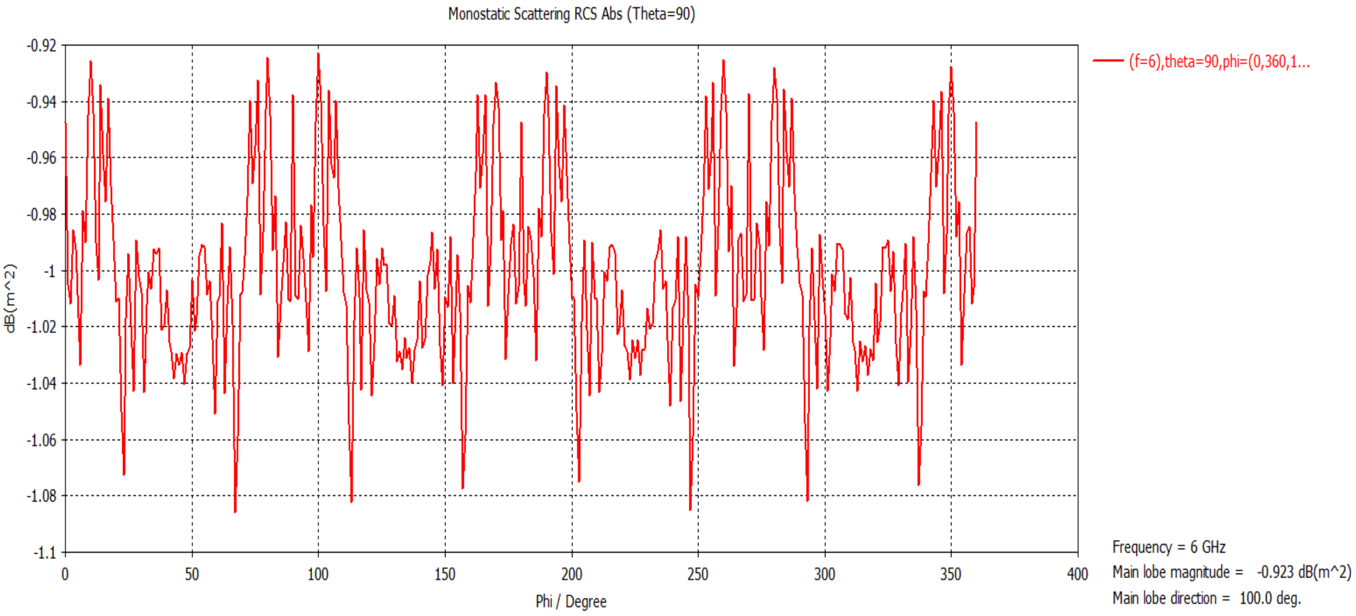

Figure 4.4: RCS analysis of a sphere simulated in CST

4.4. RCS Analysis of Rough Surface Model – Lossless Material (PEC)

To create a rough surface in CST is very difficult to achieve as the parameters which will facilitate this creation might take several months to achieve especially for a complex rough surface model. Therefore, to overcome this challenge, the rough surface already created in MATLAB is imported into CST so the RCS analysis of this rough surface can be actualised in CST. To do this, our MATLAB file (i.e. the .m file) of the rough surface is converted into a stereolithography (.stl) file (which is a 3D object) and then imported into CST for further analysis. The imported STL model is also verified to ensure the dimensions of the imported rough surface model tallies with the dimensions of the original MATLAB model prior to import. With this imported rough surface model in CST, it will be easier to define or vary the properties of the materials (say from lossless to a lossy material etc) as well as incorporate or modify various dielectric properties or constants of the rough surface model in the RCS analysis.

For the MATLAB model to be converted into an STL file, the size of the array (***N***) of the model had to be reduced from about 1500 x 1500 number of surface points to about 50 x 50 number of surface points. Also, the length of the surface (***rL***) had to be reduced from a 10m x 10m surface to a 1m x 1m surface. This is because of insufficient memory on the PC as well as inadequate computing facilities as the PC tends to struggle after the conversion if the model is not reduced. I used repeated simulations of smaller areas to compensate for any irregularities arising from this. However, other parameters like the correlation length (***cl***) and the rms height (***h***) remain the same. Furthermore, while reducing the model resolution and area introduces potential challenges, these are mitigated by statistical consistency checks, repeated simulations, and validation against analytical models. The primary trade-off is between computational feasibility and accuracy, and the chosen approach ensures a balance between computational efficiency and preserving the essential roughness characteristics of the surface.

The rough surface is then triangulated and imported into CST and the boundaries are constrained so it is like a waveguide. When this model is imported into CST, then the type of material as well as the dielectric properties of the material can be easily adjusted in CST prior to running the simulations and analysing the RCS of such rough surface. As a result, the model and its dielectric properties can be changed from a lossless material (e.g. PEC) to a lossy material (e.g. sandy soil, loamy soil, alumina etc.). Figure 4.5 shows an example of the original 2D model in MATLAB as well as the imported version in CST with the same correct dimensions while Figure 4.6 shows the equivalent for a 1D rough surface model.

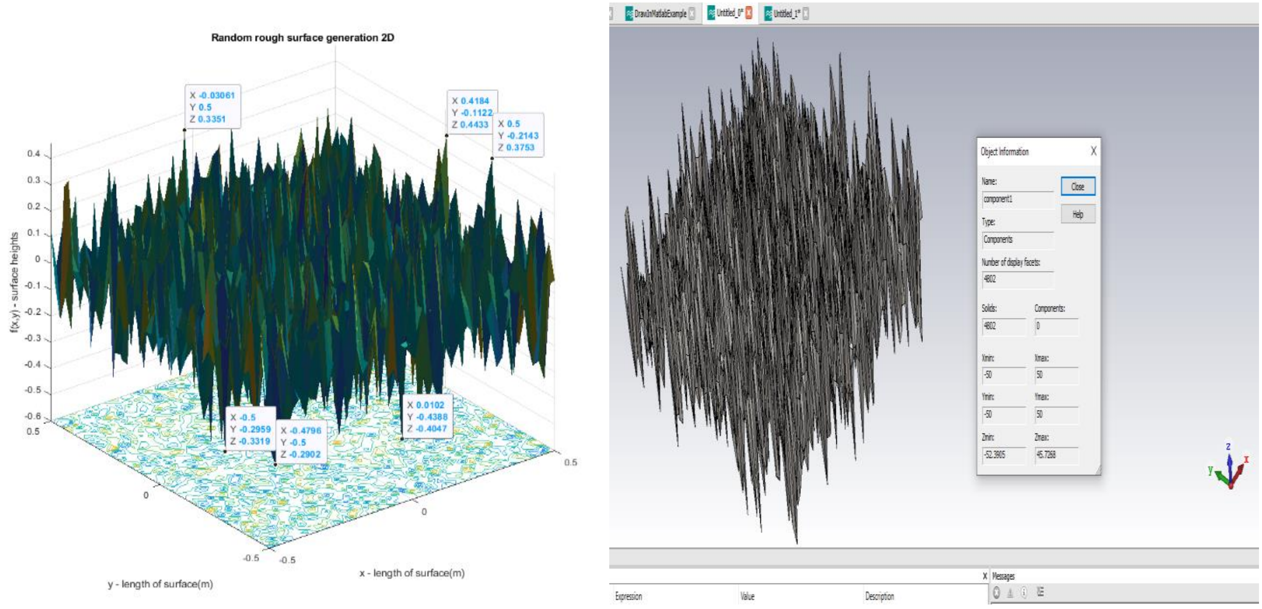

Object Information

Name: component1

Type: Components

Number of display facets: 4802

Solids: 4802

Components: 0

Xmin: -50

Xmax: 50

Ymin: -50

Ymax: 50

Zmin: -52.3905

Zmax: 45.7268

(a) 2D rough surface model in MATLAB (b) 2D rough surface model in CST

Figure 4.5: 2D rough surface model in (a) MATLAB (b) CST

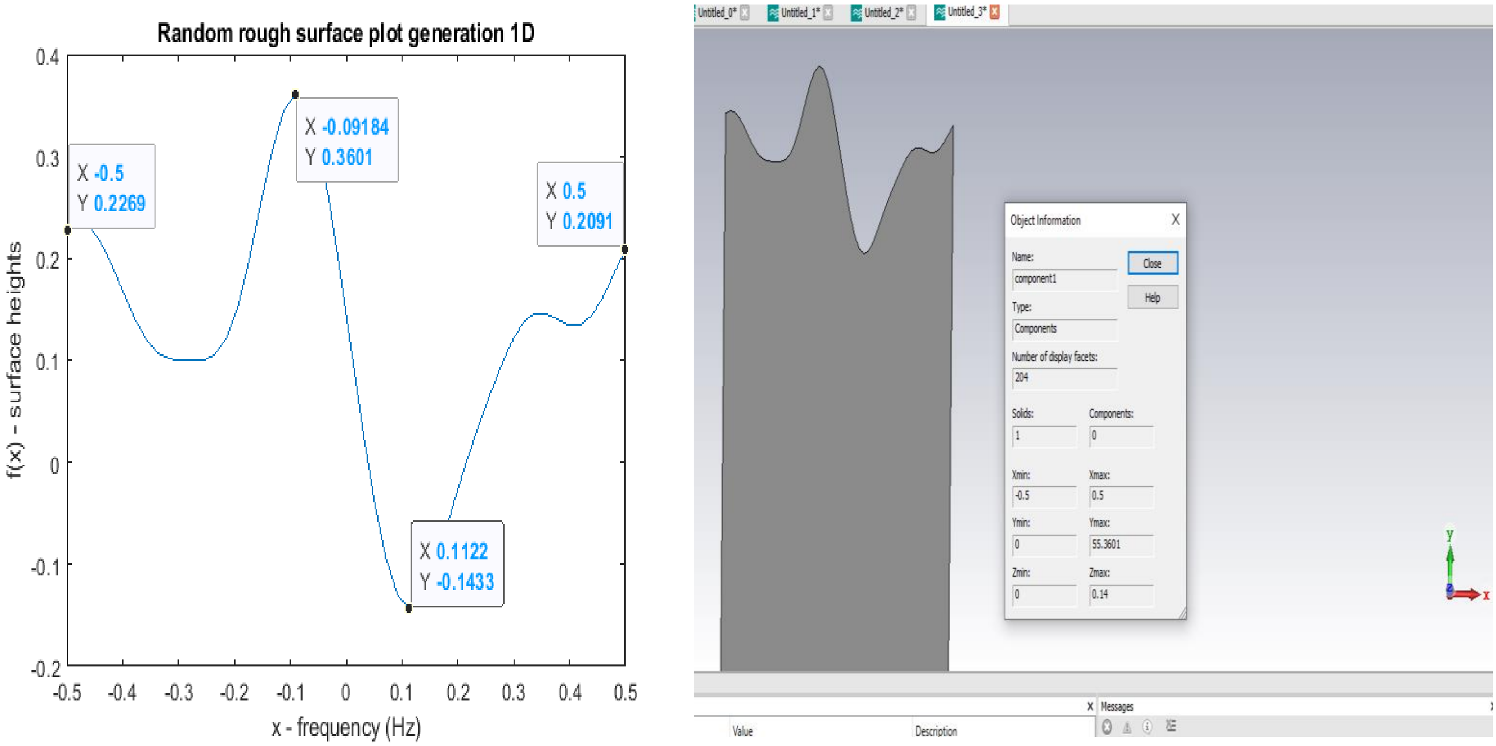

Object Information

Name: component1

Type: Components

Number of display facets: 204

Solids: 1

Components: 0

Xmin: -0.5

Xmax: 0.5

Ymin: 0

Ymax: 55.3601

Zmin: 0

Zmax: 0.14

(a) 1D rough surface model in MATLAB (b) 1D rough surface model in CST

Figure 4.6: 1D rough surface model in (a) MATLAB (b) CST

Now the rough surface model has been successfully imported into CST with the dimensions compared and accurately verified with the original model, the next task is to calculate the RCS of this 2D rough surface model in CST like it was done for a flat plate and sphere in the previous subsection. To achieve this, the RCS of a smaller dimension from the rough surface is analysed due to inadequate computing requirements in simulating a much larger or heavier rough surface model as well as incessant computational drawbacks from my PC.

The simulation parameters for the RCS analysis of my rough surface as well as the simulation parameters for the RCS analysis of common objects like a flat plate earlier discussed in section 4.2 are all provided in Table 4.3.

Table 4.3: showing the simulation parameters for the RCS analysis of a rough surface

Simulation Parameters – RCS for a rough surface and smooth (flat) surface	
Polarisation	Custom
Accuracy	Medium
Frequency	1 & 10 GHz
Observation angle sweeps	0° to 180° (steps of 10°) -90° to 90° (steps of 10°)
RCS	Monostatic
Material (lossless / lossy)	PEC / Sandy Soil
Flat plate	2m by 1m
Rough surface	1m by 1m
Number of surface points	500
Correlation lengths in (x & y)	0.125m
RMS height (roughness)	0.14m & 0.28m
Simulation run time	5½ hours (≈ 24 hrs for sandy soil)
Solver (lossless / lossy)	Asymptotic / Integral Equation

For the rough surface model, the material of the rough surface in this instant is a PEC which is a lossless dielectric material. The plane wave incident on the rough surface is custom polarised and this plane wave sweeps through from -90° to 90° in steps of 10° or from 0° to 180° also in steps of 10°. The accuracy of the Asymptotic Solver which is the solver used for this simulation has been set to medium accuracy just to have an efficient simulation. The Asymptotic Solver is very suitable for lossless materials. The frequency of the incident wave has been set to either 1GHz or 10GHz depending on the simulation. The simulation parameters listed in Table 4.3 have also been varied or modified to achieve a variety of results which will aid in the analysis of a 2D rough surface model. The results from these simulations are shown in Figures 4.7 to 4.9. Comparing figures 4.7 and 4.8, while the theoretical RCS equation for a flat plate suggests that RCS increases with frequency, real-world rough surfaces do not always follow this trend strictly. The effective RCS also depends on the incident angle, polarisation and surface irregularities. Thus, despite the theoretical expectation that shorter wavelengths should result in a higher RCS for a perfectly smooth surface, real-world roughness and scattering mechanisms reduce the effectiveness of coherent reflection, leading to a lower observed RCS of 23.8 dBm^2 at 10 GHz.

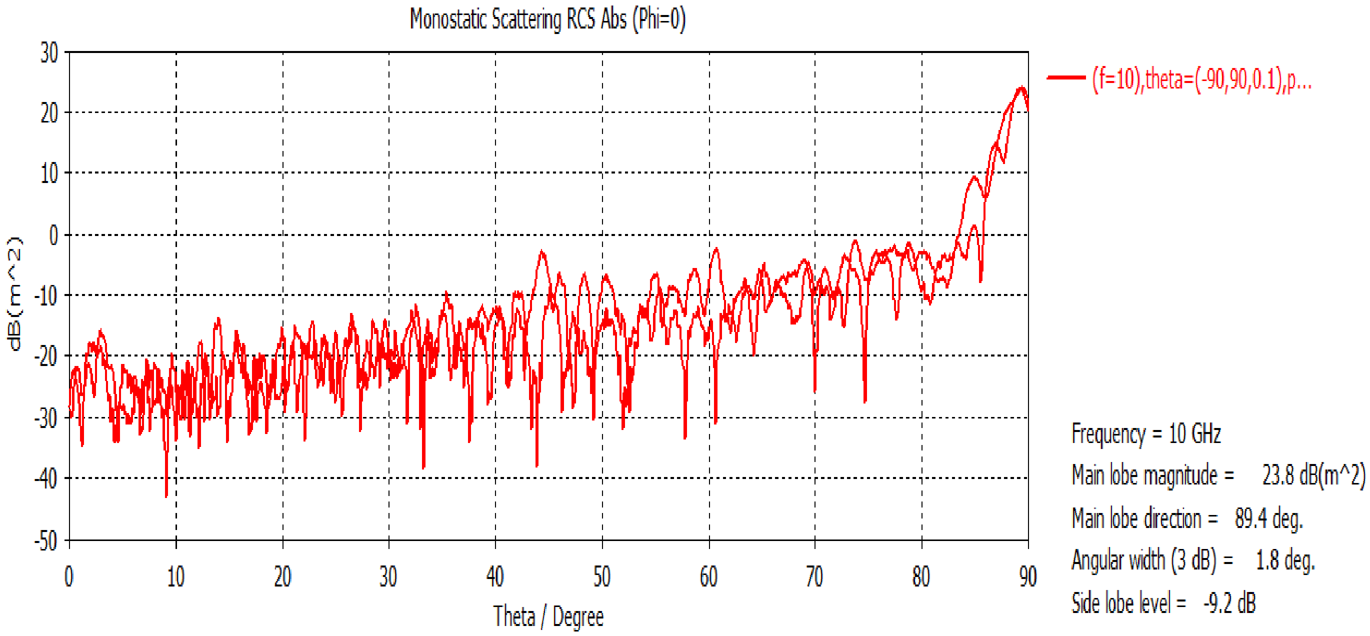

(a) RCS analysis of a rough surface (PEC) 1m x 1m (-90° to 90°) @ N = 500

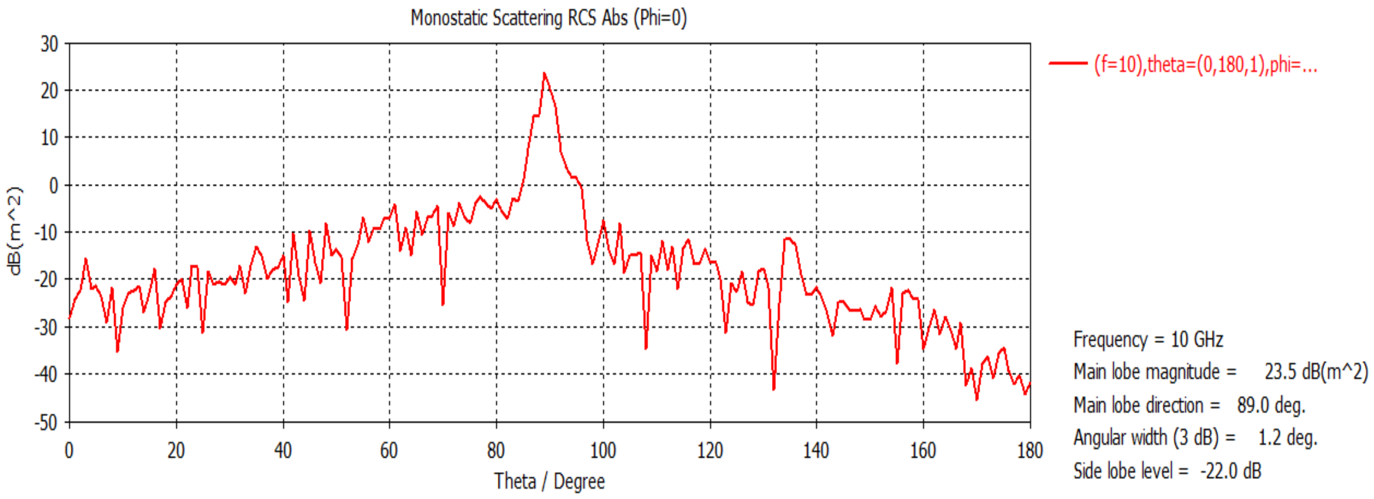

(b) RCS analysis of a rough surface (PEC) 1m x 1m (0° to 180°) @ N = 500

Figure 4.7: RCS analysis of a PEC at 10 GHz (a)- 90° to 90° (b)0° to 180°

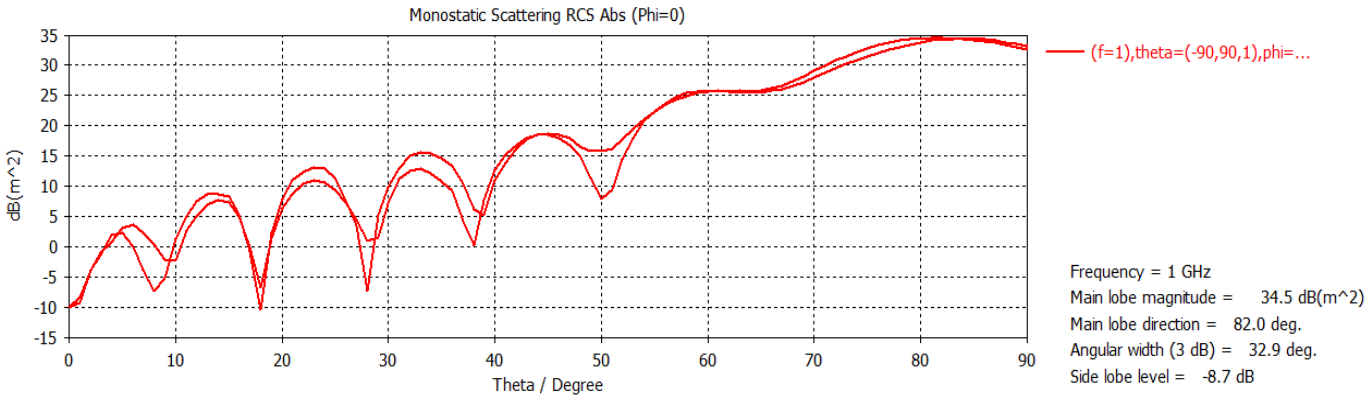

(a) RCS analysis of a rough surface (PEC) 1m x 1m (-90° to 90°) @ N = 500

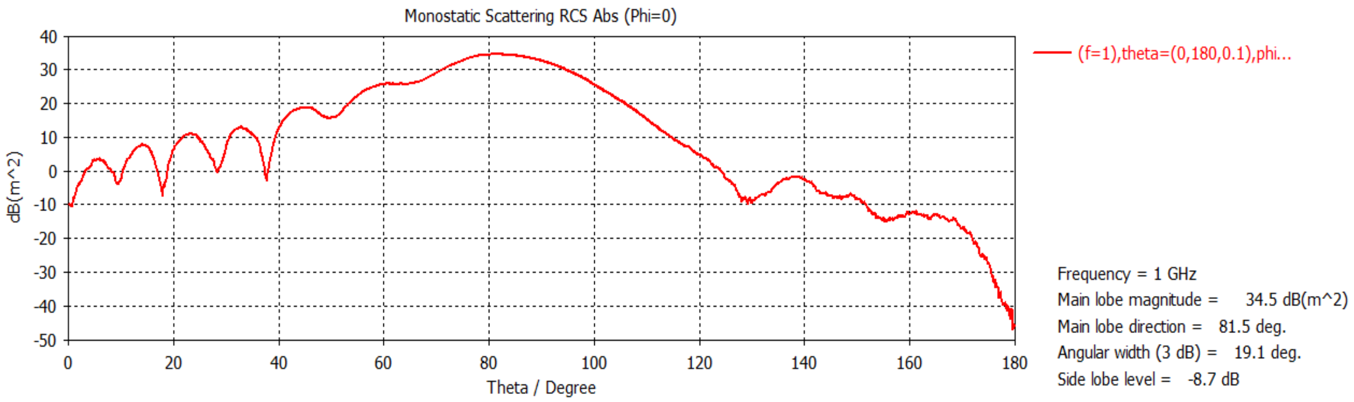

(b) RCS analysis of a rough surface (PEC) 1m x 1m (0° to 180°) @ N = 500

Figure 4.8: RCS analysis of a PEC at 1 GHz (a)- 90° to 90° (b) 0° to 180°

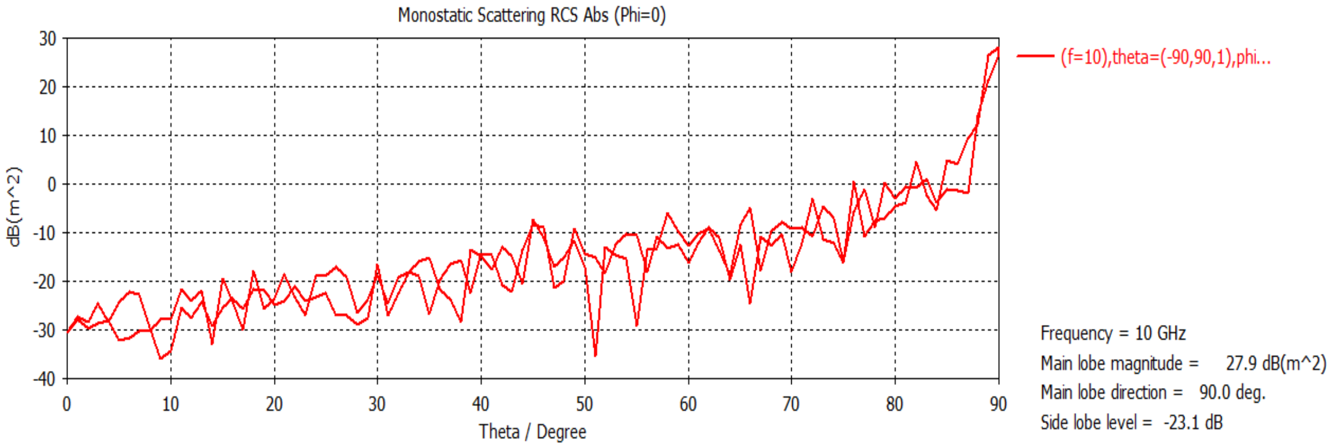

Figure 4.9: RCS analysis of a PEC (1m x1m) at 10 GHz and rms height of 28 cm

The results from Figures 4.7a and 4.7b are basically the same. The RCS was calculated to be about 24 dB(m^2). The magnitude of the main lobe was obtained to be about 90°. When this RCS value obtained is compared to the value of the RCS obtained in Figure 4.8, the result suggests that the higher the frequency of the plane wave, the lower the RCS value and vice versa for those number of surface points i.e. 500 in our case. Like was seen previously, despite the theoretical expectation that shorter wavelengths should result in higher RCS for a perfectly smooth surface, real-world roughness and scattering mechanisms reduce the effectiveness of coherent reflection, leading to a lower observed RCS at 10 GHz. In Figure 4.8, an RCS value of 34.5 dB(m^2) is obtained for a frequency of 1GHz as opposed to the value of about 24dB(m^2) obtained for 10GHz frequency. This inverse relationship between the RCS and the frequency for a lossless rough surface appears to be at variance with the relationship between the RCS and the frequency for a smooth or flat surface. If the generated roughness features are smaller than the resolution cell at higher frequencies, then the system may not be adequately resolving the roughness leading to underestimated RCS values. Increasing the number of surface points or improving spatial resolution in the simulation could provide more accurate results. For a smooth or flat surface, RCS is directly proportional to the frequency as shown by Equation 4.15. In Figure 4.3, a higher RCS value of 47.5 dB(m^2) is obtained at 10 GHz; now if the RCS for a smooth surface with same dimensions (2m x 1m) is calculated at 1 GHz, an RCS value of about 27.5 dB(m^2) is obtained.

However, If the number of surface points for our lossless rough surface is drastically reduced to 100 or 50, then the higher the frequency of the plane wave, the higher the RCS value and vice versa. This is as shown in Figures 4.10 and 4.11. In Figure 4.10a, an RCS of 17 dB(m^2) is obtained at 10 GHz, while an RCS of 15.7 dB (m^2) is obtained for 1GHz as shown in Figure 4.10b. This implies that the RCS of our lossless rough surface depends on the number of surface points that defines its roughness.

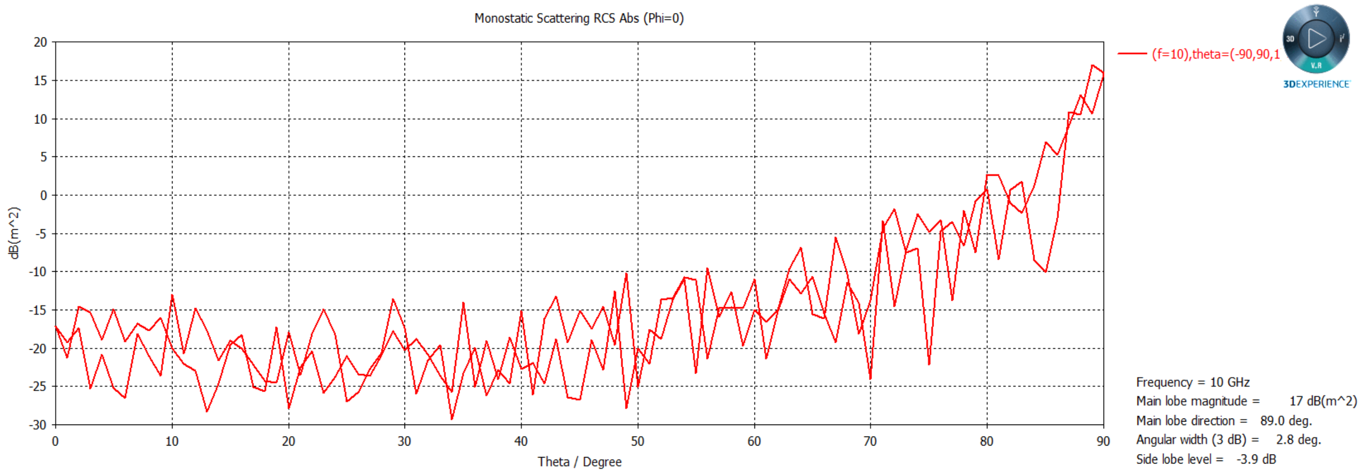

(a) RCS analysis of a rough surface (PEC) 1m x 1m for 100 samples @ 10GHz

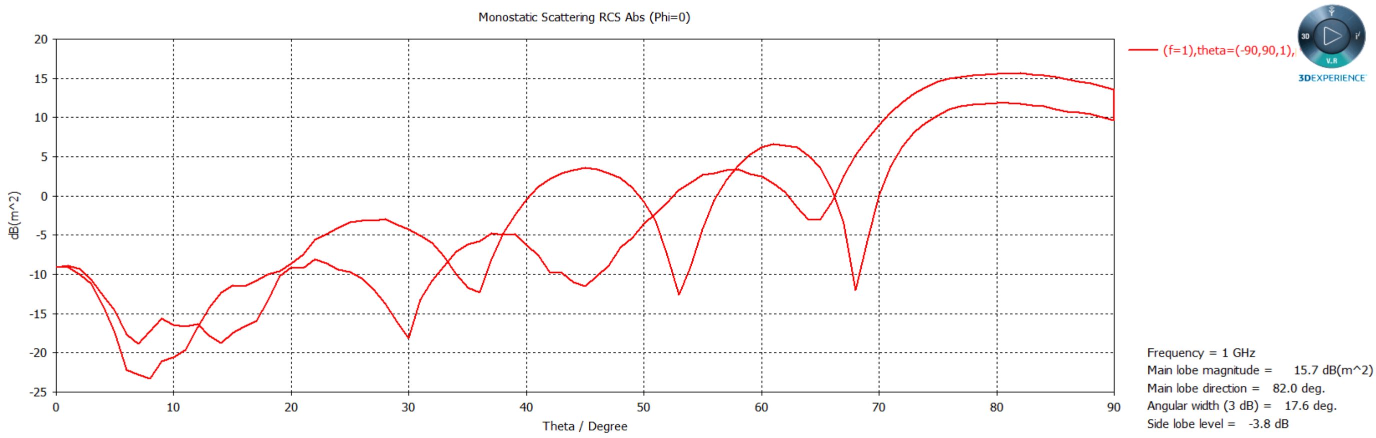

(b) RCS analysis of a rough surface (PEC) 1m x 1m for N = 100 samples @ 1GHz

Figure 4.10: RCS analysis of a rough surface PEC (a) 10 GHz b) 1GHz

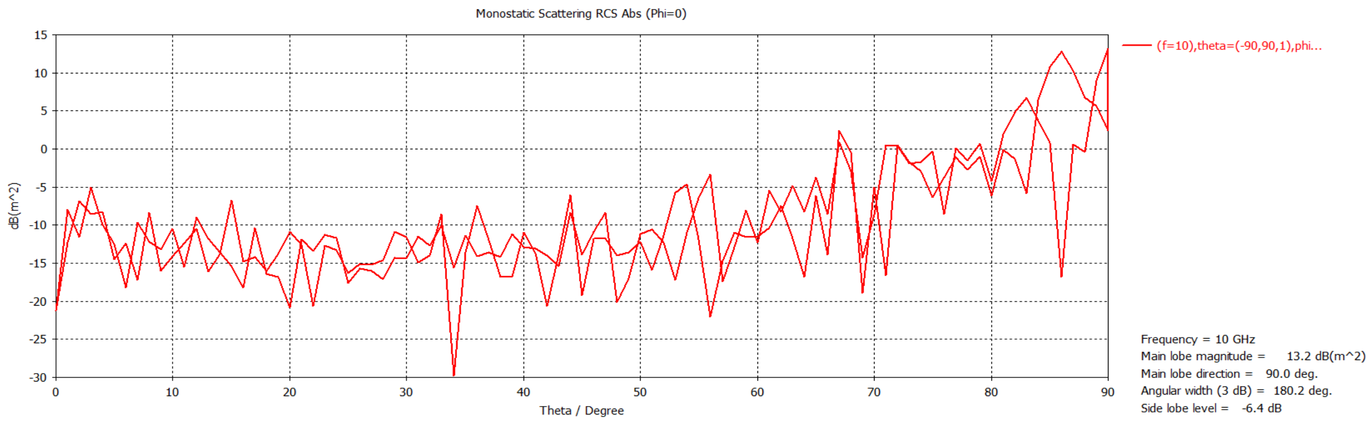

(a) RCS analysis of a rough surface (PEC) 1m x 1m for 50 samples @ 10 GHz

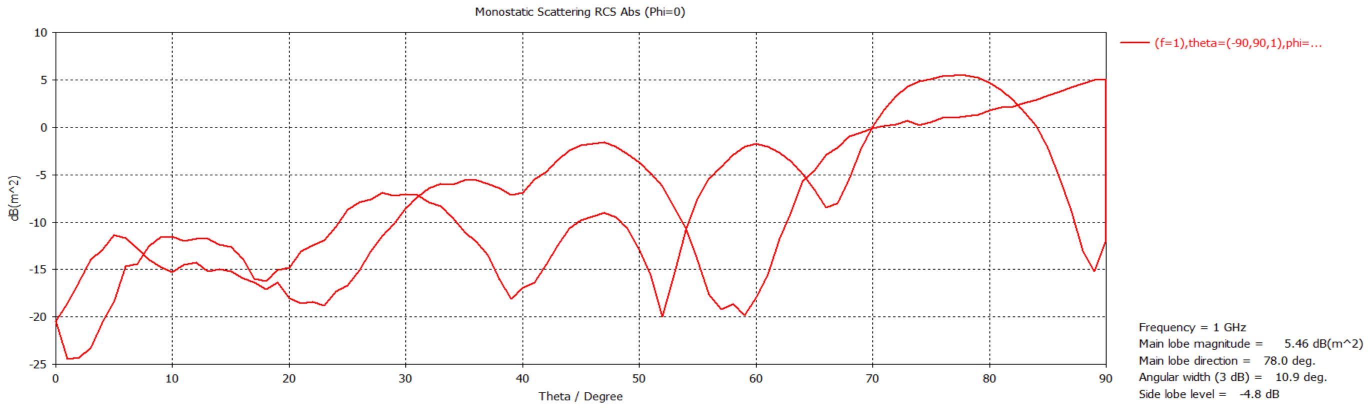

(b) RCS analysis of a rough surface (PEC) 1m x 1m for N = 50 samples @ 1 GHz

Figure 4.11: RCS analysis of rough surface PEC 50 samples (a)10 GHz (b)1 GHz

Similarly, in Figure 4.11a, an RCS of 13.2 dB(m^2) is obtained at a frequency of 10 GHz, while an RCS of 5.46 dB(m^2) is obtained for a frequency of 1GHz as shown in Figure 4.11b.

Furthermore, when the RCS values for a smooth and rough surface with similar dimensions are compared at a particular frequency, the values of RCS (in terms of the magnitude) obtained is consistent with existing literature [106] and aligns with theoretical expectations. Besides, RCS is also inversely proportional to the roughness of a surface. Therefore, it is expected that the reflectivity from a smooth surface should be higher than the reflectivity from a rough surface with the same dimensions and parameters. This is because at higher frequencies, the rough surface causes more diffuse scattering and back reflections in multiple directions, reducing the amount of energy reflected directly back to the radar. For example, at 10GHz, the RCS for a smooth surface (1m x1m) is obtained as 41.45 dB(m^2), while the RCS for a rough surface of similar dimensions and frequency is about 24 dB(m^2) as shown in Figure 4.7. However, at lower frequencies, for example at 1GHz, the RCS for a smooth surface is lower than the RCS for a rough surface. At 1GHz, a smooth surface of 1m x 1m has an RCS of 21.45 dB(m^2), while a rough surface with similar dimensions and same frequency has an RCS value of 34.5 dB(m^2) as shown in Figure 4.8. So extra care should be taken when comparing the peculiarities of these different surfaces so the correct analysis or inference can be drawn without being misled with regards the characteristics of each surface.

Looking at Figure 4.9, when the rms height is doubled for the rough surface, the value of the RCS increases (from about 24 dB(m^2) in Figure 4.7 to about 28 dB(m^2) in Figure 4.9). This might be attributed to the fact that the increase in the rms height sort of makes the rough surface a bit ‘smoother’ which now brings about an increase in the RCS value obtained. The relationship between the RCS and the rms height of a rough surface has been thoroughly investigated and this shall be extensively discussed as we progress in this thesis, beginning from the next subsection.

4.5. RCS Analysis of Rough Surface Model – Lossy Material (Sandy Soil)

In this section, the lossless material (PEC) is now changed to a lossy material (sandy soil) to analyse the RCS. To calculate the RCS of a lossy material (sandy soil), the same simulation parameters earlier highlighted in Table 4.3 are used save for some few adjustments or modifications which will be highlighted as we go along. First, the Integral Equation Solver is used and not the Asymptotic Solver used all along because losses in dielectrics are neglected by the Asymptotic Solver, thus Asymptotic Solvers do not support the RCS simulation of lossy materials. For lossy materials, the Integral Equation Solver was used for the simulation of the RCS. Furthermore, the rough surface model which is like a rough sheet as shown in Figure 4.5b was converted into a solid body because of the error in surface meshing which occurs during the RCS simulation of the rough sheet, and since there is an error in surface meshing of the rough surface sheet, then the RCS analysis of the lossy rough surface cannot be achieved. To overcome this error in surface meshing, the number of surface points (N) of the rough surface model was drastically reduced from 500 to a much lower number due to computational issues of the PC prior to being converted into a rough solid body.

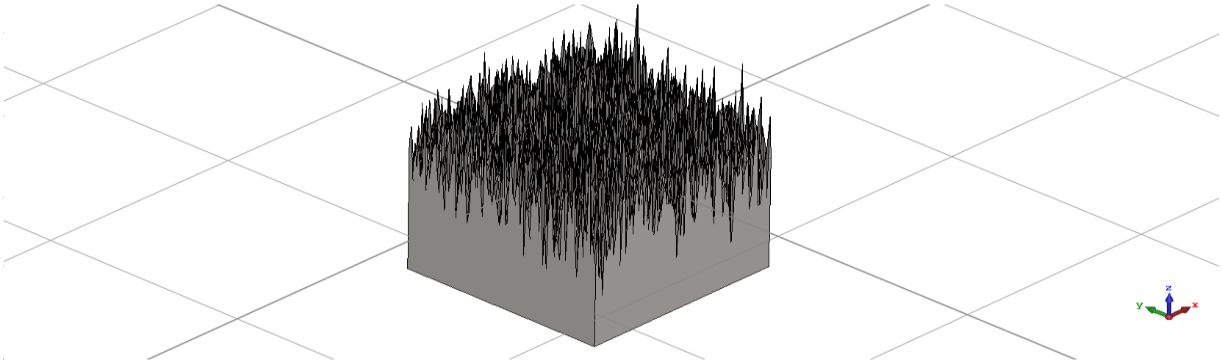

(a) Rough surface 'sheet' converted into a rough solid body with N = 100

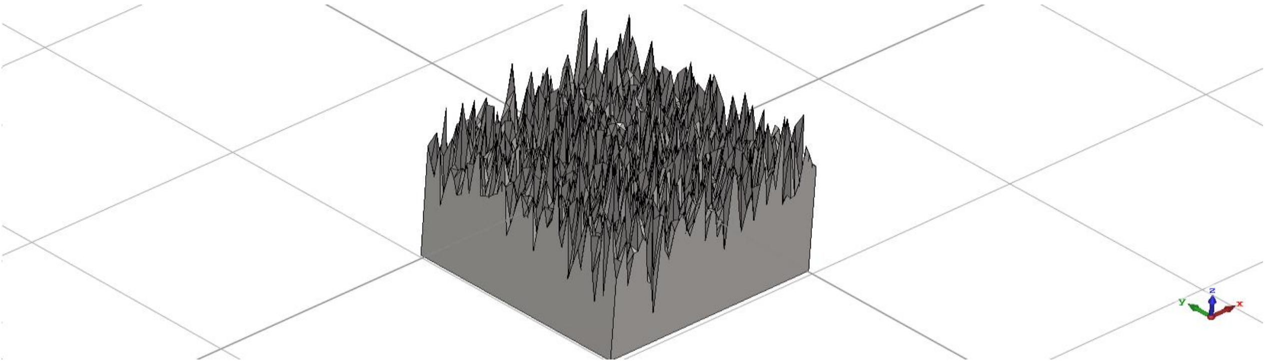

(b) Rough surface 'sheet' converted into a rough solid body with N = 50

Figure 4.12: Rough surface converted into a solid body (a) N = 100 (b) N = 50

Figure 4.12a shows a rough surface that has been converted into a rough solid body for N = 100 as the number of surface points, while Figure 4.12b is for a rough solid body with N = 50. The material for this rough surface in this instant was selected or chosen as a lossless material (PEC) and dimensions of the rough surface was chosen to be 1m x 1m.

In Figure 4.13a, the RCS of the solid rough surface (1m x 1m) at 10GHz was obtained to be about 37 dB(m^2) which is higher than the RCS of the sheet-like rough surface with similar parameters obtained as 17 dB(m^2) in Figure 4.10a. Both surfaces are made of the same lossless PEC material, so the difference in RCS is purely due to their geometric structures. The solid rough surface consists of three-dimensional features, including multiple faces and vertices, which introduce additional scattering mechanisms that contribute to a higher overall reflectivity. In contrast, the sheet-like rough surface is a two-dimensional structure without significant depth, meaning it lacks additional scattering contributions from edges and faces. This results in lower overall reflectivity compared to the solid rough surface. However, please note that this reflectivity value of the solid rough surface would be lower when compared to the reflectivity of a complete or totally smooth/flat surface.

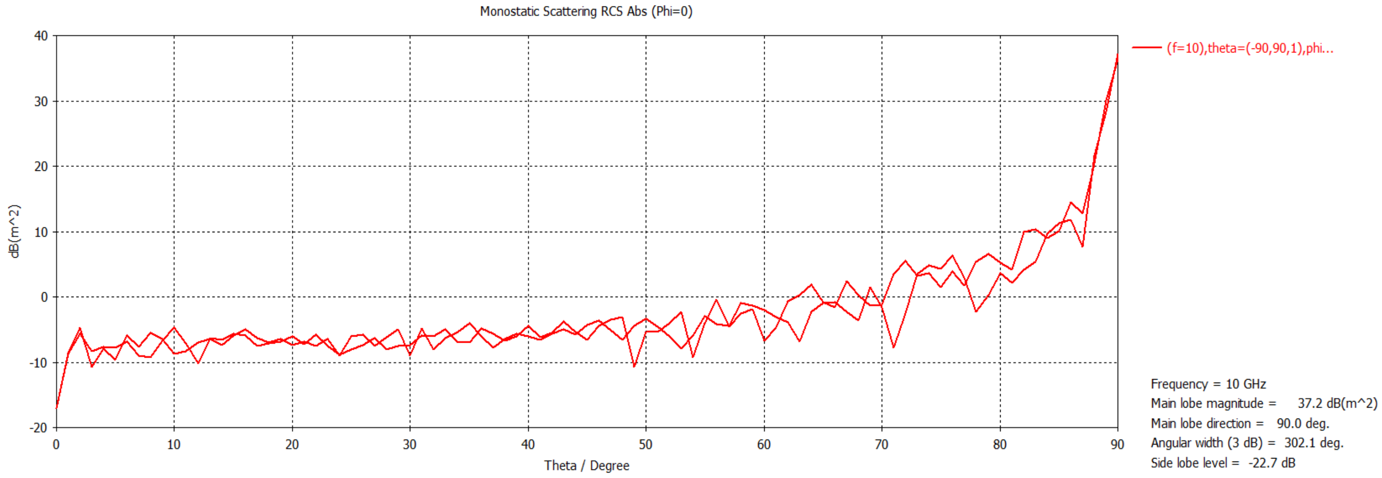

(a) RCS analysis of solid rough surface (PEC) 1m x 1m for 100 samples @ 10GHz

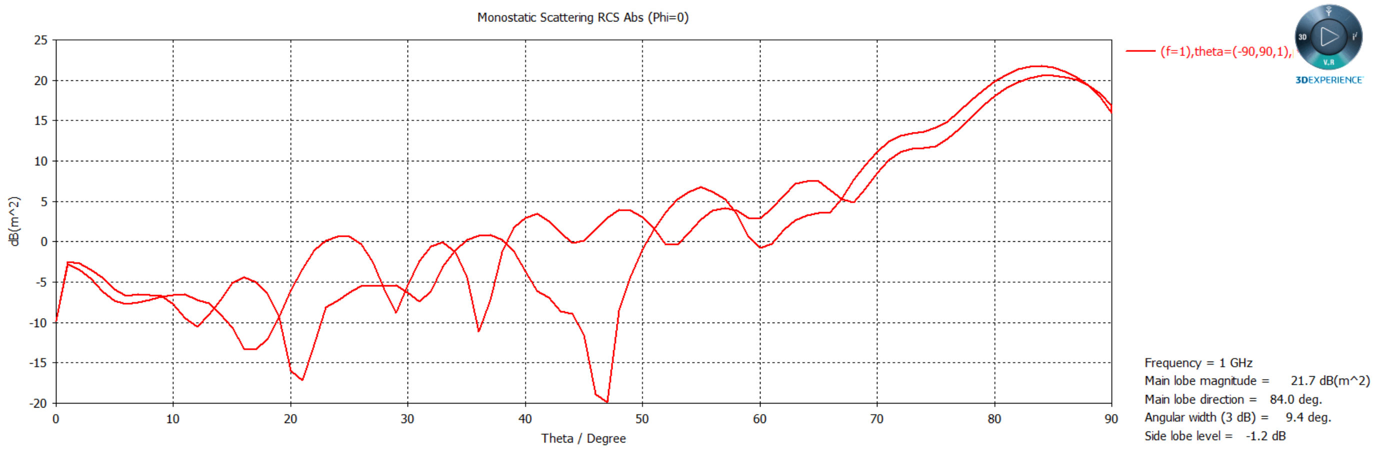

(b) RCS analysis of a solid rough surface (PEC) 1m x 1m for 100 samples @1GHz

Figure 4.13: RCS analysis of a solid rough surface PEC at (a)10 GHz (b) 1 GHz

Similarly, in Figure 4.13b, the RCS of the solid rough surface (1m x 1m) at 1 GHz was obtained to be about 22 dB(m^2) which is higher than the RCS of the sheet-like rough surface with similar parameters obtained as 15.7 dB(m^2) in Figure 4.10b and the same reasons as previously described can be adduced to this. The 3dB angular width of 9.4° suggests that energy is spread over a small angular range rather than being strictly at 90°. The shift in the RCS peak away from 90° is likely due to a combination of surface geometry, material properties, frequency effects, numerical simulation considerations, and multipath interactions. This is a common occurrence in real-world radar scattering scenarios where idealised specular reflection assumptions do not hold. Furthermore, in Figure 4.14, the RCS of the solid rough surface for N = 50, 1m x 1m and at 10 GHz was obtained to be about 36 dB(m^2) which is higher than the RCS value of the sheet-like rough surface with similar parameters obtained as 13.2 dB(m^2) in Figure 4.11a.

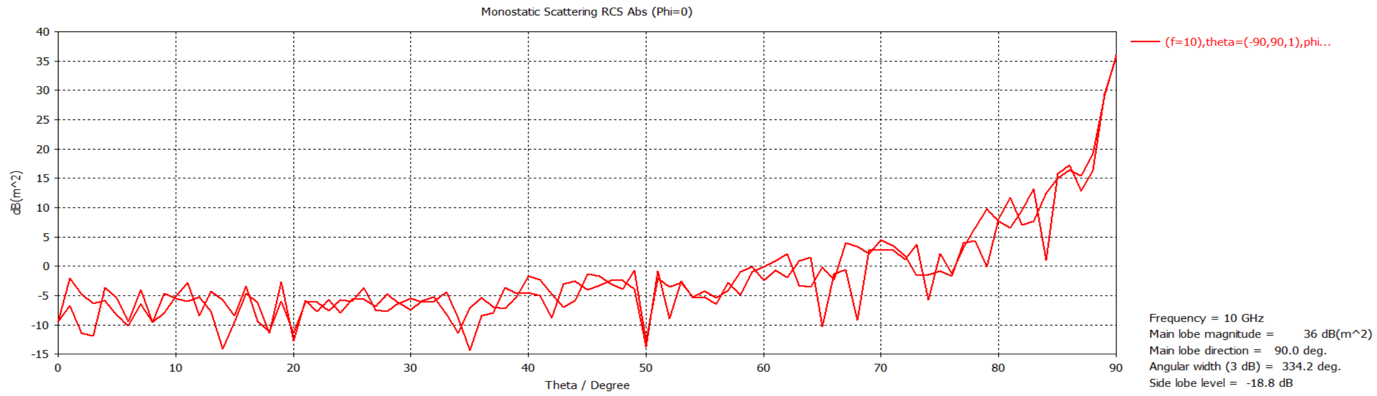

Fig. 4.14 RCS analysis of solid rough surface (PEC) 1m x 1m for N = 50 samples @ 10GHz

Figure 4.14: RCS analysis of a solid rough surface PEC, N = 50 @ 10 GHz

The next milestone in this thesis is to now convert the material of the solid rough surface from a lossless material (PEC) to a lossy material (sandy soil) with different dielectric properties and analyse the RCS for this rough surface that is made of sandy soil. When this happened, the rough surface was not meshing properly due to insufficient memory as well as inadequate computing requirements. As a result, the number of surface points (N) was significantly reduced again from about 100 as previously shown to about 10 for the rough surface to ensure proper meshing of the rough surface and facilitate successful computation and analysis of the RCS. However, this reduction in ***N*** inherently decreases the number of scatterers, which could lead to a loss of statistical significance in the results. To overcome this limitation and maintain the statistical robustness of the analysis, I employed a Monte Carlo-type approach, where I conducted multiple independent simulations of different realisations of the smaller sample size (***N = 5, 10***) & averaged the results over these repeated trials. By doing so, the overall scattering characteristics remained representative of the original surface model with ***N = 100***, ensuring that the final RCS estimates were statistically meaningful and comparable to those obtained with a higher number of scatterers. In addition, the area of the surface was also reduced from a 1m x 1m surface area to about a 20 cm x 20 cm surface area. Same reasons given earlier suffices here. This averaging approach effectively compensates for the reduction in surface points and surface area by incorporating the stochastic nature of rough surface scattering, thereby minimising the impact of numerical artifacts introduced by the meshing constraints. The Solver also used for this RCS analysis is the Integral Equation Solver as the Asymptotic Solver does not support the RCS simulation of lossy materials. The dielectric parameters for the sandy soil employed in this RCS simulation are given in Table 4.4 and they have been taken from the CST Microwave Studio Suite software and consistent with existing literature.

Table 4.4: showing the dielectric constants / parameters for sandy soil at 10 GHz

Parameter	**Value**
Dielectric Permittivity (Epsilon)	2.53
Dielectric Conductivity (Mu)	1
Dielectric loss factor	0.0036 (Const. fit)
Density (Rho)	1550 (Kg/m^3)
Thermal Conductivity	0.2 (W/K/m)
Specific Heat	800 (J/K/Kg)
Diffusivity	1.6129e-07 (m^2/s)

Figure 4.15a shows the results of the RCS analysis of a lossy rough surface made of sandy soil with dimensions 20 cm x 20 cm and number of surface points (N) = 5 at 10 GHz, while Figure 4.15b shows the results of the RCS analysis of a sandy soil rough surface with the same parameters but in this case, the area of the rough surface is 50 cm x 50 cm. An RCS of about 2 dB(m^2) was obtained in Figure 4.15a, while an RCS of 14 dB(m^2) was obtained in Figure 4.15b. This result suggests that the RCS of a solid rough surface is directly proportional to the surface area of the rough surface. However, this is not the case for a lossless rough surface sheet where the RCS is inversely proportional to the surface area of the lossless rough surface especially at lower frequencies like 1 GHz and for similar parameters. Figure 4.15a has a surface area of 0.04 m^2 while Figure 4.15b has a surface area of 0.25 m^2. So, the surface area of the rough surface in Figure 4.15b is at least six times bigger than the area of the rough surface in Figure 4.15a, hence the RCS for Figure 4.15b is bigger than the RCS for Figure 4.15a.

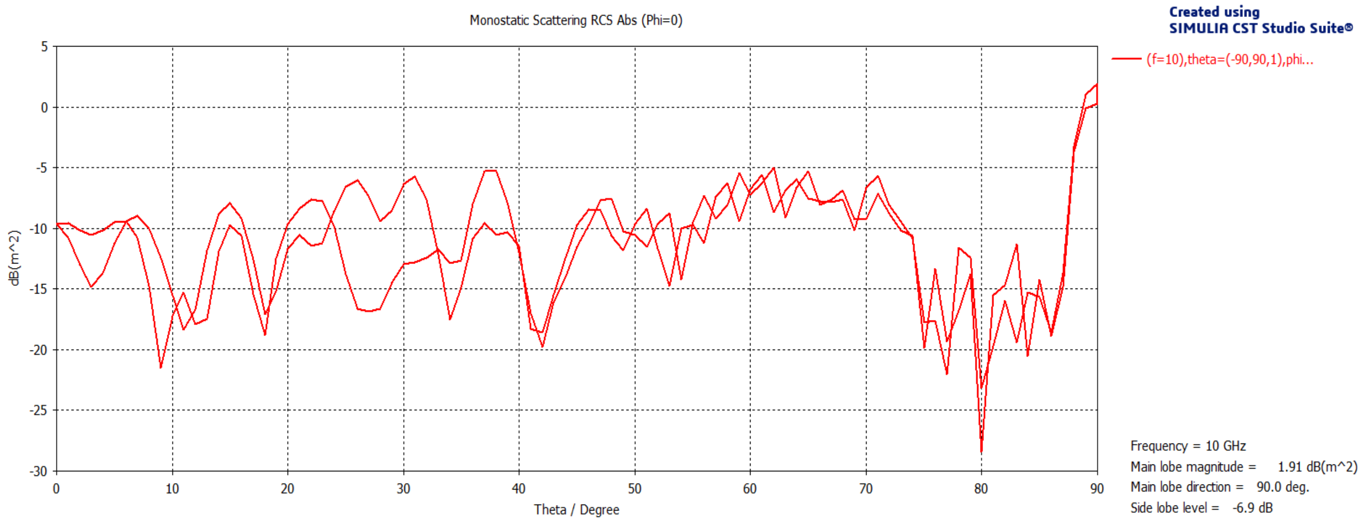

(a) RCS analysis of sandy soil surface 20cm x 20cm for N = 5 samples @ 10GHz

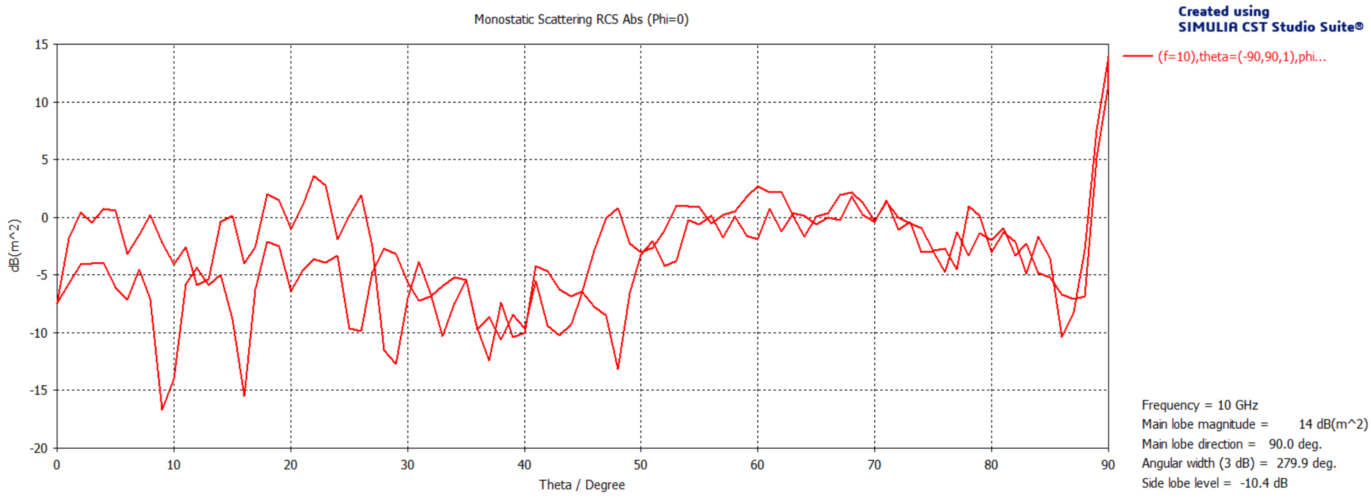

(b) RCS analysis of sandy soil surface 50cm x 50cm for N = 5 samples @ 10GHz

Figure 4.15: RCS analysis of a sandy soil surface N = 5 (a)20x20cm (b) 50x50cm

Similarly, Figure 4.16a shows the results of the RCS analysis of a lossy rough surface made of sandy soil with dimensions 20cm x 20cm and number of surface points (N) = 10 at 10 GHz, while Figure 4.16b shows the results of the RCS analysis of a sandy soil rough surface with the same parameters but in this case, the area of the rough surface is 50cm x 50cm. An RCS of about 9 dB(m^2) was obtained in Figure 4.16a, while an RCS of 14.4 dB(m^2) was obtained in Figure 4.16b. The explanation earlier given to the RCS values obtained in Figure 4.15 can also be adduced here. Furthermore, we can also see that the RCS for Figure 4.15b albeit for N = 5 is higher than the RCS obtained for Figure 4.16a even though with a higher N of 10 because of the bigger surface area for Figure 4.15b compared to Figure 4.16a. Similarly, the RCS obtained for Figure 4.16b is a lot higher (at least 18 times higher) than the RCS obtained for Figure 4.15a and this can be attributed to the bigger surface area as well as the doubled number of surface point which indicates a measure of the roughness of the surface.

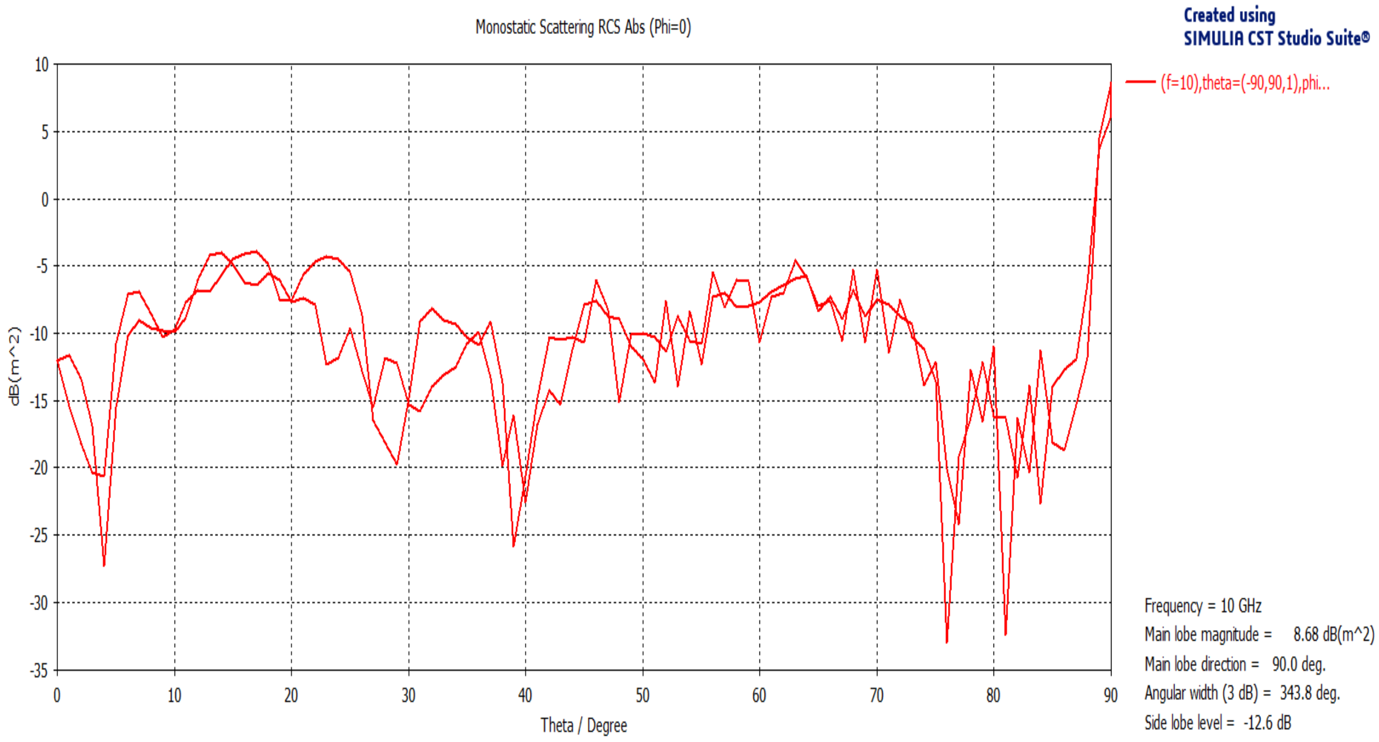

(a) RCS analysis of sandy soil surface 20cm x 20cm for N = 10 samples @ 10GHz

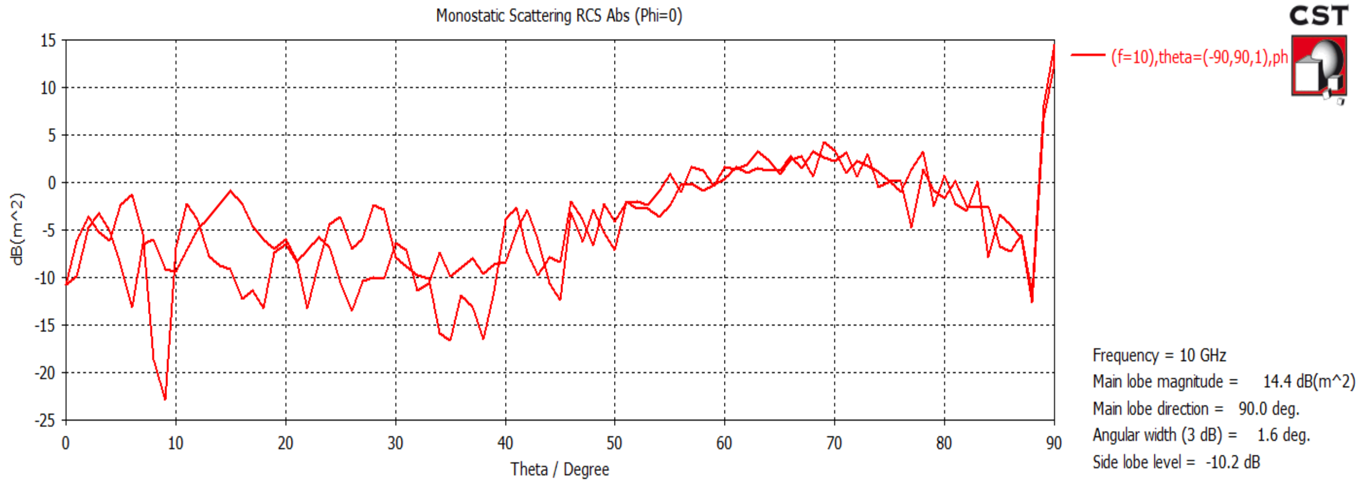

(b) RCS analysis of sandy soil surface 50cm x 50cm for N = 10 samples @ 10GHz

Figure 4.16: RCS analysis of sandy soil surface, N = 10 (a)20x20cm (b) 50x50cm

Now we shall look at various dielectrics where the angle of illumination from our radar is between 0° to 90° as well as between 30° and 60° and consider as well as analyse the RCS or reflectivity at these angles. The angles between 30° and 60° were specifically considered in the simulation, so that it can be compared to the experimental results that would be elucidated on in subsequent chapters. For the experimental setup, the angle of illumination would most likely vary between 30° and 60°. As a result, it is expedient to understand what the theoretical RCS looks like between these angles so the results can be compared with the measurements. The dielectrics which would be considered include the PEC, the dry sandy soil, the wet sandy soil, dry loamy soil, wet loamy soil as well as sandy soil that has been mixed or soaked with oil. It is worthy to also mention at this juncture that all the simulations would be done at a frequency of 10 GHz and at an rms height of 14cm.

Figure 4.17a shows the RCS analysis for a PEC between 0° and 90°, while Figure 4.17b shows the RCS analysis for a PEC between 30° and 60°. Both figures were for an area of 20 cm x 20 cm and the number of samples or surface points on the rough surface is 10 x 10. As expected, the RCS is directly proportional to the angle and that is why the RCS is 22.5 dBsqm at 90° while the RCS at a lower angle of 60° is – 12.4 dBsqm.

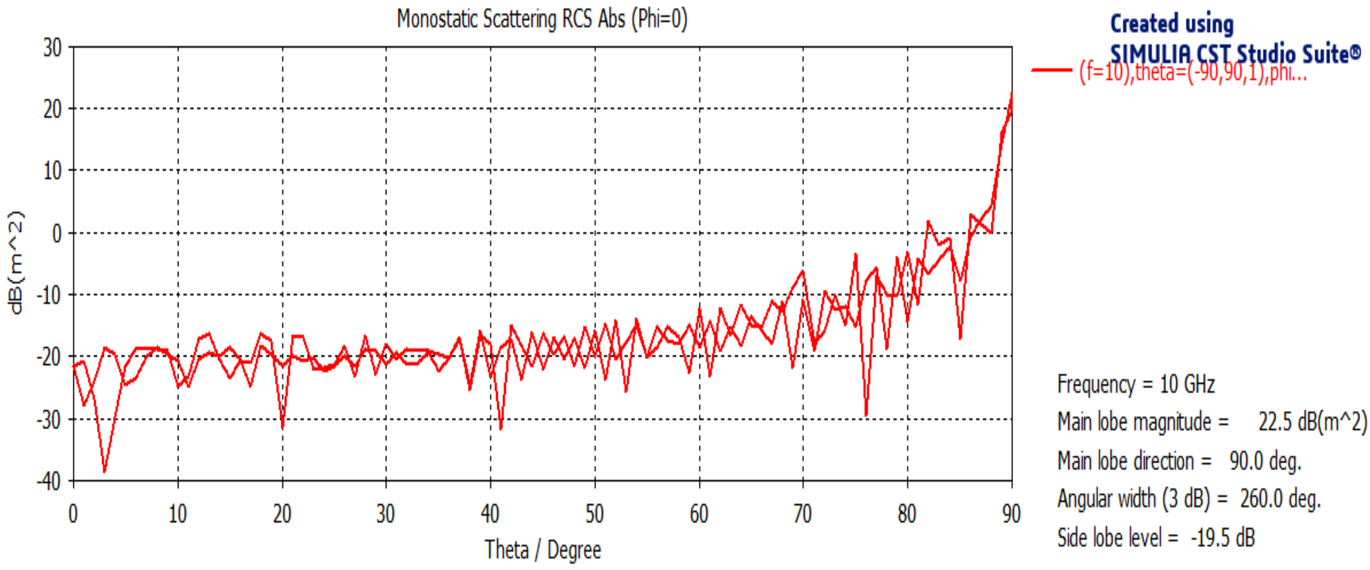

(a) RCS analysis of PEC between 0° to 90° for an area of 20 cm x 20 cm

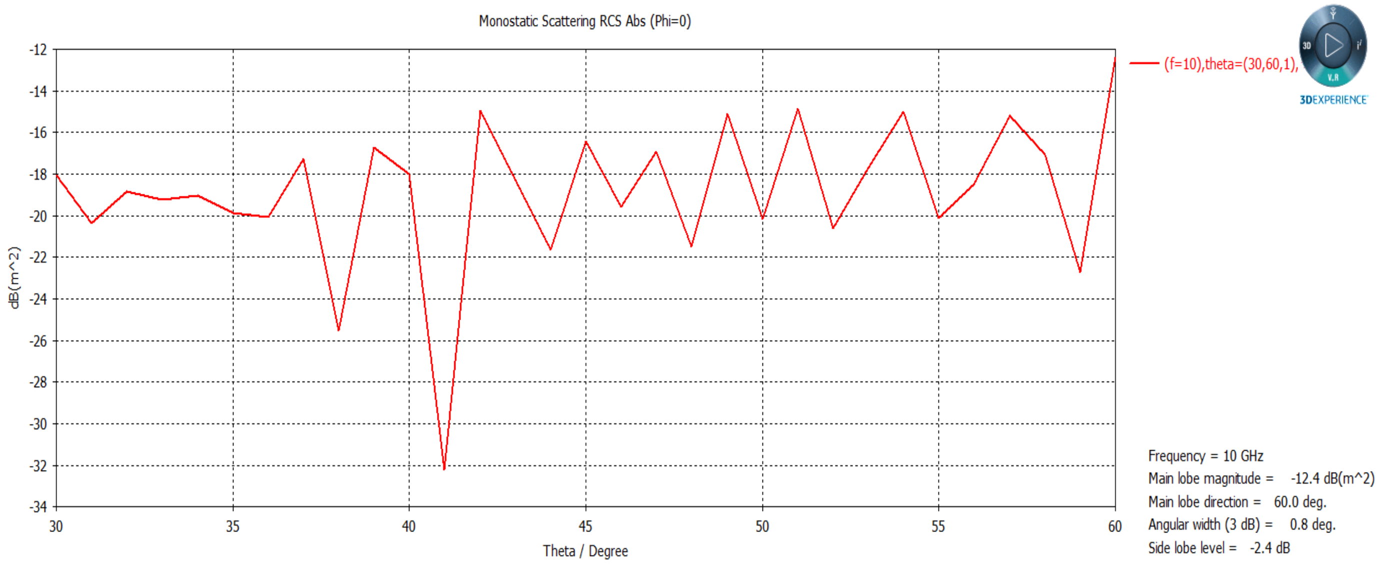

(b) RCS analysis for a PEC between 30° to 60° for an area of 20 cm x 20 cm

Figure 4.17: RCS analysis for a PEC 20cm x 20 cm (a) 0° to 90° (b) 30° to 60°

Figure 4.18a shows the RCS analysis for a PEC between 0° and 90° but for an area of ½ m x ½ m, while Figure 4.18b shows the RCS analysis for a PEC between 30° and 60° also for an area of ½ m x ½ m. Both rough surfaces have the same number of surface points i.e. 10 x 10. The RCS for figure 4.18a is obviously higher (6 dB higher) than the RCS for figure 4.17a due to the larger surface area for figure 4.18a compared to figure 4.17a since RCS is also directly proportional to the area of the surface. The same can also be said when figure 4.18b is compared to figure 4.17b as the RCS is 11.16 dB higher.

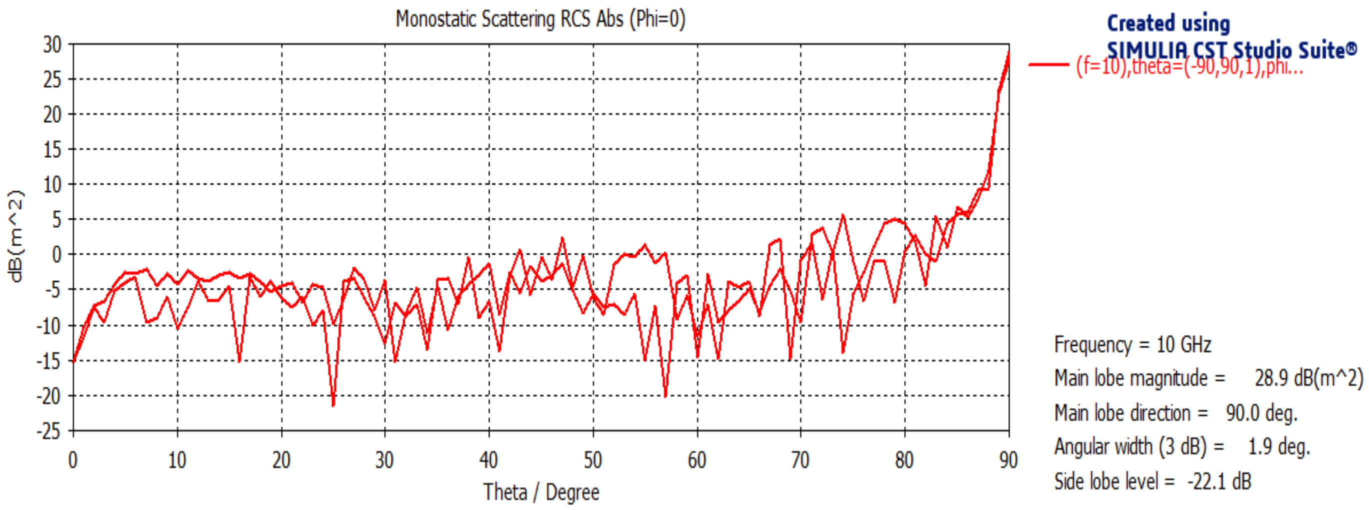

(a) RCS analysis for a PEC between 0° to 90° for an area of ½ m x ½ m

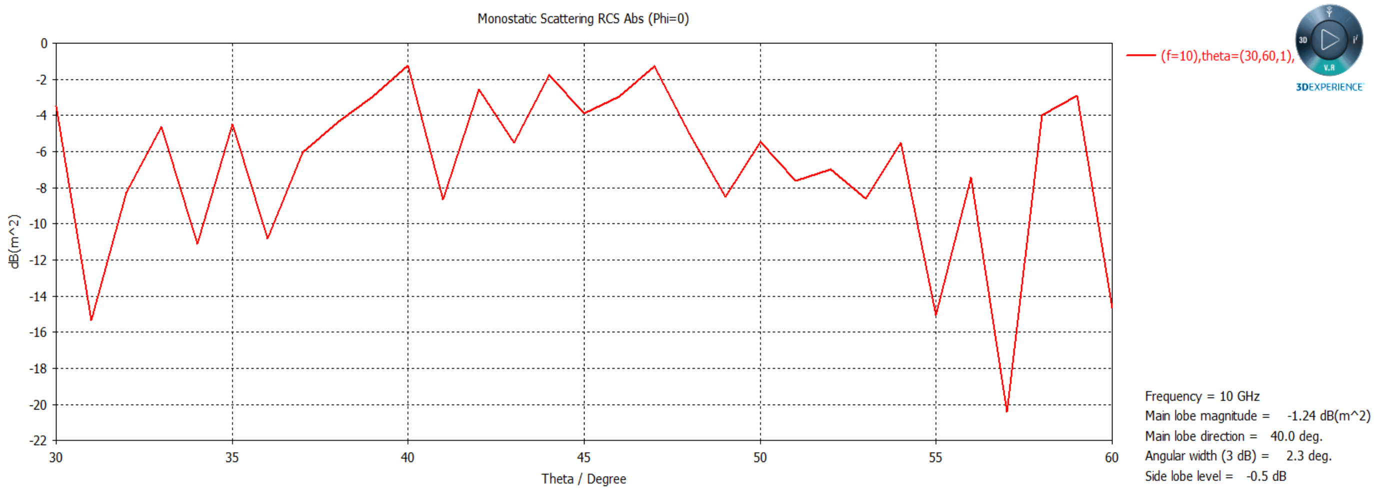

(b) RCS analysis for a PEC between 30° to 60° for an area of ½ m x ½ m

Figure 4.18: RCS analysis for a PEC ½ m x ½ m (a) 0° to 90° (b) 30° to 60°

Figure 4.19a shows the RCS analysis for dry sandy soil between 0° and 90°, while Figure 4.19b shows the RCS analysis for dry sandy soil between 30° and 60°. Both figures were for an area of 20 cm x 20 cm and the number of samples or surface points on the rough surface is 10 x 10. As expected, the RCS is directly proportional to the angle and that is why the RCS is 8.59 dBsqm at 90° while the RCS at a lower angle of 56° is – 5.93 dBsqm. These figures were also be compared to Figures 4.20a and 4.20b respectively which are for a larger surface area i.e. ½ m x ½ m. On comparison, we can see that the RCS for Figure 4.20a is about 4 times higher than RCS for figure 4.19a. Similarly, the RCS for figure 4.20b is also about 4 times higher than the RCS for figure 4.19b due to the larger surface areas of the rough surface.

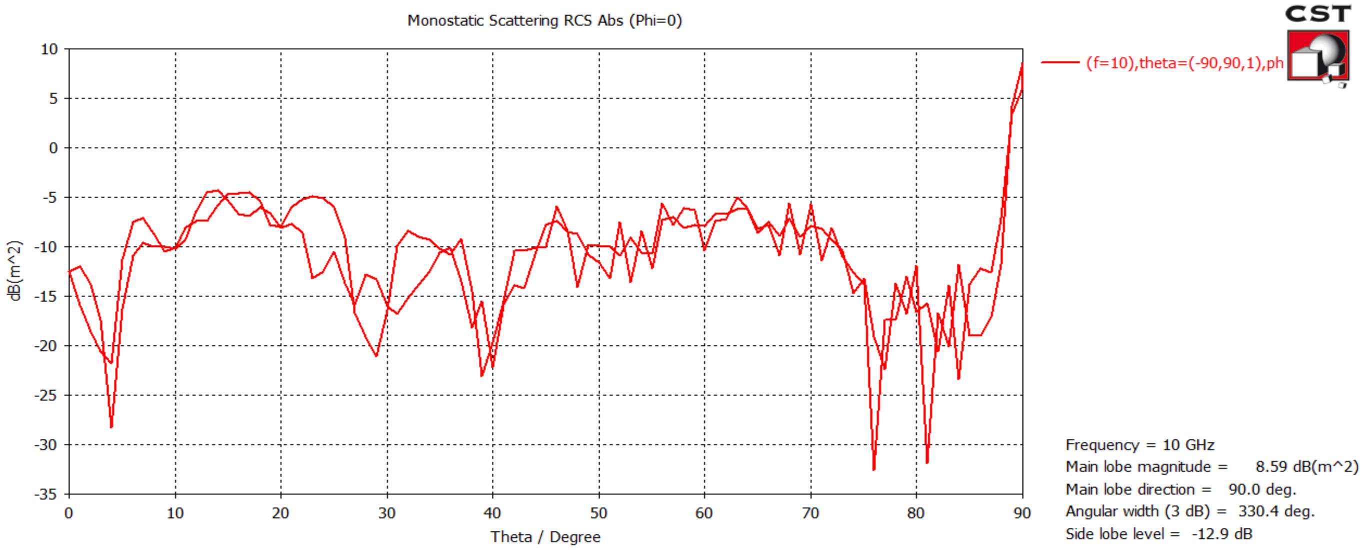

(a) RCS analysis for dry sandy soil between 0° and 90° - area of 20 cm x 20 cm

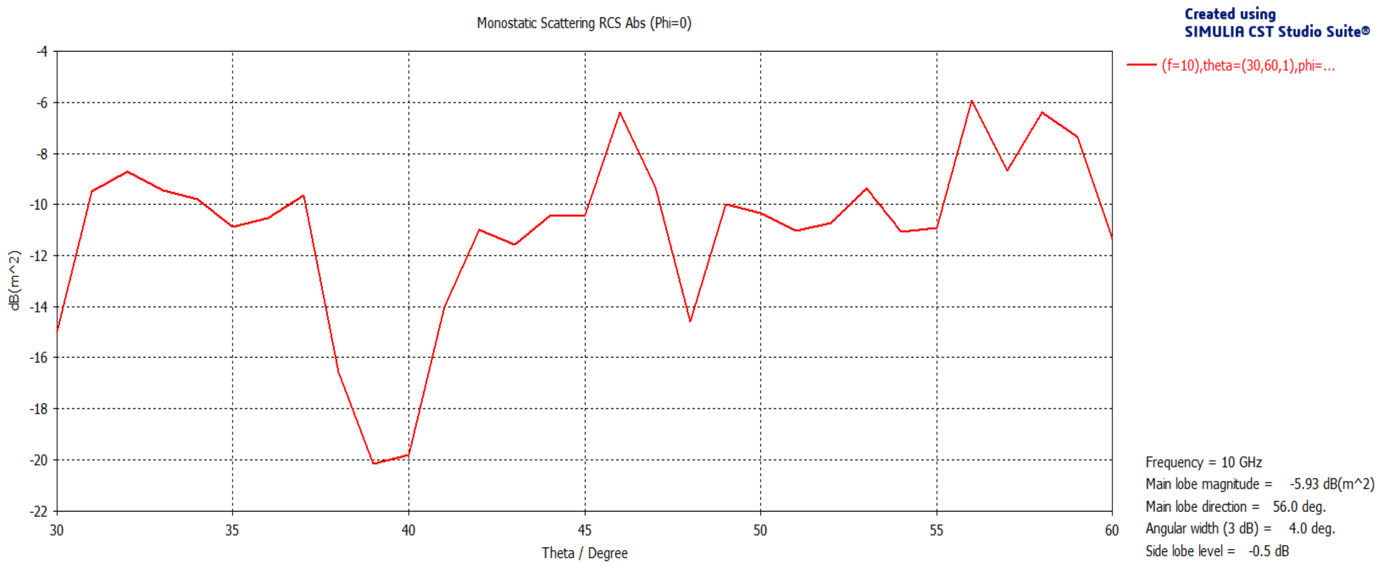

(b) RCS analysis for dry sandy soil between 30° and 60° - area of 20 cm x 20 cm

Figure 4.19: RCS analysis for dry sandy soil 20cm x 20cm(a)0° to 90° b)30°to 60°

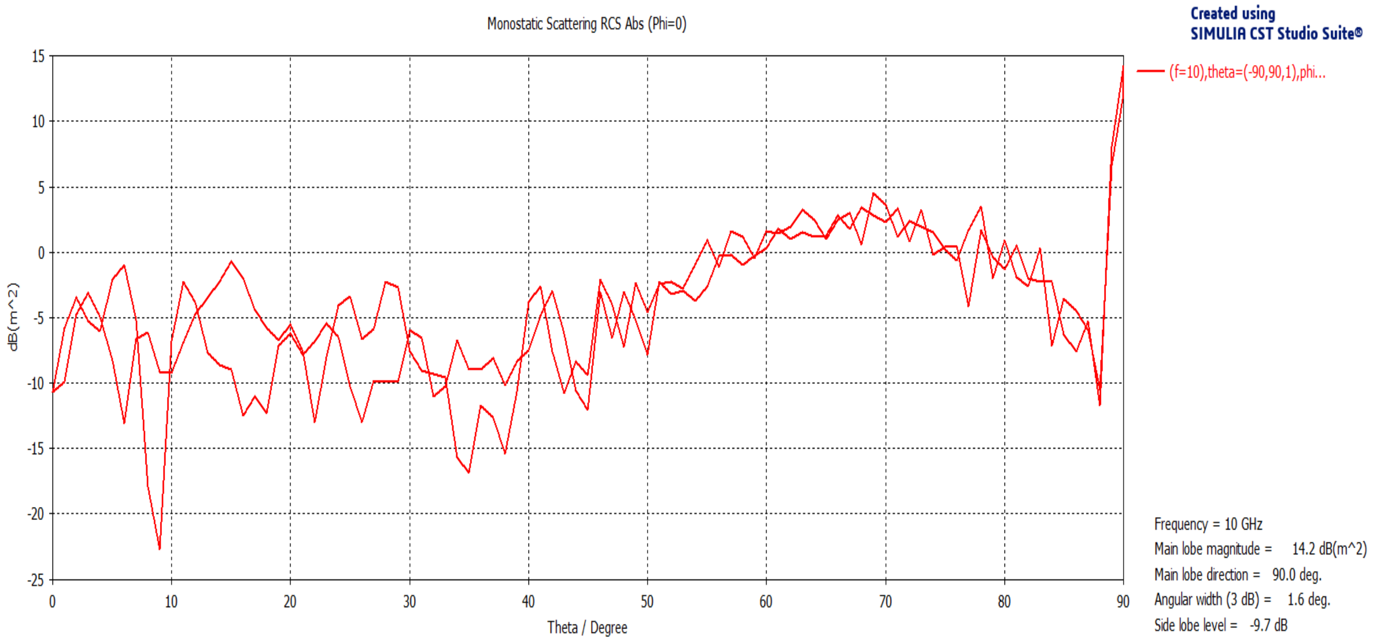

(a) RCS analysis for dry sandy soil between 0° and 90° for an area of ½ m x ½ m

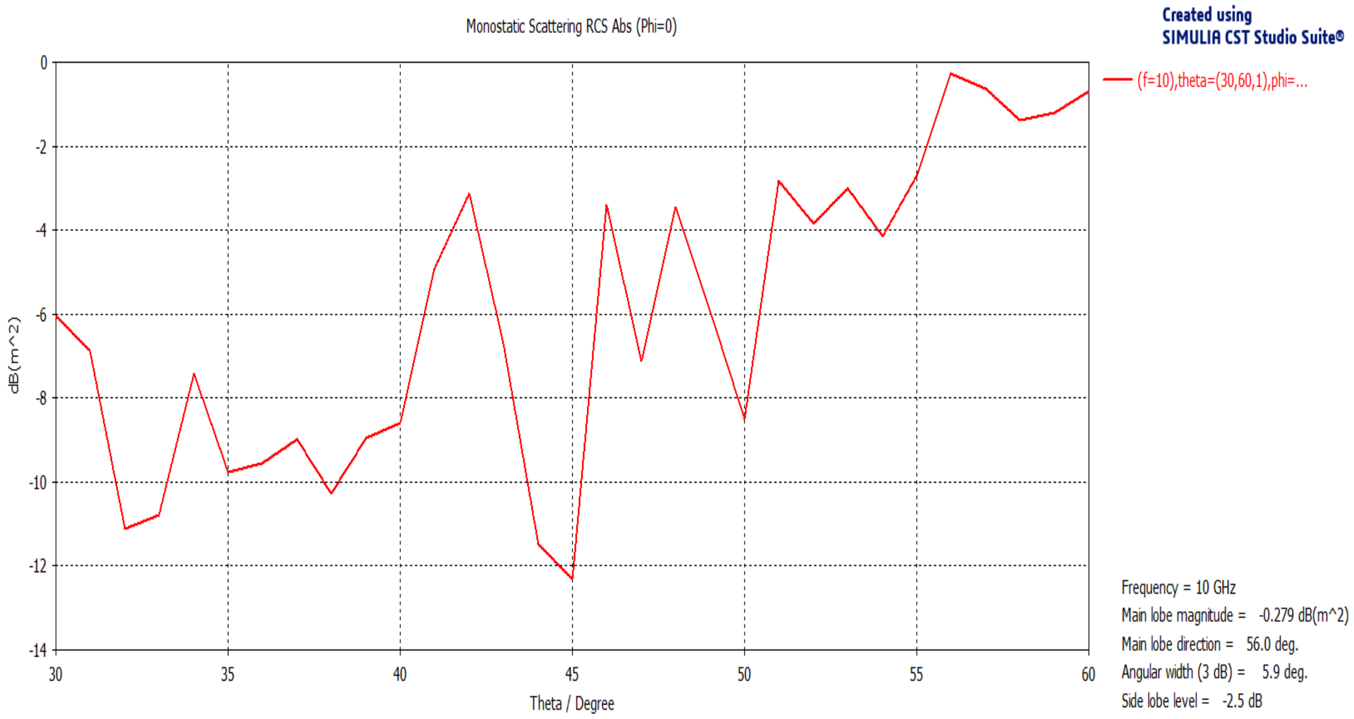

(b) RCS analysis for dry sandy soil between 30° and 60° - area of ½ m x ½ m

Figure 4.20: RCS analysis for dry sandy soil ½ m x ½ m (a) 0° to 90° (b) 30° to 60°

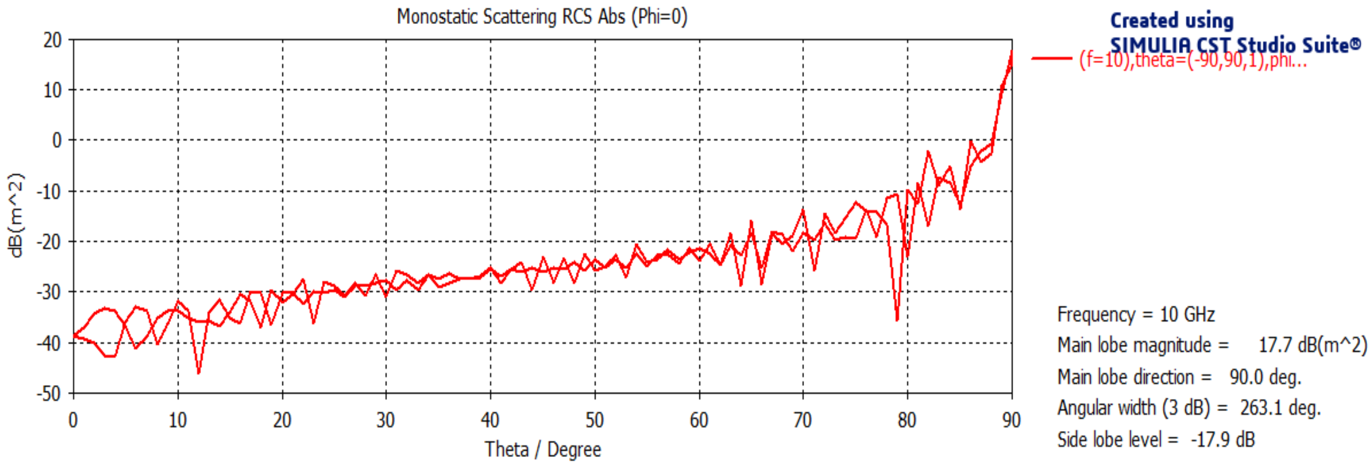

(a) RCS analysis for wet sandy soil between 0° and 90° – area of 20 cm x 20 cm

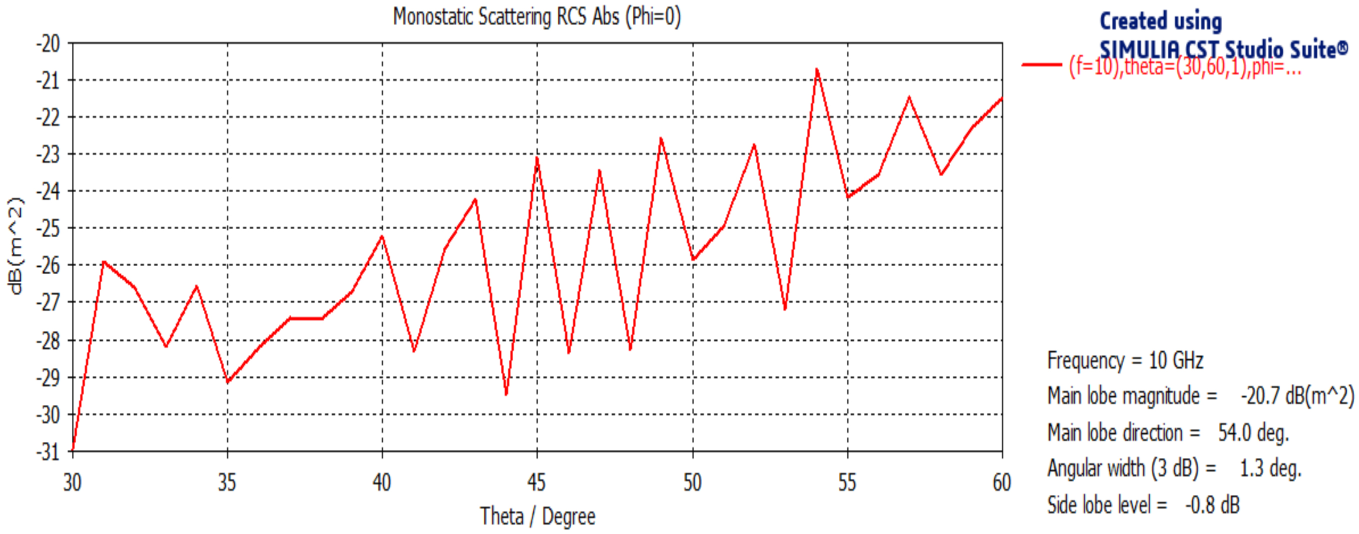

(b) RCS analysis for wet sandy soil between 30° and 60° – area of 20 cm x 20 cm

Figure 4.21: RCS analysis for wet sandy soil 20 cm x 20cm (a) 0° to 90° (b) 30° to 60°

Figures 4.21a and 4.21b show the RCS analysis for wet sandy soil between 0° and 90° as well as between 30° and 60° respectively. Both figures were also for an area of 20 cm x 20cm and the number of samples or surface points on the rough surface is 10 x 10. As expected, the RCS is directly proportional to the angle of illumination. These figures were also compared to Figures 4.22a and 4.22b respectively which are for a larger surface area of ½ m x ½ m. On comparison, we can see that the RCS for Figure 4.22a is about 4 times higher than RCS for

Figure 4.21a. Similarly, the RCS for figure 4.22b is about 23 times higher than the RCS for figure 4.21b due to the larger surface areas of the rough surfaces.

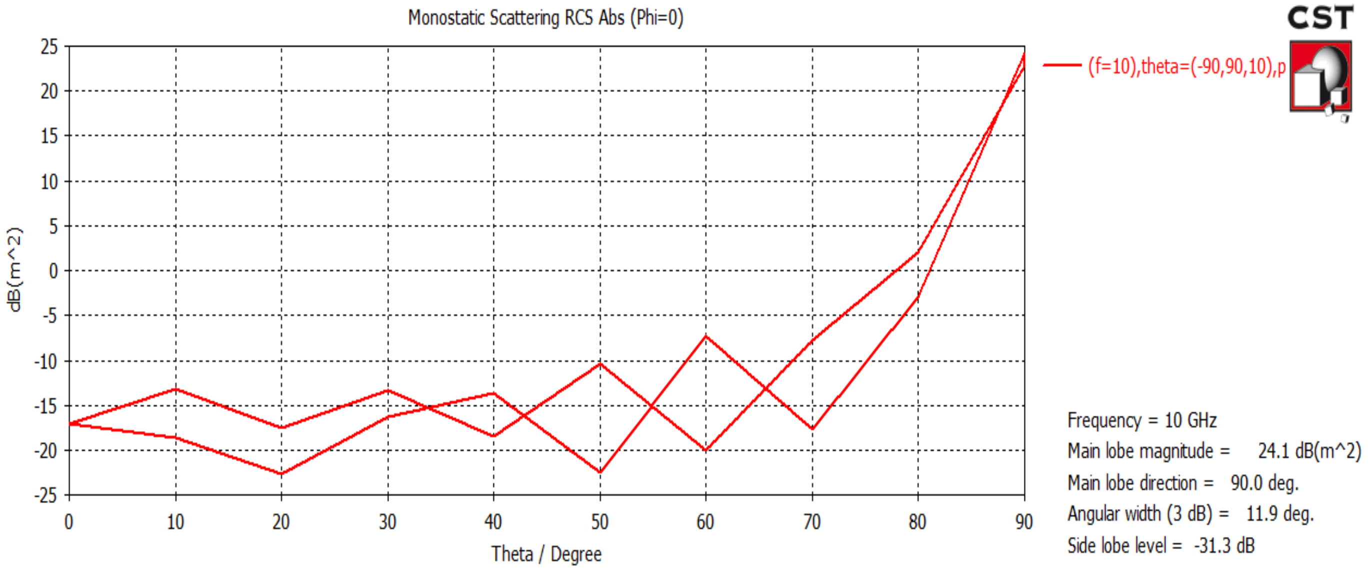

(a) RCS analysis for wet sandy soil between 0° and 90° – area of ½ m x ½ m

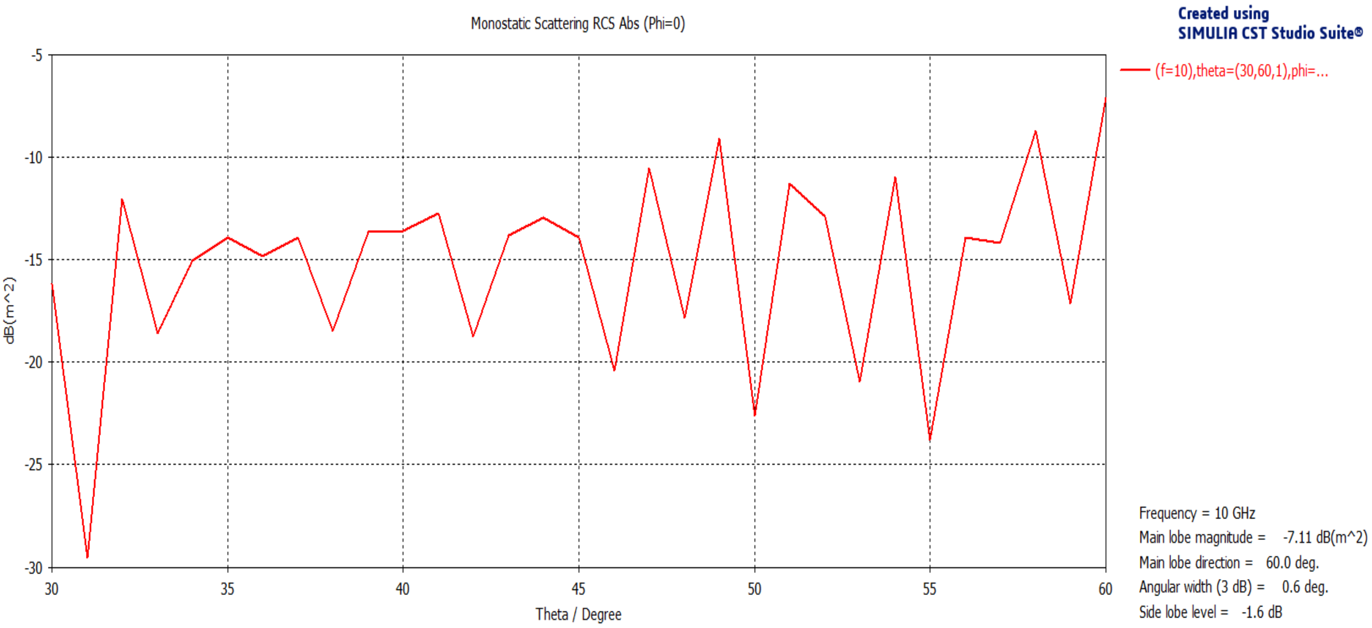

(b) RCS analysis for wet sandy soil between 30° and 60° – area of ½ m x ½ m

Figure 4.22: RCS analysis for wet sandy soil ½ m x ½ m (a) 0° to 90° (b) 30° to 60°

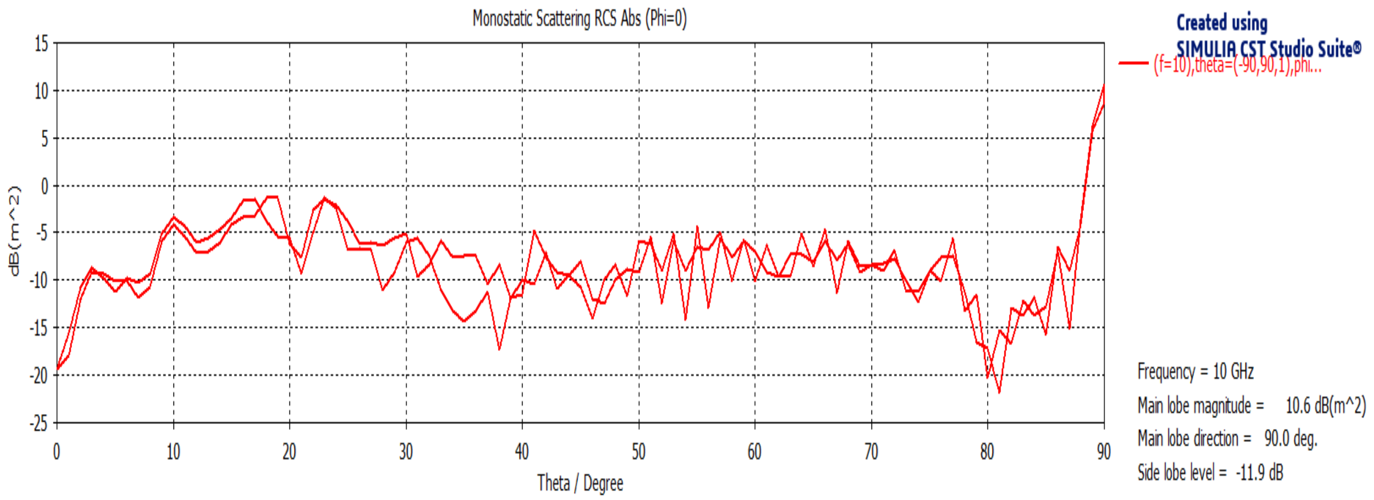

(a) RCS analysis for dry sandy soil mixed with oil – area of 20 cm x 20 cm.

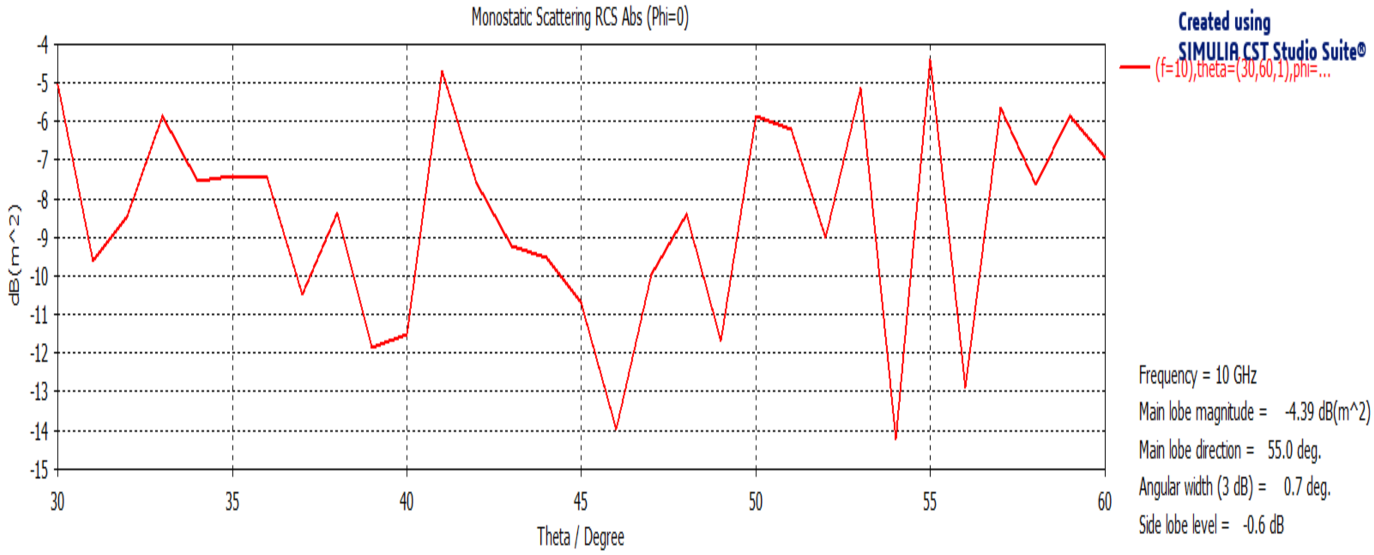

(b) RCS analysis for dry sandy soil mixed with oil – area of 20 cm x 20 cm.

Figure 4.23: RCS analysis for dry sandy soil mixed with oil 20cm x 20cm (a) 0° to 90° (b) 30° to 60°

Figure 4.23a shows the RCS analysis for a dry sandy soil mixed with oil with an area of 20 cm x 20 cm between 0° and 90° while figure 4.23b shows the RCS analysis for dry sandy soil mixed with oil for the same parameters but from 30° to 60°. When compared to Figure 4.19a which is for dry sandy soil without the oil, their RCS values are more or less the same which is in tandem with what we expected as the dielectric constant of oil is very similar to the dielectric constant of dry sandy soil. Also, the RCS for Figure 4.23a is slightly higher than the RCS for dry sandy soil due to the presence of oil as we had earlier attributed. Similarly, Figure 4.23b has a slightly higher RCS than its equivalent in Figure 4.19b due to the presence of oil.

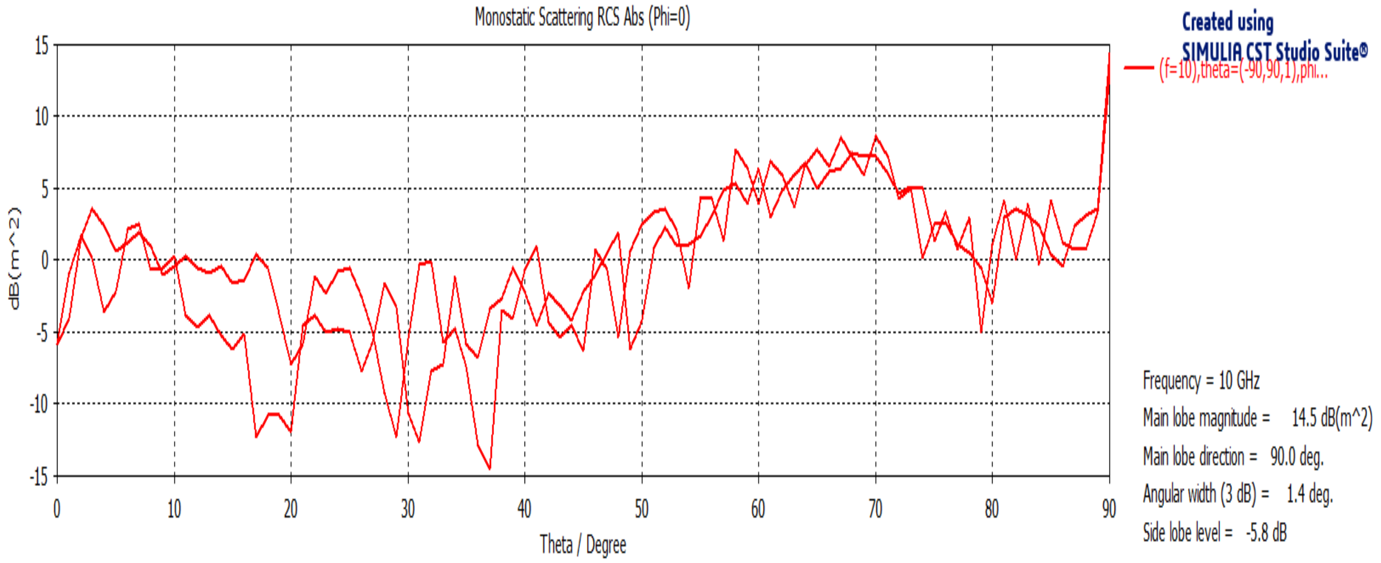

(a) RCS analysis for dry sandy soil mixed with oil – area of ½ m x ½ m.

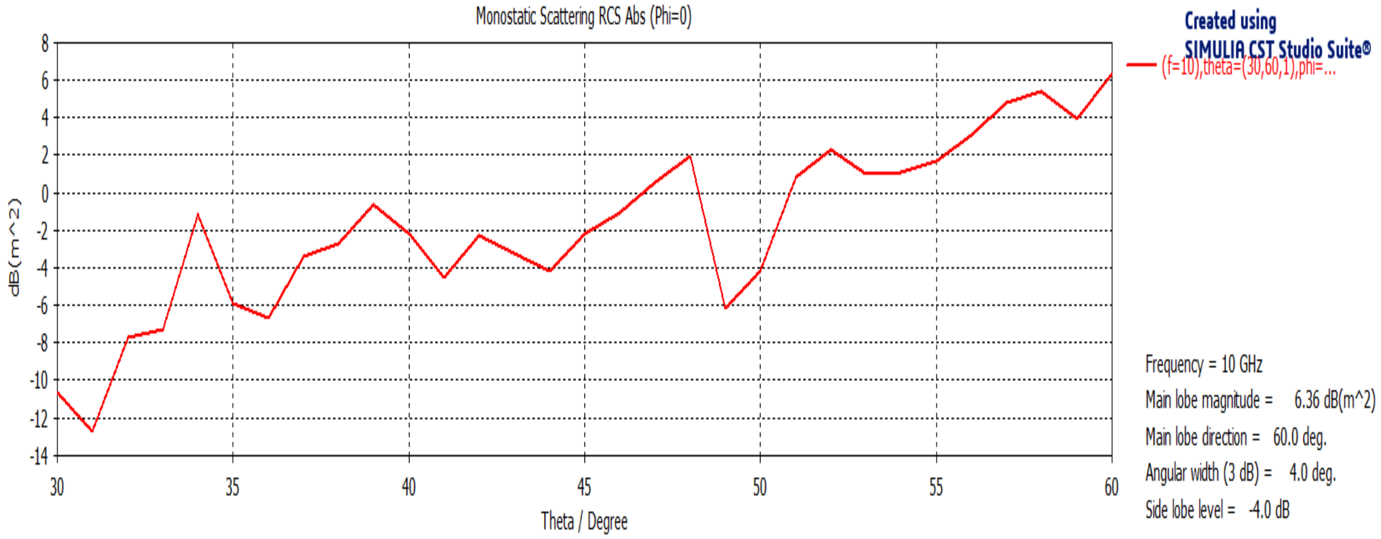

(b) RCS analysis for dry sandy soil mixed with oil – area of ½ m x ½ m.

Figure 4.24: RCS analysis for dry sandy soil mixed with oil ½ m x ½ m (a) 0° to 90° (b) 30° to 60°

Figures 4.24a and 4.24b show the RCS analysis for dry sandy soil mixed with oil but for a larger surface area i.e. ½ m x ½ m. The RCS for Figure 4.24a which is for a larger surface area is 2.5 times higher than the RCS for Figure 4.23a which is for a smaller surface area. Similarly, the RCS for Figure 4.24b is about 12 times higher than the RCS for Figure 4.23b. also when we compare Figure 4.24a with Figure 4.20a which is for dry sandy soil without oil, their RCS values are more or less the same which is also in tandem with what is expected as the dielectric constant of oil is very similar to the dielectric constant of dry sandy soil.

Now, we shall analyse what happens when the number of surface points i.e. N is doubled for all the various dielectrics.

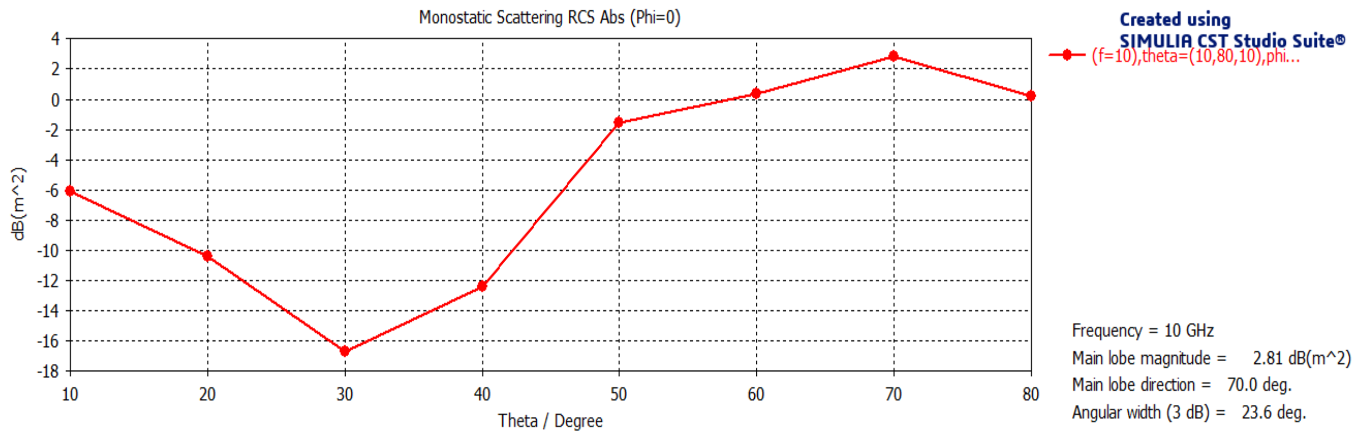

(a) RCS analysis for dry sandy soil between 10° and 80° - N = 20 x 20

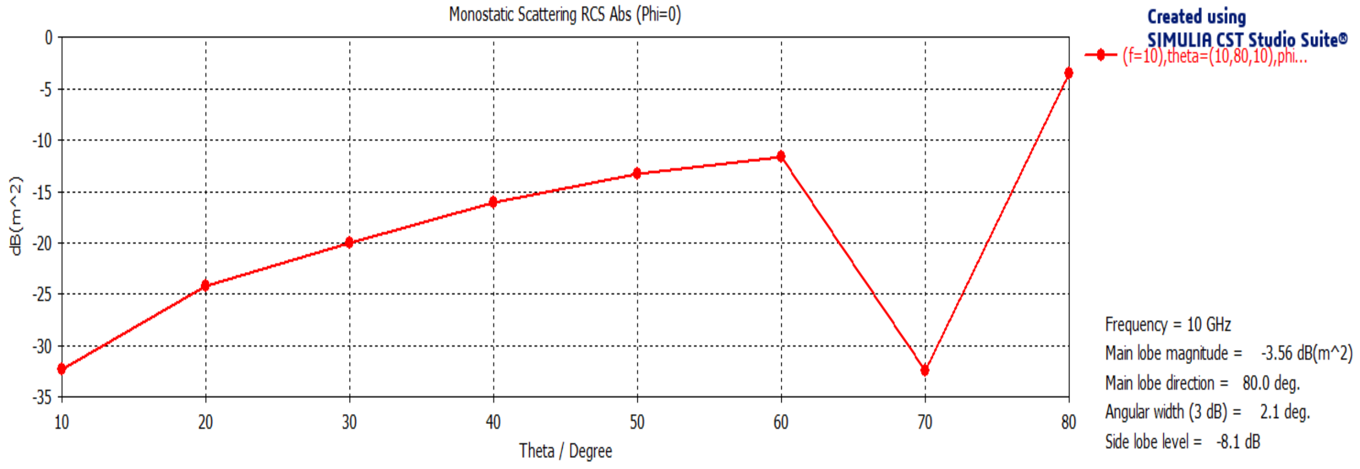

(b) RCS analysis for wet sandy soil between 10° and 80° - N = 20 x 20

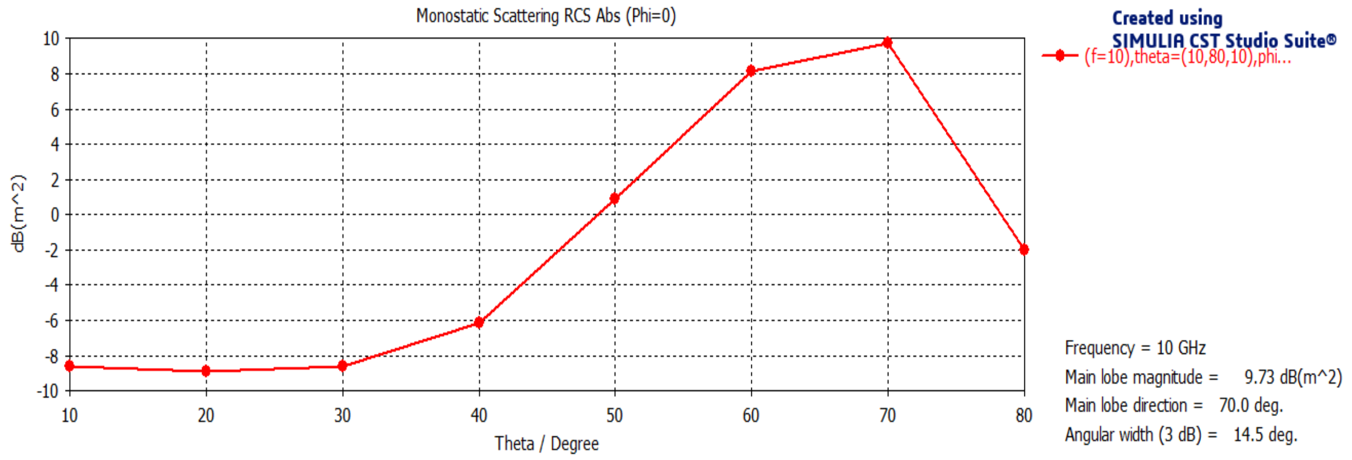

c) RCS analysis for dry sandy soil mixed with oil - N = 20 x 20

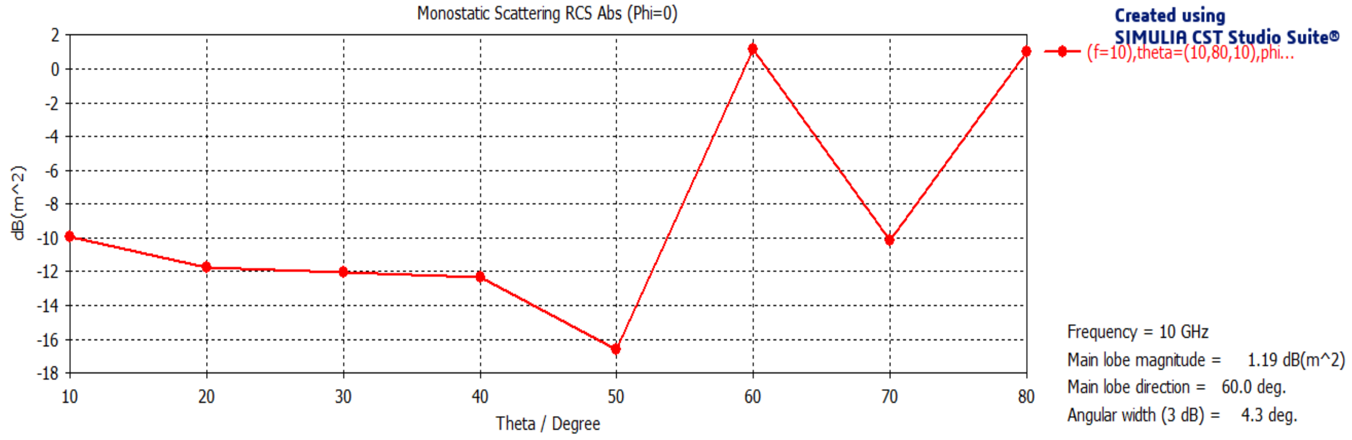

(d) RCS analysis for a PEC between 10° and 80° with N = 20 x 20 for a ½m x ½m

Figure 4.25: RCS analysis between 10° to 80° with N = 20 x 20 for a ½ m x ½ m (a)dry sandy soil (b)wet sandy soil (c) dry sandy soil mixed with oil (d) PEC

In Figure 4.25a, the number of surface points (N) is 20 x 20 as opposed to 10 x 10 used in previous simulations. The figure is for a dry sandy soil with dimensions ½ m x ½ m. The RCS generally increases as the angle of illumination also increases with the RCS obtained as 2.81 dBsqm. When compared to Figure 4.20a, which is for a dry sandy soil with N = 10 x 10 and for the same ½ m x ½ m, the RCS was about 14 dBsqm. The increase in RCS can be attributed to the fact that since the number of surface points is reduced, the surface can be likened to a "smoother" surface compared to the other surface which has a greater number of surface points i.e. 20 x 20 and can be presumed "rougher".

Figure 4.25b shows the RCS for a wet sandy soil with the number of surface points as 20 x 20. The RCS was obtained to be about – 3.56 dBsqm and when this is compared to Figure 4.22a which is also for a wet sandy soil but with N as 10 x 10, an RCS of 24.1 dBsqm is obtained. Similarly, this increase in RCS for a surface with number of surface points as 10 x 10 can be attributed to the fact that the surface is presumed "smoother" which will therefore have a higher RCS than if the surface was "rougher", therefore a lower RCS. Please note that wet sandy soil implies sandy soil with 18.8% water, and this is the case all through this thesis.

Figure 4.25c shows the RCS for a dry sandy soil that is mixed with oil for the same number of surface points – 20 x 20. The RCS was obtained to be about 9.73 dBsqm and when this is compared to Figure 4.24a which is also for a dry sandy soil mixed with oil but with N as 10 x 10, an RCS of 14.73 dBsqm is obtained. Same reasons can be attributed here as well. Please also note that 13.77% is the proportion of oil in the dry sandy soil and is the case all through.

Figure 4.25d shows the RCS for a PEC for the same number of surface points – 20 x 20. The RCS was obtained to be about 1.19 dBsqm and when this is compared to Figure 4.18a which is also for a PEC with number of surface points as 10 x 10, an RCS of 28.9 dBsqm is obtained. Same analysis can be extended to this dielectric.

Table 4.5 shows the comparison between the various dielectrics in terms of their analytical RCS values for both surface areas i.e. 20 cm x 20 cm and ½ m x ½ m. The number of surface points used for the simulation is 10 x 10 and doubled to 20 x 20. The angle of simulation varied between 0° and 90° as that is more practicable for experiments and measurements.

Table 4.5: Comparison of the RCS of various dielectric materials with varying number of surface points

Dielectric Material	**N = 10** **20cmx20cm** **0° to 90°**	**N = 10** **20cmx20cm** **30° to 60°**	**N = 10** **½m x ½ m** **0° to 90°**	**N = 10** **½m x ½ m** **30° to 60°**	**N = 20** **20cmx20cm** **10° to 80°**	**N = 20** **½mx½m** **10°to 80°**
PEC	22.5 dBm^2	- 12.4 dBm^2	28.9 dBm^2	- 1.24dBm^2	- 4.86 dBm^2	1.19 dBm^2
Dry Sandy Soil	8.59 dBm^2	- 5.93 dBm^2	14.2 dBm^2	-0.28 dBm^2	- 6.32 dBm^2	2.81 dBm^2
Wet Sandy Soil	17.7 dBm^2	- 20.7 dBm^2	24.1 dBm^2	- 7.11 dBm^2	- 11.8 dBm^2	- 3.56 dBm^2
Dry Sandy Soil mixed with oil	10.6 dBm^2	- 4.39 dBm^2	14.5 dBm^2	6.36 dBm^2	- 2.86 dBm^2	9.73 dBm^2

4.6. Simulation for different rough surfaces and comparison of the results

At this stage, we shall perform some simulations for different surfaces with same statistics and analyse the results hereafter by comparing the results for these various dielectrics. First, ten RCS simulations were conducted for the various dielectrics. These simulations were conducted for each dielectric to ascertain and assess if the same pattern or trend was followed for each run. The figures for these 10 RCS simulation plots for each dielectric are shown in the appendix and have been thoroughly discussed. From the figures, the same trend / pattern was followed for each dielectric and simulation parameters which implies that the results can be relied upon and tallies with what was expected for simulations of this nature. An average of at least ten iterations for each dielectric is shown in Figure 4.26 for the dry sandy soil; while Figure 4.27 is for the wet sandy soil and Figure 4.28 is for the dry sandy soil mixed with oil.

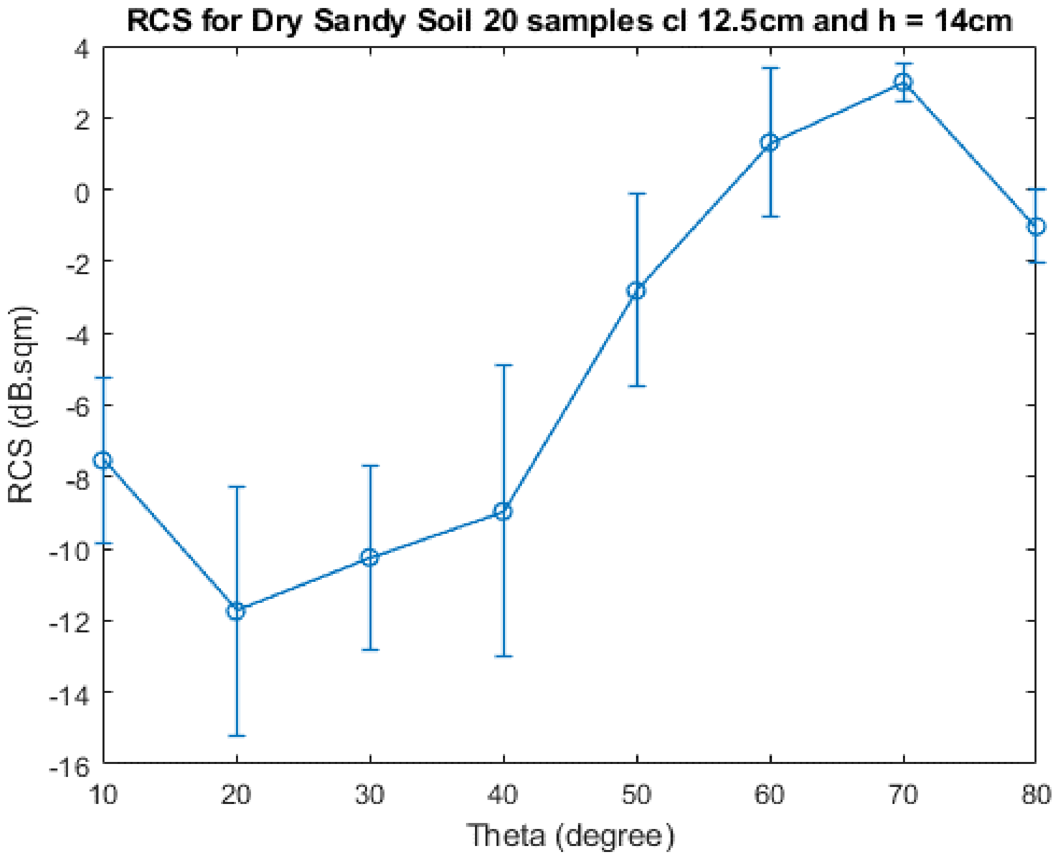

Figure 4.26: Averaged RCS analysis for dry sandy soil rms 14 cm (10 iterations)

For the dry sandy soil in Figure 4.26, the variations suggest a rougher surface with higher backscatter at larger angles and the error bars indicate variability in measurements due to surface inhomogeneity. For the wet sandy soil in Figure 4.27, the RCS values start much lower than for dry sandy soil, indicating increased absorption of electromagnetic waves. Also, the wetness increases dielectric properties, reducing reflections at smaller angles. For the oil contaminated soil in Figure 4.28, the oil layer introduces a smoothening effect which alters the dielectric properties. In terms of the implications and realisations, these RCS values provide a method to distinguish dry, wet and oil-contaminated surfaces based on scattering behaviour.

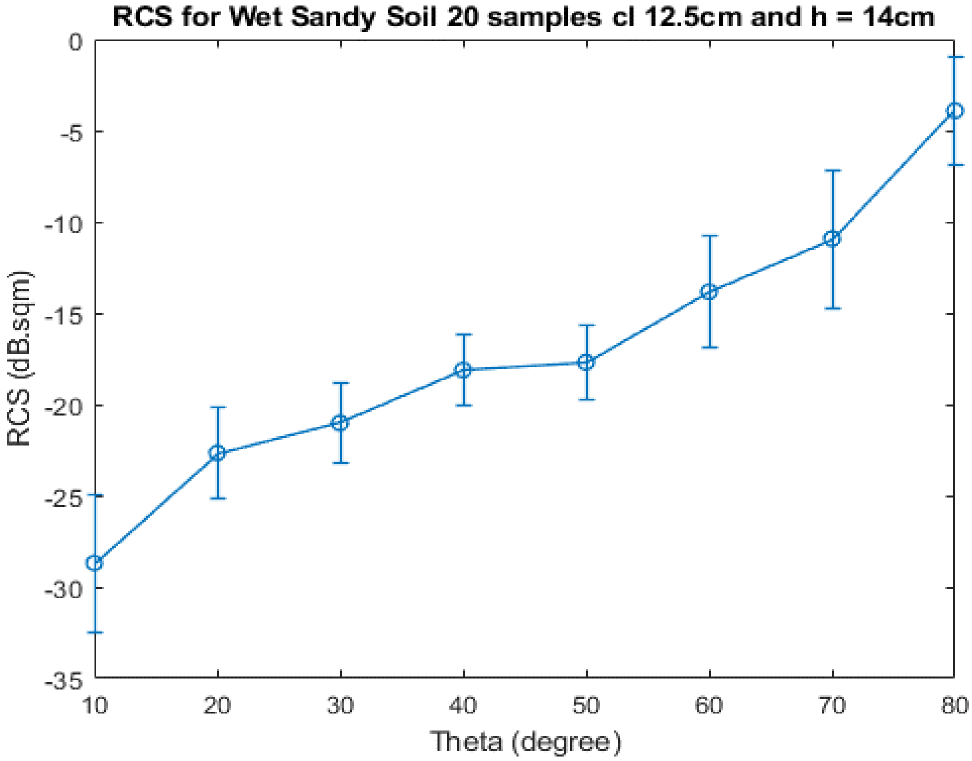

Figure 4.27: Averaged RCS analysis for wet sandy soil rms 14 cm (10 iterations)

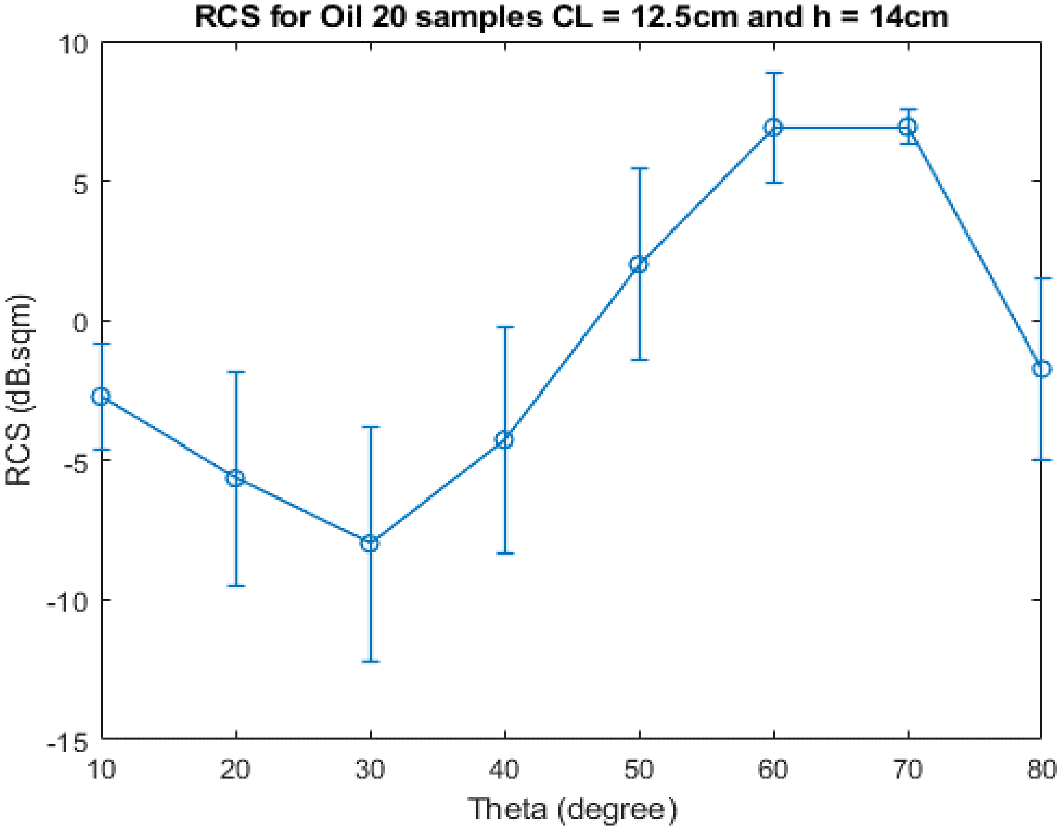

Figure 4.28: Averaged RCS analysis for Dry Sandy Soil mixed with oil rms 14cm (10 iterations)

In addition, although the dielectric constant of oil is like that of dry sandy soil, differences in their composition and interaction with electromagnetic waves lead to variations in their RCS values. The results indicate that the RCS of oil-contaminated sandy soil is consistently higher – by approximately 6 dB – compared to that of pure dry sandy soil. This increase in RCS suggests that the presence of oil alters the scattering properties of the surface, likely due to variations in absorption, conductivity, or subtle changes in surface roughness, despite the similarity in dielectric constants. Consequently, while the general trend in the results remain aligned, the observed increase in RCS highlights the distinct electromagnetic response of oil-contaminated soil. Also, oil contamination may introduce slight changes in the soil's surface roughness at a microscopic level, further influencing backscattering. These factors collectively contribute to the observed increase in RCS for oil-contaminated sandy soil compared to pure dry sandy soil. Therefore, for a dry sandy soil that is mixed with oil, we can envisage the oil emanating from spills or leaks from pipeline infrastructure.

Furthermore, a cursory look at the plots in Figures 4.26 to 4.28 shows that the reflectivity or RCS of our rough surfaces is directly proportional to the incident angle with which these rough surfaces are illuminated. We can see that for the dry sandy soil, wet sandy soil as well as sandy soil that has been mixed with oil, the higher the angle of illumination, the higher the RCS. This therefore implies that for our rough surfaces, if we want to get a higher return of our echo then it should amongst other factors be illuminated at a higher angle (say between 70° to 80°). Also, if we compare figures 4.26 and 4.28, we can also deduce that if our rough surface is mixed with oil, it has a higher reflectivity or return compared to a dry sandy soil. This is particularly useful as this concept can be used to discriminate in real life, an area that is soaked with oil and another that is not. So, we expect the area soaked in oil to have an increase in reflectivity of about 6 dB compared to the part or area of the soil not soaked in oil. This oil which soaks the soil can be because of oil spills and leaks from pipeline networks.

Now let's consider another parameter which could affect the reflectivity or RCS of our rough surfaces. We have seen how the angle of illumination affects the RCS of our rough surfaces.

We have also seen how the presence of oil in a dry sandy soil affects the reflectivity or RCS of our rough surfaces. The next point to consider in this analysis is the degree of roughness of our rough surface and how it affects reflectivity. The rms height defined for these rough surfaces is 7cm as opposed to 14 cm which we considered earlier for Figures 4.26 to 4.28. Similarly, 10 RCS simulations were conducted for each of the dielectrics – dry sandy soil, wet sandy soil and dry sandy soil mixed with oil, to ascertain whether the same trend was followed for each dielectric. The figures for these 10 RCS simulation plots per dielectric are shown in the appendix and have been discussed. From the figures, the same trend has been observed for the 3 dielectrics which implies the results can be relied upon and tallies with what was expected. An average of at least ten iterations for each dielectric is shown in Figure 4.29 for the dry sandy soil, Figure 4.30 for the wet sandy soil and Figure 4.31 for the dry sandy soil mixed with oil.

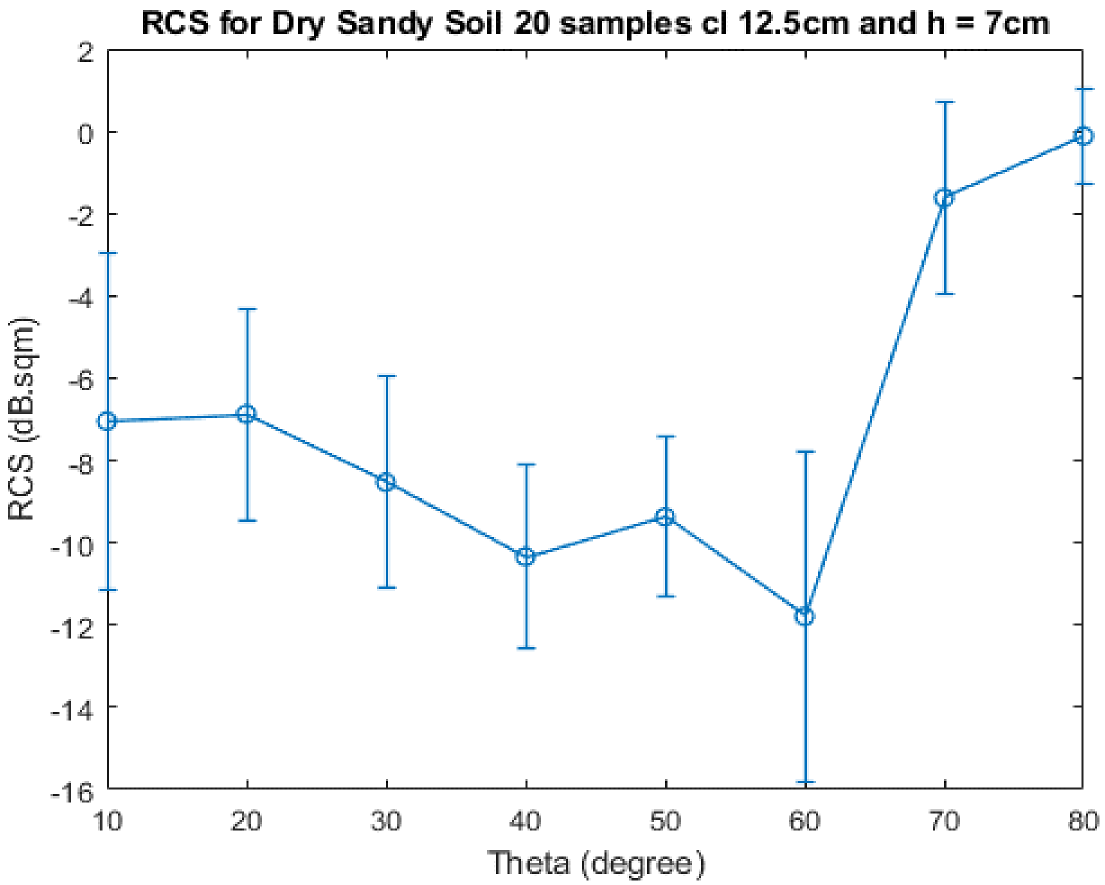

Figure 4.29: Averaged RCS analysis for dry sandy soil rms 7 cm (10 iterations)

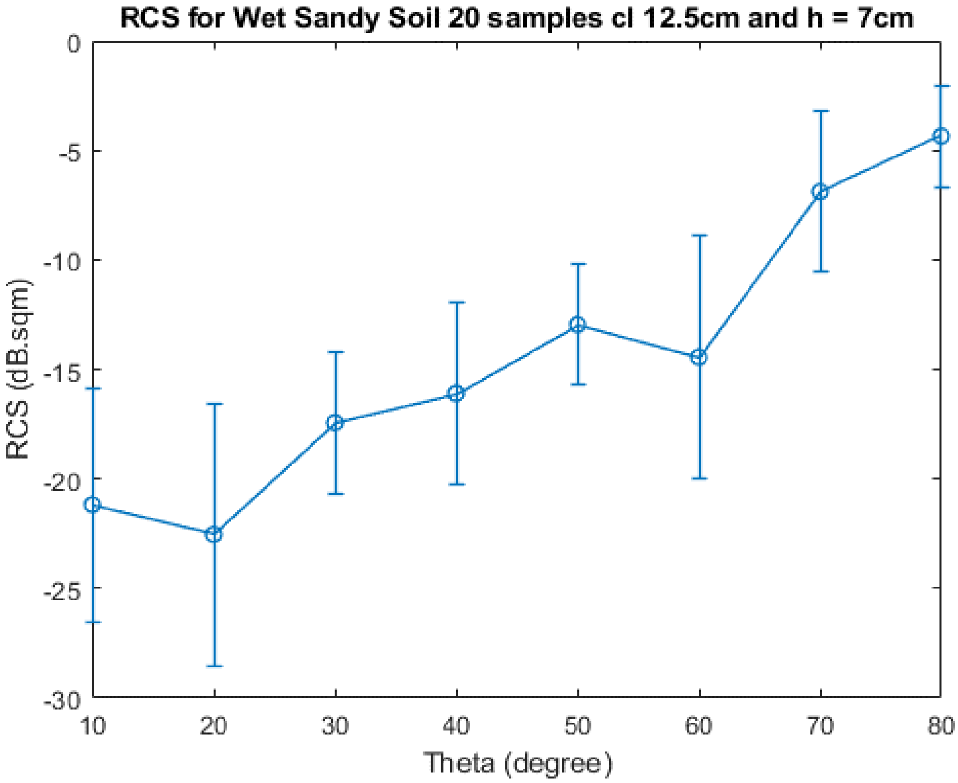

Figure 4.30: Averaged RCS analysis for Wet Sandy Soil rms 7 cm (10 iterations)

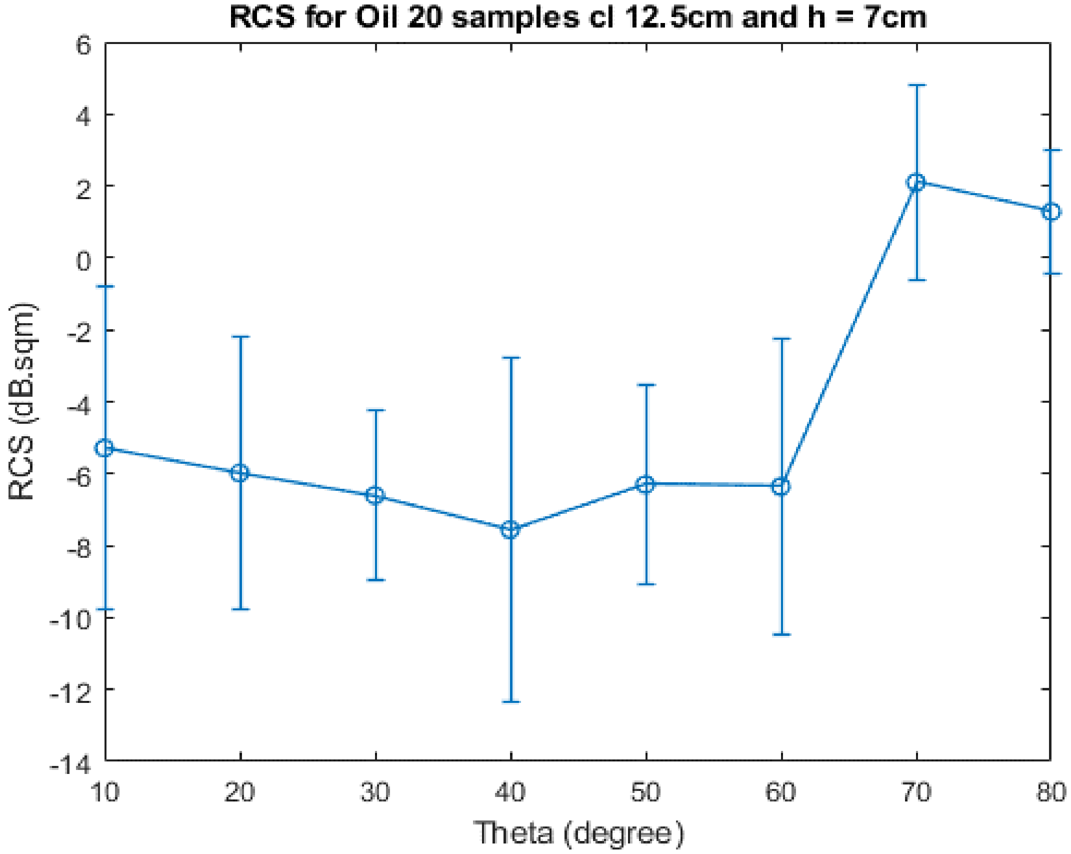

Figure 4.31: Averaged RCS analysis for Dry Sandy Soil mixed with oil rms 7cm (10 iterations)

In Figure 4.29 which is for the dry sandy soil, the range of the plot in terms of the RCS varied from about 0 dBsqm to about – 12 dBsqm as opposed to from about 4 dB sqm to about -12 dB sqm for Figure 4.26 which is for the corresponding dry sandy soil but with a higher surface roughness. Same analogy can be extended to the Figures 4.30 and 4.31 when compared to Figures 4.27 and 4.28 respectively. This therefore implies that the higher the surface roughness, the easier it is to detect the reflectivity or RCS from that rough surface. In addition, a surface that is rougher will have a higher reflectivity than a surface that is less rough. This applies to the three categories of soil surfaces being considered so far.

Furthermore, Figures 4.32 to 4.34 show the average for the three various rough surfaces under consideration but for a rms height of 3.5 cm. Please note that various iterations for each dielectric are shown in the appendix. We have earlier posited that the reflectivity or RCS of our rough surfaces is also dependent on the roughness of the rough surface in a direct relationship. This invariably means the rougher the surface, the higher the reflectivity and this is further buttressed and analysed in Figures 4.32 to 4.34. The implication of this is that when oil spills or leaks from our pipeline infrastructure, we are more likely to get a high return signal or echo if the surface upon which the oil leaks or spills onto is very rough compared to if it was just a smooth or a not-so rough surface. So, the higher the surface roughness, the higher the RCS of my rough surface and vice versa.

Also, we can see from the figures that if we compare Figures 4.32 to Figure 4.29 and to Figure 4.26 which are for the dry sandy soil for 3.5cm, 7cm and 14cm rms heights respectively, it can be observed that as the rms height increases, the reflectivity also increases; whereas a lower rms height results in reduced reflectivity. The same can be said for the wet sandy soil as well as the dry sandy soil mixed with oil for all the three rms heights earlier described.

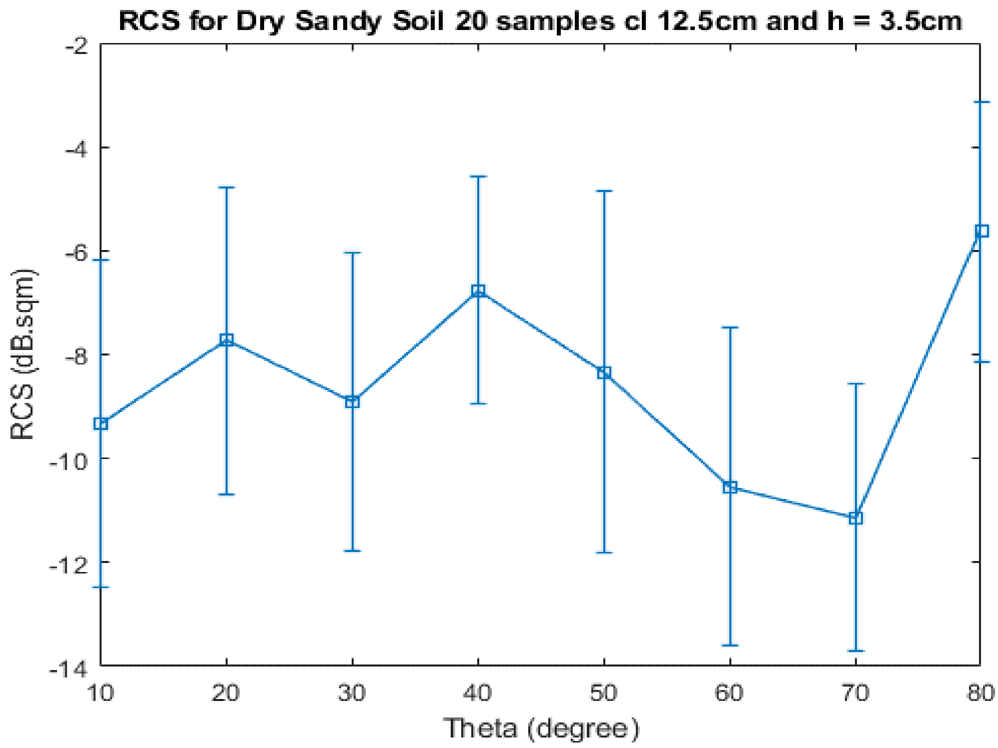

Figure 4.32: Averaged RCS analysis for dry sandy soil rms 3.5 cm (10 iterations)

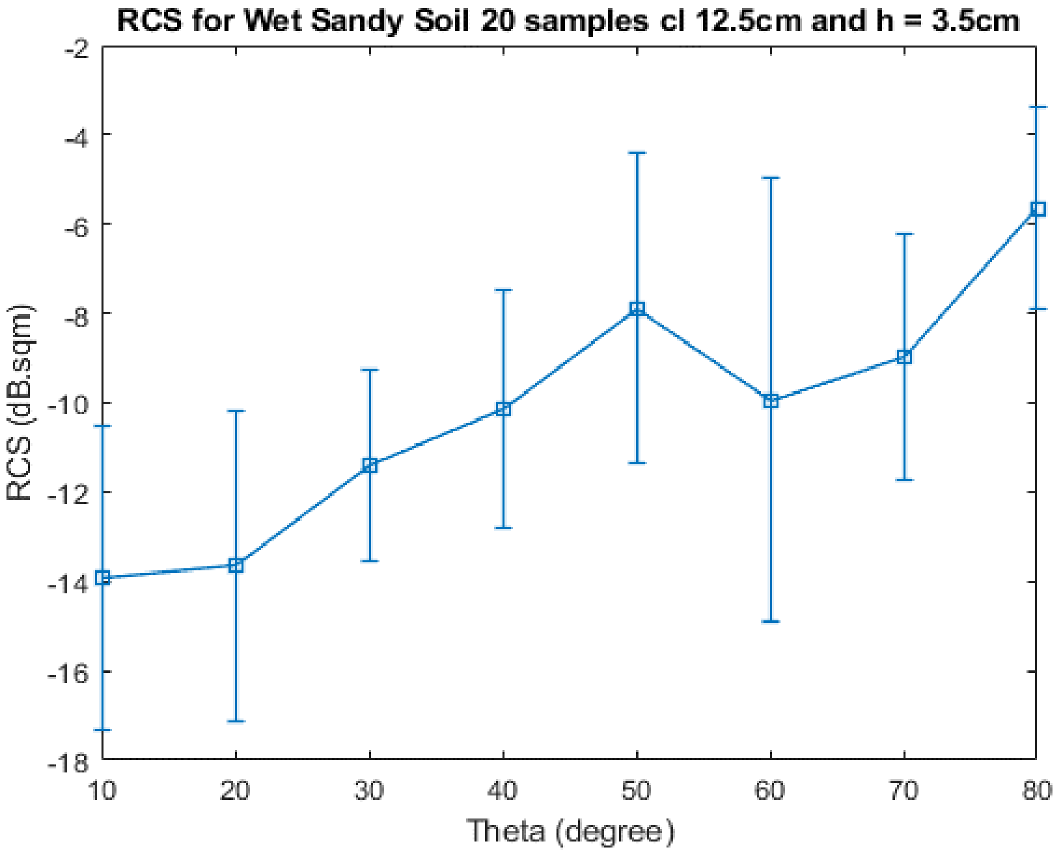

Figure 4.33: Averaged RCS analysis for Wet Sandy Soil rms 3.5cm (10 iterations)

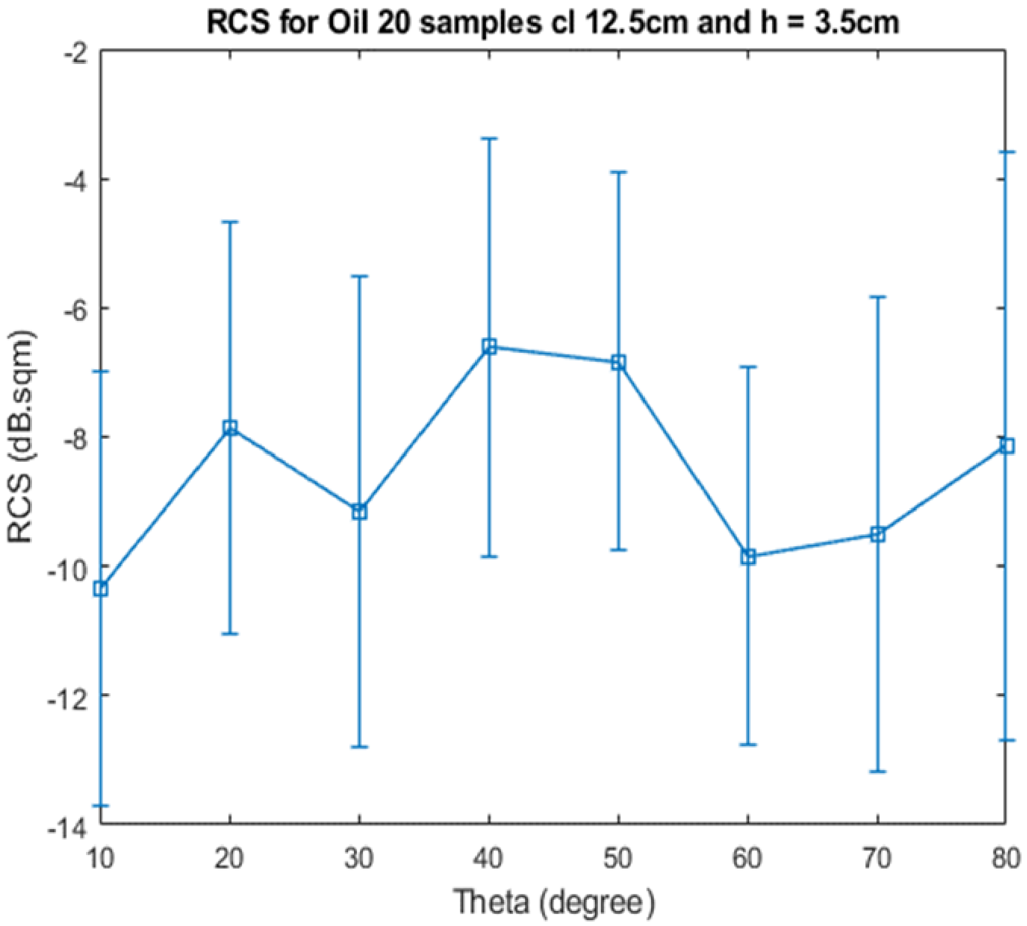

Figure 4.34: Averaged RCS analysis for Dry Sandy Soil mixed with oil rms 3.5cm (10 iterations)

Figure 4.35 shows the average RCS measurements (after 7 iterations as shown in the appendix) for dry sandy soil with rms height as 21cm and with the same parameters earlier described – correlation length of 12.5 cm, for an area of ½ m by ½ m. When figure 4.35 is compared to figures 4.32, 4.29 and 4.26 which are all for dry sandy soils with the same parameter except for the rms height, we can see that the higher the roughness of the surface, the higher the RCS or reflectivity and vice versa. This is also in tandem with what we expect. The error bars which show the margin of error amongst the various iterations for each surface roughness are also indicated on the averaged plot across all the figures.

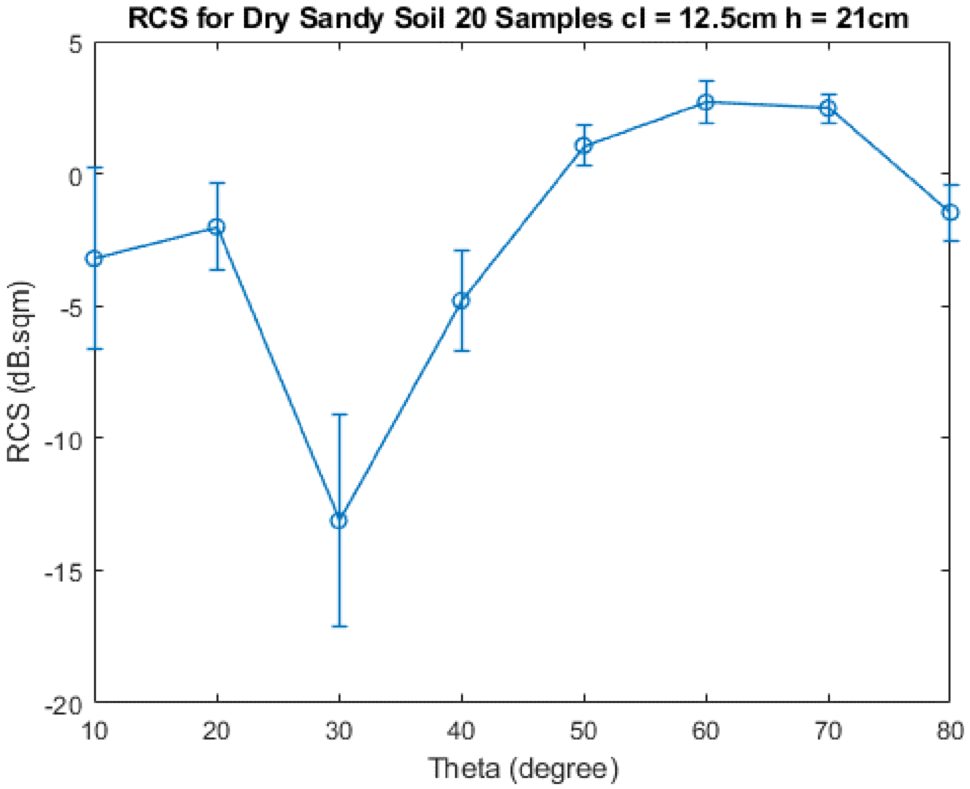

Figure 4.35: Averaged RCS analysis for dry sandy soil rms 21 cm (7 iterations)

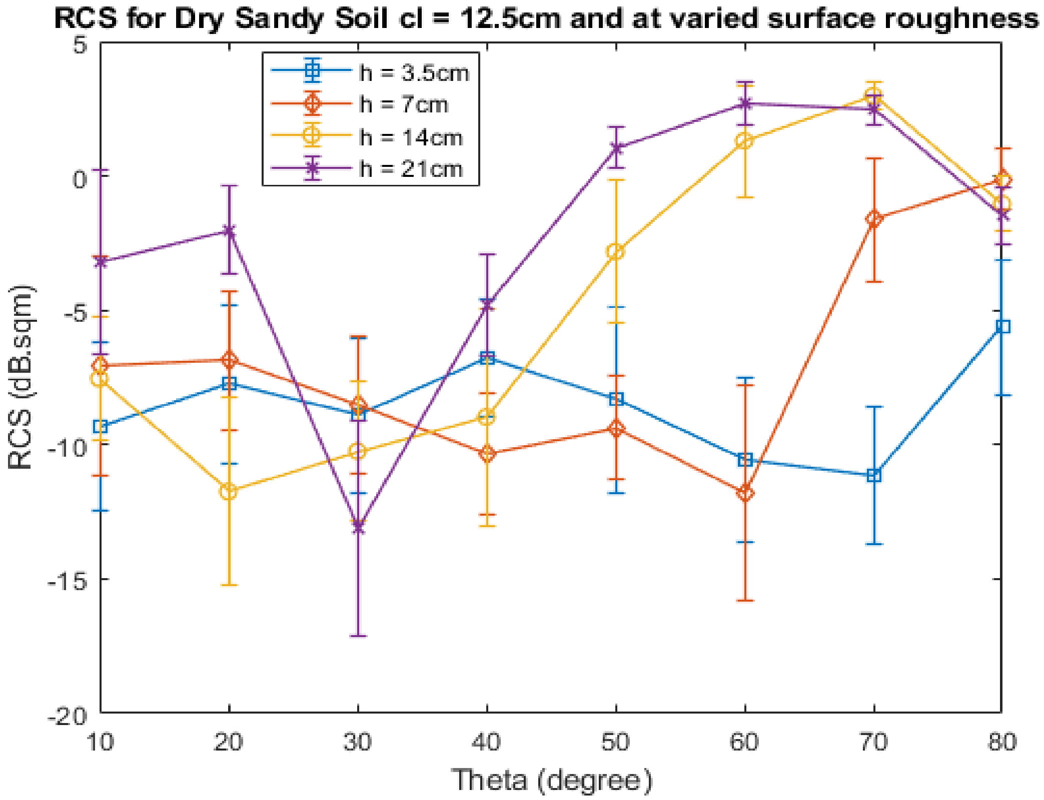

Figure 4.36: Combination of the averaged RCS plots for Dry Sandy Soil

Figure 4.36 shows the combined averaged RCS plots for dry sandy soil. As always, the average of the plots for each scenario or surface roughness was obtained based on the number of plots across all figures. From the figure, we can see that the rougher the surface for dry sandy soil, the higher the RCS or reflectivity as earlier explained. Also, we can see from the combined plot that the reflectivity or RCS tends to increase as the angle of illumination increases which invariably might mean that as oil spills or leaks into the surroundings of the pipelines, it will be easier to detect these leaks if the angle of illumination is high (say between 60° to 80°) or the dry sandy soil surface is rough.

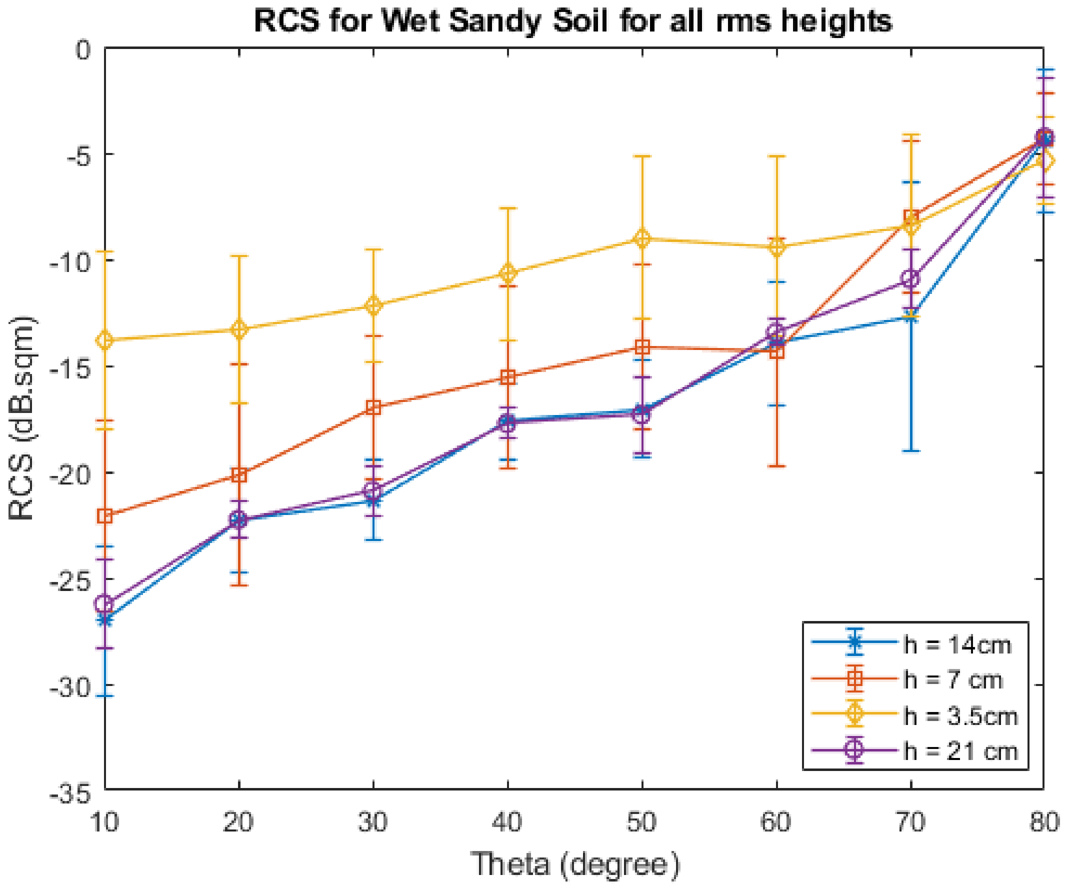

Figure 4.37: Combination of the averaged RCS plots for Wet Sandy Soil

Figure 4.37 shows the combined averaged RCS plots for wet sandy soil. From the figure, we can see that the smoother the surface, the higher the RCS or reflectivity which is at variance to what we experienced with the dry sandy soil. This variance could be attributed to the percentage of water already in the sandy soil, which makes it a smooth (or a not so rough) surface. Therefore, the less rough it is, the higher the RCS or echo from that surface and vice versa. Furthermore, the reason water makes sandy soil smoother and increases RCS does not directly apply to oil-contaminated sandy soil because of the distinct physical and dielectric properties of oil compared to water. Water has a high dielectric constant (≈ 80), which significantly alters the soil's electromagnetic response and reduces surface roughness by binding particles together more effectively. This smoothing effect enhances reflectivity. In contrast, oil has a much lower dielectric constant (like dry sandy soil), meaning it does not drastically change the soil's electromagnetic properties. Additionally, oil tends to coat individual sand particles rather than binding them cohesively like water, which can preserve or even enhance surface roughness rather than reducing it. As a result, the oil-contaminated soil does not exhibit the same RCS behaviour as wet sandy soil. Also, we can see from the combined plot that the reflectivity or RCS tends to increase as the angle of illumination increases which invariably might mean that as oil spills or leaks into the surroundings of the pipelines, it will be easier to detect these leaks if the angle of illumination is high (say between 60° to 80°) or the wet sandy soil surface is less rough.

Now when these plots i.e. Figures 4.34, 4.31 and 4.28 are now combined, we obtain Figure 4.38 which is the combination of the averaged RCS plots for dry sandy soil that has been mixed with oil. From Figure 4.38, we can see that the results for dry sandy soil mixed with oil is very similar to the results for dry sandy soil. It is no surprise because of the reasons earlier adduced and the permittivity of dry sandy soil and oil are very close or like each other. Therefore, for a dry sandy soil that is mixed with oil, we can envisage the oil emanating from spills or leaks from pipeline infrastructure. So based on the results, it will be easier to detect the oil spill or leak from a dry sandy soil surface that is soaked with oil if the surface is rough, than when it is a smooth or a not-so rough surface. Furthermore, the higher the angle of illumination, the higher the reflectivity and vice versa. These results are in tandem or align with what we expect in these scenarios.

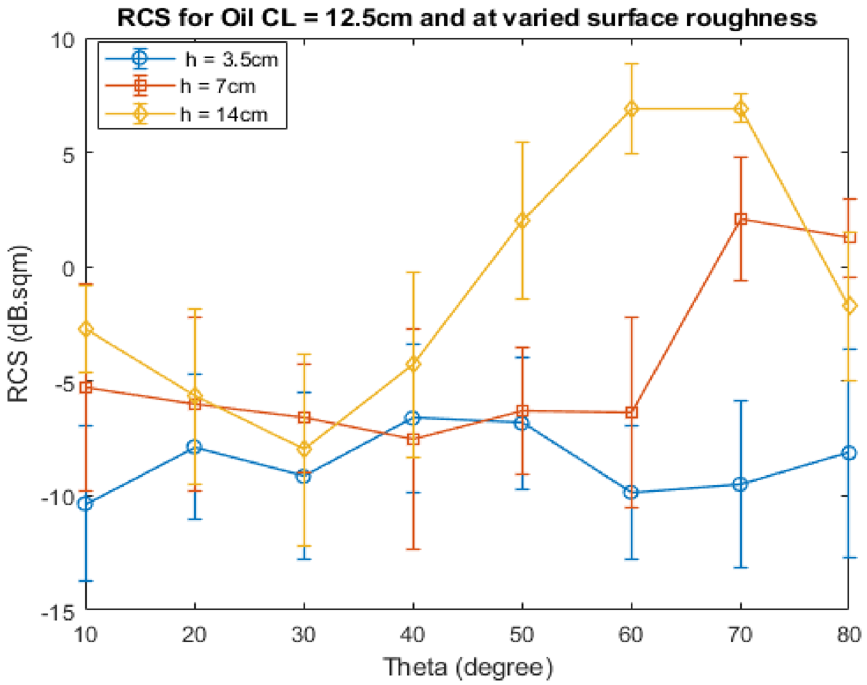

Figure 4.38: Combination of the averaged RCS plots for Dry Sandy Soil mixed with oil

Table 4.6 summarises the key findings from the simulation analysis of dry, wet and oil-contaminated sandy soils with varying surface roughness. The results highlight how RCS behaviour changes with surface conditions and incidence angles.

Table 4.6: Comparative analysis of the RCS behaviour of dry, wet and oil contaminated sandy soils across varied roughness profiles

Condition	Surface Roughness	Max RCS (approx)	Min RCS (approx)	Key Angular Behaviour / Overall Insight
Dry Sandy Soil	3.5, 7, 14, 21 cm	+3 dB.sqm (h = 21 cm)	-17 dB.sqm (h = 14 cm, θ=30°)	Higher RCS at large θ, especially for 14/21 cm; surface roughness significantly increases RCS at high angles

Wet Sandy Soil	3.5, 7, 14, 21 cm	-5 dB.sqm (h = 14 cm)	-30 dB.sqm (h = 14 cm, θ=10°)	Smooth increase in RCS with θ; generally low values; moisture reduces RCS significantly, masking roughness influence
Oil-Contaminated Soil	3.5, 7, 14 cm	+7 dB.sqm (h = 14 cm)	-13 dB.sqm (h = 3.5 cm)	Peaks sharply at θ = 50°–70° for higher roughness; oil contamination amplifies RCS significantly with surface roughness interaction

The next stage in the analysis of these results is to combine the results of the various dielectrics and compare and analyse them. Figure 4.39 shows the averaged plots for the various dielectric materials when combined for the same rms height of 14 cm and correlation length of 12.5 cm. From this figure, we can see that the dry sandy soil mixed with oil has a higher RCS compared to the dry sandy and wet sandy soils. This implies that when sandy soil has been soaked with oil, the RCS or reflectivity of the soil increases due to the presence of oil. So, in an environment where oil spills have occurred, we expect the echoes or return signal to be higher in reflectivity for areas that are soaked compared to areas that are just dry or wet. With this technique of increased reflectivity or RCS values, my radar system can discriminate where oil leaks or spills have occurred and immediately alert the relevant authorities to forestall further leakage. From the figure, we can also see that the wet sandy soil has reduced reflectivity, which implies that if an area has been flooded with water, the RCS is greatly reduced (about 25dB at lower angles) compared to if the flood is due to oil spills and leaks from pipeline network. We shall also analyse the situation for other rms heights.

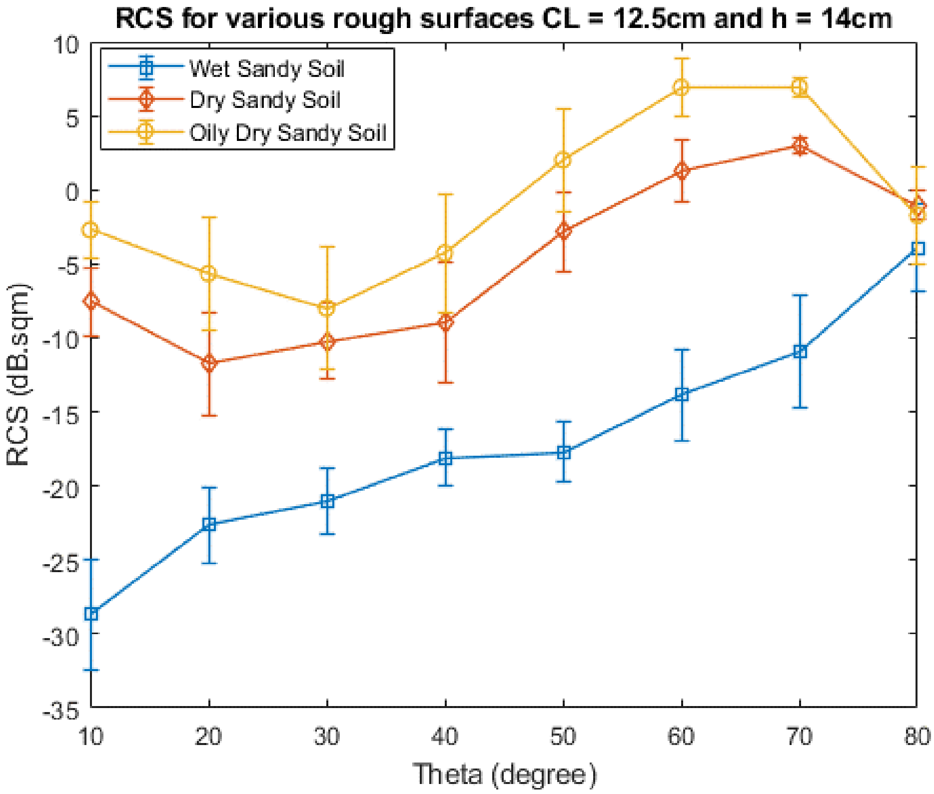

Figure 4.39: Combination of the various dielectric materials with rms 14cm

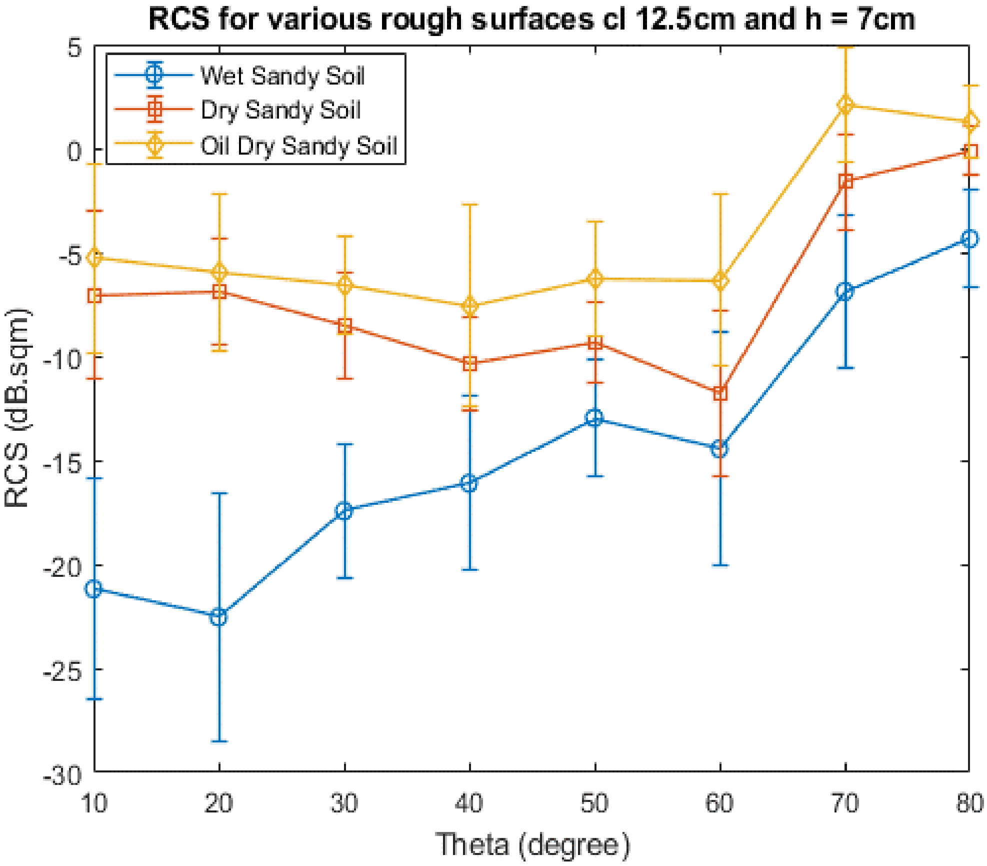

Figure 4.40: Combination of the various dielectric materials with rms 7 cm

Figure 4.40 shows the averaged plots for the various dielectric materials when combined for the same rms height of 7 cm and correlation length of 12.5 cm. From this figure, we can see that the dry sandy soil mixed with oil has a higher RCS compared to the dry sandy and wet sandy soils. However, the gap between the dry sandy soil as well as the dry sandy soil mixed with oil is reduced (about 2 or 3 dB) due to the reduced surface roughness i.e. from 14cm to 7cm. Previously, this gap between the dry sandy soil as well as the dry sandy soil mixed with oil was about 5 or 6 dB for 14cm surface roughness. This also implies that when sandy soil has been soaked with oil, the RCS or reflectivity of the soil increases due to the presence of oil. So, in an environment where oil spills have occurred, we expect the echoes or return signal to be higher in reflectivity for areas that are soaked compared to areas that are just dry or wet. With this observed increase in reflectivity or RCS values, a comparative radar experiment over an area suspected of oil leakage can reveal changes in reflectivity, allowing for detection of contaminated regions. However, if the surface roughness is significantly reduced (e.g. an rms height of 3.5 cm), the ability to distinguish oil-contaminated areas from dry or wet soil becomes more challenging, reducing detection confidence. In such cases, increasing the radar frequency could enhance sensitivity to subtle variations in reflectivity, improving the reliability of oil spill detection. From the figure, we can also see that the wet sandy soil has increased reflectivity, which implies that if an area has been flooded with water, the difference in RCS is greatly reduced (about 15dB at lower angles) compared to if the flood is due to oil spills and leaks from pipeline network. This 15dB difference at lower angles for Figure 4.40 is due to the reduced surface roughness when compared to a 25 dB difference at lower angles for a 14cm rough surface shown in Fig. 4.39. This also implies that the rougher our surface, the more likely we will be able to discriminate between the various dielectrics.

When we look at Figure 4.41 which is for a rough surface of 3.5cm, we can see that due to the reduced surface roughness, it is much more difficult to discriminate between the dry sandy soil as well as the dry sandy soil mixed with oil. This result is in tandem with what's expected when compared to Figures 4.39 and 4.40. Similarly, the RCS or reflectivity for the wet sandy soil is much increased (- 14 dB at 10°) for a 3.5 cm surface roughness and the difference between an area where you have soil soaked with water and another area where the soil is flooded with oil is massively reduced (about 5 dB) compared to a 25-dB difference at 14cm surface roughness and 15 dB difference in RCS for a 7 cm surface roughness.

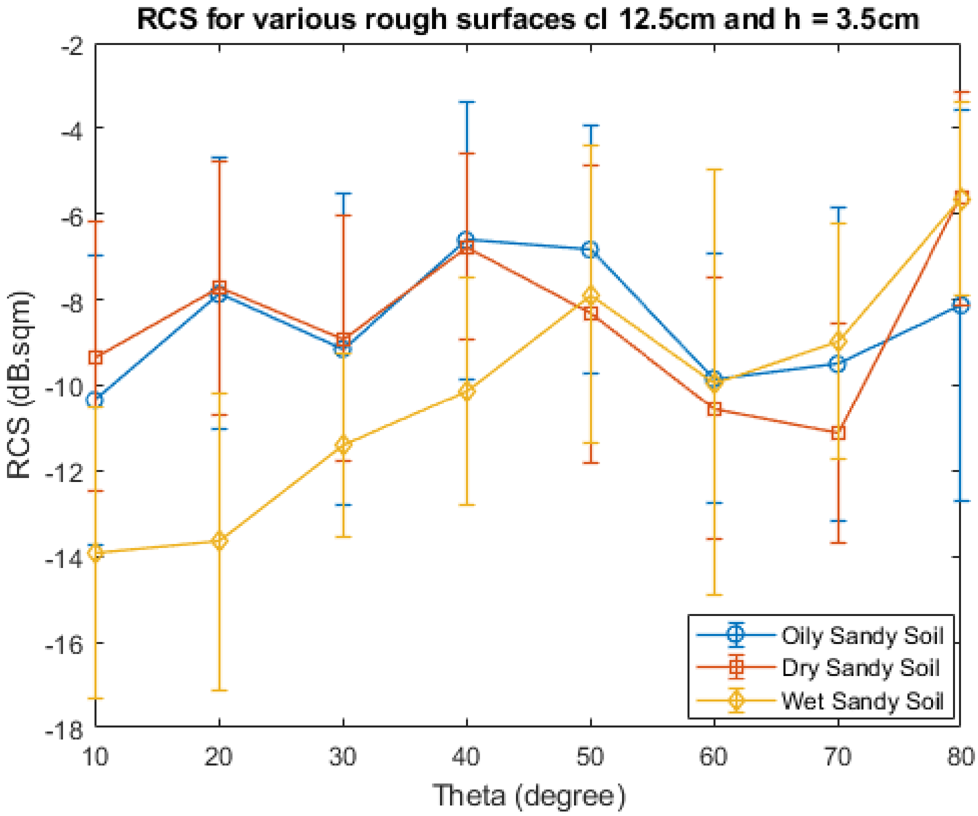

Figure 4.41: Combination of the various dielectric materials with rms 3.5 cm

When we look at Figure 4.42 which is for a rough surface of 21 cm, we can see that there is also about a 25 dB difference between the dry sandy soil and the wet sandy soil especially at lower angles. What this implies is that it would be easier to detect oil spills or leaks on a dry sandy soil compared to a wet sandy soil; and even at higher angles, oil on dry sandy soil will be easily detected compared to a wet sandy soil as shown in the figure. Considering how the dielectric property of oil is close to that of dry sandy soil and drawing conclusions from the previous plots in previous sections, it is safe to also say that for dry sandy soil mixed with oil, the plot already shown would be similar for oily sandy soil. Due to computational bottlenecks, the 21 cm for an oily sandy soil could not be generated despite persistent and repeated trials.

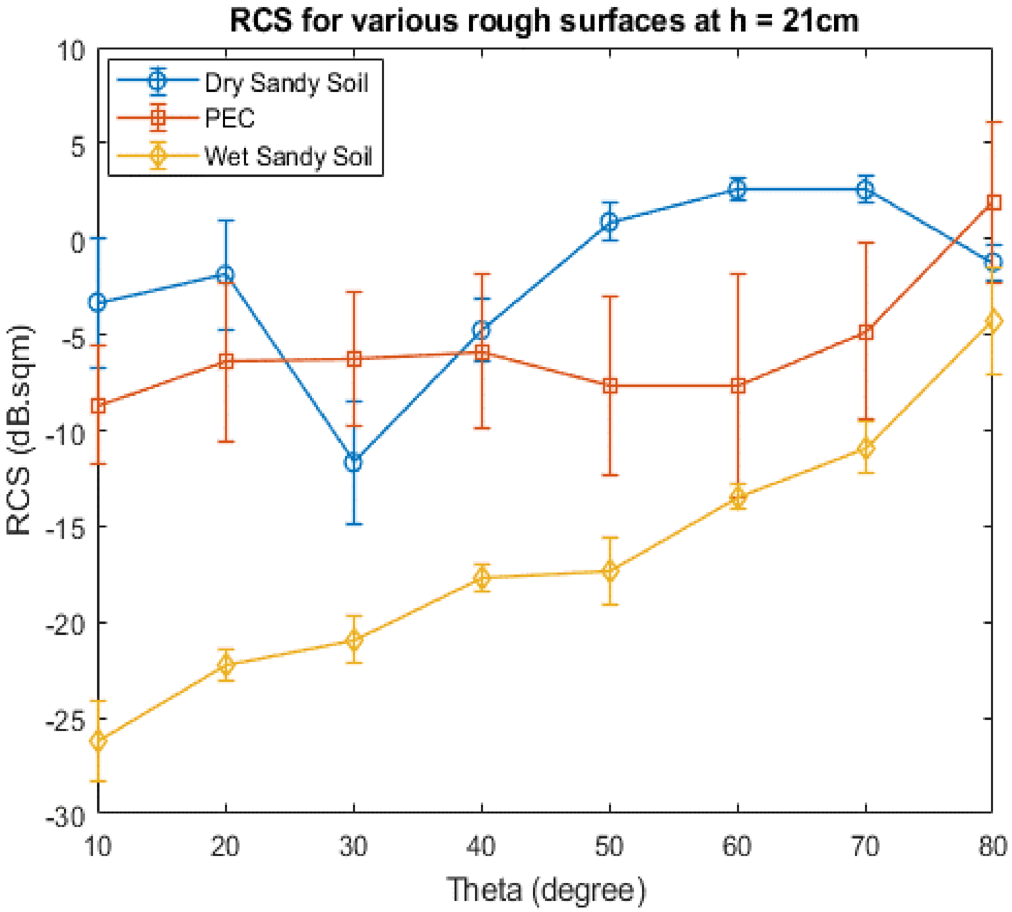

Figure 4.42: Combination of the various dielectric materials with rms 21 cm

Table 4.7 shows a summary of the key findings from the analysis of various rms heights

Table 4.7: Summary of key findings from the analysis of various rms heights

Surface Roughness (h)	Observation: Wet Soil	Observation: Dry Soil	Observation: Oily Soil / PEC	Key Finding
3.5 cm	Lowest RCS across all angles; peaks around -6 dB.sqm	Moderate RCS (-10 to -6 dB.sqm); follows angular trend	Fluctuating but close to dry; slightly higher at high angles	At low roughness, RCS curves for all soils are close; wet consistently lowest
7 cm	Still low; gradually increases with angle but remains < -5 dB.sqm	Consistent RCS ~ -8 dB.sqm with slight upward slope	Consistently higher than wet/dry, peaks at +4 dB.sqm	RCS differentiation begins to emerge; oil has most influence
14 cm	Significant RCS suppression; peaks around -4 dB.sqm	RCS increases with angle, peaks at ~ +6 dB.sqm	Dominant RCS: reaches +9 dB.sqm at peak	Oily soil clearly separates with highest RCS; dry follows, wet suppressed
21 cm	Very low RCS, starts from -28 dB.sqm and peaks near -7 dB.sqm	RCS increases with angle and peaks around +7 dB.sqm	PEC used as baseline; dry soil approaches PEC above 60°	Dry soil outperforms PEC at some angles; wet remains suppressed

The next step is to now generate different rough surfaces but with same statistics for dry and wet sandy soil, then extract and analyse the RCS statistics. Furthermore, we will investigate how oil can be introduced into the dry sandy soil template in CST. Newer rough surface models would be developed that would appear to become smoother because of the introduction of oil at various levels and in various quantities. Once that is done, then a comparison of the reflectivity results for varied dielectric properties will be discussed and analysed. Also, there will be a comparison of the theoretical and the experimental results for dry sandy soil. All these simulations will be conducted on the High-Performance Computing (HPC) facility of the Birmingham Environment for Academic Research (BEAR) as current computing or computational facilities are inadequate considering the size of my models.

For the experiment, I built a rough surface profile for 3.5 cm, 7cm and 14cm roughness heights which would be used along the sand tray to create repeatable rough surface profiles of the rms heights that can then be relied upon instead of just making arbitrary holes or spacings on the sand. This shall be elucidated upon in chapter five and we shall also explore the experimental results and compare to the simulation results as well.

4.7: Modified Rough Surface Models in CST & comparison of the results

In this sub section, the rms height which determines the roughness of the rough surface models would be modified. The rms heights are modified to mimic a situation where oil leaks from a pipeline infrastructure spill onto a rough surface and like we expect, as the leaks increase on the rough surface, the ridges of the rough surface would continue to be covered until the oil spills cover the entire rough surface and invariably turns the original rough surface into a 'smooth' surface. The RCS of the initial rough surface would thus be compared to the RCS of the 'smooth' surface to help our understanding of how the RCS of our theoretical models varies from a very rough surface to a 'smooth' surface due to the introduction of various levels or quantities of oil on the rough surface. The results of this RCS analysis would also be compared to the RCS obtained via experiments where various quantities of oil would be poured onto our rough surface profiles on the tray filled with sand. They would be poured gently onto the sand filled tray depending on the rough surface profiles, until the entire tray is covered with oil to also mimic a 'smooth' surface. Both sets of results i.e. from modelling and experiments, would thus be compared and analysed.

Figure 4.43 shows a rough surface model with original rms height of 3.35 cm and when the rough surface is modified due to the introduction of 'oil', the surface roughness is impacted, hence the surface is less rough and the rms heights begin to reduce from the 3.35cm to 2.96 cm, then 2.49 cm and to 1.73 cm until it finally gets to 0.50 cm as shown in the Figure 4.56. The modified rough surface models therefore have a reduced or smaller surface roughness depending on the level or quantity of oil which has been applied to that rough surface.

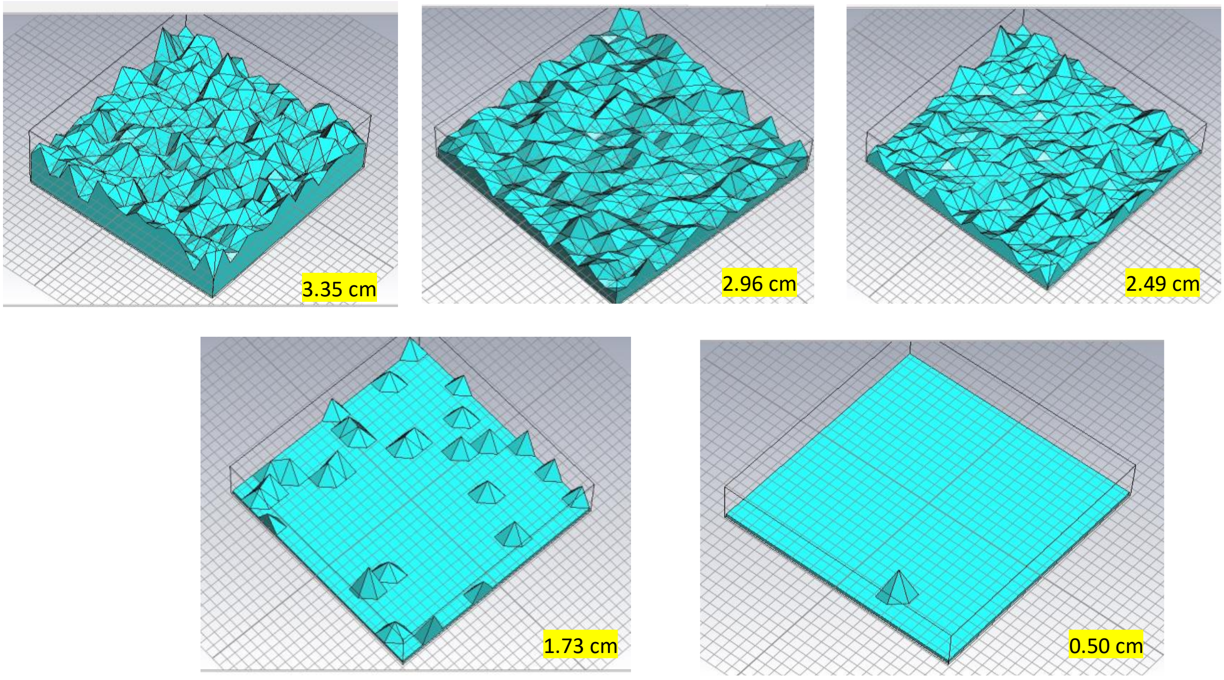

Figure 4.43: Modified rough surface models with original rms 3.5 cm

Similarly, Figure 4.44a shows a rough surface model with rms height of 7.13cm while Figure 4.44b shows an updated figure when that same rough surface model has been modified albeit with the introduction of oil which maybe emanated from oil spills and leaks. The introduction of oil now makes the surface less rough and the rms height is thus reduced. The modified rough surface model therefore has a reduced surface roughness of 5.07cm and it is further reduced until 1.19 cm.

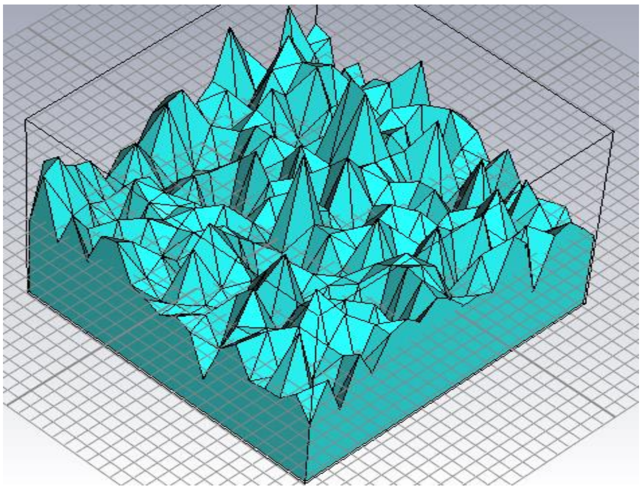

(a) Original rough surface model with rms height of 7.13 cm

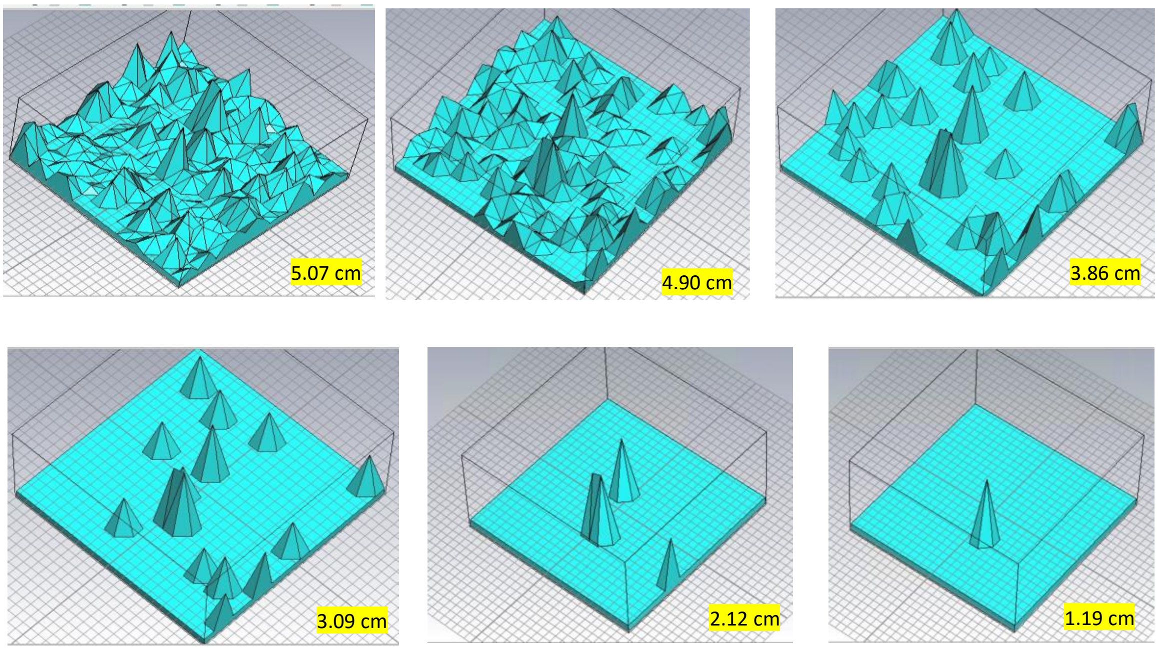

(b) Modified Rough surface models with original rms height of 7 cm

Figure 4.44: Modified rough surface models with original rms 7 cm (a) original (b) modified

Furthermore, Figure 4.45a shows a rough surface model with rms height of 13.72 cm while Figure 4.45b is the updated version of Figure 4.45a after the model has been modified and the rms height reduced to 9.57 cm and further reduced until 1.89 cm.

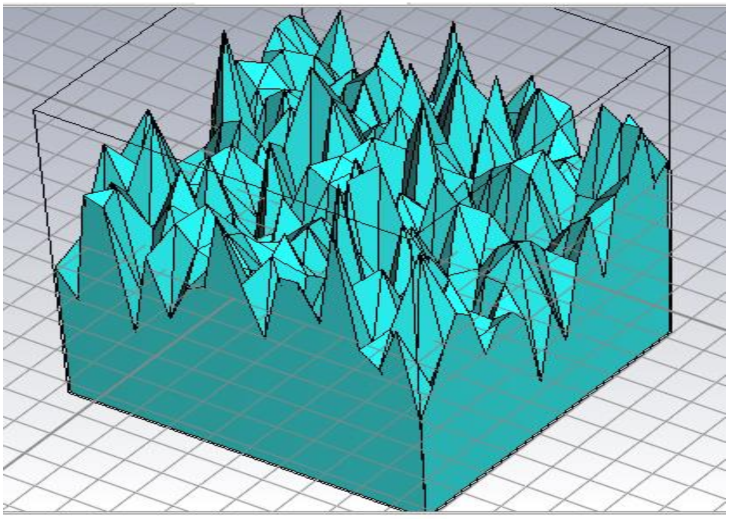

(a) Original rough surface model with rms height of 13.72 cm

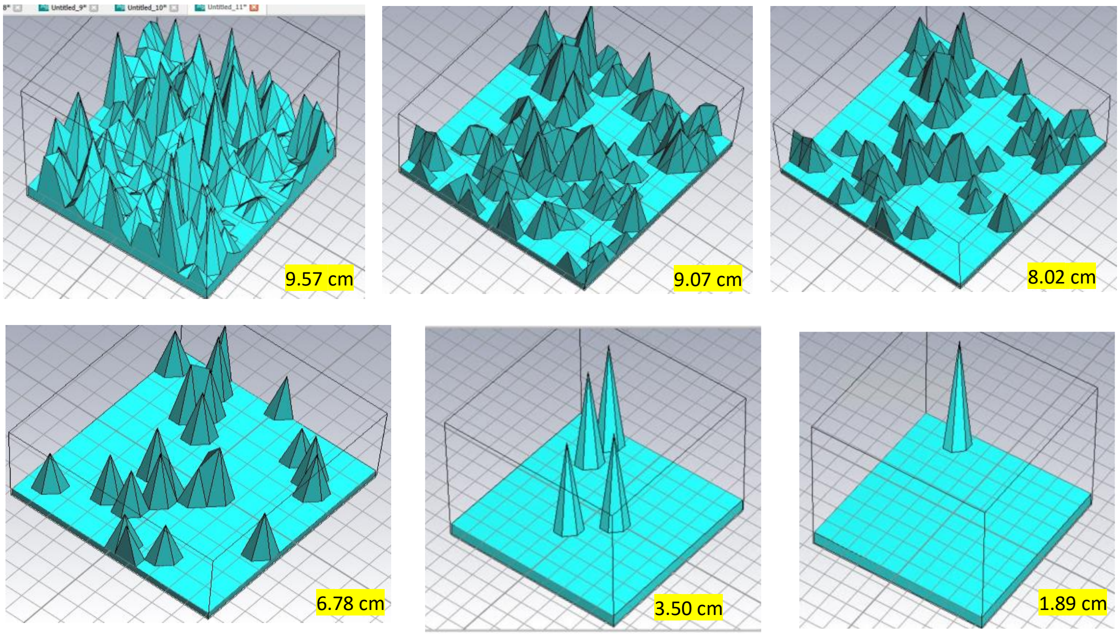

(b) Modified Rough Surface Models with original rms height of 14 cm

Figure 4.45: Modified rough surface models with original rms 14 cm (a) original (b) modified

Also, Figure 4.46 shows a modified rough surface model with original rms height of 21.33 cm but has been updated and this modified rough surface model has been reduced to rms heights of 14.91 cm, 13.59cm, 11.39cm, 9.52cm, 6.35cm and 3.5 cm as shown

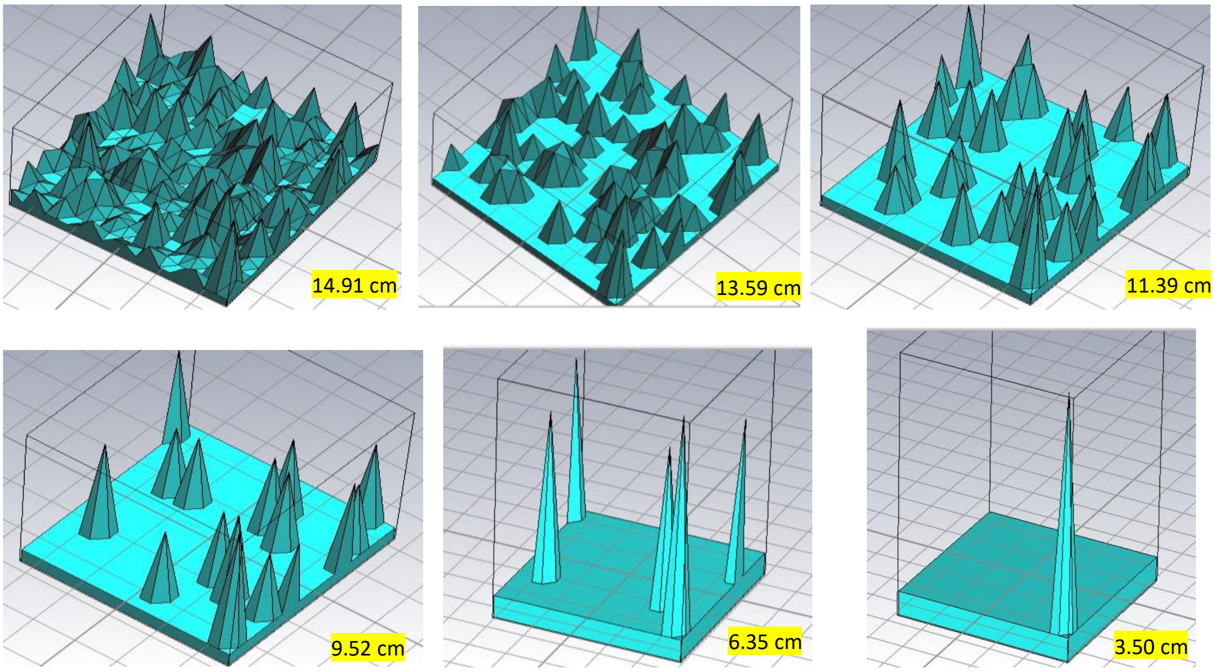

Figure 4.46: Modified rough surface models with original rms 21 cm

Now when we take Figure 4.43 into consideration, CST simulation is performed for all the five subplots in the figure to analyse their RCS for various dielectric materials. Figure 4.47 shows the plot of the RCS for both the original rough surface model as well as the modified rough surface models for a dry sandy soil. Figure 4.48 shows the plot of the RCS for both the original rough surface model as well as the modified rough surface models for a dry sandy soil mixed with oil. Figure 4.49 shows these same plots for a PEC while Figure 4.50 shows these same plots for a wet sandy soil. From these figures, particularly figures 4.47 to 4.49, we can see that the original rough surface models with a higher rms height i.e. 3.5cm have higher RCS compared to the modified rough surface models with a reduced or lower rms height. This agrees with what we had earlier explained for similar dielectrics i.e. dry sandy soil, oily sandy soil and PEC, where the higher the rms height, the higher the reflectivity and vice versa. For Figure 4.50 which is for a wet sandy soil, the reverse is the case. The higher the rms height, the lower the RCS and vice versa. This is particularly true for wet sandy soils where the less rough it is, the higher the reflectivity because a less-rough wet sandy soil surface is somewhat likened to a smooth surface, whereas the rougher it is, the lower the RCS due to scattering.

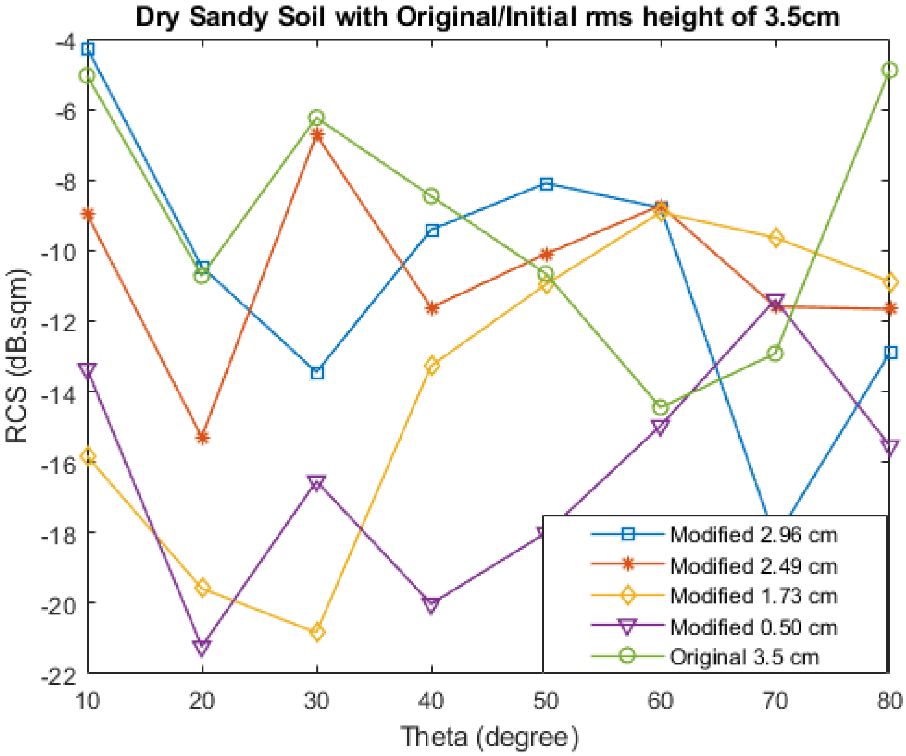

Figure 4.47: Dry sandy soil with original rms height of 3.5cm and modified surface roughness

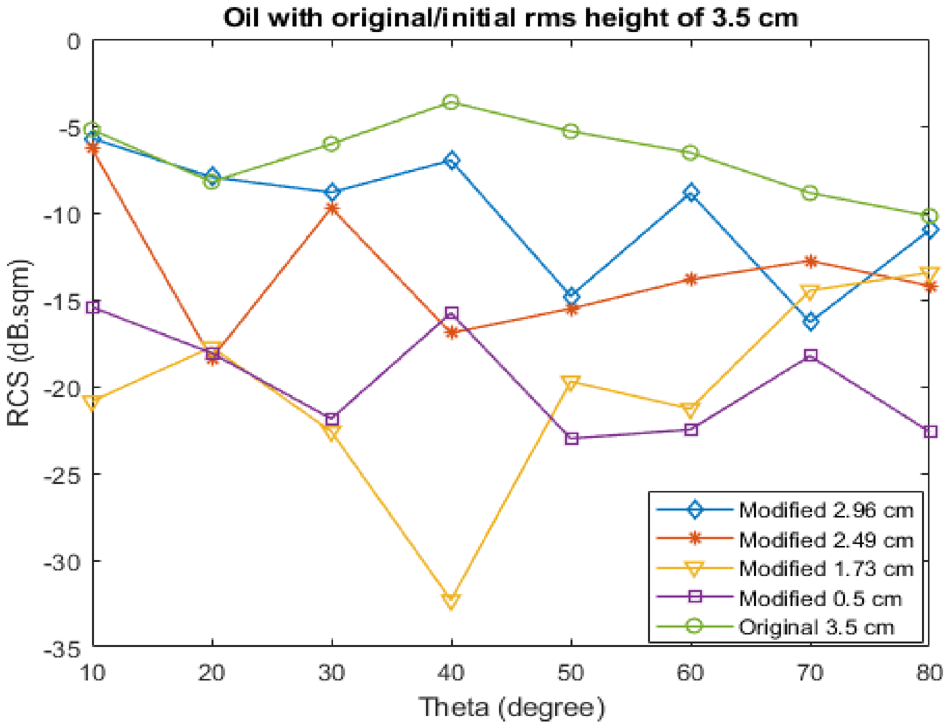

Figure 4.48: Oily sandy soil with original rms height of 3.5cm and modified surface roughness

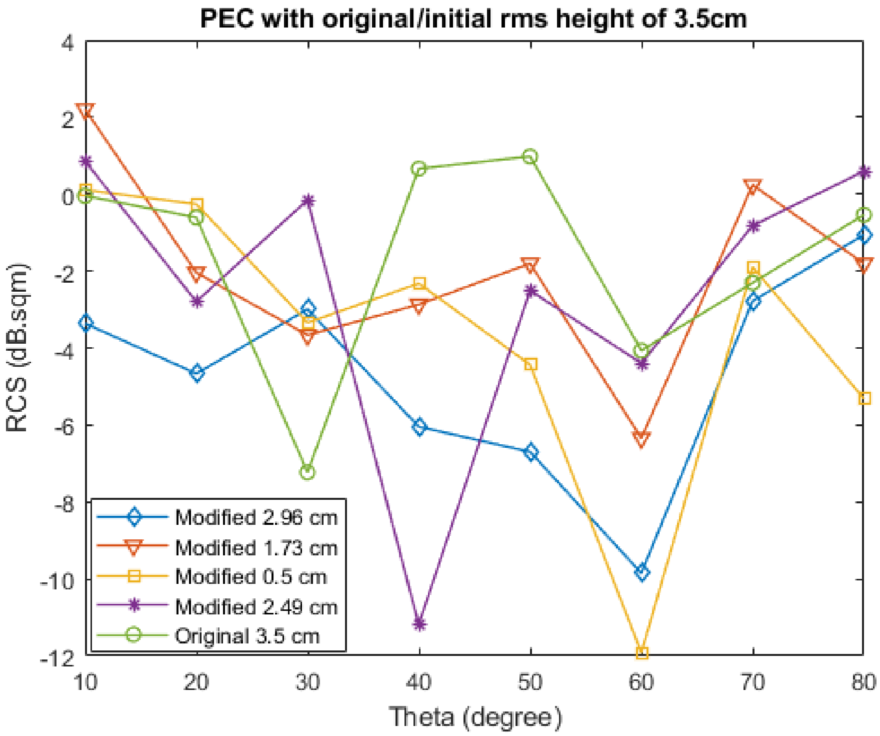

Figure 4.49: PEC with original rms height of 3.5cm and several modifications of the rms height

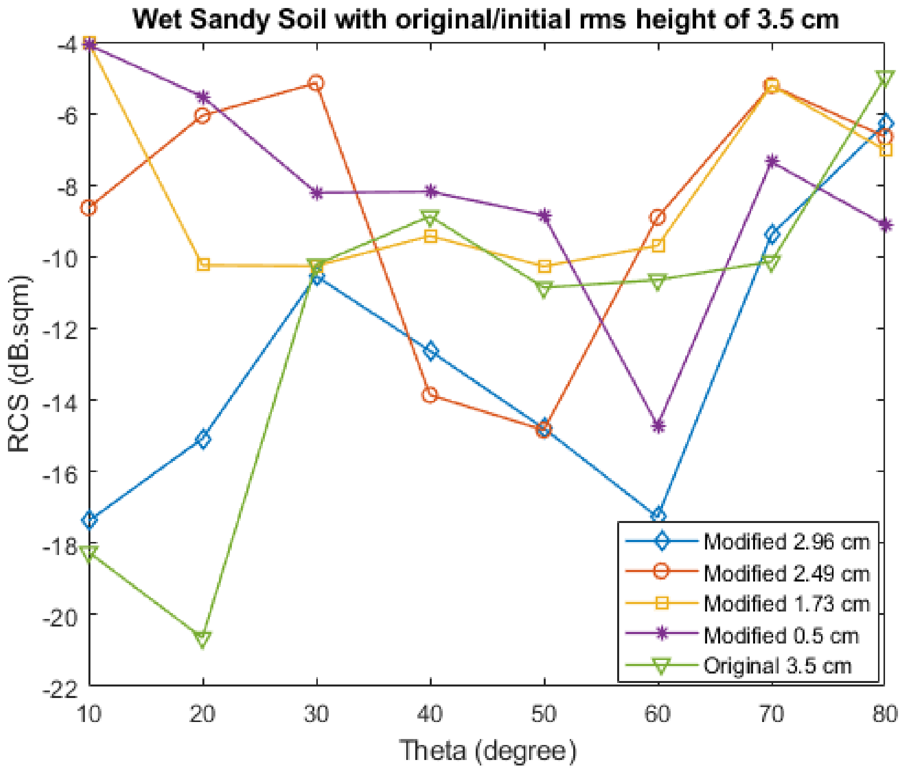

Figure 4.50: Wet Sandy soil with original rms height of 3.5cm and modified surface roughness

Now we take all the plots in Figure 4.44(a & b) into consideration. CST simulation is performed for all the seven subplots and the RCS for the various dielectrics is analysed. Figure 4.51 shows the RCS plot for both the original rough surface model as well as the modified rough surface model for a dry sandy soil. Figures 4.52 and 4.53 show similar plots for a dry sandy soil mixed with oil as well as PEC respectively. Similar to the results for the 3.5 cm rms height for these dielectrics which have already been discussed, the models with the reduced rms heights have a lower RCS compared to the initial models with original rms heights of 7.13 cm. Figure 4.54 shows the plot for wet sandy soil and like the results obtained for Figure 4.50, the modified rough surface model with a reduced rms height has a higher RCS compared to the original rough surface model with a greater rms height of 7.13cm. The implication of this is that if oil spills onto a wet rough surface like this, it will be easier to detect the oil spill if the surface is less rough than when it is rough because of the reduced RCS for a wet rough surface.

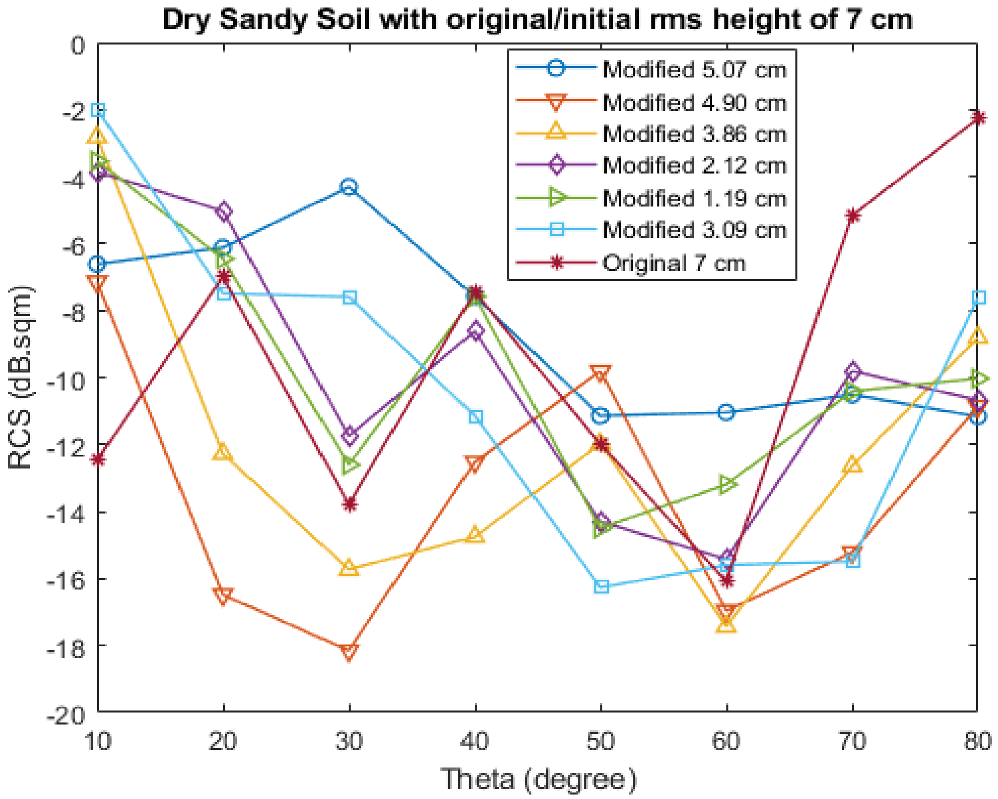

Figure 4.51: Dry sandy soil with original rms height of 7 cm and modified surface roughness

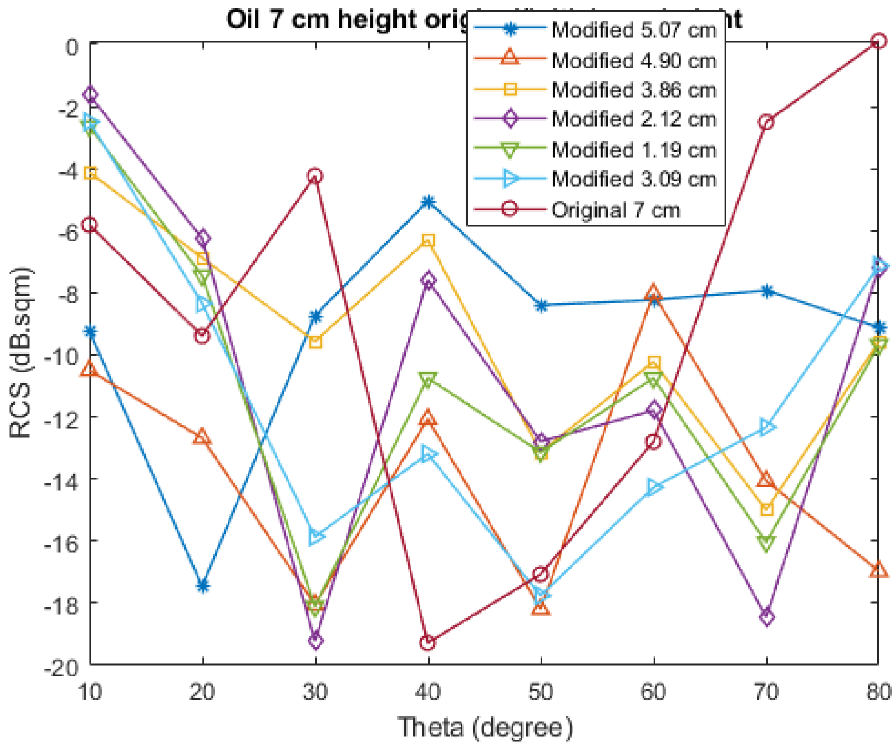

Figure 4.52: Oily sandy soil with original rms height of 7cm and modified surface roughness

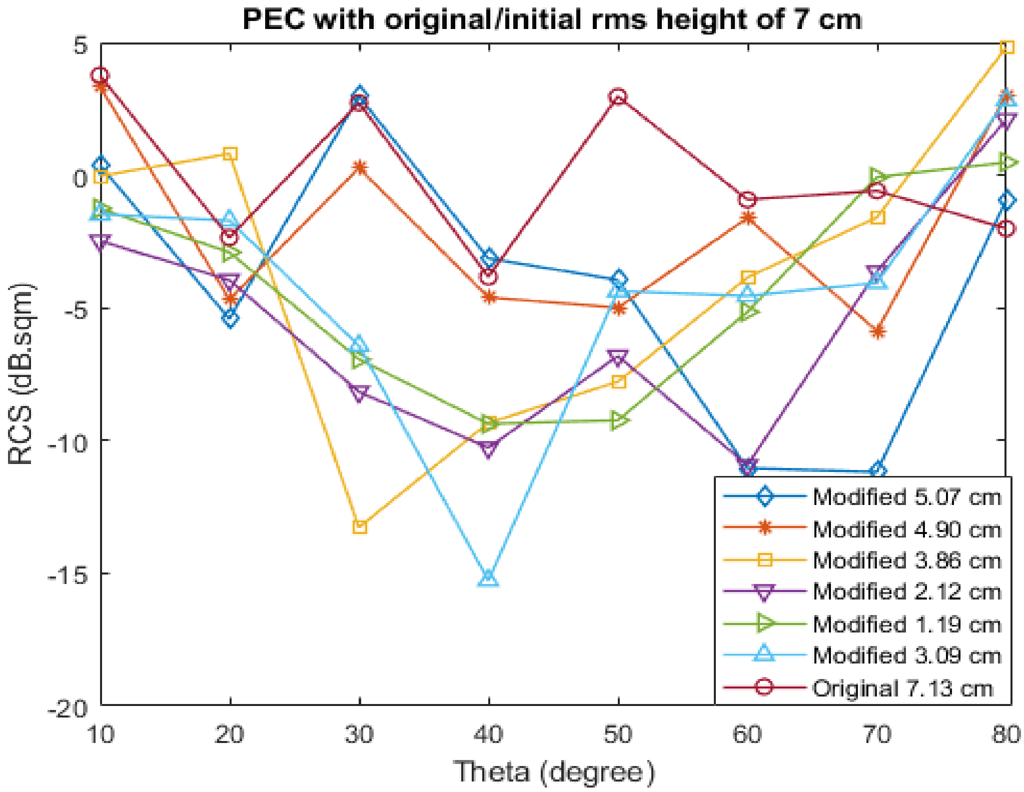

Figure 4.53: PEC with original rms height of 7cm and several modifications of the rms height

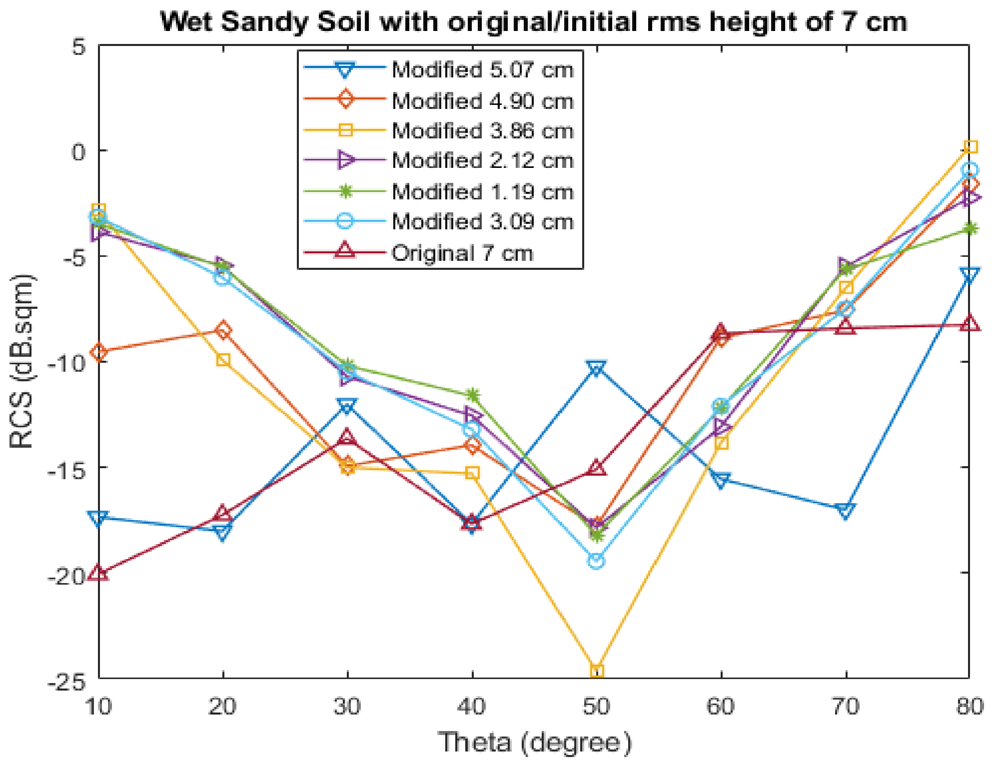

Figure 4.54: Wet Sandy soil with original rms height of 7cm and modified surface roughness

Now we shall consider the next rough surface models with an initial or original rms height of 14 cm prior to being modified and for various dielectrics as shown in Figures 4.45a and 4.45b. Figure 4.55 shows the RCS plots for a dry sandy soil for both the original and modified rms heights. Figure 4.56 shows the RCS plots for a dry sandy soil soaked with oil for both the original and modified rms heights. From both figures, we can see that the rougher the surface, the higher the RCS for both cases. The modified rough surface has a reduced rms height, therefore, the RCS is lower compared to the original rough surface with rms height of 14 cm. The implication of this is that if oil spills onto dry sandy soil, it will be easier to detect the leaks/spills if the surface is rougher, an average of about 12 dB difference from when the surface is less rough especially at high grazing angles. Figure 4.57 shows the RCS plots for a PEC for both the original and modified surface roughness while Figure 4.58 shows the RCS plots for wet sandy soil for both the original and modified rms heights. From both figures, it can be observed that the rough surface with the modified rms height has a higher RCS compared to the original rough surface with the rms height of 14 cm. The PEC at 'high' rms heights (14cm compared to 7cm and 3.5cm) behaves like a wet sandy soil surface where the RCS is higher at lower rms heights and lower at higher rms heights due to scattering.

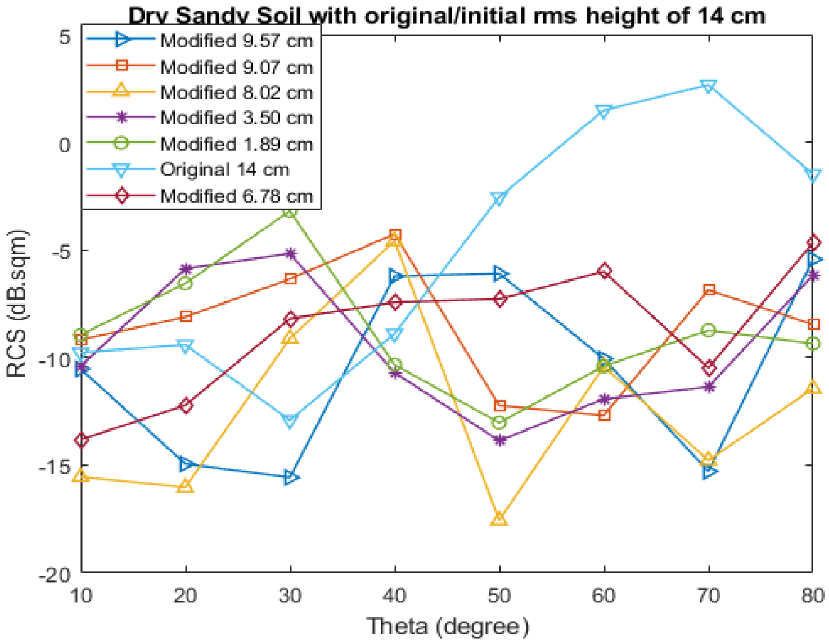

Figure 4.55: Dry sandy soil with original rms height of 14 cm and modified surface roughness

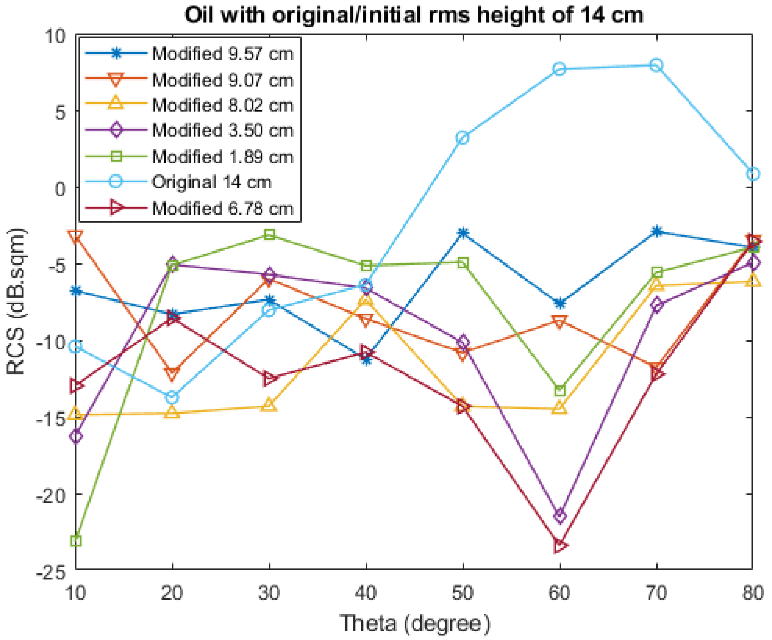

Figure 4.56: Oily sandy soil with original rms height of 14cm and modified surface roughness

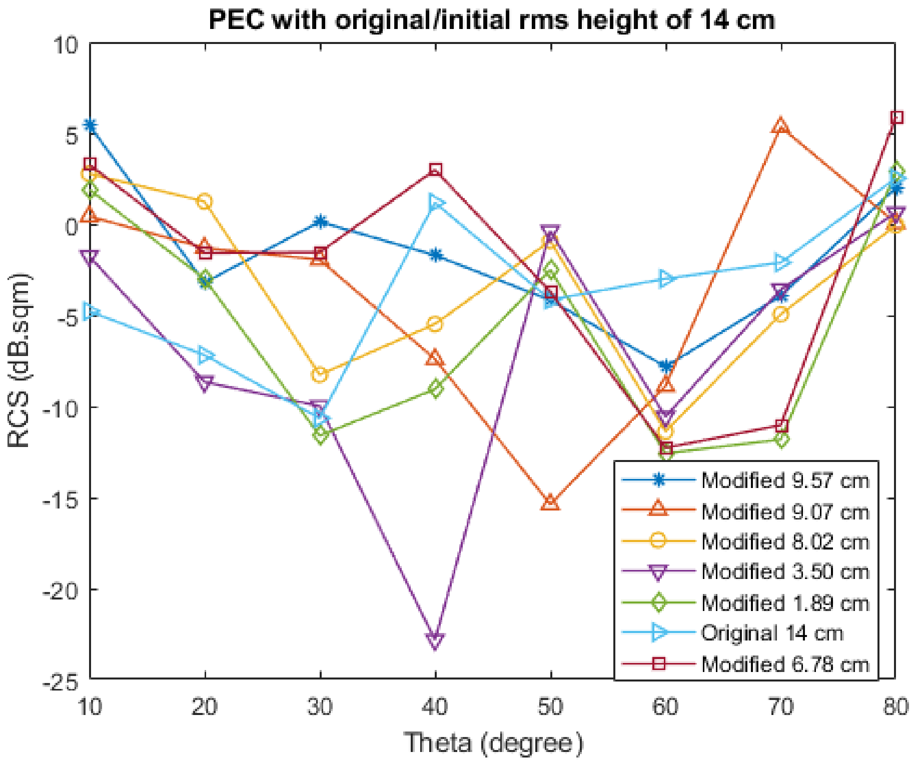

Figure 4.57: PEC with original rms height of 14cm and several modifications of the rms height

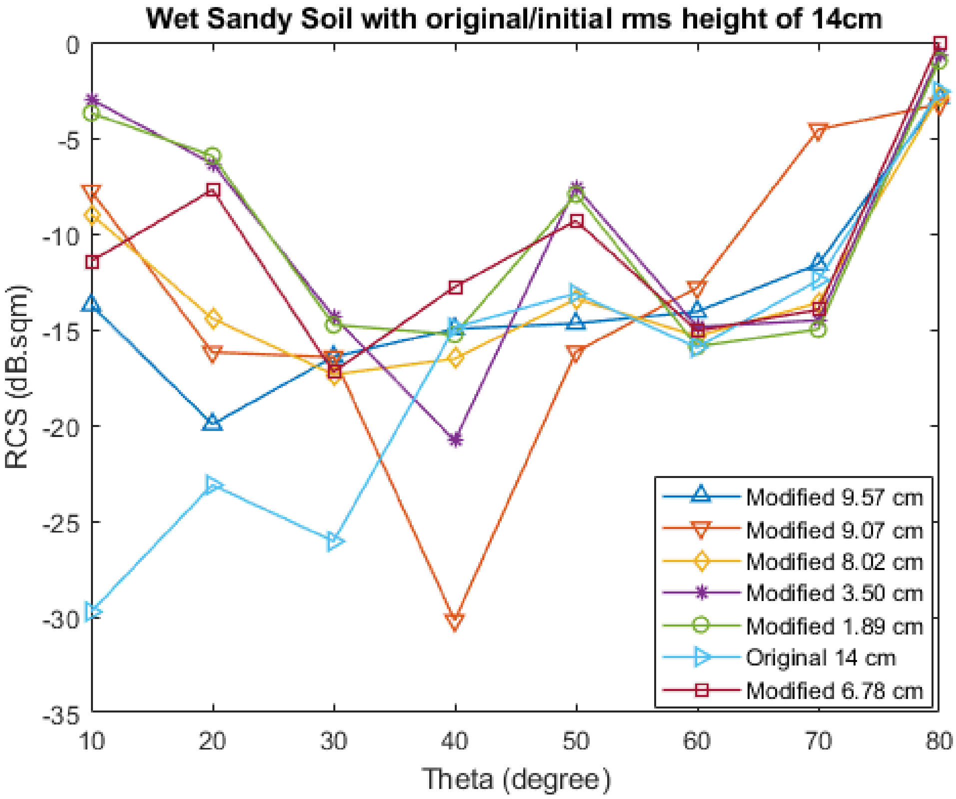

Figure 4.58: Wet Sandy soil with original rms height of 14cm and modified surface roughness

Figure 4.46 is now considered, and CST simulations have been performed for these figures. Figure 4.59 shows the RCS plots for dry sandy soil with the original and modified surface roughness. From the figure, we can see that on the average, the higher the surface roughness, the higher the RCS and vice versa. Figure 4.60 shows the RCS plots for the PEC. From the figure, we can also see that on the average, the higher the surface roughness, the lower the RCS, and vice versa. This is also similar to the results obtained for Figure 4.57. Figure 4.61 shows the plots for the Wet sandy soil. From the figure, it can also be deduced that the lower the surface roughness, the higher the RCS and vice versa. It is also worthy to mention at this juncture that the simulation for oil at 21cm did not materialise due to computing requirements and limitations in the use of CST and BlueBEAR. However, I expect the results to be like that of the dry sandy soil since they have similar dielectric constants.

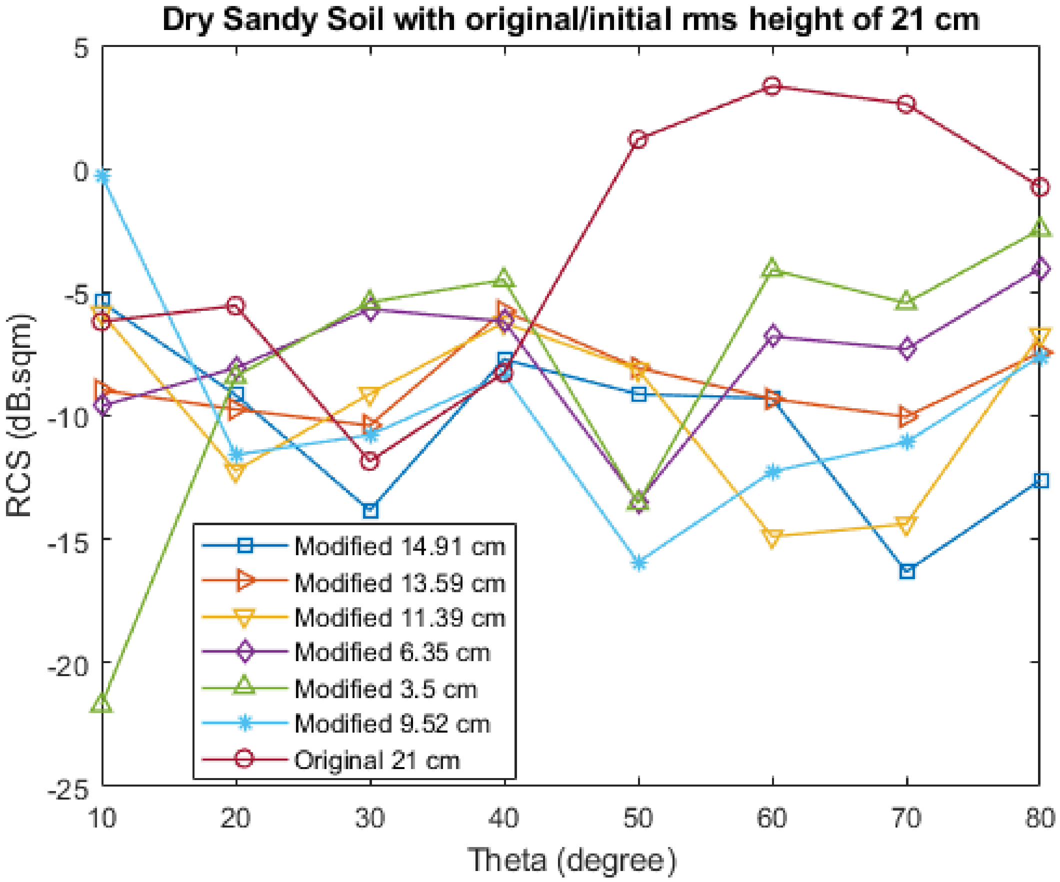

Figure 4.59: Dry sandy soil with original rms height of 21 cm and modified surface roughness

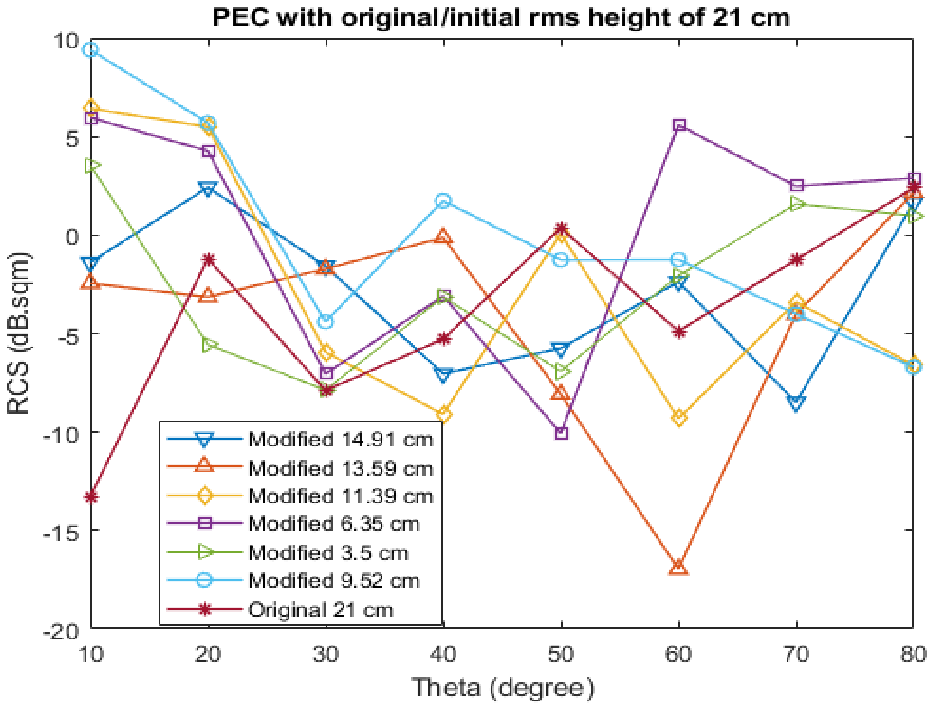

Figure 4.60: PEC with original rms height of 21cm and modified surface roughness

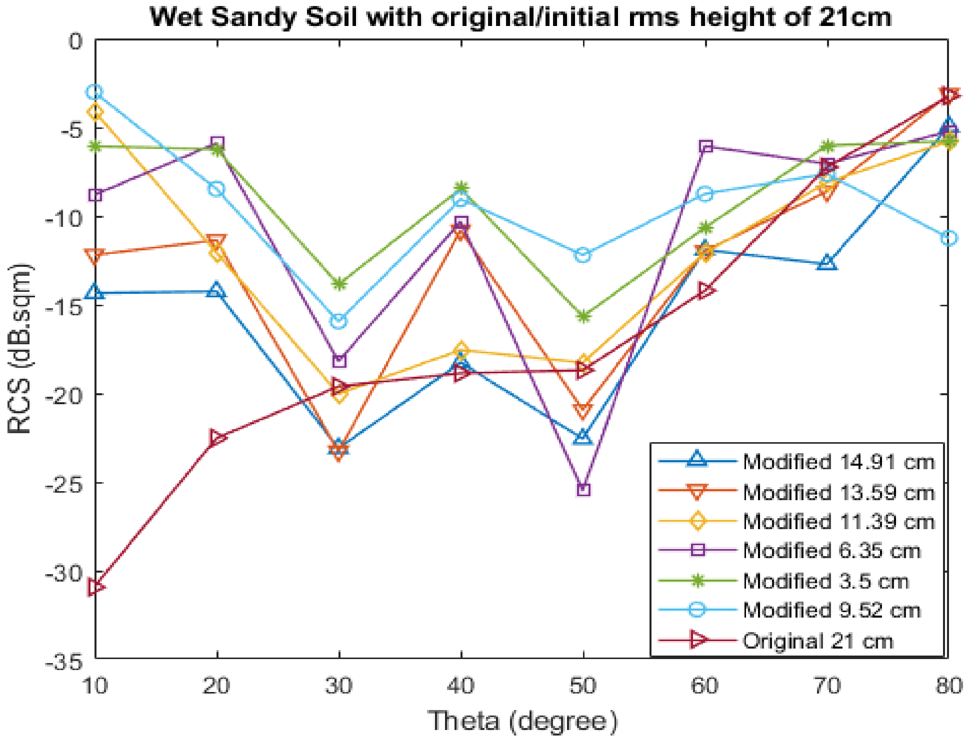

Figure 4.61: Wet Sandy soil with original rms height of 21cm and modified surface roughness

Table 4.8 shows a summary of the key findings from the various original rms heights that were modified (as a result of oil leakage) for all the various dielectrics.

Table 4.8: shows a summary of the key findings as well as the RCS trend from the modified rough surfaces for the various dielectrics

Material	**RCS Trend (Modified vs Original)**	**Max RCS (approx)**	**Min RCS (approx)**	**Key Finding**
Dry Soil (3.5 cm)	Original 3.5 cm shows moderate RCS; RCS decreases as RMS height reduces; max RCS ~ -4 dB.sqm	-4 dB.sqm (Original)	-21 dB.sqm (Modified 0.5 cm)	Higher RMS gives stronger backscatter; smoother surfaces suppress RCS
Oil (3.5 cm)	Original RCS stays highest; modified RMS (1.73 cm) shows sharp drop to ~ -30 dB.sqm	-5 dB.sqm (Original)	-33 dB.sqm (Modified 1.73 cm)	Oil makes RCS highly sensitive to RMS change; rougher profiles significantly stronger
PEC (3.5 cm)	Original maintains > 0 dB RCS; modified RMS reduces RCS; min ~ -12 dB.sqm	2 dB.sqm (Original)	-12 dB.sqm (Modified 2.96 cm)	PEC retains high RCS; smooth profiles lose reflectivity
Wet Soil (3.5 cm)	Modified RMS (2.49 cm) has highest RCS; original RCS lowest at low angles	-4 dB.sqm (Modified 2.49 cm)	-21 dB.sqm (Original)	Wet soil shows peak with certain modifications; original underperforms
Dry Soil (7 cm)	Original 7 cm peaks near 0 dB.sqm; RCS decreases with reduced RMS	0 dB.sqm (Original)	-18 dB.sqm (Modified 4.90 cm)	Dry sandy soil RCS increases with roughness even at high incidence angles
Oil (7 cm)	Original shows peak near 0 dB.sqm; others ~ -10 to -18	0 dB.sqm (Original)	-19 dB.sqm (Modified 4.90 cm)	Oil further amplifies RCS variability across RMS changes

	dB.sqm; 3.09 cm fluctuates			
PEC (7 cm)	Original RCS stable around 2-4 dB.sqm; modified values dip lower	4 dB.sqm (Original)	-15 dB.sqm (Modified 3.09 cm)	PEC maintains strong signal unless smoothed; best at original RMS
Wet Soil (7 cm)	All modified RMS values overlap; RCS suppression consistent	0 dB.sqm (Multiple)	-22 dB.sqm (Modified 5.07 cm)	Wetness consistently suppresses RCS, regardless of surface profile
Dry Soil (14 cm)	Modified 9.57 cm shows strongest RCS up to +5 dB.sqm; lower RMS leads to decline	+5 dB.sqm (Modified 9.57 cm)	-16 dB.sqm (Modified 3.5 cm)	Increased RMS boosts RCS; original sits mid-range
Oil (14 cm)	Original outperforms most modifications; 1.89 cm shows significant drop to -24 dB.sqm	+5 dB.sqm (Original)	-24 dB.sqm (Modified 1.89 cm)	Oil sensitivity to RMS is significant; smoother surfaces lose RCS rapidly
PEC (14 cm)	High variability: original stable, modified 3.5 cm drops to -20 dB.sqm	+5 dB.sqm (Multiple)	-22 dB.sqm (Modified 3.5 cm)	PEC maintains high RCS with roughness; smoother surfaces suppress response
Wet Soil (14 cm)	RCS peaks with mid-range RMS (6.78–9.07 cm); original suppressed below -10 dB.sqm	0 dB.sqm (Modified 9.07 cm)	-30 dB.sqm (Original)	Wet soil benefits from moderate roughness; original RMS performs poorly
Dry Soil (21 cm)	Original (21 cm) maintains highest RCS; 14.91 cm next strongest; others below -10 dB.sqm	+6 dB.sqm (Original)	-15 dB.sqm (Modified 6.35 cm)	Very rough dry soil maximizes radar return; smoothing reduces signal
Oil (21 cm)	Original again leads; lower RMS decreases	+5 dB.sqm (Original)	-17 dB.sqm (Modified 13.59 cm)	Oil maintains RCS strength at high RMS;

	RCS, reaching below -15 dB.sqm			lower profiles underperform
PEC (21 cm)	PEC results highly fluctuating; original 21 cm relatively stable near 0 dB.sqm	+8 dB.sqm (Modified 13.59 cm)	-15 dB.sqm (Modified 3.5 cm)	PEC's RCS peak not necessarily at highest RMS; profile shape matters
Wet Soil (21 cm)	Wet conditions suppress all RCS; original RMS shows worst values (to -30 dB.sqm)	0 dB.sqm (Modified 6.35 cm)	-32 dB.sqm (Original)	Wetness overwhelms surface profile; consistent attenuation across angles

Table 4.9 shows a summary of the average RCS difference in dB between the highest rms height and the lowest rms height for various dielectrics

Table 4.9: shows a summary of the average RCS difference in dB between the highest rms height and the lowest rms height for the various dielectrics

Dielectric Material	**Varying rms heights 3.5cm ½ m x ½ m 10° to 80°**	**Varying rms heights 7 cm ½ m x ½ m 10° to 80°**	**Varying rms heights 14 cm ½ m x ½ m 10° to 80°**	**Varying rms heights 21 cm ½ m x ½ m 10° to 80°**
PEC	5dB	8 dB	6 dB	3 dB
Dry Sandy Soil	8 dB	5 dB diff	9 dB	6 dB
Wet Sandy Soil	10 dB	5 dB	9 dB	12 dB
Dry Sandy Soil mixed with oil	12 dB	6 dB	12 dB	-

Furthermore, in these recent results, we have seen how the RCS varies with the surface roughness of our dielectric materials. Now we shall consider how the frequency we are operating at affects our RCS. From our simulations, it has been observed that the lower the surface roughness (specifically for 3.5 cm), then the impact of frequency on the RCS of our dielectric materials is inconclusive. This can be seen in Figures 4.62 and 4.63 for PEC and wet sandy soil respectively. From the figures the RCS fluctuates arbitrarily for each dielectric between 1 GHz and 20 GHz and particularly at lower frequencies. We can also see that no specific conclusion can be made across all the dielectrics, because at times the RCS increases with increase in frequency and at certain angles, while in some other instances, the RCS increases with a decrease in frequency. This inconsistency is particularly noted for all dielectrics considered as well as the degree of roughness of the surfaces of the dielectrics which is 3.5 cm.

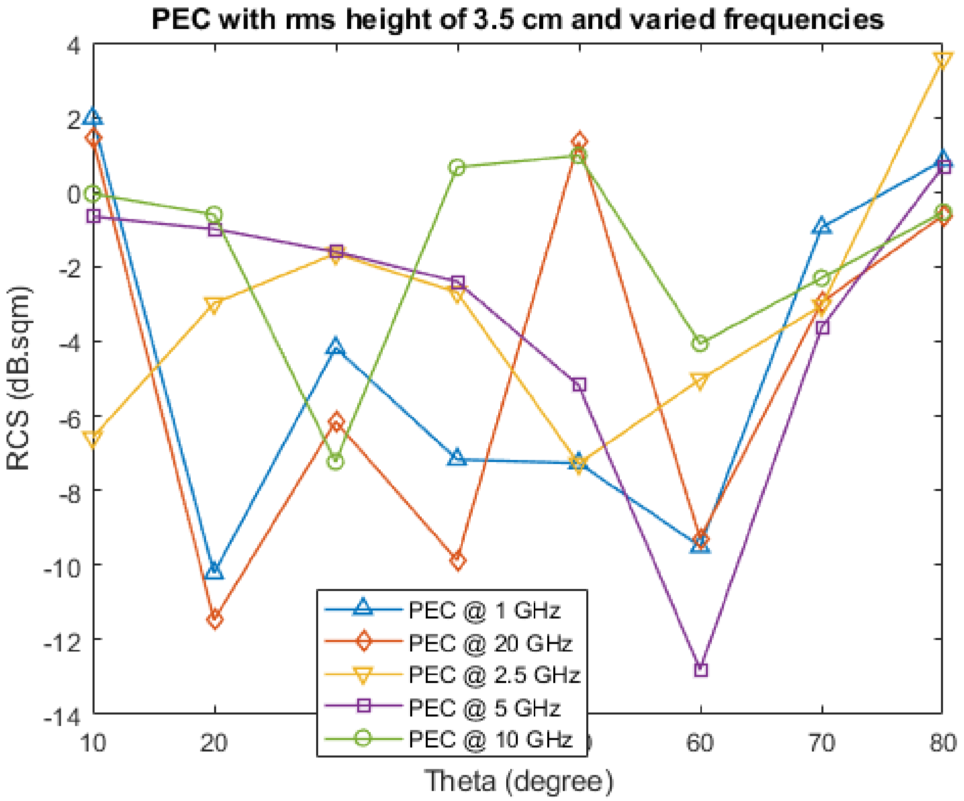

Figure 4.62: PEC with rms height of 3.5 cm and a varying frequency range

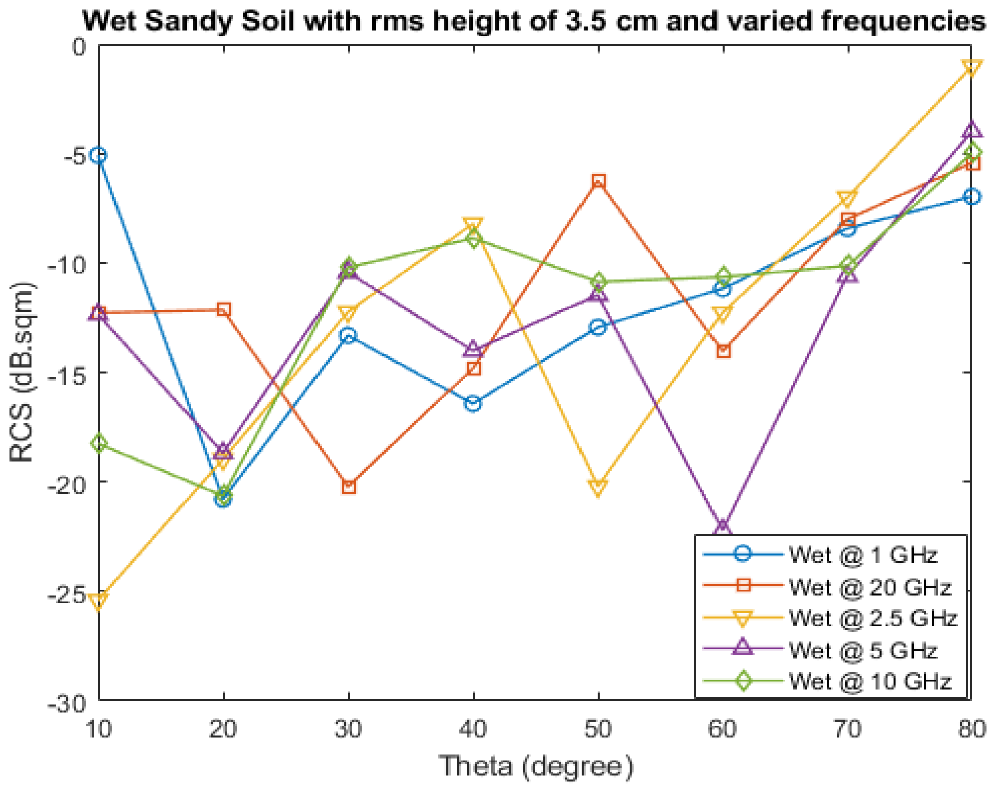

Figure 4.63: Wet sandy soil with rms height 3.5cm & a varying frequency range

Now when the surface roughness is increased to 7cm and above, there is a marked difference in the relationship between the RCS and the variation in frequency. Figures 4.64 to 4.66 show how RCS varies with frequency for a PEC, oily sandy soil, as well as wet sandy soil respectively for 7cm rms height. From the figures, we can see that the higher the frequency, the greater the RCS and vice versa. The frequencies used varied between 1 GHz and 20 GHz.

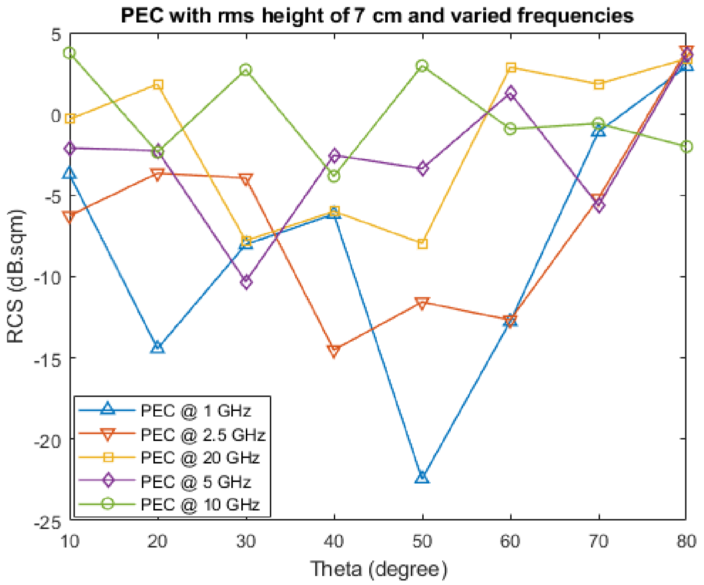

Figure 4.64: PEC with rms height of 7 cm and a varying frequency range

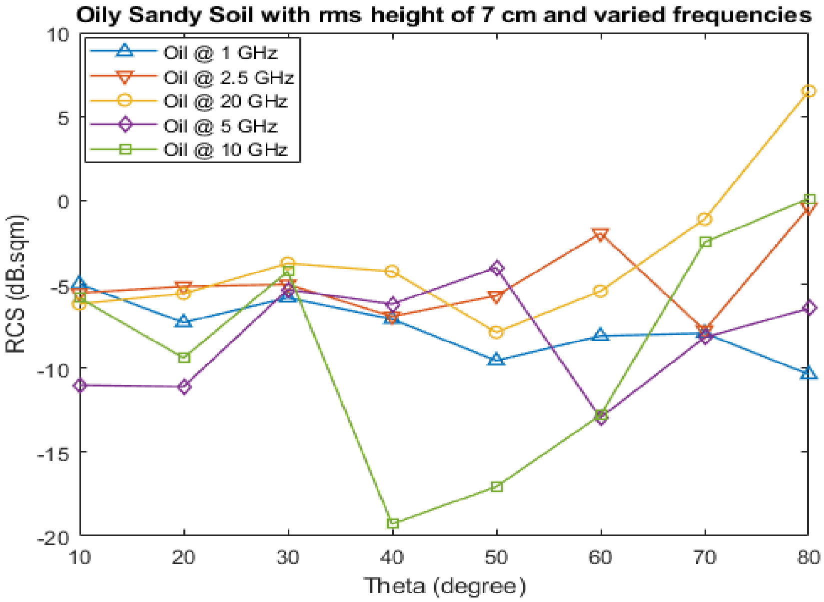

Figure 4.65: Oily sandy soil with rms height 7 cm & a varying frequency range

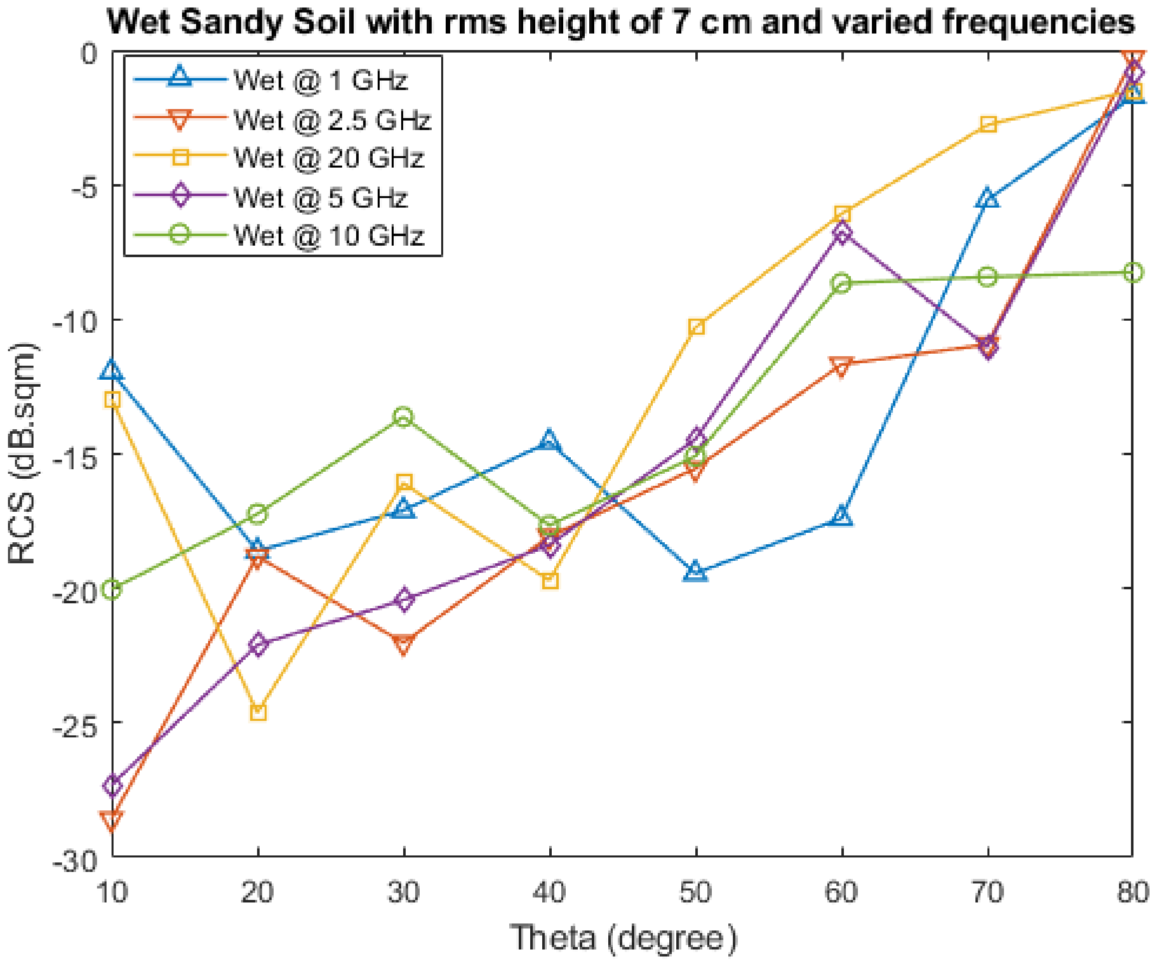

Figure 4.66: Wet sandy soil with rms height 7 cm & a varying frequency range

The implication of this is that when we operate at higher frequencies for very rough surfaces i.e. from 7cm and above, it will be easier to detect oil spills and leaks from that rough surface than if we operated at lower frequencies. Figures 4.67 to 4.70 show the relationship between the RCS and varying frequency for 14cm rms height for all dielectrics. Due to computational restrictions, we were not able to simulate 20 GHz for the oily sandy soil surfaces and therefore not included in the analysis.

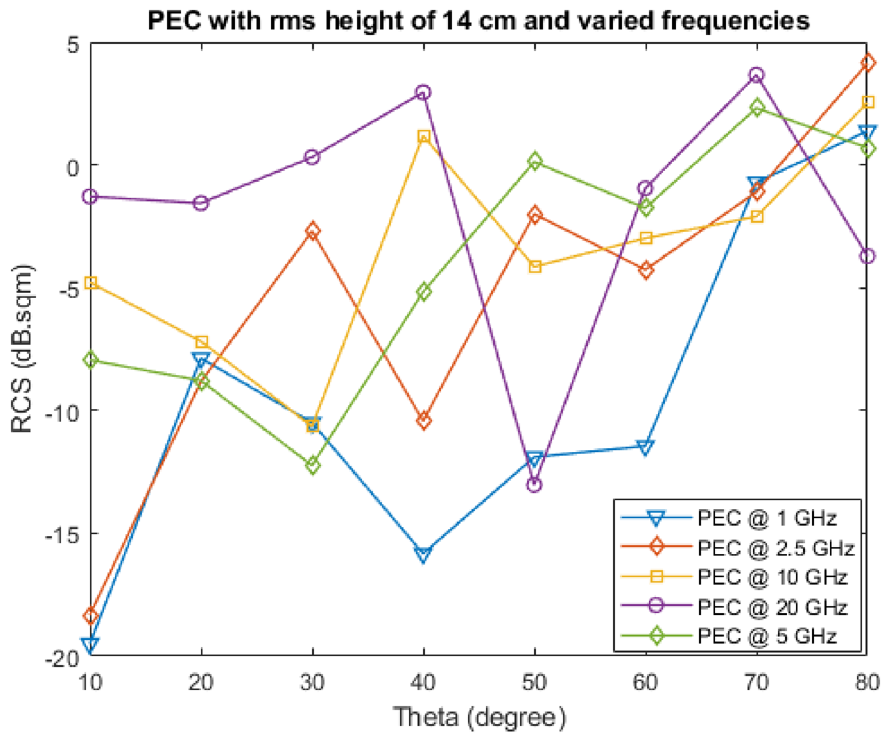

Figure 4.67: PEC with rms height of 14 cm and a varying frequency range

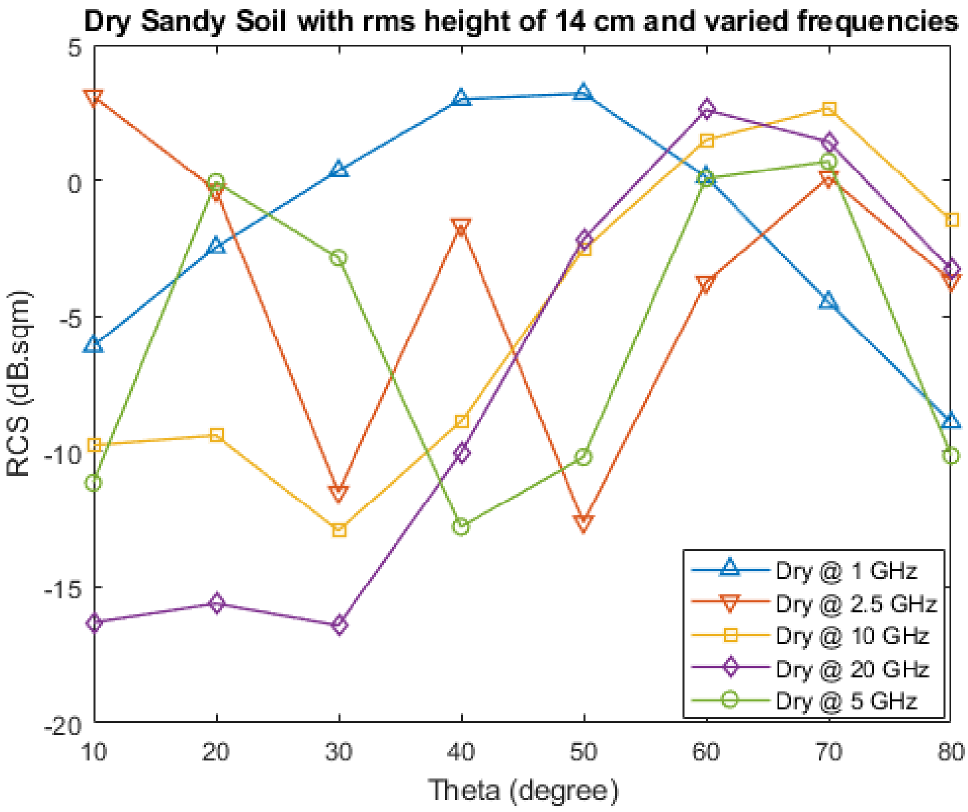

Figure 4.68: Dry sandy soil with rms height 14 cm & a varying frequency range

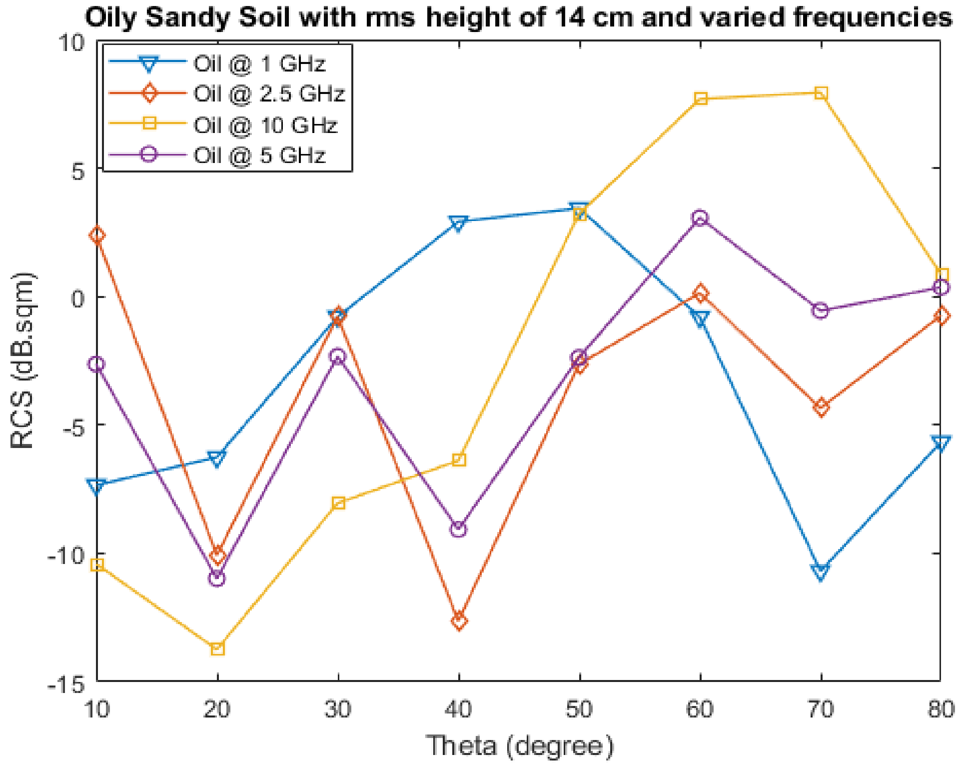

Figure 4.69: Oily sandy soil with rms height 14 cm & a varying frequency range

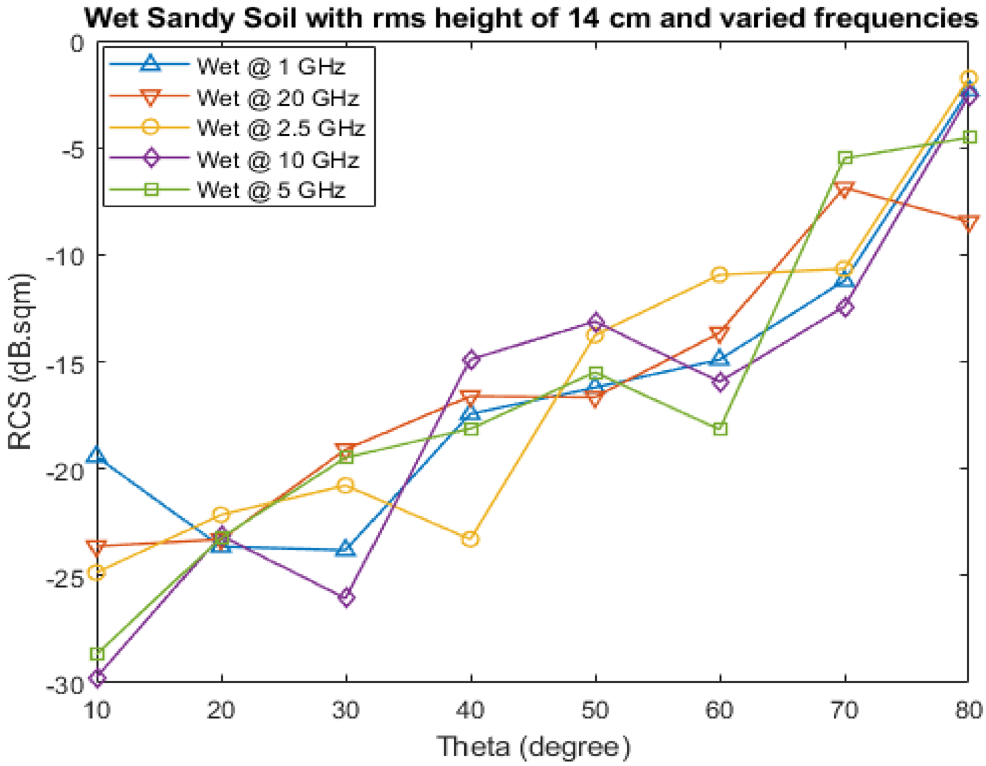

Figure 4.70: Wet sandy soil with rms height 14 cm & a varying frequency range

Now we shall look at how the RCS varies with frequency for a rough surface with rms height of 21cm. Figures 4.71 to 4.73 show how RCS varies with frequency for PEC, dry sandy and wet sandy soils. Due to computational restrictions for such heavy models at 21 cm, simulations at 20 GHz were only performed for PEC. Therefore, the analysis involving other dielectrics will stop at 10 GHz. The frequency used was between 1 and 20 GHz for PEC. From the figures, we can see that the higher the frequency, the greater the RCS and vice versa.

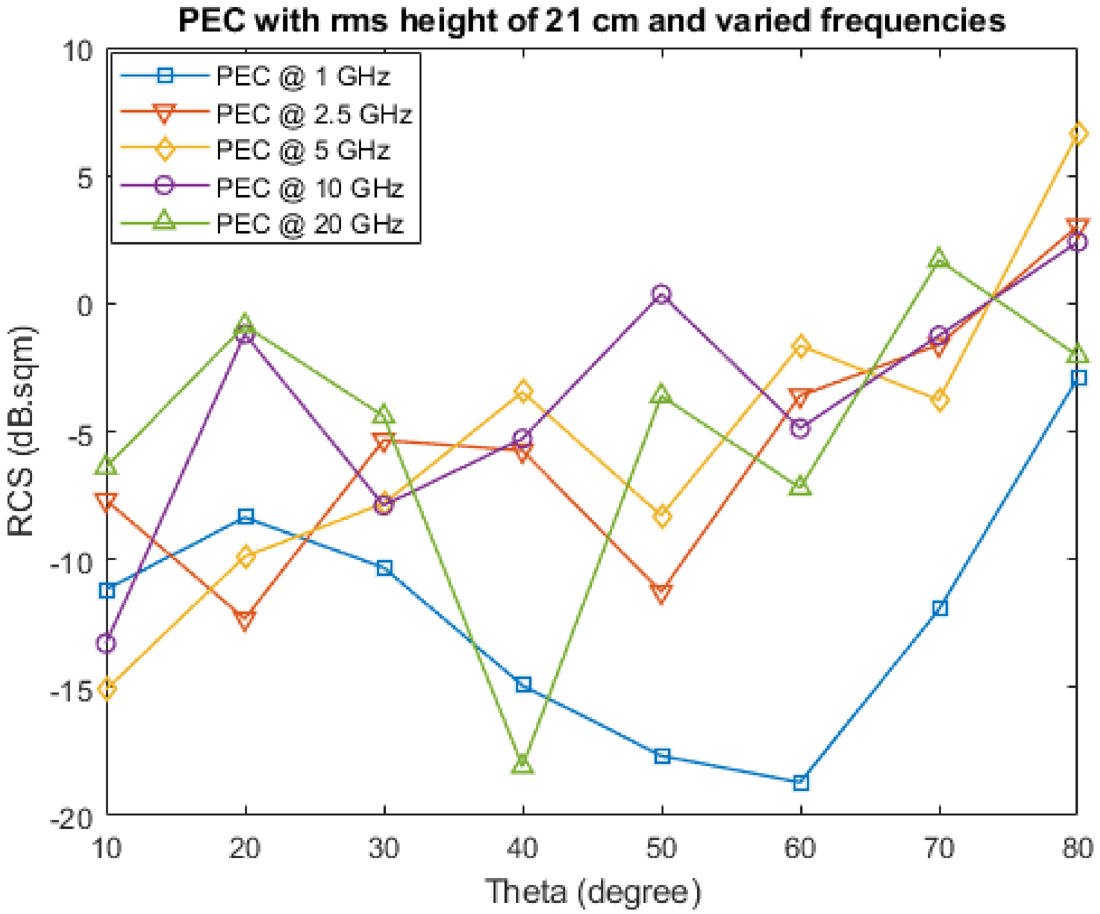

Figure 4.71: PEC with rms height of 21 cm and a varying frequency range

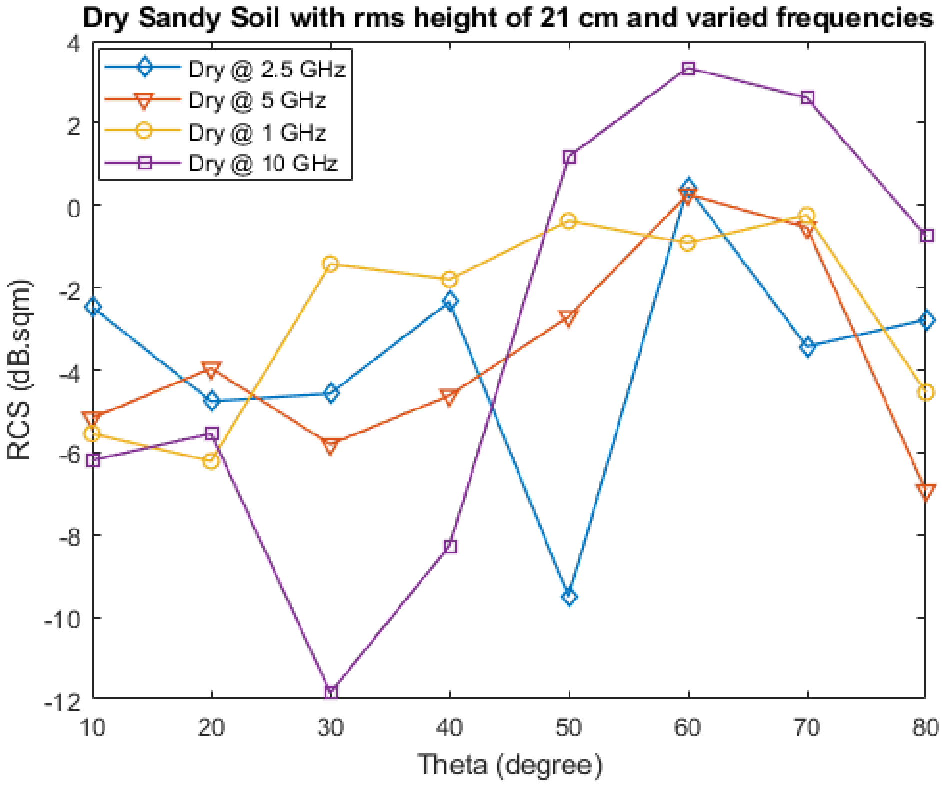

Figure 4.72: Dry sandy soil with rms height 21 cm & a varying frequency range

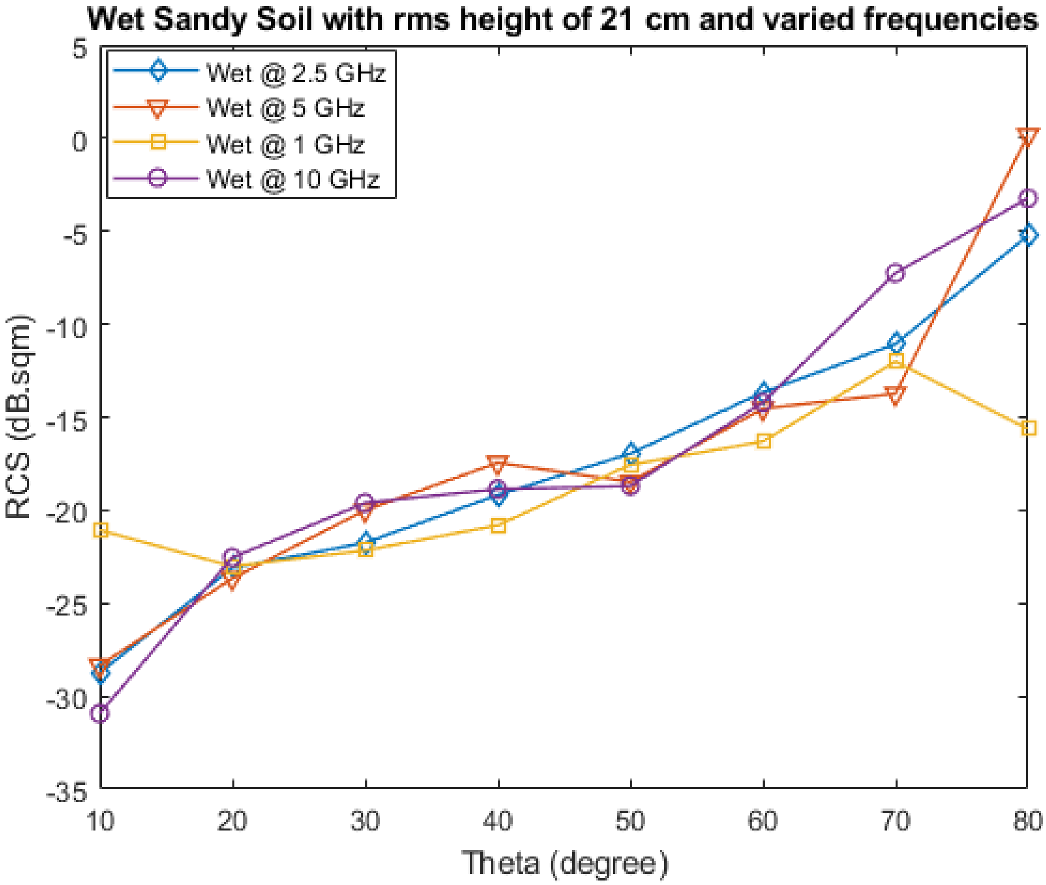

Figure 4.73: Wet sandy soil with rms height 21cm & a varying frequency range

Table 4.10: shows a summary of the average difference in magnitude between the highest frequency and the lowest frequency for the various dielectrics

Dielectric Material	**Varying freq for 3.5cm ½ m x ½ m 10° to 80°**	**Varying freq for 7 cm ½ m x ½ m 10° to 80°**	**Varying rms heights 14 cm ½ m x ½ m 10° to 80°**	**Varying rms heights 21 cm ½ m x ½ m 10° to 80°**
PEC	Inconclusive	8 dB	6 dB	10 dB
Dry Sandy Soil	--	6 dB	7 dB diff	5 dB
Wet Sandy Soil	5 dB	4 dB	5 dB	6 dB
Dry Sandy Soil mixed with oil	-	11 dB	10 dB	-

4.8. Summary

In this chapter, we have looked at the theoretical and analytical development of a rough surface model, as well as the mathematical equations leading to the creation of a random rough surface. Preliminary simulation results of the rough surface model have been extensively discussed and thoroughly analysed. The RCS analysis of common objects like a flat plate or sphere have also been calculated as well as its implications. Taking it a step further, the RCS analysis for a lossless rough surface e.g. PEC was also calculated and extensively analysed. The results obtained tallies with what is obtainable in literature. Furthermore, the RCS analysis of a lossy rough surface e.g. sandy soil was also calculated and thoroughly analysed. The dielectric parameters of sand were defined and utilised in the simulation. The results show a trend or relationship between the roughness of a lossy surface and the reflectivity from a rough surface. Other parameters such as frequency as well as its relationship with the reflectivity from a rough surface was also discussed and its implications extensively analysed. It is noteworthy to also mention that the results of the parameters (such as correlation lengths, rms heights etc) after simulation agreed in principle with the parameters of the rough surface model prior to simulation which implies these results can be relied upon. Finally, the RCS of various dielectric materials was extensively analysed and discussed. As envisaged, the RCS for larger surface areas was higher compared to smaller surface areas. Also, the RCS increased as the angle of illumination increased and vice versa. Similarly, as the number of surface points increased, the RCS decreased and vice versa. Some of the results in this section also indicate that as we fill up the surface with oil, the reflectivity decreases by a lot i.e. about 5 dB for a 7 cm rough surface and about 10 dB for a 14 cm rough surface.

Chapter 5. EXPERIMENTAL PLAN / SET -UP

In the experiment, the radar cross section (RCS) of rough surfaces specifically sandy soil samples have been studied at microwave frequencies, specifically at 10 GHz and much later at 24 and 77 GHz. The measurements were characterised by measuring the ratio of the reflected signals from a reference target (e.g. a sphere or corner reflector) at first before measuring the ratio of the reflected signals from the dry soil sample. The effect of obscurants such as water or /and oil on the RCS or reflectivity of the soil sample was also measured and analysed. The measurements were compared to theoretical models (where obtainable), and they demonstrated a reasonable agreement. Water is the most common obscurant in both indoor and outdoor applications, but vegetable oils (with different dielectric properties) was also used as an obscurant. The essence of using vegetable oils is to mimic the reflectivity of typical oil from sandy soil when it is now perhaps soaked with refined Premium Motor Spirit (PMS) leaking out of a network of pipelines. The ultimate essence of this work is for my radar to be able to measure and analyse the differences in the RCS of a soil surface with oil (probably emanating from oil leaks/spills from pipelines) as well as another soil surface without oil with a view to detecting oil leaks/spills in pipeline infrastructure real-time. These experiments concentrated on the different levels of reflectivity obtained from different volumes or quantities of oil mixed with the soil sample. The reflectivity obtained when oil and water are also mixed and contained in a soil sample will also be investigated and analysed. When oil is contained in a soil sample, and depending on the roughness of the soil, the RCS results showed poor reflectivity because of the dry lossy rough surface and this reflectivity increased with increase in volume or quantity of oil or water being introduced or added to the soil sample. The results also showed higher signal reduction with increasing frequency for a dry soil sample because of scattering and back reflections from the dry lossy rough surface. Furthermore, for a dry soil sample mixed with water or oil, the reflectivity at increasing frequency increased with corresponding increase in the volume or quantity of oil or water being added to the sample. For outdoor experiments, the performance of the radar sensors in terms of obtaining the reflectivity in the presence of different contaminants like mud, grit, leaves etc. as well as various weather conditions like rain, fog, snow etc. has also been investigated and discussed.

5.1. Measurement Methodology

The measurement methodology is based on the direct implementation of the radar principle i.e. considering explicitly the ratio of the signal strength reflected from a reference target or the soil sample (with or without oil/water) without obstructing the signal received at normal incidence. The coefficient of the surface was measured first after calibrating the sphere (or corner reflector), before starting the actual measurements. A rough sketch of the measurement setup is as shown in Figure 5.1. The monostatic radar consisting of collocated transmit and receive antennas is positioned vertically and is pointing downwards. The transmit and receive signals are shown by P_t and P_r in Figure 5.1. A reference target – a corner reflector – with a known RCS was characterised prior to commencing the measurements with the soil sample. A sample of the sandy soil surface is placed on a holder (as shown) and placed under the monostatic radar in the path of the signal. A sample holder (in my case a flat tray made of plastic) that is sufficiently rigid to provide a stable and robust platform and does not sag under the weight of the sample was provided. This was also replaceable after each measurement (in scenarios or cases where different soil samples with peculiar characteristics are to be investigated). Other important characteristics for the sample holder are low reflection and low attenuation of the signal that require having a thickness equal to an integer of half–wavelength, low refractive index, and low loss tangent. After the initial measurements where the antenna is perpendicular to the soil sample, the dry sandy soil sample which is placed/laid flat on the sample holder also has the antenna ultimately rotated in such a way that the direction of propagation of the signal or the grazing angle will vary from 0° to 90° with respect to the stationary/flat surface using a spirit-level & protractor to correctly change these angles. So, at first, initial measurements will involve the antenna been placed at 90° (perpendicular to the surface), about 45° and at 5° (almost parallel to the surface) in such a way as not to obscure the radar beam. Subsequent measurements will be then made in graduations of 10°

for each measurement. The area that the sample needs to cover should be greater than the footprint of the illuminating beam, defined by the 3-dB roll-off of the radiation pattern, to guarantee that most of the energy gets to the soil sample. An advantage of this simple setup (as described in Fig. 5.1) is that different soil samples (based on different roughness parameters as well as sizes of sand particles, also different soil classes/types) can be introduced without requiring further alignment.

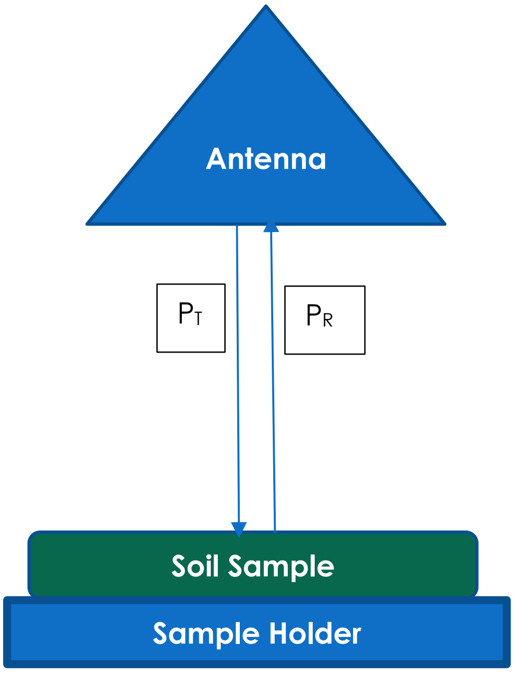

Figure 5.1: General Measurement set-up for the radar reflectivity analysis of sandy soil

The measurements were conducted using the radar equipment and systems in the laboratory. The specifications and suitability of the Vector Network Analysers (VNAs) as well as the antennas were extensively analysed and thoroughly assessed prior to the commencement of the experiment. The possible risks in the measurement setup as well as the suitability of the measurements for the entire experiment were conducted, thoroughly assessed, and subsequently approved. Excerpts from these risk assessments have been attached to the appendix in this thesis.

Reflection coefficient or RCS measurements are sensitive to surface roughness. One of the challenges encountered in this experimental phase of the project or the measurements especially for the outdoor scenario was to quantify the impact of evaporation on the oil or water that would have diminished if the RCS measurements were conducted over a longer period (say over an hour), as the volume or quantity of water or oil present in the soil sample should have an effect on the reflectivity been measured or analysed.

The expected process of water (or oil) evaporation during multiple outdoor measurements will change the RCS values and should be taken into consideration during analysis. The disparities in the RCS measurement results for indoor scenarios should not be so evident but should be technically similar, compared to the outdoor measurements and analyses [107].

The measurement results from the experiment would also be thoroughly analysed and extensively discussed as we progress in this thesis. The RCS of the soil sample can also be obtained by utilising Equation 5.1 below:

$$RCS_{Sample}(dB) = Theoretical\ RCS_{Ref} - Experimental\ RCS_{Ref} - Experimental\ RCS_{Sample} \tag{5.1}$$

5.2. Calibration of Experimental Set – Up

In terms of calibration, preliminary calibration was conducted using the portable Field Fox VNA (N9918A) and two horn antennas (transmit and receive) facing the object that would be used for calibration, in this case, a sphere with a defined radius. Figure 5.2 shows the setup used for this preliminary calibration with a sphere of 13.35cm radius placed on an area of 3.6m x 3m which is the area of illumination categorised for this purpose. The horn antennas are wideband antennas with a gain range of approximately 1.3 to 12.8 dBi depending on frequency. For this research, they were operated at a gain of 8.1 dBi, corresponding to a frequency of around 10 GHz with a 3dB beamwidth of between 40° and 60° for both E and H planes. The specification sheet for the antenna has been attached to the appendix which provides further details. Three spheres were used in the preliminary calibration at different times and the reflectivity of the sphere obtained via experiment or calibration was compared to the cross-sectional area of the target (in this case the sphere). The values of reflectivity obtained from experiment agreed with the theoretical values of the cross-sectional area for these spheres.

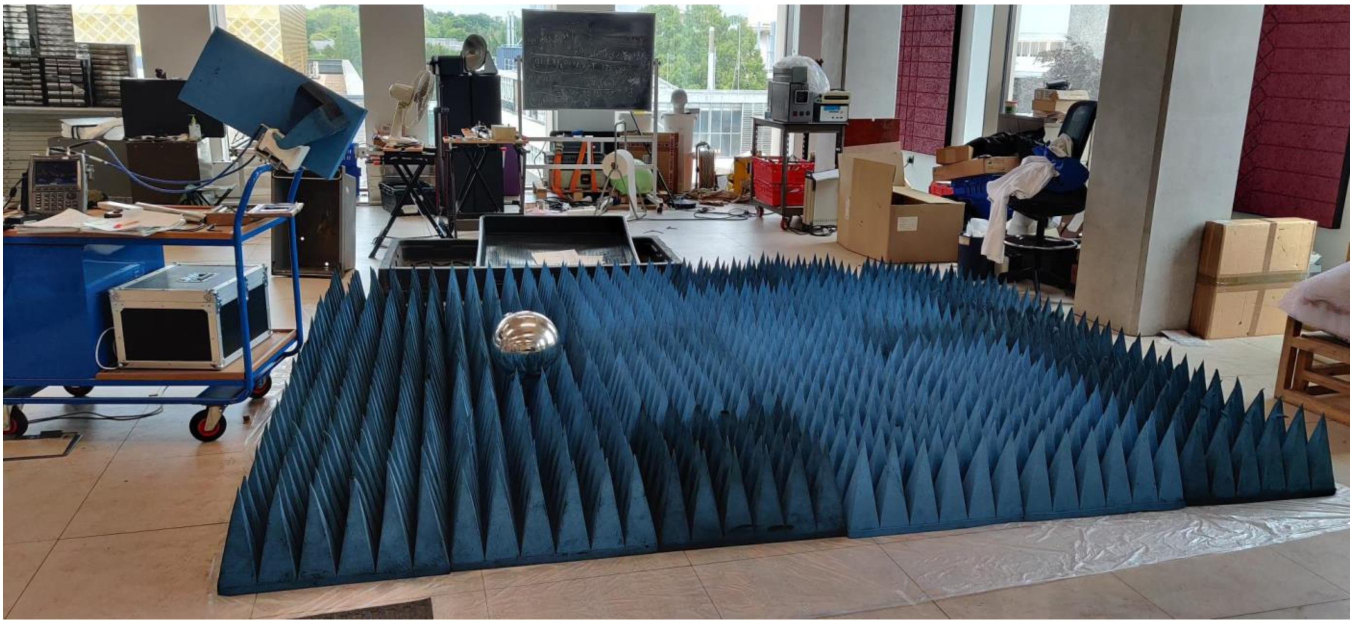

Figure 5.2: Experimental layout for Preliminary Calibration

From the experiment and using a sphere of radius 13.35 cm, the S21 parameter which is the ratio of the received power P_R to the transmit power P_T is about - 60.5 dB as shown in Figure 5.3. The distance between the antenna and the sphere is about 1.03m and using the parameters earlier described for the antenna and the VNA, then the cross-sectional area of the sphere can be calculated using the radar equation and calculating for the cross-sectional area as shown in Equation 5.2.

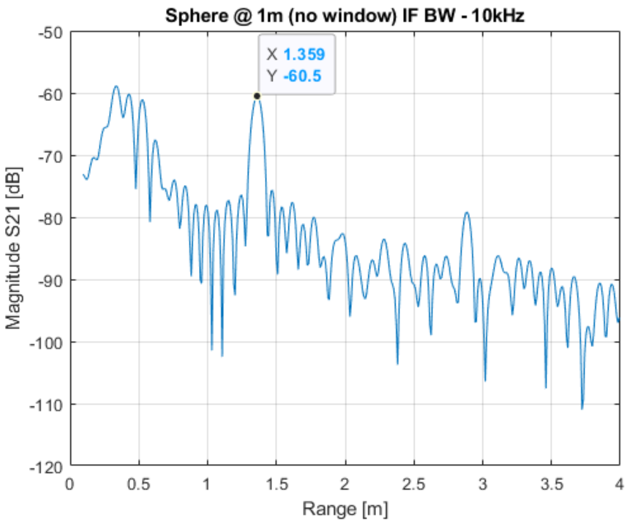

Figure 5.3: 13.35cm sphere at 1.03 m from the antennas and IF BW of 10kHz

$$\sigma = \frac{P_R(4\pi)^3 f^2 R^4}{P_T C^2 G^2} \tag{5.2}$$

From the above calculation, the cross-sectional area of the sphere is therefore obtained to be **– 12.75 dBsqm**. The distance between the antenna and the sphere was also increased to about 3m and the cross-sectional area of the sphere obtained at this distance of 3m was about **– 12.2 dBsqm**.

To calculate the RCS theoretically, the RCS of a sphere is given by Equation 5.3 as

$$\sigma = \pi r^2 \tag{5.3}$$

where r is the radius of the sphere and given as 13.35 cm. From Equation 5.3, the theoretical cross-sectional area of the sphere is therefore obtained to be **– 12.52 dBsqm** which is very similar to the experimental RCS calculated for the same sphere for both a 1m and a 3m distance from the antenna.

For a radius of sphere 6.15cm, the S21 parameter i.e. the ratio of P_R to P_T was obtained to be about – 69.08 dB for a distance of 1.11m between the antenna and the sphere as shown in Figure 5.4.

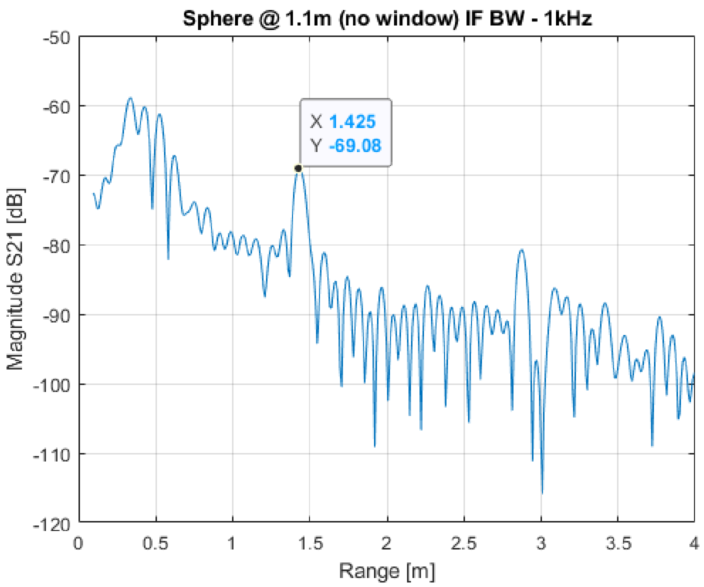

Figure 5.4: 6.15 cm sphere at 1.11 m from the antennas and IF BW of 1 kHz

This ratio was also obtained to be about – 85.34 dB for a distance of about 3m between the antenna and the sphere. By using equation 5.2 again, the RCS of the sphere was obtained to be about **– 20.03 dBsqm** and **– 19.02 dBsqm** respectively. When these values are compared to the theoretical cross-sectional area of the sphere using equation 6.3, the values are quite similar as the theoretical cross-sectional area of the sphere is obtained to be about **– 19.25 dBsqm**. Calibration using targets with known RCS will help us in the actual experiment.

For a much smaller sphere of radius 3.2 cm, the ratio of P_R to P_T was obtained to be about – 76.60 dB for a distance of 1.2m between the antenna and the sphere as also shown in Figure 5.5. Using equation 5.2, the RCS of the sphere is therefore obtained to be **– 26.2 dBsqm**. The theoretical RCS value obtained from equation 5.3 is **– 24.9 dBsqm**. When these two values are compared, we can see that it gives a very close correlation which implies the calibration can be relied upon and the experiment can thus be conducted.

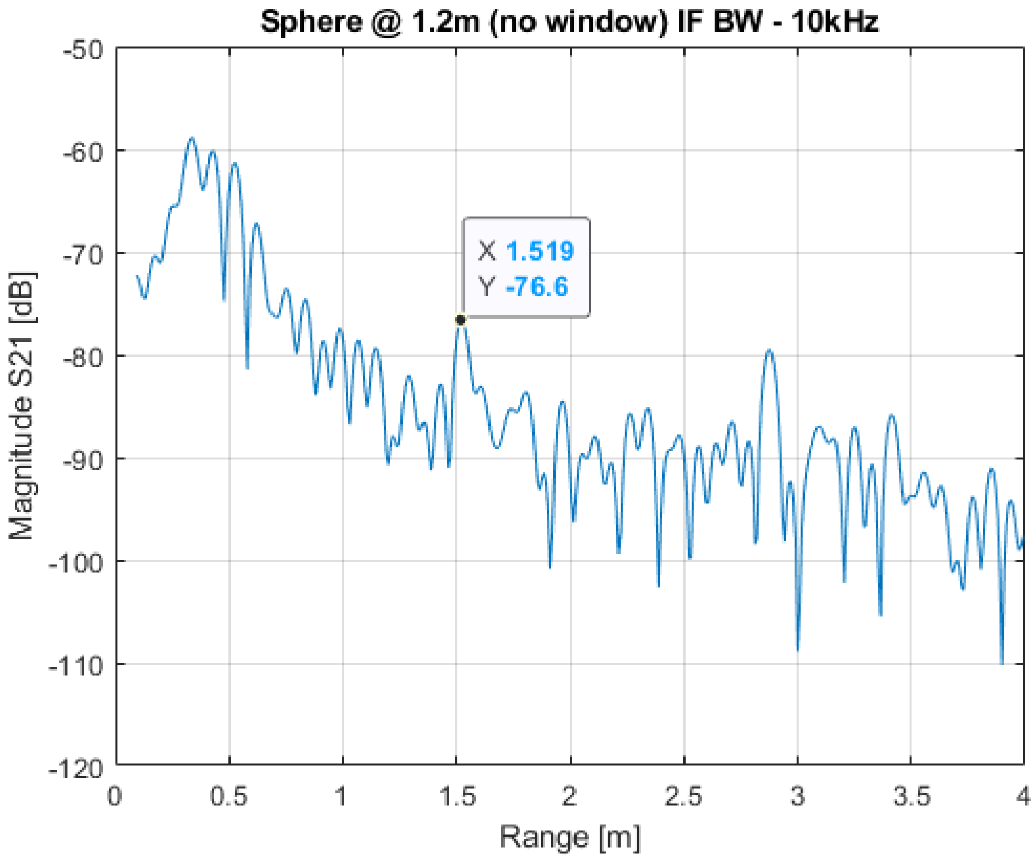

Figure 5.5: 3.2 cm sphere at 1.2m from the antennas and IF BW of 10 kHz

It is pertinent at this juncture to state that the value for S21 obtained for the various spheres and at the various distances was an average of at least ten repeated measurements for each scenario and the values from these measurements were closely related prior to being averaged. Thus, the average obtained for the S21 parameters in each case is correct and can be relied upon for the experiment.

Table 5.1 shows the calibration results for spheres of different dimensions as well as the values obtained when the RCS is calculated theoretically. From this Table, we could see that both experimental and theoretical RCS values align with each and in line with what's expected. The distance between the sphere and the antennas is about 1.20m and the S21 parameter is obtained for spheres of different radii from which the experimental RCS is calculated.

Table 5.1: Calibration results for spheres of different dimensions

Radius (cm)	**Range (m)**	**S21 (dB)**	**RCS (dBsq.m) Experimental**	**RCS (dBsq.m) Theoretical**
23.80	1.25	- 59.07	- 7.96	- 7.50
17.10	1.20	- 60.82	- 10.42	- 10.37
13.35	1.25	- 63.84	- 12.73	- 12.52
6.75	1.20	- 66.68	- 16.28	- 18.44
6.15	1.20	- 68.00	- 17.59	- 19.25

From the figures in Fig. 5.3 – 5.5, Gaussian windowing is applied to each of these figures to assist with a bit of filtering of these calibrated signals. The Gaussian window applied to the calibrated reduces the magnitude of the signals but makes the calibrated signals smoother and more useful for our analyses. Figures 5.6 - 5.8 show when Gaussian window has been applied to the calibration setup for Figures 5.3 - 5.5 respectively.

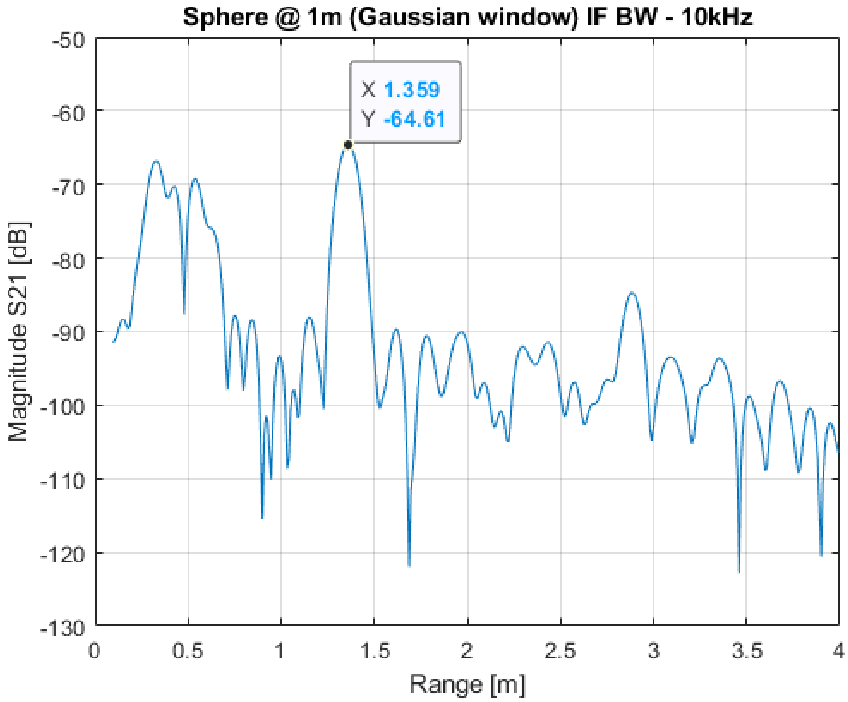

Figure 5.6: 13.35cm sphere 1.03m from antennas - Gaussian window applied

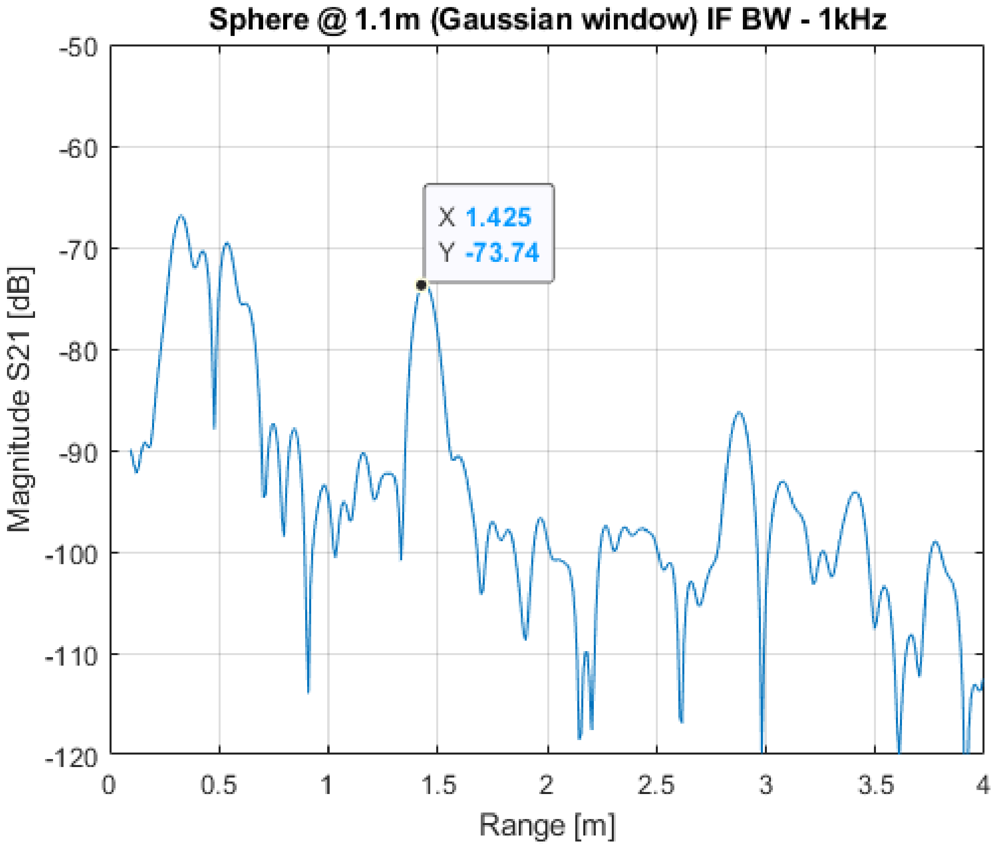

Figure 5.7: 6.15cm sphere 1.11m from antennas - Gaussian window applied

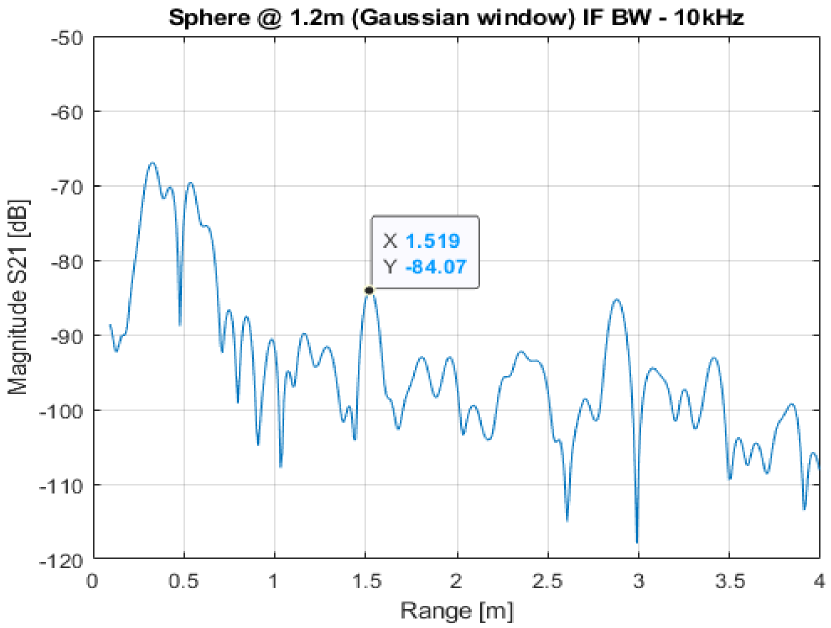

Figure 5.8: 3.2cm sphere at 1.2m from antennas - Gaussian window applied

5.3. Measurements using the 3 Rough Surface Profiles in Oil

Now in continuation of the experiment, three rough surface profiles were developed so they can be used to mimic a rough surface on a sandy soil for the experiment. To accurately replicate rough surfaces on sandy soil for the experiment, three distinct rough surface profiles were designed using CAD software, corresponding to rms roughness heights of 3.5 cm, 7 cm and 14 cm, as shown in Figures 5.9 – 5.11. Each profile was modelled as a repeating triangular wave pattern with precise dimensions to ensure consistency in amplitude and wavelength. These CAD models were then fabricated into physical prototypes using 3D printing and laser cutting techniques, which were subsequently applied to trays filled with sand to imprint uniform roughness patterns. To verify that the intended roughness was achieved, ground-truth measurements were conducted using vernier callipers and profilometers to confirm that the height of the peaks and valleys matched the designed specifications (e.g. 35.07 mm, 70.13 mm, and 139.99 mm). Additional visual inspections and repeatability tests were performed to ensure that the profiles remained consistent across multiple trays. This approach provided a reliable and controlled method for generating uniform surface roughness, enabling the experiments to be repeatable and the results to be trustworthy. Therefore, comparison could be made between experimental and theoretical (simulation) outcomes, ensuring a robust validation process and the results can be relied upon. The oil which would now be introduced at various levels and quantities for all the surface profiles would also be repeated theoretically in CST so both results i.e. experiment & modelling can be compared & analysed.

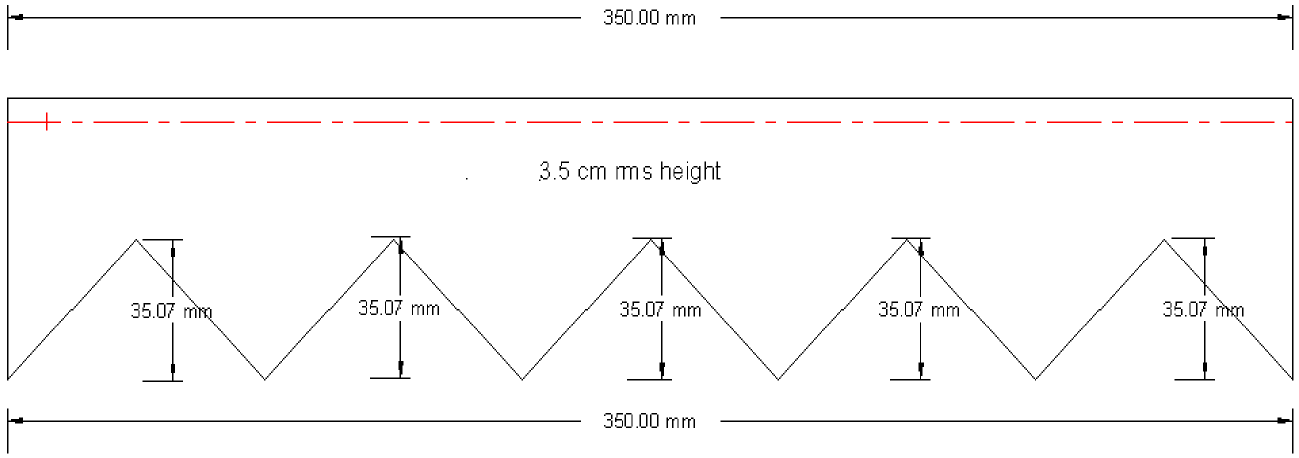

Figure 5.99: 3.5 cm rough surface profile

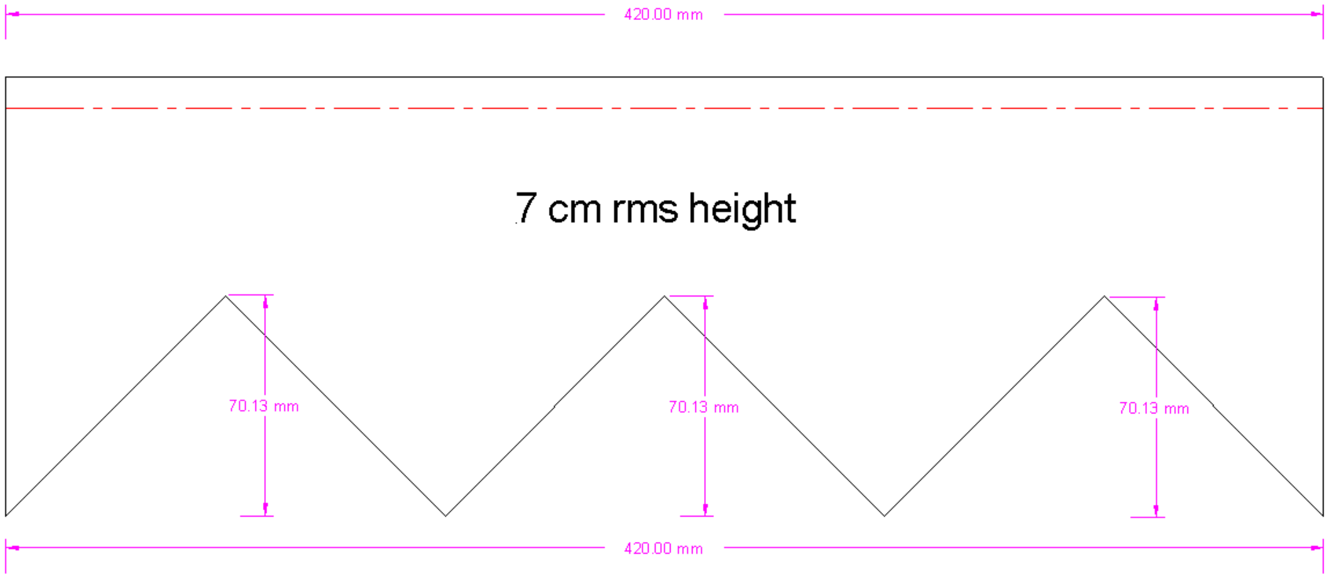

Figure 5.100: 7 cm rough surface profile

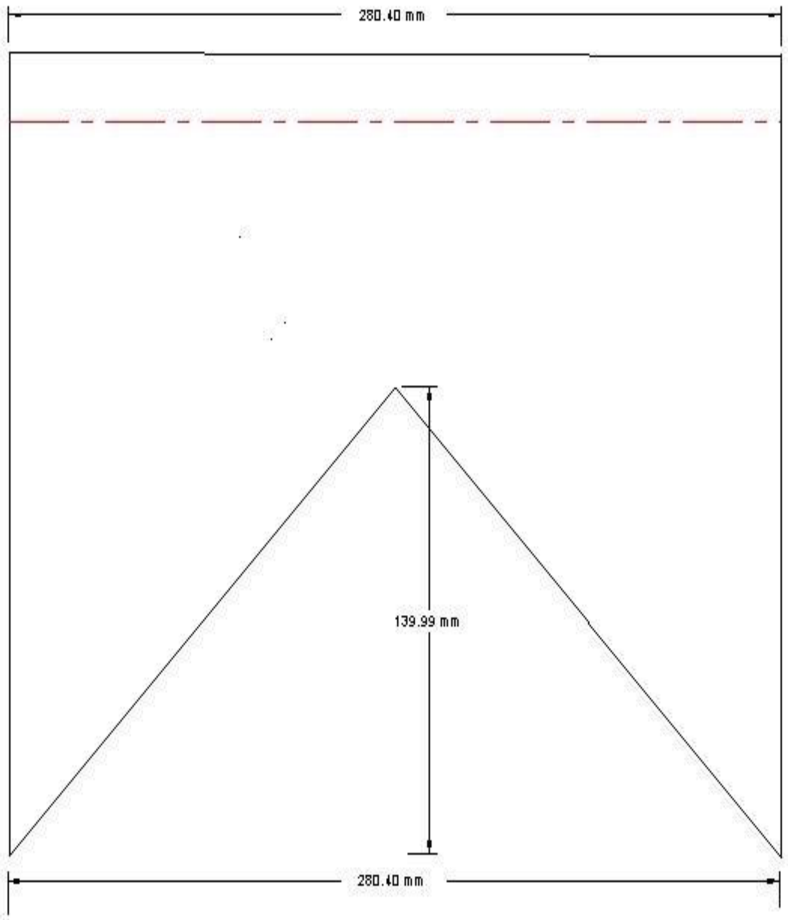

Figure 5.11: 14 cm rough surface profile

These rough surface profiles were used in the experiments and the results would be elucidated upon as we progress in this thesis.

Meanwhile, before we commence the experiment, we would have to calibrate the setup. The initial set of measurements were conducted in the anechoic chamber. A photo of the experimental setup is shown in Figure 5.12. The anechoic chamber was used for these measurements because there was much reduced back reflections compared to if the measurements were taken in an open lab space because of the wideband antennas used.

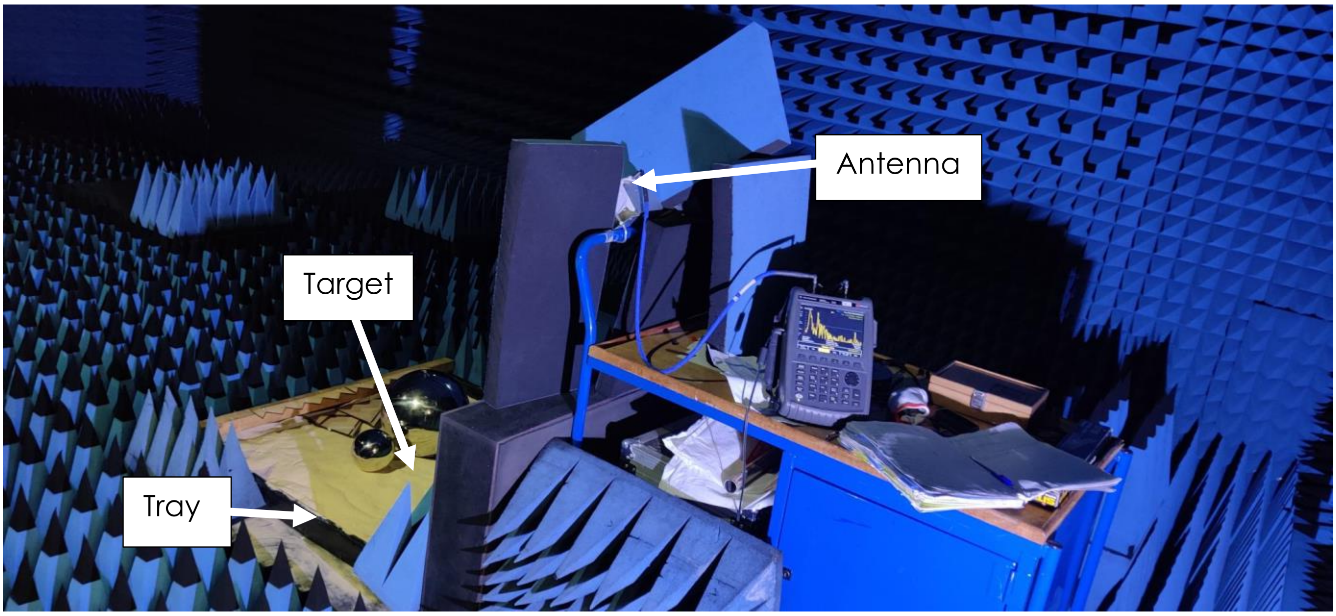

Figure 5.12: Experimental setup inside the anechoic chamber

Figure 5.13 shows the initial calibration results of the tray when filled with sand. The tray is 1m in length and is positioned between 1.2 m to 2.2 m along the range axis of the plot. To enhance the dielectric properties and improve reflectivity, a controlled amount of water was added to the sand. Specifically, the sand was moistened to achieve a defined water content level, thereby increasing its permittivity and enabling more precise electromagnetic measurements during calibration. Figure 5.14 shows the calibration result of the tray under this moist/wet sand condition. In both measurements, a minimum of 10 iterations were conducted for consistency, and the average values were computed and plotted. A comparison of figures 5.13 and 5.14 reveals that the signal amplitude increased by approximately 5 dB between 1.2 m and 1.8m under moist conditions, indicating improved reflectivity due to the increased dielectric constant of the moist/wet sand. This observation does not contradict earlier findings regarding surface roughness and RCS. It is important to emphasise that for wet sandy soil, smoother surfaces tend to yield higher RCS values due to enhanced coherent reflection, whereas for dry sandy soil, rougher surfaces exhibit higher RCS owing to increased diffuse scattering. Thus, the improved reflectivity observed with moist sand in Figure 5.14 aligns well with the theoretical expectations and contributes to more sensitive and accurate calibration of the experimental setup.

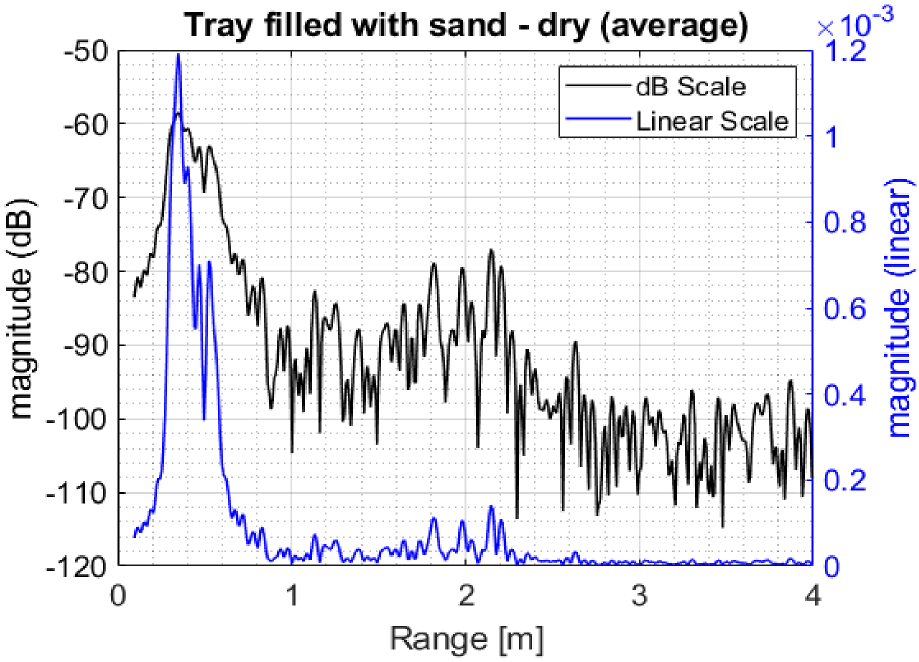

Figure 5.133: Tray filled with flat dry sand – average

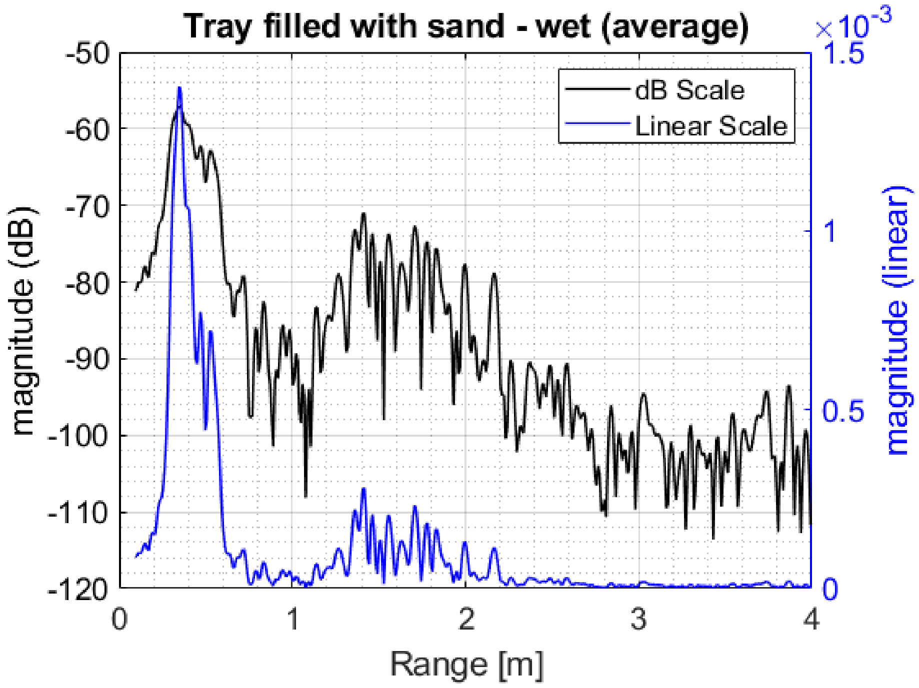

Figure 5.144: Tray filled with flat sand and slightly wet – average

The 3 rough surface profiles are used to make rough surfaces on the tray filled with sand. Figure 5.15 shows the rough surfaces created by the 3.5cm rough surface profile, while Figure 5.16 shows the rough surfaces created by the 7 cm rough surface profile. When both figures are compared, we can see that between the 1.4m and 2m where the tray filled sand is, the magnitude of the rough surface increased by an average of about 8 dB between the 7 cm rough surface and the 3.5 cm rough surface profiles. The implication of this is that when measurements are taken, it would be easier for the oil spills and leaks to be detected from a rougher surface (in this case the 7 cm rough surface profile) than from a ‘not so rough’ surface (in this case the 3.5 cm rough surface profile). This is also in tandem or agreement with our simulations or modelling results which states that for a dry sandy soil, the rougher the surface, the greater the RCS or reflectivity and vice versa. This also implies that our experimental and modelling results agree with each other as the experiment and modelling validate each other. Figure 5.17 shows the rough surfaces created by the 14 cm rough surface profile. A cursory look at the figure between 1.4m and 2 m shows three ‘peaks or sharp edges’ which coincide with the edges or ridges formed when the 14 cm rough surface profile is dragged across flat sand on the tray. Also 10 iterations were made for each plot & the averages plotted accordingly

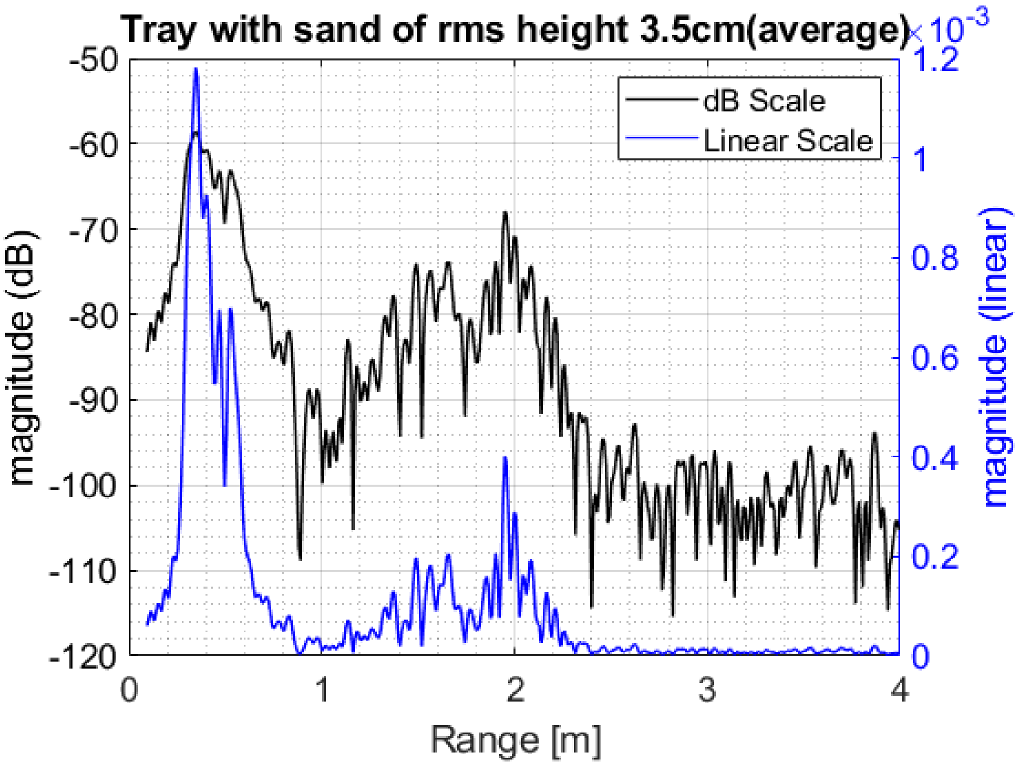

Figure 5.155: Tray filled with dry sand and surface roughness 3.5 cm – average

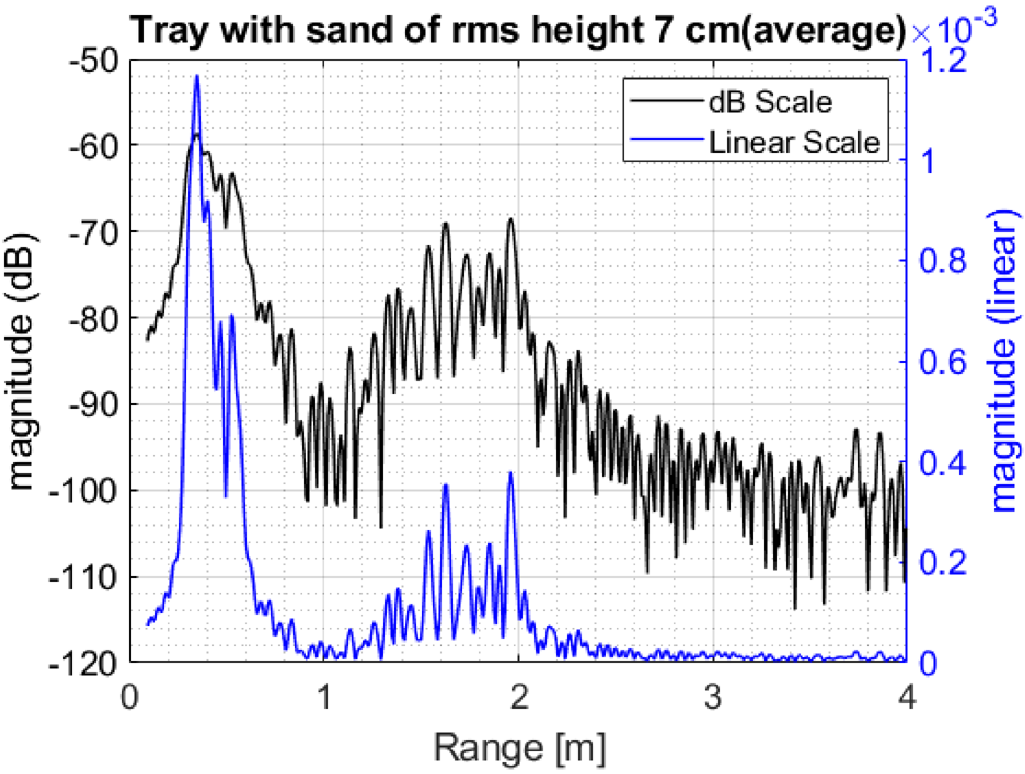

Figure 5.166: Tray filled with dry sand and surface roughness 7 cm – average

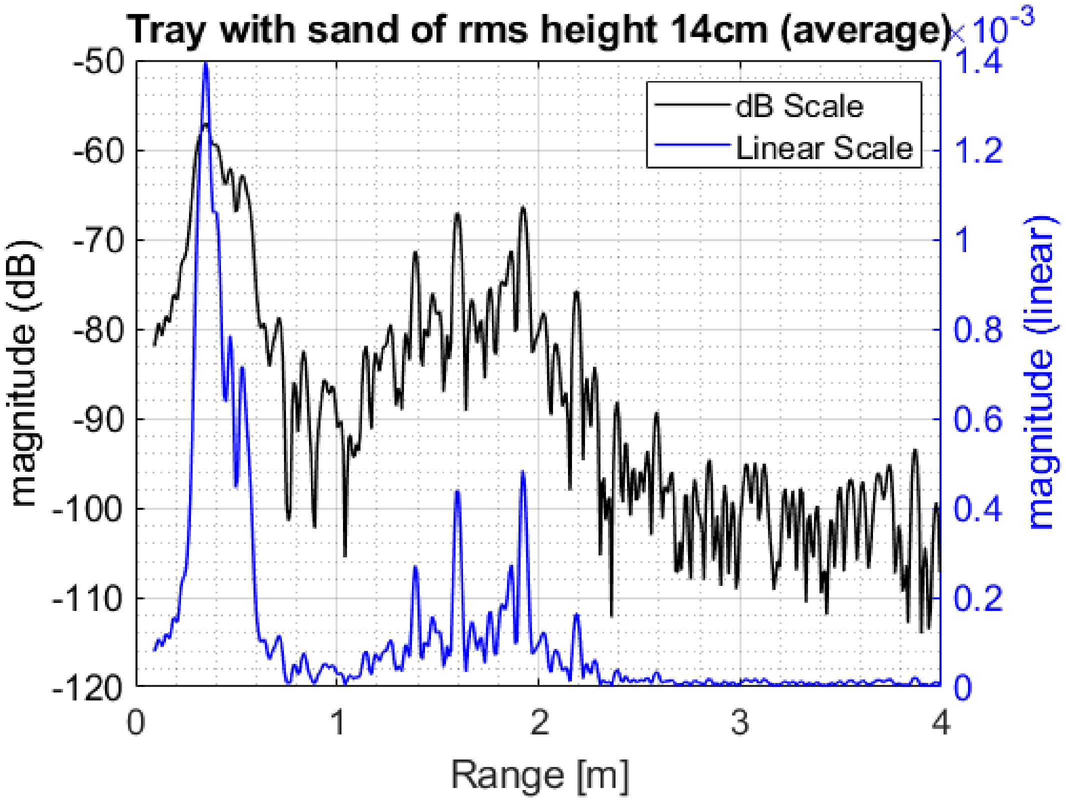

Figure 5.17: Tray with dry sand and surface roughness 14 cm – average

Now these four plots (Figures 5.14 – 5.17) are combined, and Blackman windowing technique applied to it to yields Figure 5.18. From the figure, we can see immediately how the various rough surface profiles vary and relate with each other especially within the area of interest i.e. 1.5m and 2m. We can see that the 14 cm rough surface profile has the highest average magnitude as expected, and the ‘flat’ profile has the lowest. This aligns with theory where the rougher the surface, the higher the reflectivity for a rough surface and the lower the reflectivity, the ’smoother’ the surface for a rough surface. This is also buttressed in Table 5.2 where the average for each profile has been calculated. The results agree with what was expected and in line with the modelling results. The average before windowing and after windowing was calculated and as expected for each dielectric material, the average after windowing has a better response because of the filtering applied to the raw output. In addition, we can also see that there is a progressive increase in the reflectivity from dry sand to 14 cm surface roughness.

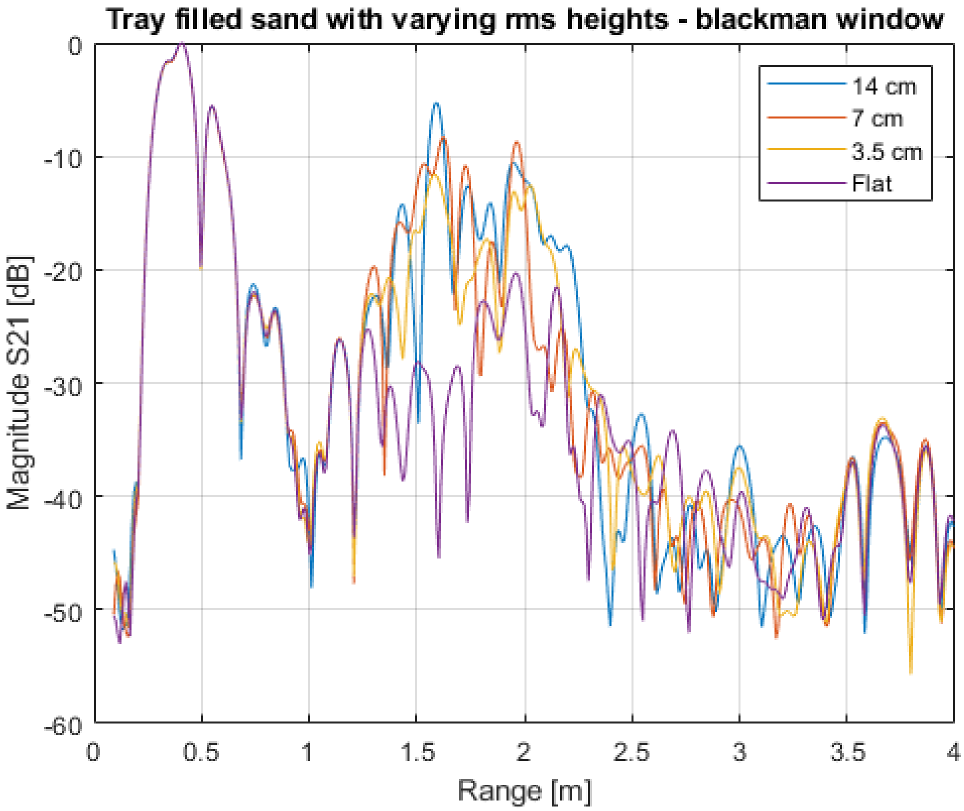

Figure 5.18: Tray filled sand with varying surface roughness and Blackman window applied

Table 5.2: Comparison of average for various dielectrics with windowing tech.

Material / Dielectric	**1.5m & 2.0 m** **Before windowing**	**1.5m & 2.0 m** **After windowing**
Tray filled with sand – dry	- 86.70 dB	- 94.32 dB
Tray filled with sand – wet	- 86.11 dB	- 93.99 dB
Filled tray with 3.5 cm rms height	- 77.20 dB	- 84.11 dB
Filled tray with 7 cm rms height	- 75.18 dB	- 80.80 dB
Filled tray with 14 cm rms height	- 74.78 dB	- 80.53 dB

Now when the rough surfaces have been created on the sand filled with tray, the next step is to pour oil on the various rough surfaces and extract the reflectivity or RCS of oil based on that rough surface profile. This shall be further discussed in this section. The oil was also poured on just one half of the tray so that the other half which does not have the oil can be used as a sort of 'control' for the experiment. The control refers to the half of the tray that does not have oil applied to it (the dry surface). This dry half serves as a baseline or reference condition against which the effect of oil on the rough surface can be measured or compared. By keeping one half of the tray dry, you can isolate and observe the changes in reflectivity or RCS that are specifically due to the presence of oil on the other half. This helps in understanding the influence of the oil layer on surface reflectivity by providing a direct point of comparison. If you have oil covering one half of the tray and no oil on the other half, the reflectivity results will exhibit clear differences between the two regions due to change in dielectric properties and surface roughness introduced by the oil layer. For the half with no oil (dry surface), the reflectivity will be determined purely by the rough surface of the tray and its material properties. Also, the roughness will scatter the incident waves more diffusely, reducing specular reflection. However, for the half with oil (wet surface), the presence of oil alters the surface's dielectric properties, increasing the effective permittivity of the interface. Since oil typically has a higher permittivity than air, reducing the impedance mismatch between the surface and the incident wave, this can lead to lower reflectivity at certain angles or an increase in reflection at specific frequencies, depending on the oil's thickness and electrical properties. The oil may also smoothen the rough surface, leading to reduced scattering and potentially a higher specular reflection component. In summary, this setup is indeed interesting because it allows for a direct comparison of how the presence of oil affects wave interactions with a rough surface. The difference in reflectivity between the two halves is therefore leveraged in oil spill detection as well as remote sensing applications.

The oil that was used thru out the experiment was vegetable oil from a retail shop as the use of crude oil is prohibited in the laboratory space because of carcinogens as well as other health and safety related risks. The vegetable oils are not normally considered hazardous in the quantities involved. Vegetable oils and crude oils differ significantly in their chemical composition, physical properties, and environmental impact which makes vegetable oils a safer and more suitable option especially for indoor experiments.

In terms of composition, vegetable oils are composed mainly of fatty acids and glycerol, they are biodegradable and non-toxic whereas crude oils are a complex mixture of hydrocarbons, often containing toxic and carcinogenic compounds. Vegetable oils also have low volatility and minimal toxicity, which makes them safer for indoor use; whereas crude oils have high volatility, releasing harmful vapours that pose health risks in confined spaces. In terms of the environmental and health impacts, vegetable oils are biodegradable and non-hazardous, thereby reducing risks of contamination or hazardous waste disposal; whereas crude oils are persistent pollutants that can cause severe environmental and health hazards. Furthermore, vegetable oils are less flammable than crude oil, with higher flash points; whereas crude oils are highly flammable and pose fire hazards in indoor settings. As a result of all the above, vegetable oils are ideal substitutes for crude oils in experiments related to oil spills and leaks behaviour. By using vegetable oils instead of crude oil, especially for indoor experiments, we can ensure safer, environmentally friendly and controlled indoor experimental conditions without compromising on the relevant study outcomes. Besides, after each experiment, the contents of the tray were disposed properly and the area cleaned up.

Also in the modelling, it was oil that was used in the simulation to give a sort of semblance to the oil used in the experiments. It is also worthy to note at this juncture that the sand in the tray is placed in such a way that the ‘ridges or profile’ is perpendicular to the propagation of the electromagnetic wave from the antenna. This was done to allow for maximum echoes reflected from the ridges as opposed to if the profile was parallel to the electromagnetic waves from the antenna.

5.4. Experimental Verification of Theoretical Results

Now the white horn antennas and the portable Field Fox Vector Network Analyser (Field Fox VNA N9918A) was used to perform an experiment for the rough surface profile of 3.5 cm where the sand has been soaked with oil. The antennas were placed at an angle of 41° to the tray. Figure 5.19 shows a tray of dry sand with a rough surface profile of 3.5 cm, where half of the sand in the tray has been soaked with oil.

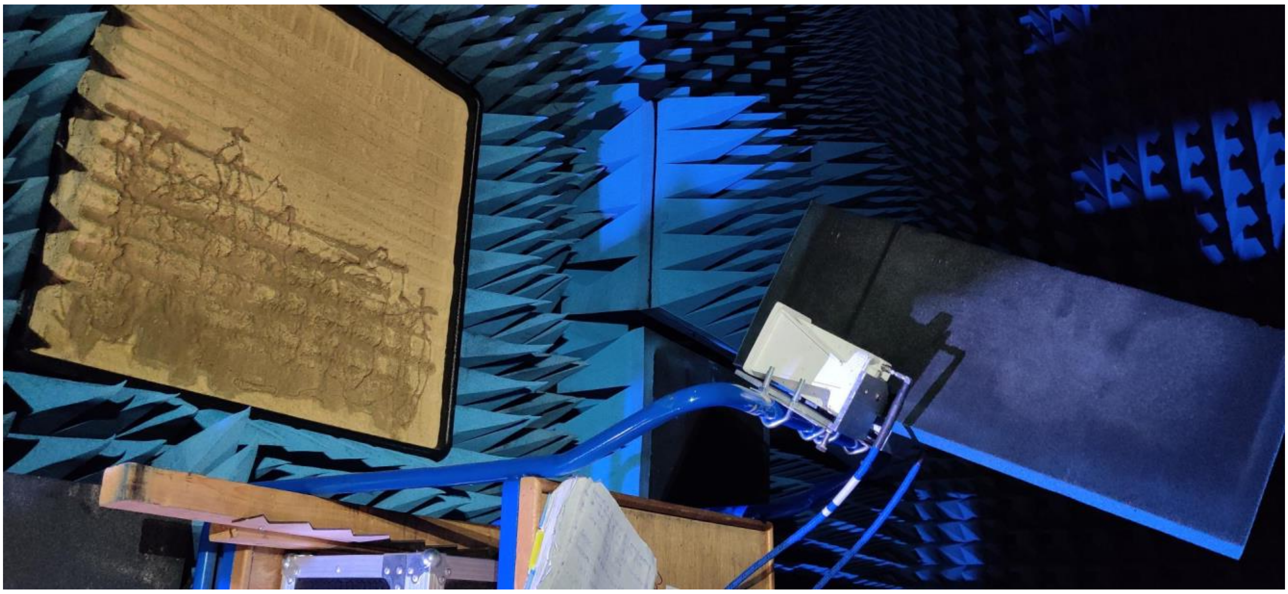

Figure 5.19: Rough surface profile with 3.5cm rms height and oil applied to half of the surface

The sand was first sprayed with oil to keep the profiles in check or ‘in shape’ once the rough surface profile has been dragged thru the sand to form a rough surface. Three litres of vegetable oil was applied on three different occasions on one half of the tray as shown in the result in Figure 5.20. The oil covered from about 1.25m to 1.7m on the plot which is equivalent to about half of the dimensions of the tray. The edge of the tray is at about 2m on the plot. From the plot, we can also see that as the oil is applied, the reflectivity reduces as the quantity of oil increases. In the first instance which is called ‘applied oil 1st’ on the plot, a litre of oil was applied to the rough surface; and a litre of oil is always applied to the rough surface at each instance as shown in the plot. It is important to note that the observed reduction in reflectivity with increasing oil application does not contradict the earlier simulation results. In fact, it aligns well with them. As previously established in the simulations, surfaces with higher rms heights (i.e. rougher surfaces) exhibited higher RCS, while modified surfaces with reduced rms heights – such as those influenced by oil spillage – showed lower RCS. Similarly, in the experimental setup, the application of oil smoothens the surface, effectively reducing the surface roughness and consequently lowering the reflectivity. This consistent trend between the simulation and experimental results reinforces the validity of our observations.

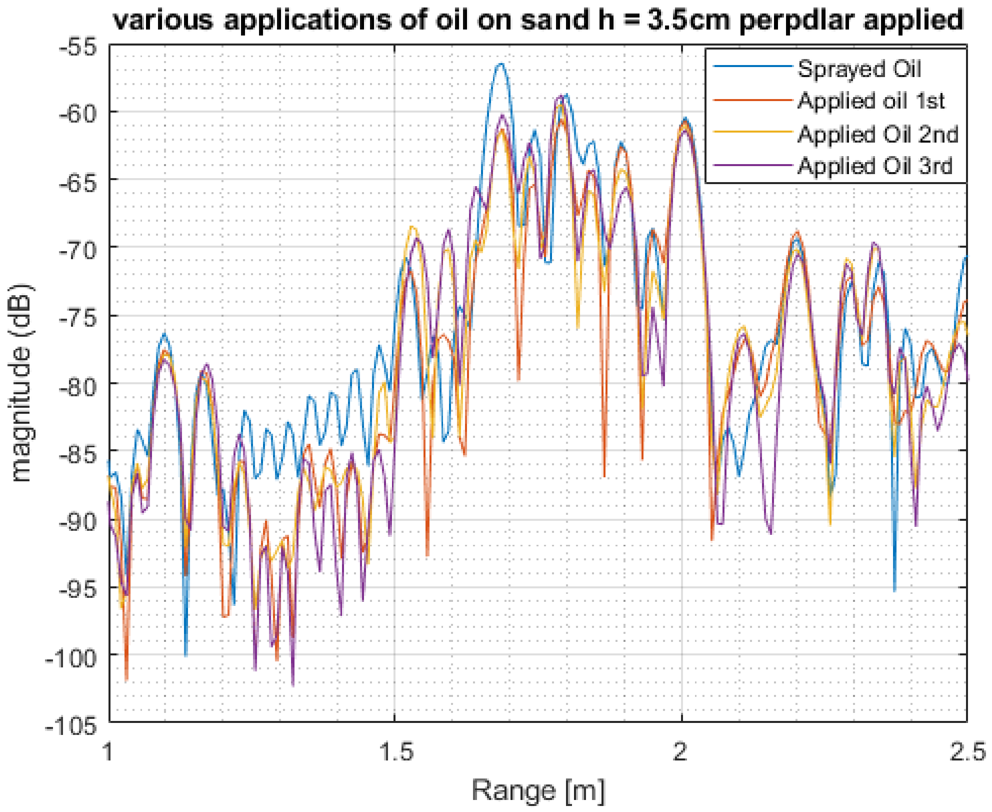

Figure 5.20: Various applications of oil on sand for 3.5cm rough surface profile

At about 1.68 m, the magnitude of the dry sandy soil that has been sprayed with oil is – 56.5 dB, while the magnitude is about – 60.05 dB the first time the oil was applied. It further reduced to – 61.05 dB for the second application of oil and – 62.5 dB for the third application of oil. Using the radar equation, the cross-sectional area of the target is obtained to be about – 0.25 dBsqm for the dry sandy soil (without oil). The cross-sectional area of the target for the 3rd application of oil is however obtained to be about – 6.25 dB sqm. This RCS value is compared to the average RCS for oily sandy soil and the average RCS is about – 6.38 dBsqm for modelling results on CST. From this RCS value, we can see that the experimental results tallied with the modelling results which also gives credence to this work as well as theory. Figures 5.21 and 5.22 show the mean of 5 trials for dry sandy soil as well as when the sandy soil has been soaked with oil (which mimics the 3rd application of oil in this instance for the experiment). From both plots, we can also see that the oily sandy soil has a lower magnitude than the dry sandy soil which agrees with what is expected.

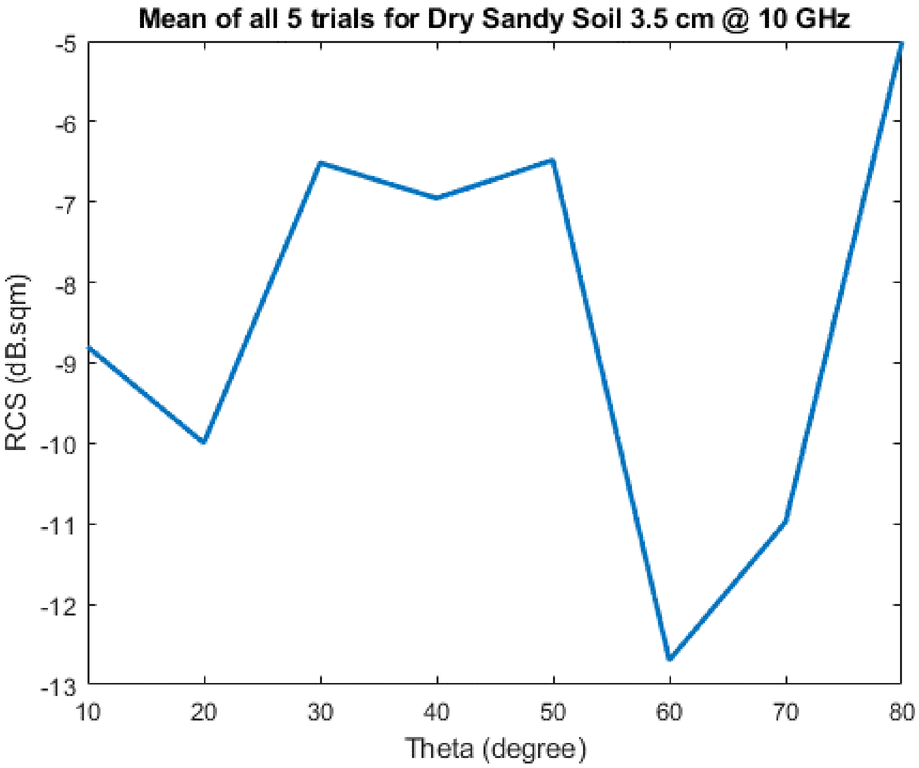

Figure 5.21: Mean of 5 trials for dry sandy soil with rms height 3.5cm @ 10 GHz

Figure 5.22: Mean of 5 trials for Oily sandy soil with rms height 3.5cm @ 10 GHz

Although the difference in RCS between dry and oily sandy soil appears relatively small, this aligns with expectations due to the modest change in dielectric properties and partial surface smoothening. The observed reduction in reflectivity, albeit subtle, is consistent with theoretical and simulation predictions that oil reduces effective surface roughness and impedance mismatch, thereby influencing scattering behaviour. In electromagnetic studies, even small dB-level changes in RCS are significant and represent measurable physical effects.

Table 5.3 shows the comparison between the experimental and simulation RCS values between 1.5m and 2m for a dry sandy soil that has been soaked with oil. The RCS at 1.68 m for the experiment is – 6.25 dBsqm which was obtained via calculations using the radar equation and the magnitude of the S21. The theoretical RCS value obtained from simulation is about – 6.20 dBsqm which aligns with the results obtained from the experiment.

Table 5.3: Comparison of RCS values for oily sandy soil for experiment and simulation

Sandy Soil	Range (m)	S21 (dB)	RCS (dBsqm) Experimental	RCS (dBsqm) Simulation
Dry Sandy soil	1.68	- 56.50	-0.25	-5.10
With 3rd appl. of oil	1.50	- 72.05	-17.72	-6.20
With 3rd appl. of oil	1.60	-69.00	-13.60	-6.20
With 3rd appl. of oil	1.68	-62.50	-6.25	-6.20
With 3rd appl. of oil	1.70	-63.50	-7.05	-6.80
With 3rd appl. of oil	1.80	-64.00	-6.56	-7.05
With 3rd appl. of oil	1.90	-66.50	-8.12	-8.00
With 3rd appl. of oil	2.0	-61.50	-2.22	-5.50

When Figure 5.20 is zoomed into, Figure 5.23 is obtained which shows a more detailed plot of the experimental results between 1.6m and 1.90m. Figure 5.24 shows the average of each dielectric between 1.6 m and 1.90m. From the plot, we can see that the reflectivity reduces as the application of oil increases. There is about a 3 dB difference between dry sandy soil and the second application of the oil on the 3.5 cm rough surface. This difference should get bigger as the surface roughness increases or the quantity of oil increases. When Figures 5.21 and 5.22 are combined, which are for the theoretical /simulation results, Figure 5.25 is obtained. From the Figure, we can see that the oily sandy soil has a higher reflectivity compared to the dry sandy soil at the angle of interest i.e. 41°. The values of RCS obtained for both dielectrics also tally with the RCS values in Tables 5.3 which has also been thoroughly discussed.

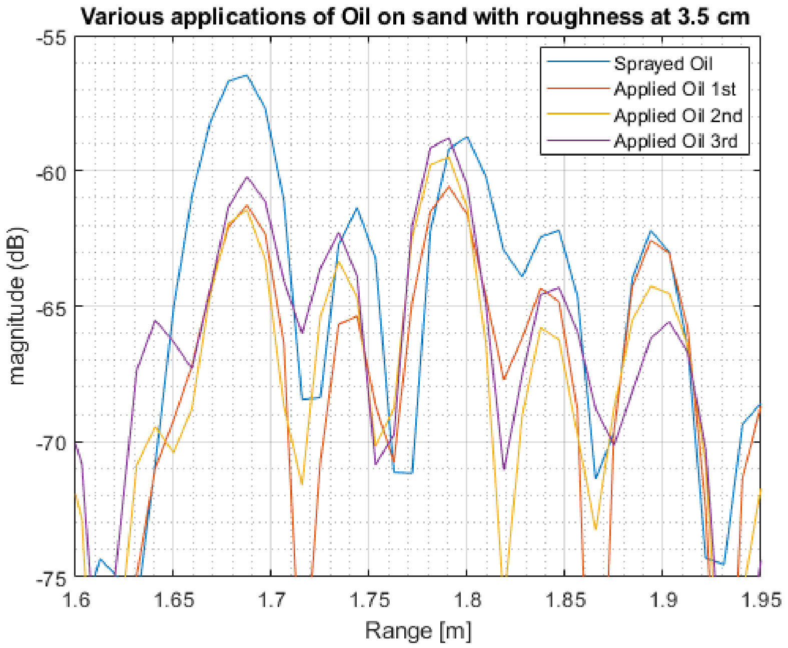

Figure 5.23: Various applications of oil with rms height 3.5 cm and between 1.6m and 1.9m

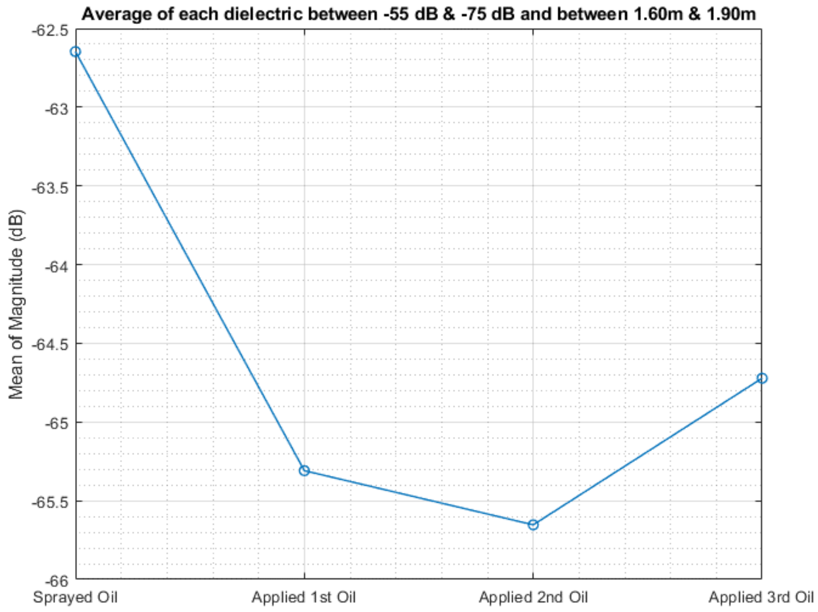

Figure 5.24: Average of each dielectric between -55dB and -75dB and between 1.6m and 1.9m

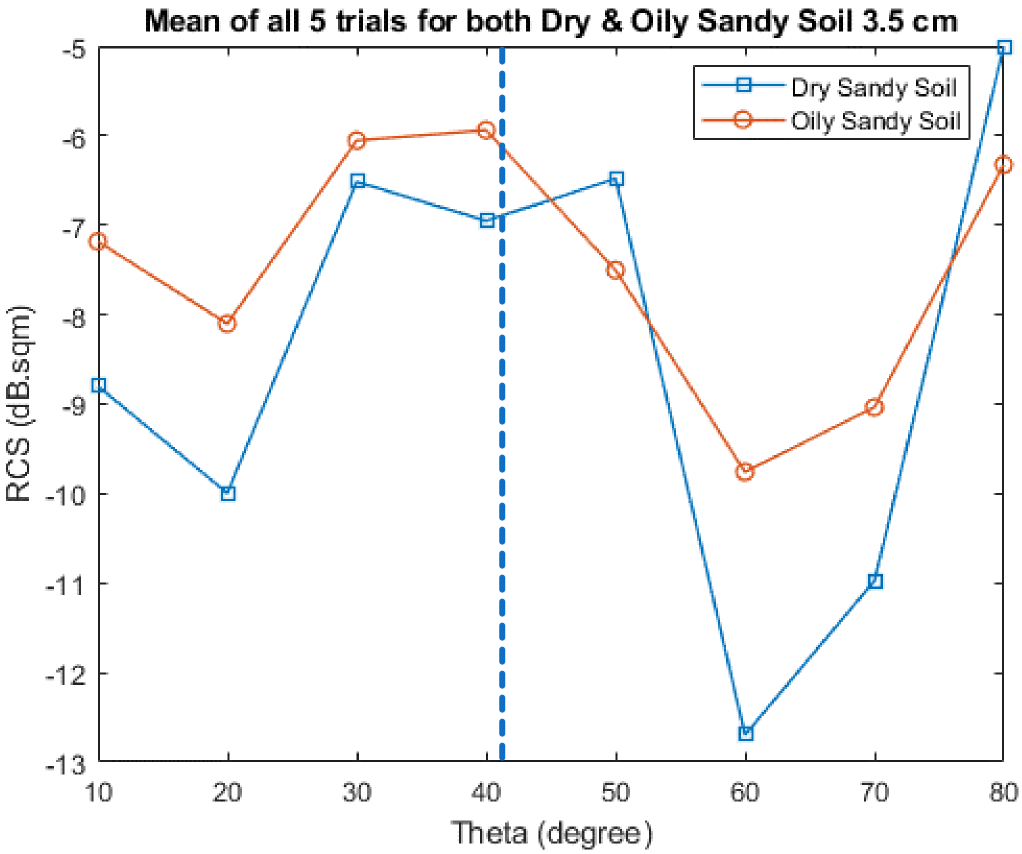

Figure 5.25: Mean of 5 trials for both dry & oily sandy soil at 3.5cm rms height

Furthermore, when Figure 5.20 is zoomed into, Figure 5.26 is obtained which shows a more detailed plot of the experimental results between 1.2m and 1.90m. From this figure, we can see that the section of the tray which has the oil has a bigger difference in magnitude (about 7 dB) between the dry sandy soil as well as the oily sandy soil compared to about an average of 2 – 3 dB for the area where there is no oil i.e. 1.6 to 1.9m and as previously analysed. Figure 5.27 therefore shows the average of each dielectric between 1.2 m and 1.50m. From the plot, we can see that the reflectivity reduces significantly (i.e. 6.4 dB) as the application of oil increases. There is about a 6.4 dB difference between dry sandy soil and the final application of the oil on the 3.5 cm rough surface between 1.2m and 1.5m. This difference should get bigger as the surface roughness increases or the quantity of oil increases as well. When figure 5.24 is compared to figure 5.27, the part where the oil spread has a bigger difference in magnitude compared to the other half of the tray without the oil. The difference in magnitude of the reflectivity for both cases is in line with what was expected.

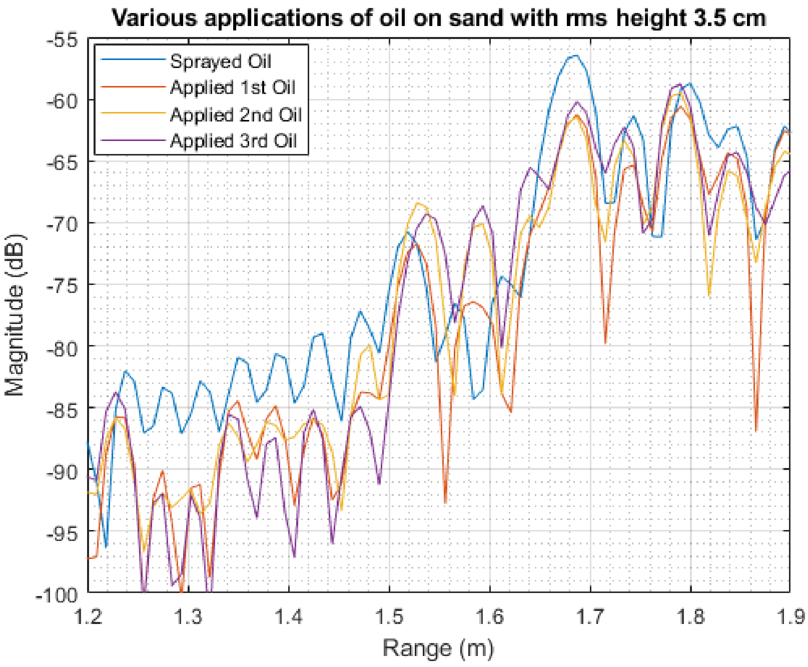

Figure 5.26: Various applications of oil with rms 3.5cm & between 1.2m & 1.9m

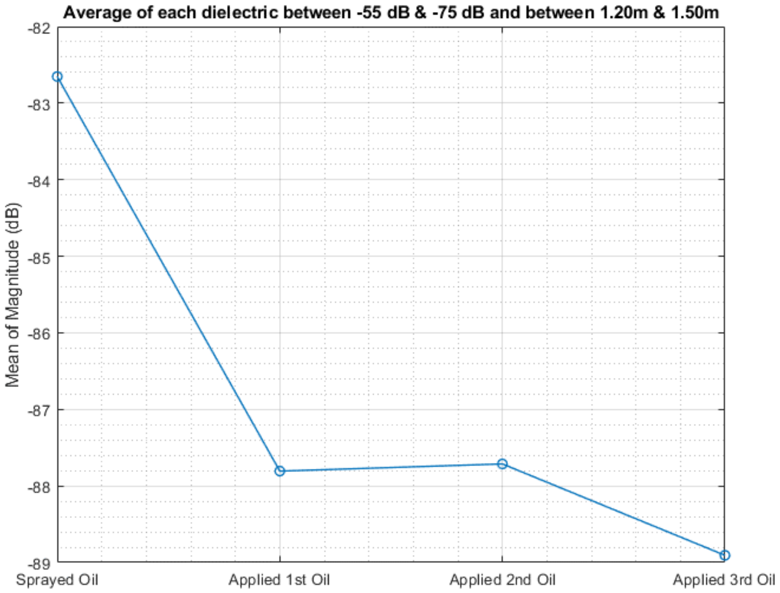

Figure 5.27: Average of each dielectric between -55dB & -75dB between 1.2m & 1.5m

The results of the experiment were critically analysed further, and we got to the conclusion to change the hardware. Because we were working with a vector network analyser (VNA) at so short a range, our echo signals were being masked under the sidelobes of the leakage FMCW signal. Instead, a pure pulse signal of 1ns duration is used together with two standard gain horn antennas of 20 dB gain each (Standard gain horn Model 12240-20 Flann Microwave). These high gain antennas have practically no leakage between them, as well as the fact that the leakage and return signals are separated in time. The current white horn antennas being used are wide band, with lots of leakage between both transmit and receive antennas and therefore incorporates lots of noise and unwanted reflections. Due to the fact the system operates at 4 GHz for most of the time, which is about 7.5 cm wavelength, then it is expedient to use just two rough surface profiles for the experiment which are the 7cm and 14cm rough surface profiles. Figure 5.28 shows the experimental setup in the anechoic chamber with the antennas tilted at an angle.

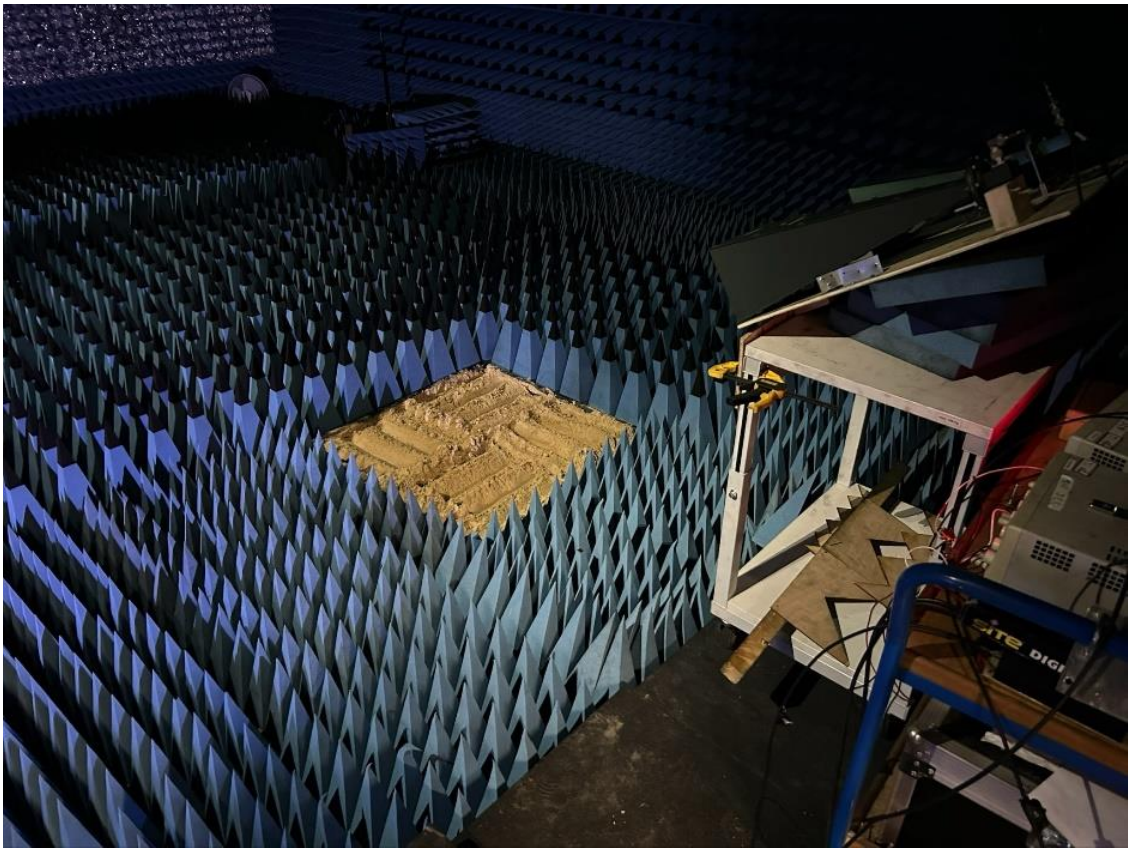

Figure 5.28: Experimental setup with the standard gain horn antennas

The radar is put on and allowed to warm up for at least an hour. Three different spheres with diameters 50 cm, 20 cm and 12 cm are placed on the tip of the absorber one by one and used for calibrations. The data have been recorded in a proper format and the amplitude ratio corresponds to the RCS of the spheres. An empty tray surrounded by the absorber is placed in the path of the antennas and the reflection is recorded. The antennas which have a narrow beamwidth of 20° and gain of 20 dB are placed at a grazing angle of about 45°. The slant range between the antennas and tray is about 1.6m. To evaluate the antenna footprint at this range using a beamwidth 20° results in an antenna footprint diameter of 0.56m. The tray is then filled with dry sand to the top and the data is recorded. The smallest sphere with diameter of 12 cm is placed in the middle of the tray and the data is recorded. Same goes for the medium sized sphere with a diameter of 20 cm as well as the largest sphere of diameter 50 cm. Figure 5.29 shows the calibration results for flat sand after it has been integrated with 200 pulses as well as filtered. The far edge of the tray is at 71 ns while the tray on the ground covers from about 66 ns to about 72 ns. This 6 ns difference results in a 0.9m in range using this formula where R = C x T / 2

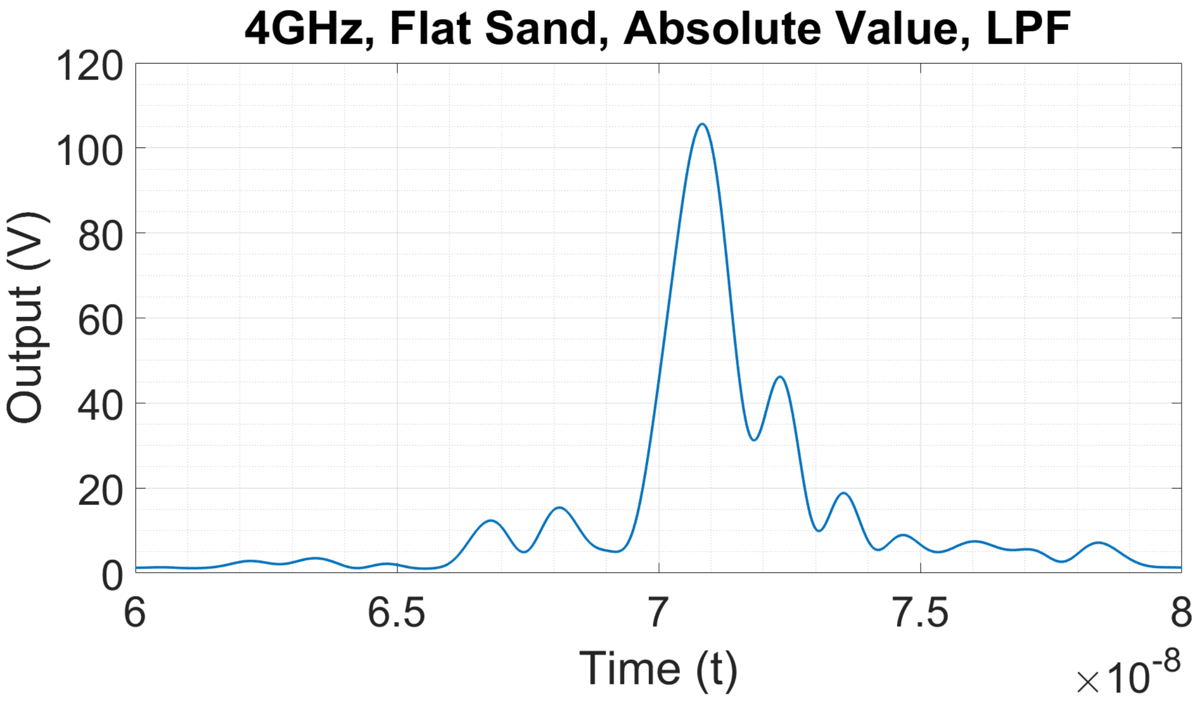

Figure 5.29: Calibration results for flat dry sand

Figure 5.30 shows the calibration results for the big sphere with diameter of 50 cm placed on the dry flat sand. The bigger peak shows where the sphere is on the tray, while the other peak is the edge of the tray which appears to have been slightly shifted due to the big sphere. Figure 5.31 shows the calibration results for the medium sphere with diameter of 20 cm placed on the dry flat sand. The position of the sphere corresponds to about 66 ns from the plot while the other major peak at 71 ns corresponds to the edge of the tray.

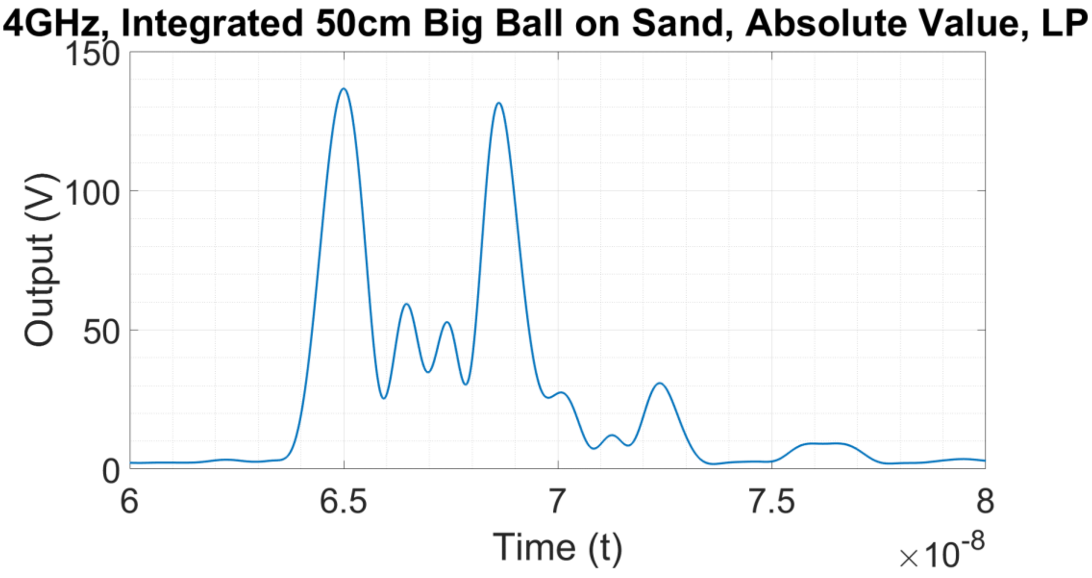

Figure 5.30: Calibration results for a big sphere with diameter 50 cm

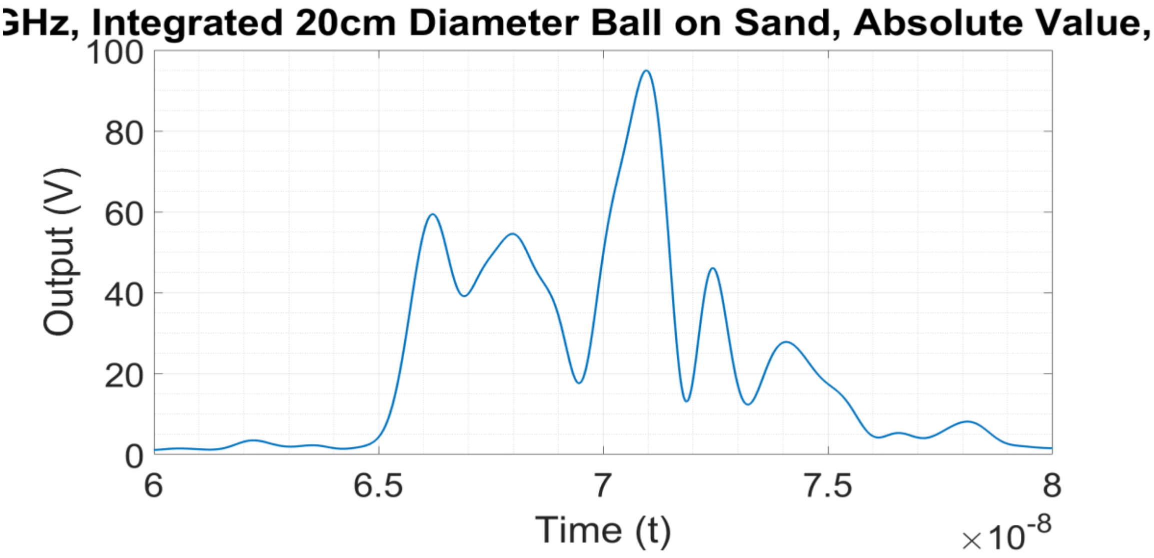

Figure 5.31: Calibration results for a medium sphere with diameter 20cm

Figure 5.32 shows the calibration results for the smallest sphere of 12 cm diameter placed on the dry flat sand. The peak at about 67 ns shows the position of the smallest sphere while the bigger peak at about 71ns shows the far edge of the tray as previously discussed.

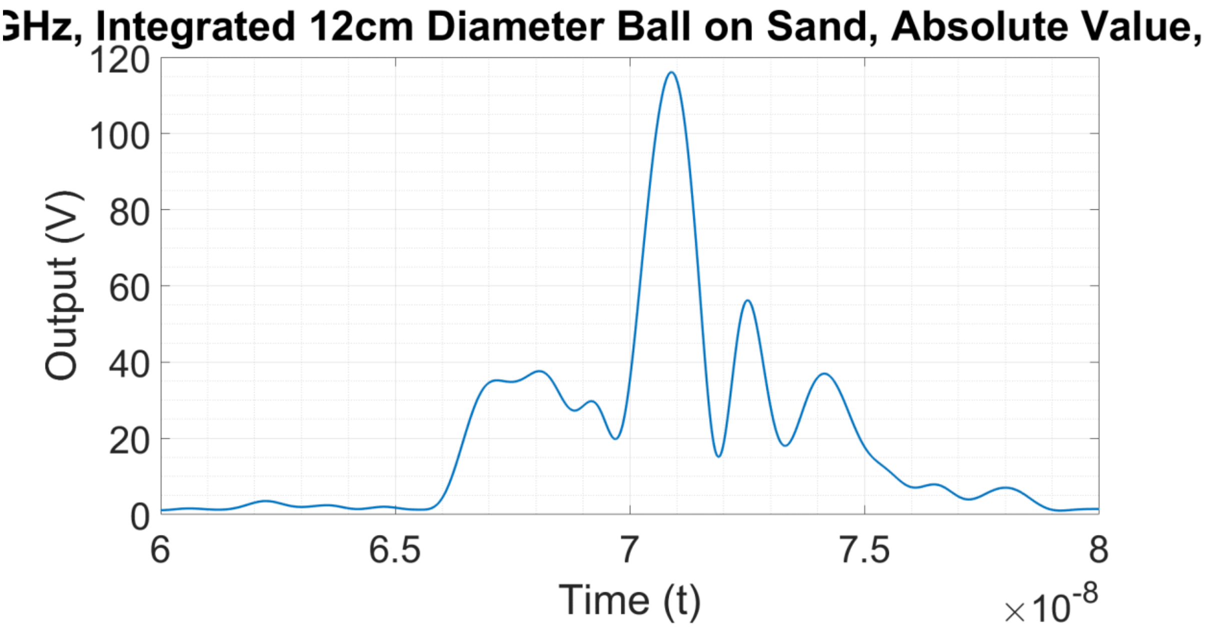

Figure 5.32: Calibration results for smallest sphere with diameter of 12cm on dry sand

After this set of calibration, the flat sand was made slightly wet with sprayed oil to keep the ridges of the rough surface in check once the rough surface profile has been dragged across the sand tray. Rough surface profiles were now made using the 7 cm and 14 cm rough surface profiles. The calibration results have been discussed and extensively analysed and the next set of experiments which involves the impact of oil on various rough surface profiles will also be discussed and extensively analysed.

Figures 5.33, 5.34 and 5.35 show the sand profiles for dry flat sand from smooth/flat sand to 7 cm surface roughness as well as 14 cm surface roughness respectively. Figure 5.36 shows the 7 cm sand profile when oil of different quantity has been poured onto the sand profile, while Figure 5.37 shows the 14 cm sand profile when oil of different quantity has been poured onto the sand profile.

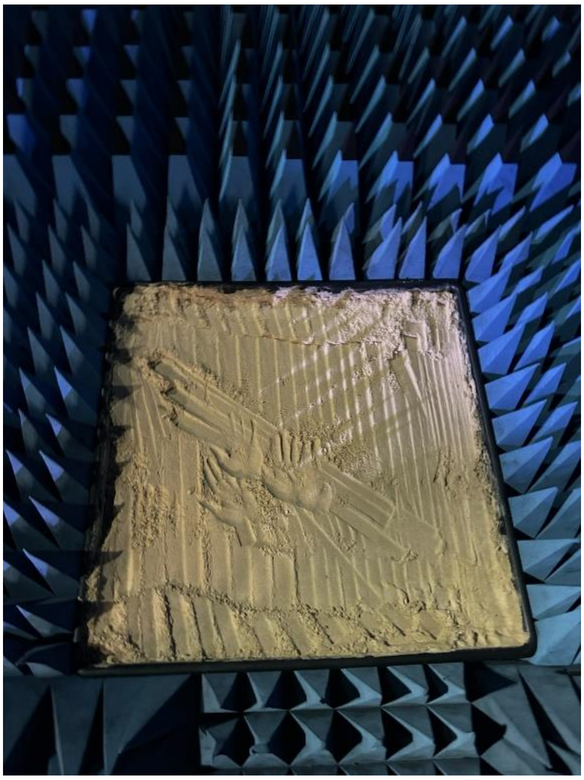

Figure 5.33: Flat sand profile

Figure 5.34: Dry sand rough surface profile with 7 cm surface roughness

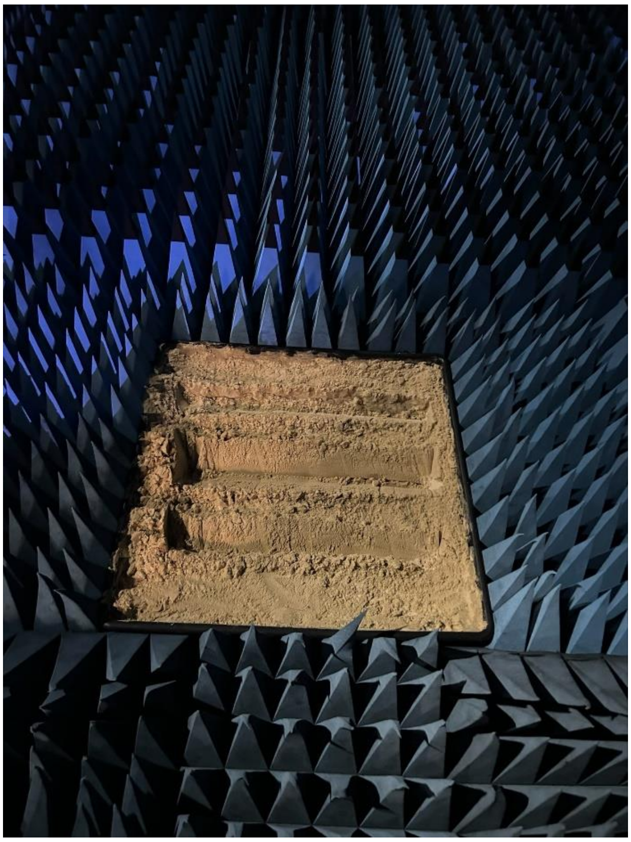

Figure 5.35: Dry sand rough surface profile with 14 cm surface roughness

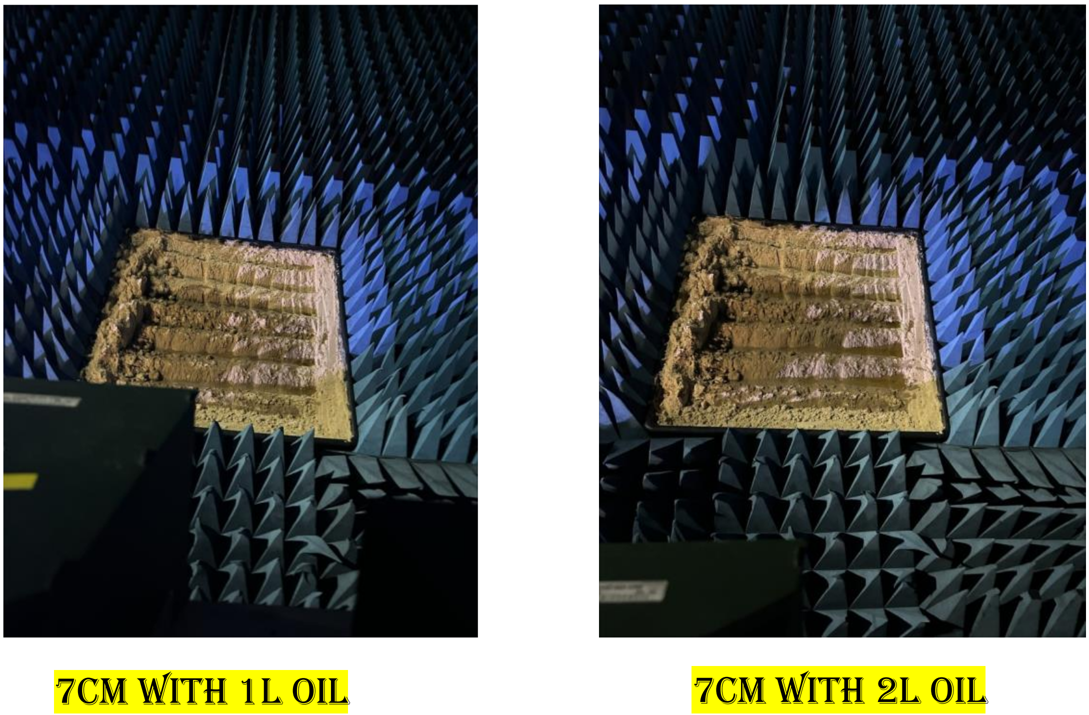

7CM WITH 1L OIL

7CM WITH 2L OIL

Figure 5.36: 7 cm surface roughness with varying quantities of oil i.e. 1L and 2L

14CM WITH 1L OIL

14CM WITH 2L OIL

Figure 5.37: 14 cm surface roughness with varying quantities of oil i.e. 1L & 2L

Figure 5.38 shows the results for the 7 cm surface roughness when the oil has been applied to the rough surface. From the figure, we can see from the area of interest which is between 66 ns and 71 ns that the flat sand / profile has the lowest magnitude compared to the dry rough surface profile of 7cm rms height which has been denoted as ‘no oil’ and the other two cases where oil of 1 L and 2 L have been applied. As expected, the rough surface profile with no oil has the highest magnitude, and as oil is being applied, this magnitude decreased for 1L application of oil and further decreased when the 2L oil was applied as expected.

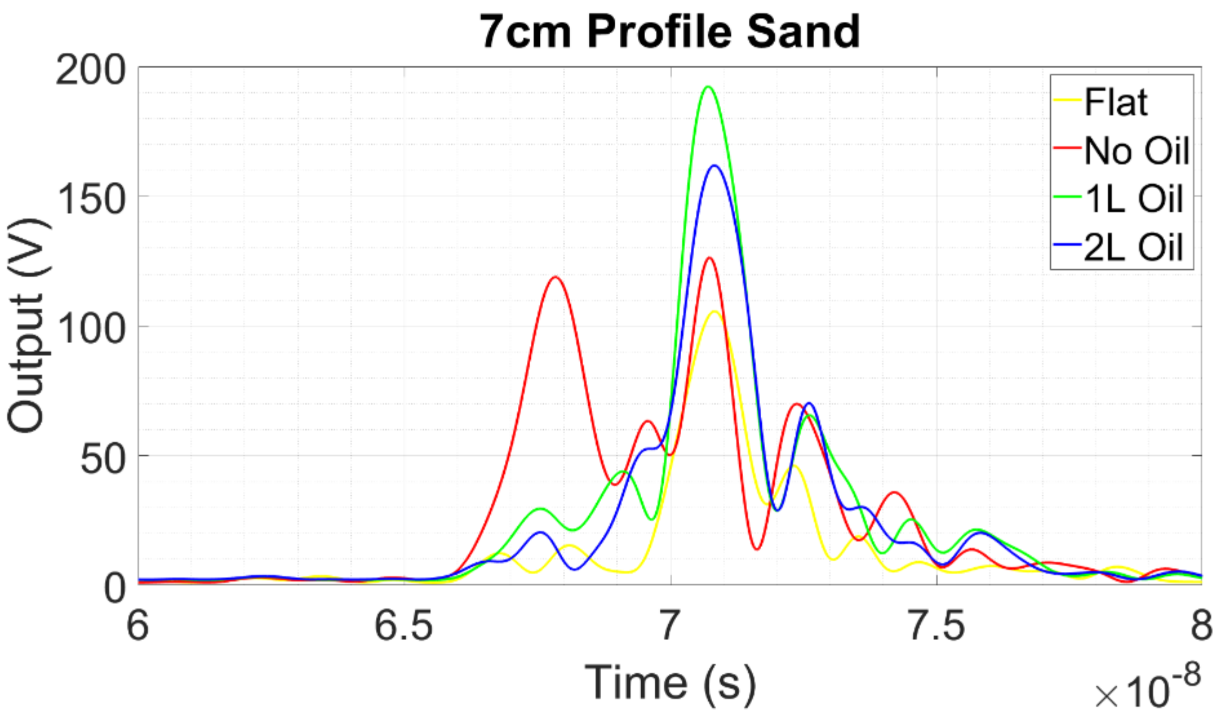

Figure 5.38: 7 cm surface roughness with application of 1L and 2L of oil

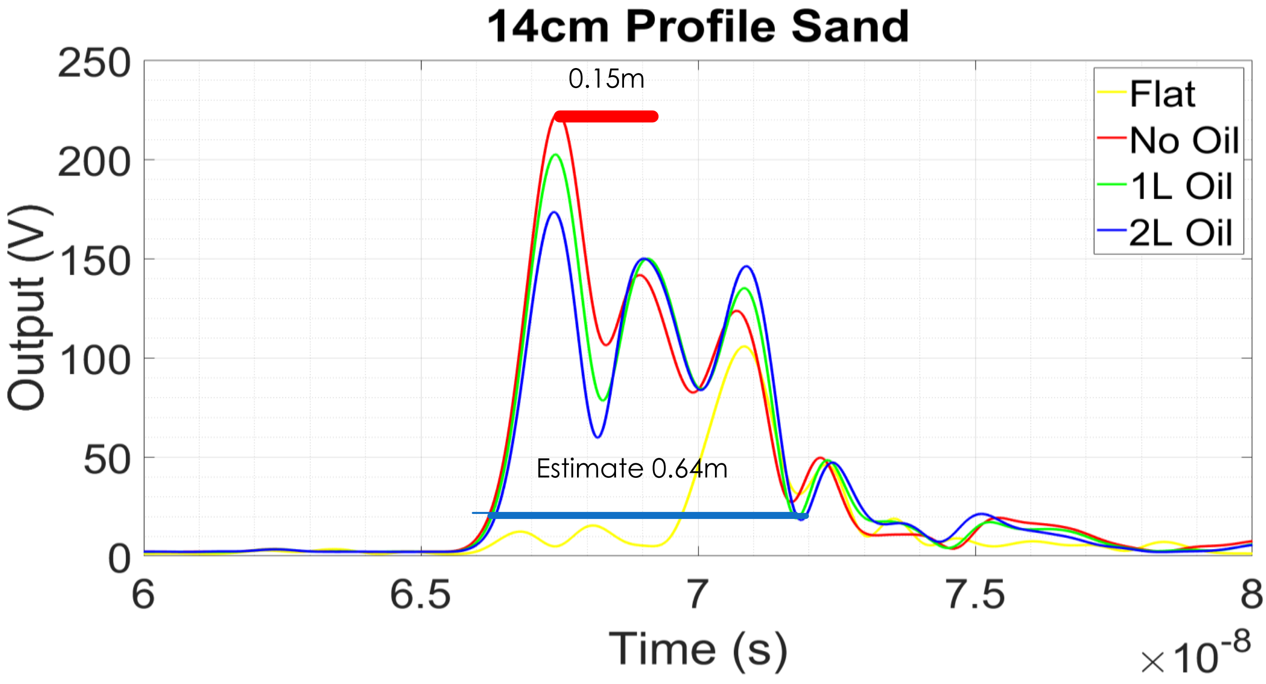

Figure 5.39: 14 cm surface roughness with application of oil i.e. 1L & 2L

Figure 5.39 shows the results for the 14 cm surface roughness when the oil has been applied to the rough surface. From the figure, we can see from the area of interest which is between 66 ns and 72 ns that the flat sand has the lowest magnitude compared to the dry rough surface profile of 14 cm rms height which has been denoted as ‘no oil’ as well as the other two cases where oil of 1L and 2L have been applied. As expected, the rough surface profile with no oil has the highest magnitude and as oil is being applied, this magnitude decreases for the 1 L application of oil and further decreased when the 2L oil was applied. The differences between the flat, rough and various levels of oil is not more pronounced compared to the 7 cm profile. This could be because at 14 cm, the profile may enter a fully diffuse or multiple scattering regime, where the oil becomes less influential than the surface structure; and interference effects cause convergence of signals from different oil levels. Also, on highly rough surfaces (14cm), geometry dominates – so oil induced changes in reflectivity become less distinct. In addition, the non-uniform distribution of the oil could reduce the expected dielectric constant, making 1L and 2L appear too similar.

Now when the 7 cm profile is compared with the 14 cm profile, the 7 cm profile provides better signal separation between oil levels, suggesting it is more useful classification tasks. The 14 cm profile, although producing higher voltages, shows waveform compression and overlapping, reducing its effectiveness for oil differentiation. The peak time shifts and tail behaviour suggest that increased roughness introduces multi-path scattering or deeper signal penetration. These results demonstrate the significance of carefully selecting surface profile geometry in radar-based sensing applications for optimal feature discrimination.

Table 5.4 presents an experimental comparison of waveform responses from radar returns over sandy surfaces with 7 cm and 14 cm profile roughness.

Table 5.4: Experimental comparison of waveform responses from radar returns over sandy surfaces with 7 cm and 14 cm profile roughness

Comparison Area	**7 cm Profile Sand**	**14 cm Profile Sand**	**Key Insights**
Peak Amplitude (V)	Max ~180 V (1L Oil); No Oil ~110 V	Max ~225 V (No Oil); 2L ~160 V	Higher surface roughness = higher voltage response
Effect of Oil Application	1L Oil produces strongest peak; clear separation between 1L/2L/No Oil	All signals elevated; less separation among oil levels	7 cm is more responsive to oil-induced dielectric changes
Flat vs Rough Profile	Flat curve lowest; others clearly elevated	Flat is still lowest but closer to others	Roughness drives backscatter, oil enhances it selectively
Waveform Shape	Pronounced peaks, well separated; ripple structure evident	Waveforms overlap heavily, especially after first peak	Increased profile complexity compresses waveform distinction
Peak Timing	Main peak at ~7.0e-8 s	Main peak earlier (~6.75e-8 s)	Timing shifts may relate to deeper penetration or denser return paths
Separation Between Conditions	Significant visual difference among curves	Smaller difference between curves	Mid-profile (7 cm) offers better discrimination than 14 cm
Oil Sensitivity	Highly sensitive to oil quantity; 1L stronger than 2L	Less sensitive to oil level; curves cluster	14 cm may enter multiple-scatter regime, dampening differences
Signal Duration / Tail	Shorter signal tail	Longer trailing tail	Longer tail implies multiple returns or internal reflections

Furthermore, this figure for the 14 cm rough surface profile with the application of oil is thoroughly analysed to verify if the grooves or ridges on the profile corresponds to what is obtained on the plot. To help us analyse this, let's consider Figure 5.40 and analyse it in greater depth. The vertical height h_R of the antenna above the ground is 1.15m while the slant range R from the antenna to the middle of the tray is 1.6m. The grazing angle α is 45° while the antenna has a narrow beamwidth ε of 20° but still concentrated just within the tray. So, to evaluate the antenna footprint, we use equation 5.4 below which states

$$antenna\ footprint = R\ \mathcal{E} = 1.6\ x\ 20° = 0.56\ m \tag{5.4}$$

To now obtain the width *a* of the sand in the tray, we use equation 5.5 below which states

$$a = \frac{antenna\ footprint}{\sin(\alpha)} = \frac{0.56}{\sin 45} = 0.79\ m \tag{5.5}$$

This 0.79m indicates the width of the tray covered by the sand and it makes sense considering that the length of the tray is 1m but when viewed from the top, it would appear smaller which in this case is 0.79m.

For the ridges covered by the oil, it is expedient to verify that the distances between the peaks or grooves covered in 'real-life' during the measurements is very similar to the distances these grooves cover in the plot in Figure 5.39. A careful look at the plot shows that the grooves which contain a significant portion of the oil, covers from 66ns to 72 ns. This 6 ns difference results in 0.9m in range using the formula where R = C x T / 2. Therefore, when this is multiplied by the grazing angle i.e. 45°, we will therefore obtain 0.9 m x sin 45° which results in about 0.64m. 0.68m was also the distance between the two extremes of the grooves / ridges in real life when it was also measured which validates the measurement results.

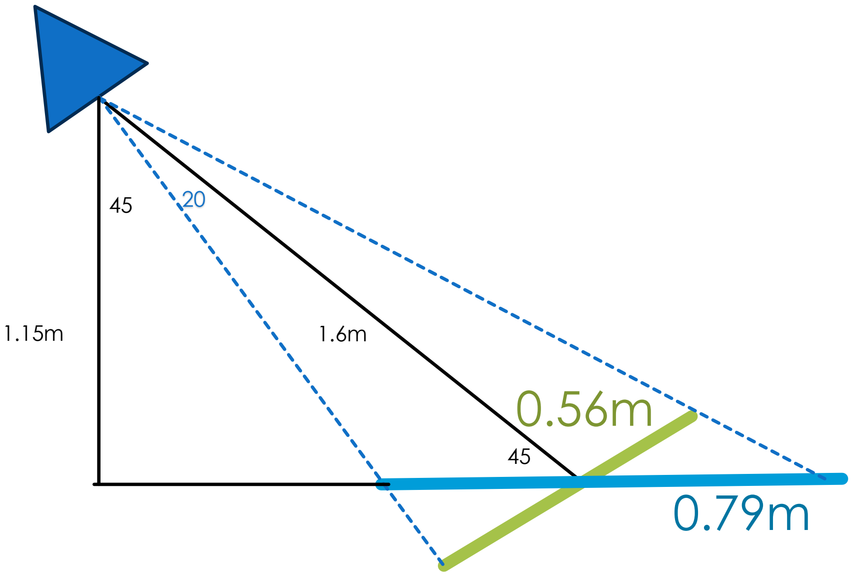

20° between the two dotted lines

45° between two thick lines (black)

R range

ϵ beamwidth

α grazing angle (45°)

h_R vertical height

Figure 5.40: Sketch of the experimental setup with an analysis of the angles and dimensions

Furthermore, the distance between the grooves closest to each other is calculated using the same principle previously described. Taking the first two prominent grooves, the distance between them is about 1.4 ns (67.6 ns to 69 ns). This 1.4 ns difference results in 0.21m in range using the formula (R = CT/2). Therefore, when this is also multiplied by the grazing angle, we will therefore obtain 0.21m x sin 45 which results in about 0.15m. In real life, the distance between the grooves is about 14cm which looks alright, considering it is a rough surface with rms height of 14 cm. Figure 5.41 shows what the 14 cm surface roughness looks like with the appropriate dimensions. There are practically three grooves on this figure, which also tallies with the three prominent grooves contained in the plot in Figure 5.39.

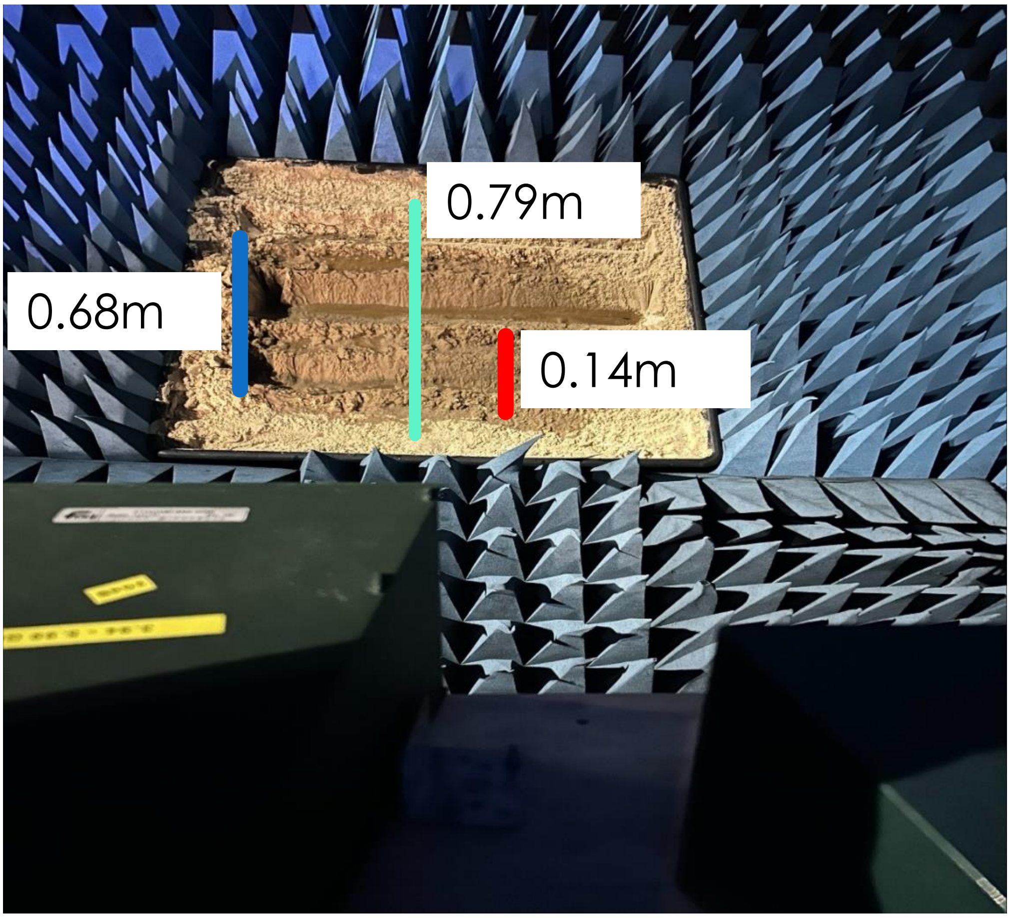

Figure 5.41: 14 cm surface roughness with 2L oil and the dimensions described

These set of measurements have been done with just 2L of oil which is insufficient considering the size of the tray and the quantity of sand. The next set of measurements will involve at least

9L of oil in other to assess the reflectivity of oil if the surface is flooded which is like a leakage occurrence that has happened over a long period. In addition, just one half of the tray will be soaked with oil, to enable us to analyse in an instant what the difference in reflectivity is between a section of a rough surface soaked with oil and another that is not. This will help us better understand the effects of oil and how the varying quantities of oil on a rough surface affects the reflectivity of rough surfaces with different surface roughness. These as well as the calibration set up for the measurements would be investigated next, and the results thoroughly analysed and extensively discussed.

5.5. Final Reflectivity Measurements – Calibration Methodology & Set up

Figure 5.42 shows the experimental calibration set up for an empty tray with dimensions 1m x 1m. The actual height of the antenna from the ground is 1.03m and this height is enough for the antenna beamwidth to cover not just the tray but for the illumination area to also extend beyond the dimensions of the tray on the floor. The distance between the near edge of the tray and the antenna is about 1.74 m, while the distance from the antenna to the far edge of the tray is about 2.64m. Corner reflectors with dimensions 22 cm x 22 cm are placed one at a time around the tray to identify the illumination area.

EXPERIMENTAL SET UP FOR EMPTY TRAY

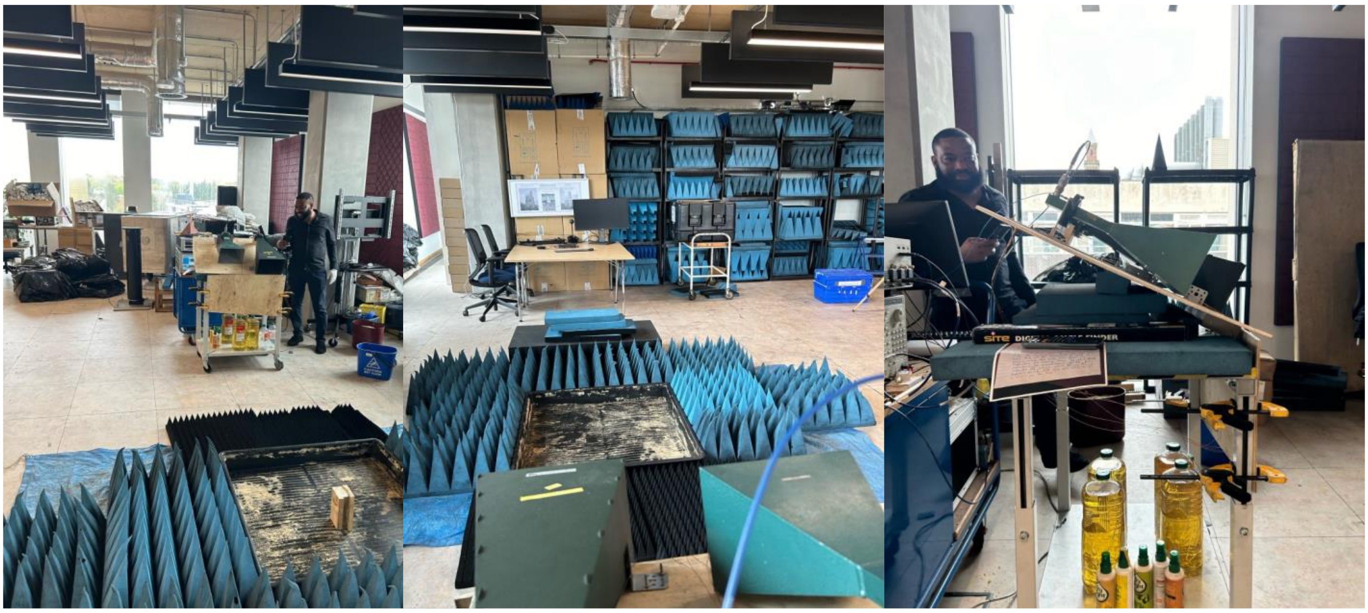

Figure 5.42: Experimental setup for an empty tray with dimensions 1m x 1m

For this illumination area to be identified and marked, the oscilloscope is looked at to pick up points where the reflections from the reflectors are coming down by about 10 dB relevant to the measurement of the first reflector which is placed at the exact centre or middle of the tray. Please also note that only one reflector at a time is placed on the floor for this calibration. The angle of illumination is 25.6° as shown in Figure 5.43 which is the experimental set up for a flat sand profile. The same angle of illumination was maintained throughout the experiment.

EXPERIMENTAL SET UP FOR FLAT SAND PROFILE

Figure 5.43: Experimental setup for a flat sand profile

To calculate the distance or the slant range ***R*** between the antenna and the middle of the tray, we use equation 5.6 as highlighted below

$$a \approx R\varepsilon \frac{1}{\sin\alpha} = \frac{h_R \varepsilon}{(\sin\alpha)^2} \tag{5.6}$$

Where a = twice the radius of the tray i.e. 2 x r = $\sqrt{2}$ m, h_R is the minimum vertical height of the antenna from the ground to allow for proper illumination = 0.75m, Ɛ = antenna beamwidth which is 20°, grazing angle α is 25.6°. So, from equation 5.6, ***R*** = 1.78 m

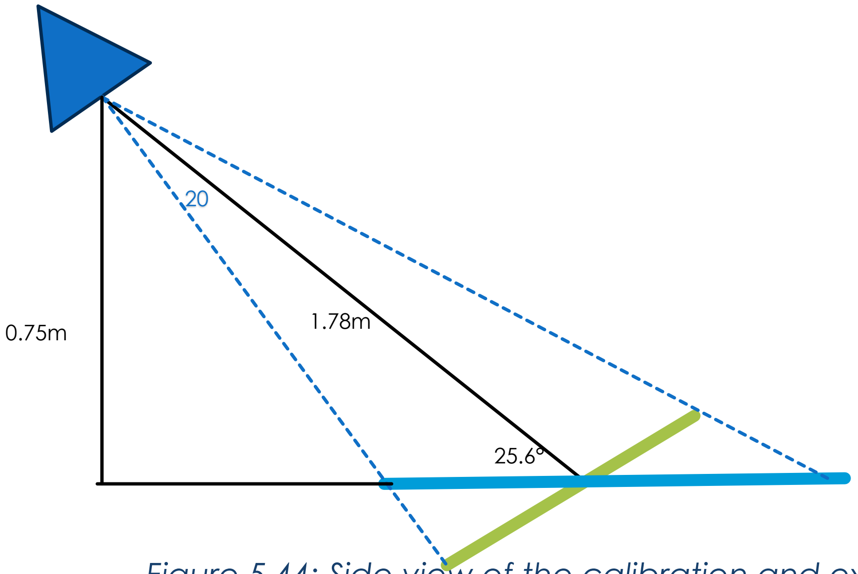

20° between the two dotted lines

R *range = 1.78 m*

ϵ *beamwidth = 20°*

α *grazing angle (25.6°)*

h_R *vertical height*

Figure 5.44: Side view of the calibration and experimental setup

Figure 5.44 shows the side view of the calibration setup and a pictorial description of the experimental set up. The vertical height as well as the grazing angle was fixed, measured and maintained for all the calibration and experiments. Throughout the measurements, a corner reflector was also placed after the far edge of the tray but still within the illuminated area. Reflection from this corner reflector served as the reference throughout the measurements. The corner reflector was placed at about 3 range resolutions from the far edge of the tray.

Before the commencement of the calibration and subsequent measurements, an empty tray is placed in the middle as shown in Figure 5.42. It is expedient to understand the reflection from the tray edges as well as the anechoic materials. Once that was done, the second step was to fill the tray with sand, making the sand at the level of the tray walls or edges. Once this is recorded, then other experiments which involve the rough surface profiles followed. However, whatever the shape of the sand profiles, the sand at the walls or edges of the tray were always kept at the same level as the tray wall to minimise reflections from the walls and edges of the tray that is not fully covered with sand. These results were analysed prior to commencement of the main experiments which had to do with the rough surface profiles and the introduction of oil onto the rough surface. These results as well as the measurement results will be discussed shortly but let us give a brief description of the experimental set up.

Figure 5.45 shows a block diagram of the experimental setup. An arbitrary waveform generator (Tektronix AWG7102) is used to create the waveform that we are transmitting. We are transmitting a pulsed signal with 1ns pulse duration, a pulse repetition time (PRT) of 10 ms, and at a carrier frequency of 4 GHz for 200 pulses. The 10 dB attenuator which is connected to the AWG is to ensure that the input power into the first amplifier is not too high. This is now connected to a power amplifier (ZHL-4240+) which has a noise figure NF of 8 dB and a gain of 42dB to increase the power of the transmit signal. From there, it goes through a 3 dB attenuator between the amplifier and the antenna to mitigate any reflections in the cable. Then on the receive arm, the antenna goes to the 3 dB attenuator to stop reflections again. From there, it goes to the power amplifier (ZX60-83) which has a noise figure NF of 1.5 dB and a gain of 22 dB and from there to the oscilloscope (Tektronix DPO72304SX) for making and recording the measurements. The range resolution is 15 cm.

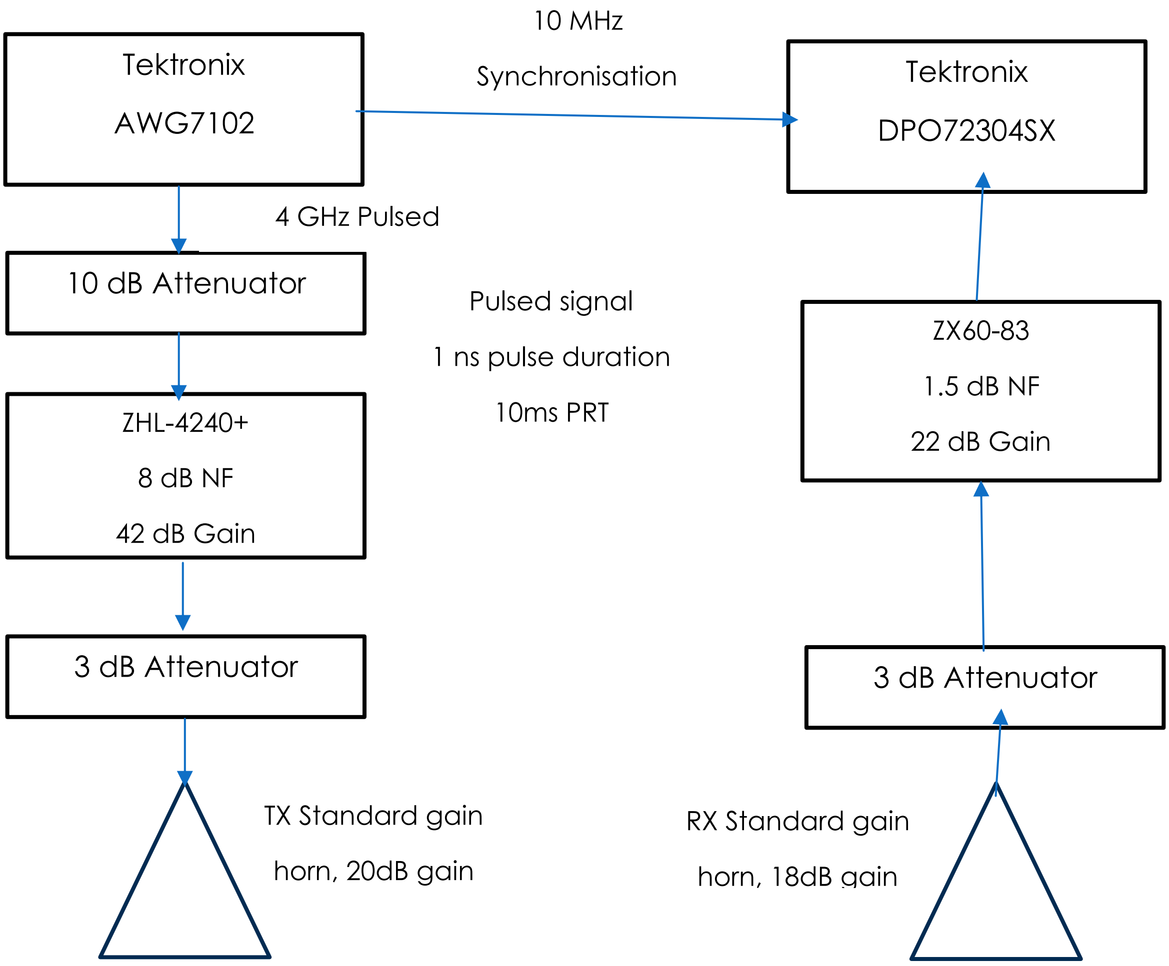

Figure 5.45: Block diagram of the experimental set up

Figure 5.46 shows the calibration results of the empty tray without sand. The largest peak could be attributed to the fact that the tray is reflective, and that peak is just a bright spot in the middle of the antenna beam. The area of interest for us in the plot is between 25 and 31 ns which corresponds to about 90 cm which is similar to the length of the tray (1m)

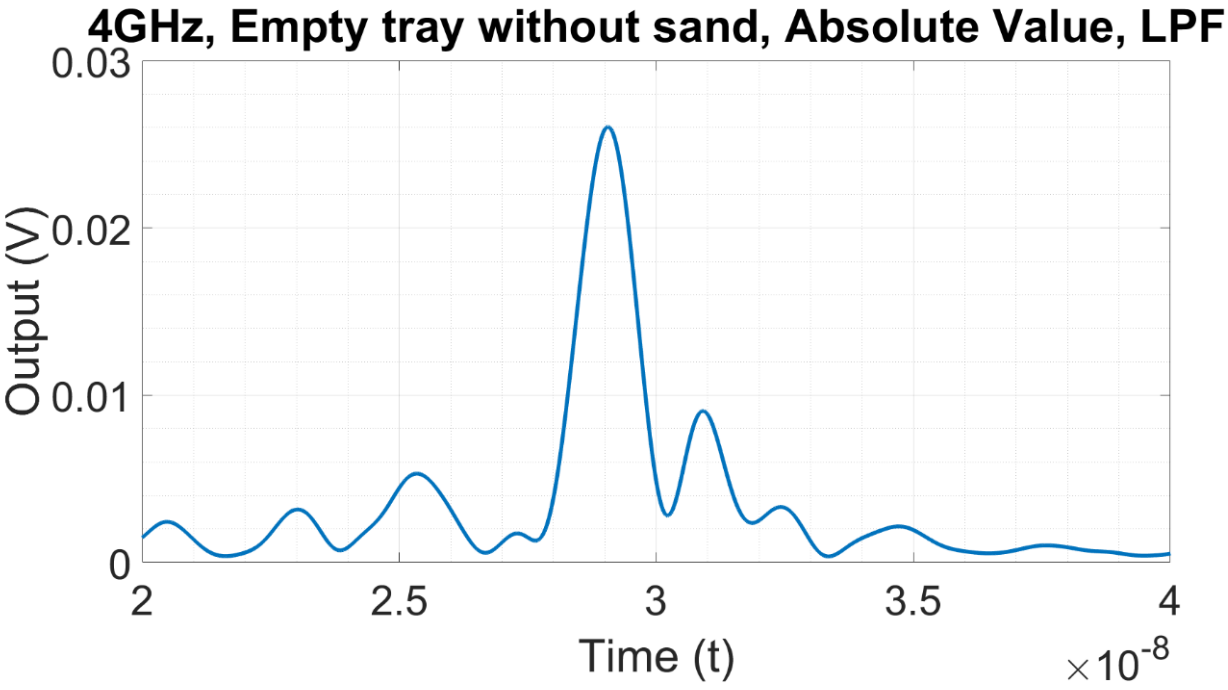

Figure 5.46: Calibration result of empty tray without sand

Figure 5.47 shows the calibration results of an empty tray without sand and two corner reflectors placed outside the tray, specifically one before the near edge of the tray and the other corner reflector after the far edge of the tray which has a bigger dimension than the corner reflector close to the near edge of the tray. They appear at the 23ns and 36 ns mark on the plot. From the figure, we can also see that there is a subdued peak right at the middle of the tray, at 29 ns which also aligns with the explanation given in Figure 5.46 that the tray is reflective, and the peak is just a bright spot in the middle of the antenna beam

Figure 5.48 shows the calibration results of an empty tray without sand and a small sphere of radius 3.2 cm placed at the middle of the tray. From the figure, we can see that the peak at about 28.5 ns corresponds to the position of the sphere in the middle of the tray. The reflectivity also tallies with what is expected of a sphere of such size and dimension. Please note that for this figure, 2 corner reflectors were placed at the near and far edges of the tray which corresponds to 23.5 ns and 36.5 ns respectively.

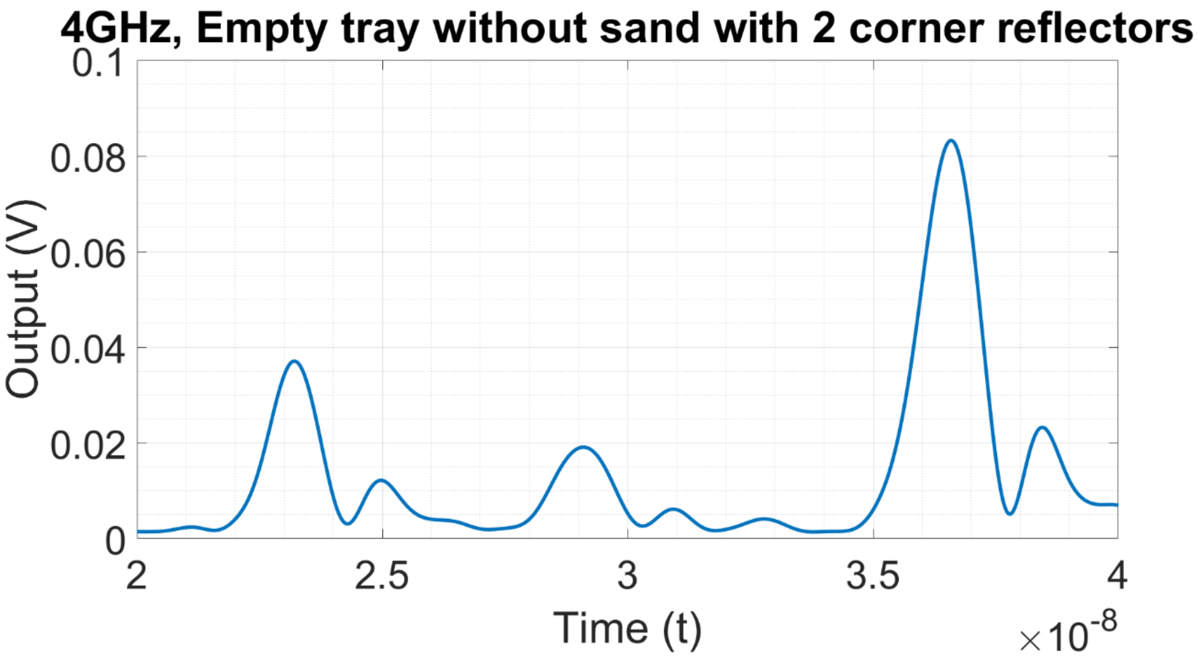

Figure 5.47: Calibration result of empty tray with two corner reflectors

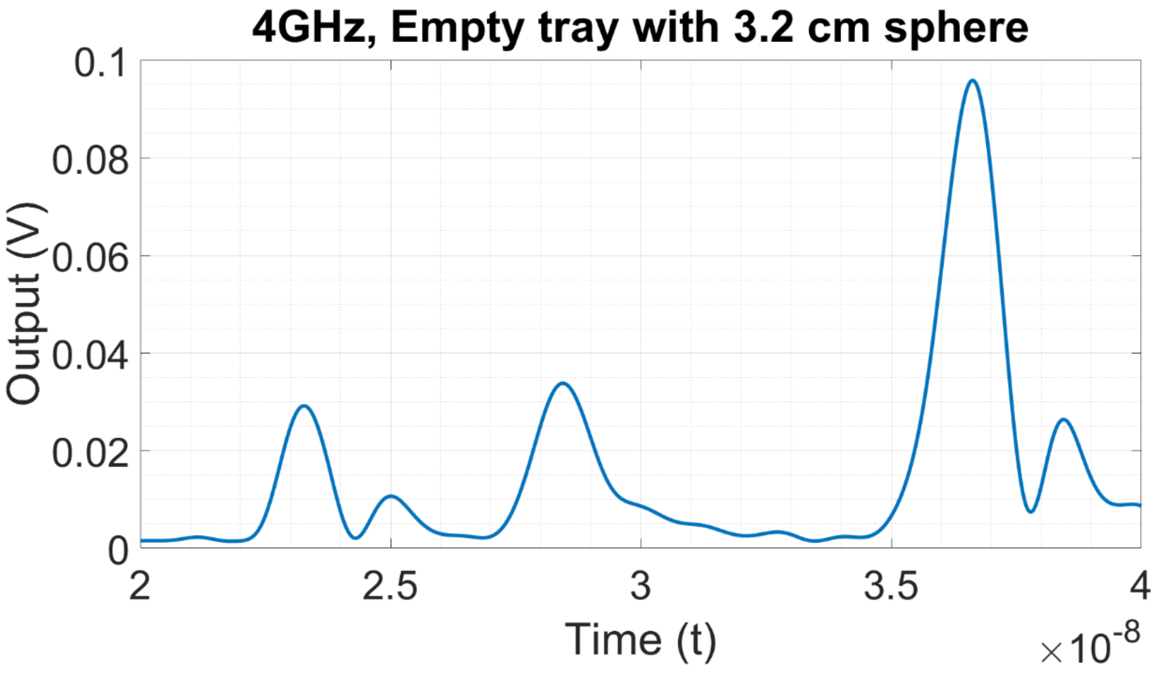

Figure 5.48: Calibration result of empty tray with a sphere of radius 3.2cm

Figure 5.49 shows the calibration results of the flat dry sand, which is for the figure shown in figure 5.43. In the calibration for this flat dry sand, please also note that 2 corner reflectors were placed towards the near and far edges of the tray which corresponds to the 23 ns and 36.5 ns positions respectively to give some sort of boundary or demarcation to the exact position of our tray. Also note that for the measurements for the actual profiles and introduction of oil which shall be shown hereafter, there is no corner reflector positioned at the near edge of the tray. From this Figure 5.49, the peak at the middle of the flat sand is the reflection from the sand which is closely positioned at the walls or far edge of the tray.

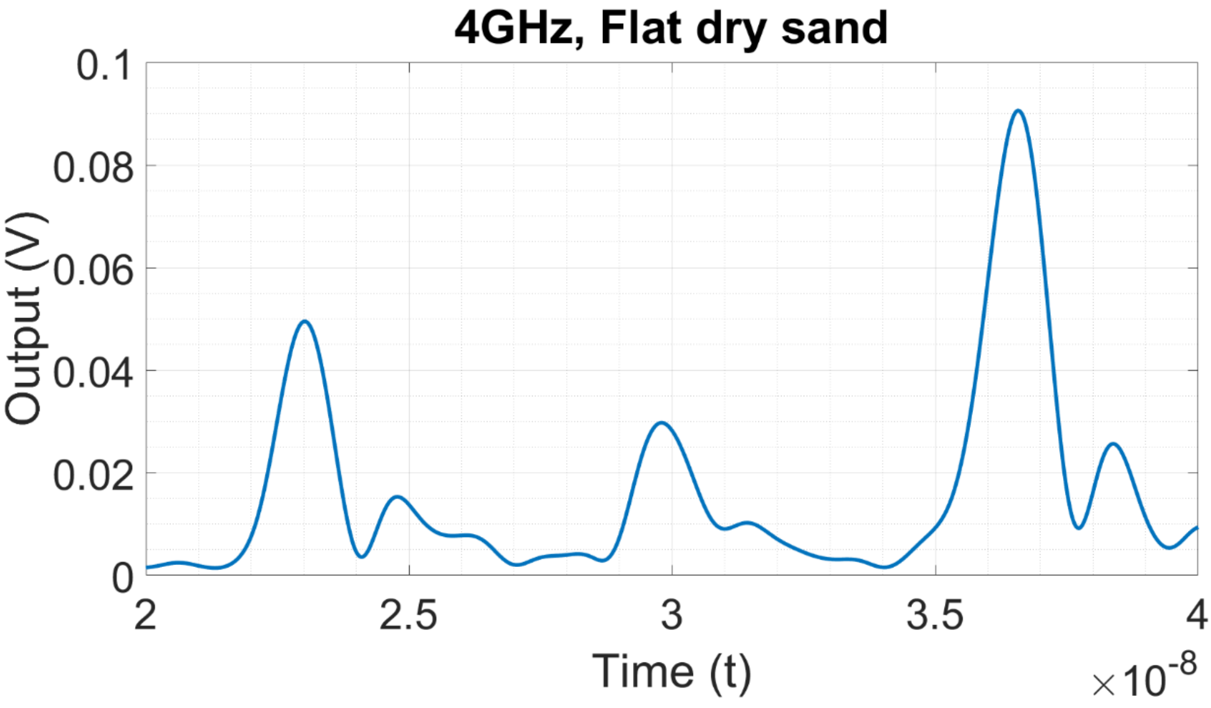

Figure 5.49: Calibration of sand filled tray with a flat profile

5.6. Final Reflectivity Measurements – Rough Surface Profiles and Oil

Now we shall explore and consider the results from the final reflectivity measurements with the rough surface profiles as well as the introduction of varying quantities of oil. Figure 5.50 shows the dry flat sand profile, 7 cm rough surface profile as well as the 14 cm rough surface profile without oil.

Figure 5.50: Dry Flat sand profile as well as 7cm & 14cm rough surface profiles

Figure 5.51 shows the reflectivity results for dry flat sand, 7 cm rough surface profile as well as 14 cm rough surface profiles. From the results, we can see that the 14 cm rough surface profile has a higher reflectivity compared to the 7 cm rough surface as well as the flat sand profiles. The large peak at about 3.8 m shows the position of the corner reflector placed towards the far edge of the tray to help us know the position of our tray during processing. The tray covers from 2.3 m to 3.3m (which is equivalent to 1m) while the rough surface profiles cover from about the near edge of the tray which is about 2.5 m to 3.15m which is equivalent to the region covered by the 'grooves' or 'ridges' of the rough surface profiles and this is about 65 cm as extensively discussed and analysed in section 5.4.

An average of the magnitudes between 2.5 m and 3.15 m for each of the scenarios i.e. flat sand, 7 cm and 14 cm rough surface profiles is shown in Figure 5.52. This is done so that we could appreciate the differences in dB between any of the profiles at the area of interest. From the figure, we can see that there is a 12 dB increase in magnitude between the flat sand & the 7 cm profile, while there is a 13.5 dB increase for the 14 cm profile with respect to the flat sand

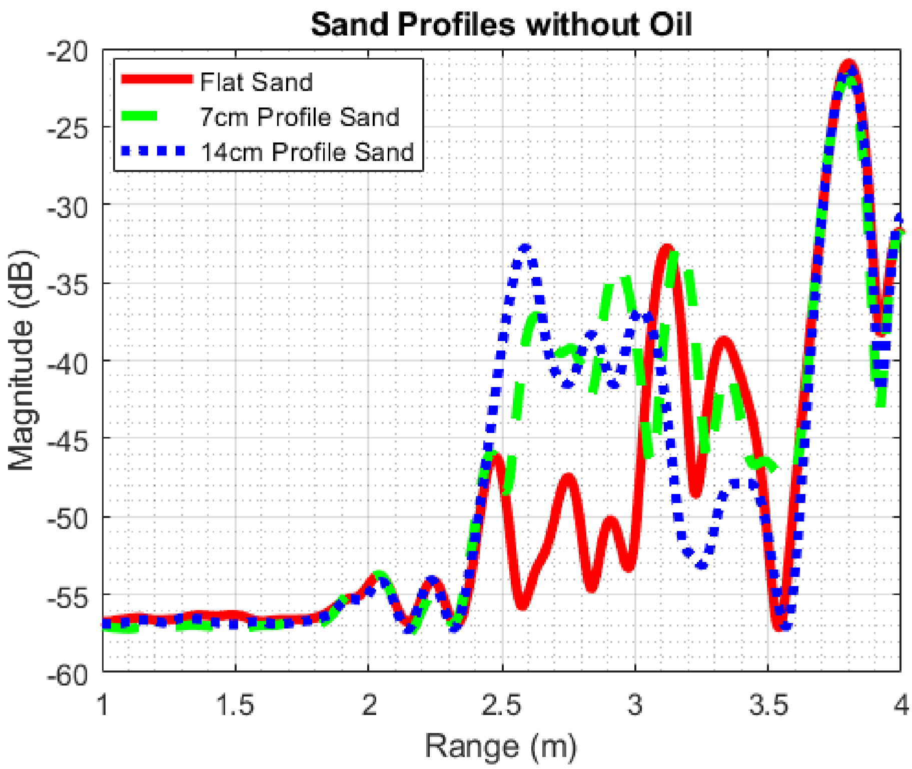

Figure 5.51: Reflectivity results from the dry flat sand, 7cm and 14cm rough surface profiles

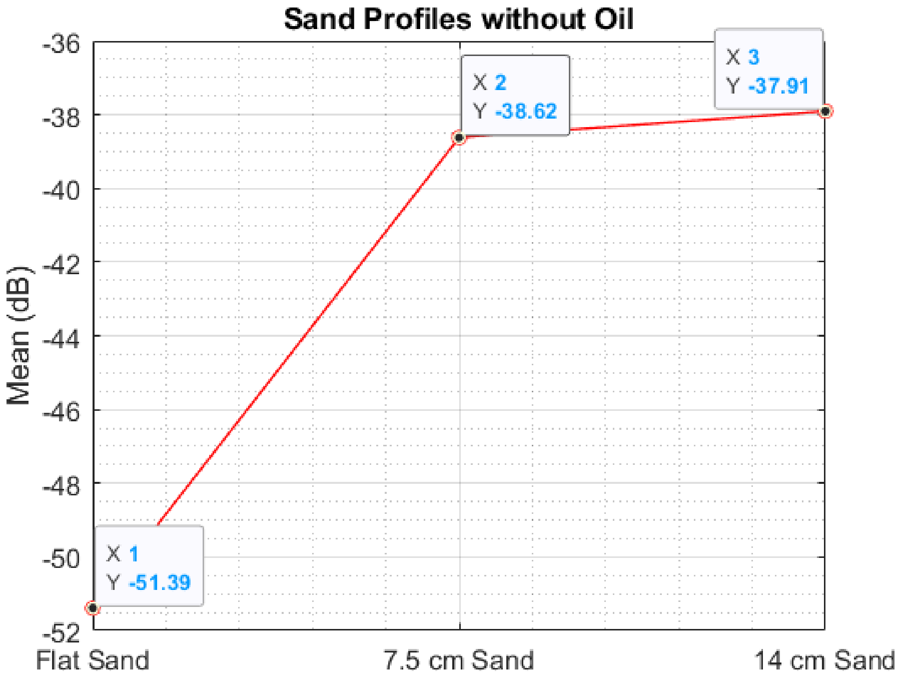

Figure 5.52: Average of the various sand profiles without oil

The next step is to now consider the effect of varying quantities of oil on the various rough surface profiles starting with the 7 cm rough surface. Figure 5.53 shows the experimental setup for the 7 cm rough surface profiles with varying levels of oil application. The oil levels varied from 0L to 9L of oil. Not all the oil levels have been shown in Figure 5.53. The quantity of oil used was sufficient to cover just one half of the tray which is the area under consideration.

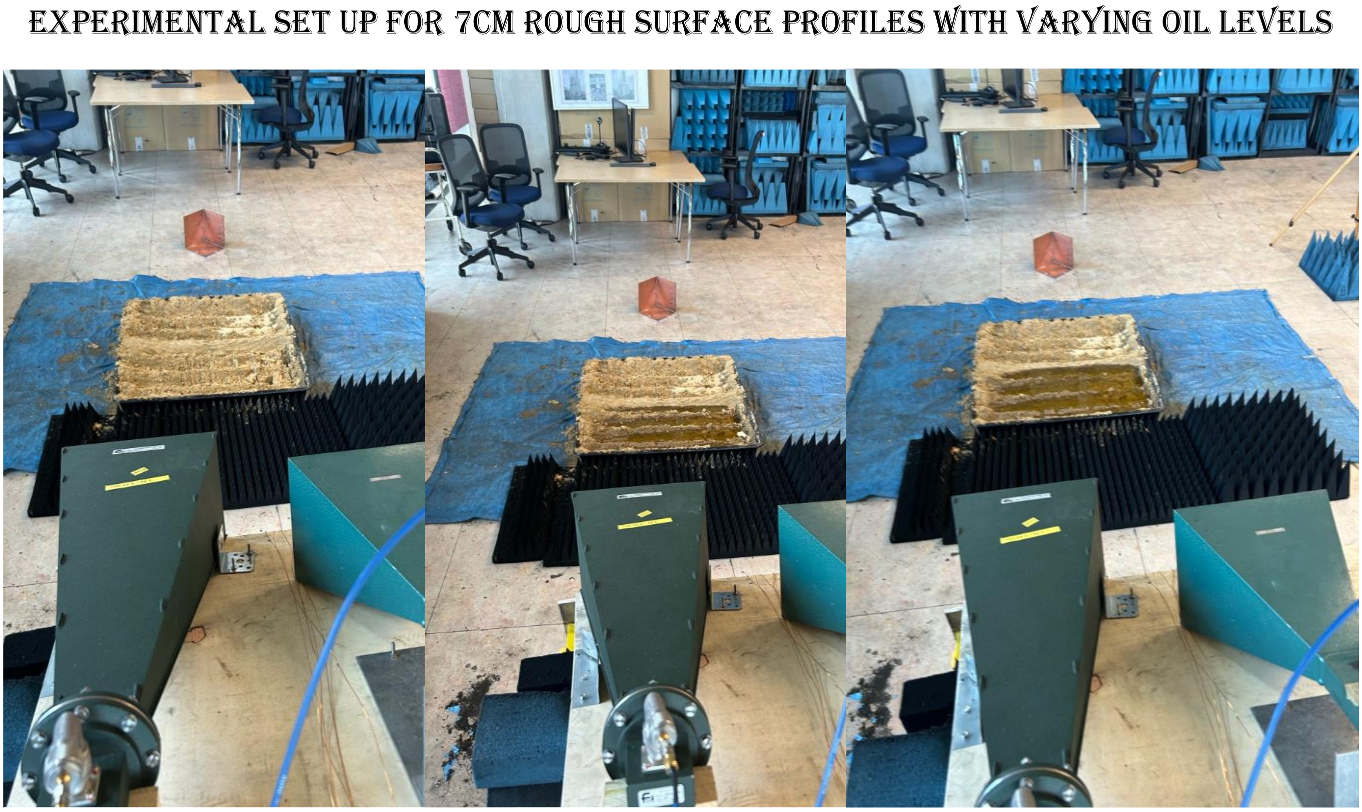
EXPERIMENTAL SET UP FOR 7CM ROUGH SURFACE PROFILES WITH VARYING OIL LEVELS

Figure 5.53: Varied applications of oil (0L to 9L) on 7 cm rough surface profile

Figure 5.54 shows the reflectivity results from the varied application of oil on the 7 cm rough surface. From the figure, we can see that the ‘No Oil’ had the highest reflectivity while the ‘9L Oil’ had the lowest reflectivity and this is line with what is expected, where an increase in the application of oil leads to a reduced reflectivity as previously and extensively discussed and analysed. Now the next step is to get the average for the area under consideration.

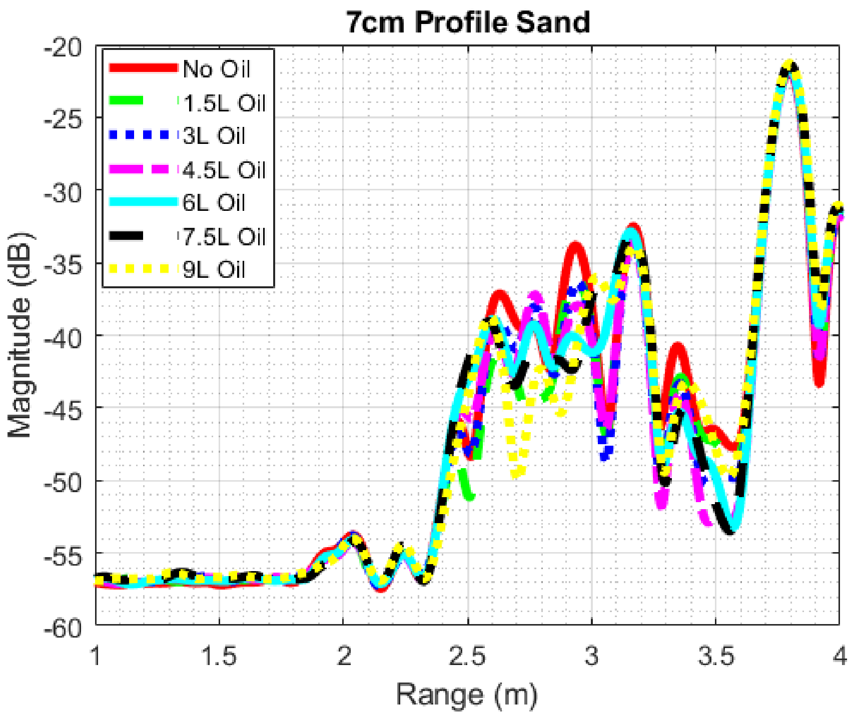

Figure 5.54: Reflectivity results from the varied application of oil on a 7 cm rough surface

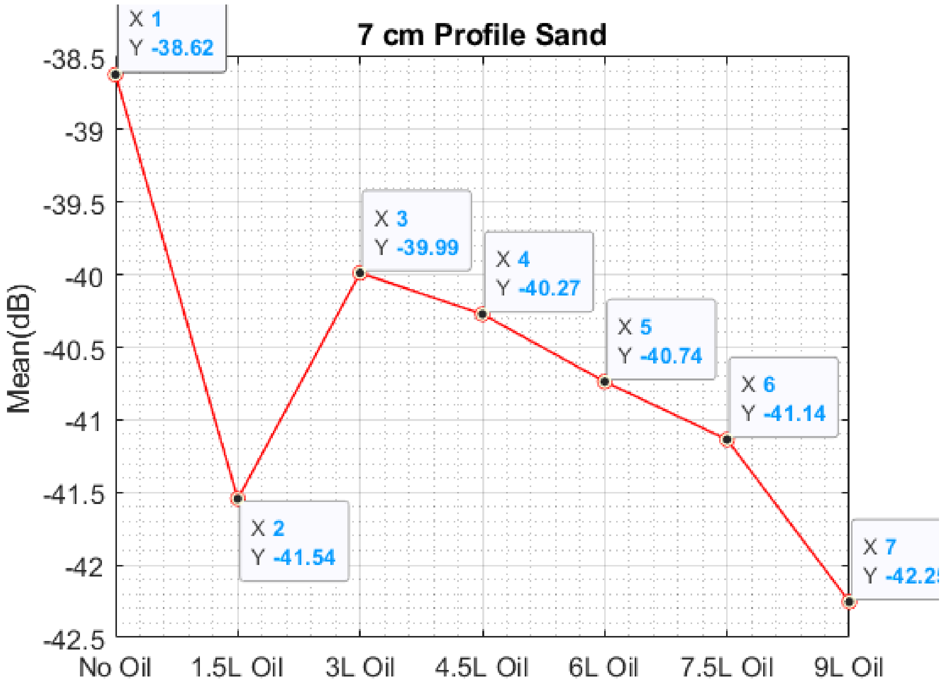

Figure 5.55: Average reflectivities of the varied applications of oil on the 7cm rough surface

An average of the magnitudes between 2.5 m and 3.15 m for each of the scenarios i.e. No Oil to 9L oil is shown in Figure 5.55. This is done so that we could analyse the differences in reflectivity between each stage of the application of oil within the area of interest. From the figure, we can see that the reflectivity decreases as the application of oil also increases. There is about a 4 dB decrease in reflectivity between the 7 cm rough surface when there is no oil and the same rough surface that has been soaked by 9L of oil, probably emanating from oil leaks/spills. This 4 dB difference in reflectivity is quite significant and if the quantity of oil continues to increase, it is envisaged that the difference in reflectivity will also continue to increase more than the 4 dB obtained for 9L oil. The implication of this is that, if we have a 7 cm rough surface and oil spills onto it from say our pipeline infrastructure, then our radar system will be able to detect a 4 dB difference in reflectivity for that rough surface and at about 9L oil. On the average, it implies every dB difference in reflectivity equates to about 2L of oil leaks for a 7 cm rough surface.

Furthermore, considering Figure 5.55, it appears there is a small dB difference across oil levels, which might make classification a bit difficult with only Mean(dB). As a possible solution, additional features, and not just mean dB, can be used. Some of these additional features include peak values, skewness, time delay, as well as waveform shape metrics. Also grouping similar oil levels to reduce sensitivity to small differences could be considered. The unexpected dip at 1.5L is likely due to uneven spreading, leaving patches of dry sand. This leads to complex reflections, possibly more destructive interference hence the sharp dip.

Let us now consider the effect of varying quantities of oil on the 14 cm rough surface. Figure 5.56 shows the experimental setup for the 14 cm rough surface profiles with varying levels of oil application. The oil levels varied from 0L to 9L of oil. Not all the oil levels have been shown in Figure 5.56. When this figure is compared to figure 5.53, the quantity of oil used which is 9L did not cover the entire half of the tray due to the variation in surface roughness. At the 7cm rough surface profile, the 9L oil covered the entire half of the tray, but in this 14 cm rough surface, the quantity of oil was just halfway through the rough surface profile since the 14 cm rough surface is double the initial rough surface profile of 7 cm. Since the 9L oil covered the tray in the 7 cm rough surface, the 9L oil for the 14cm rough surface was just halfway through for the area under consideration.

Figure 5.57 shows the reflectivity results from the varied application of oil on the 14 cm rough surface. From the figure, we can see that the 'No Oil' had the highest reflectivity while the '9L Oil' had the lowest reflectivity and this is line with what is expected, where an increase in the application of oil leads to a reduced reflectivity as extensively discussed & analysed previously

EXPERIMENTAL SET UP FOR 14CM ROUGH SURFACE PROFILES WITH VARYING OIL LEVELS

Figure 5.56: Varied applications of oil (0L to 9L) on 14 cm rough surface profile

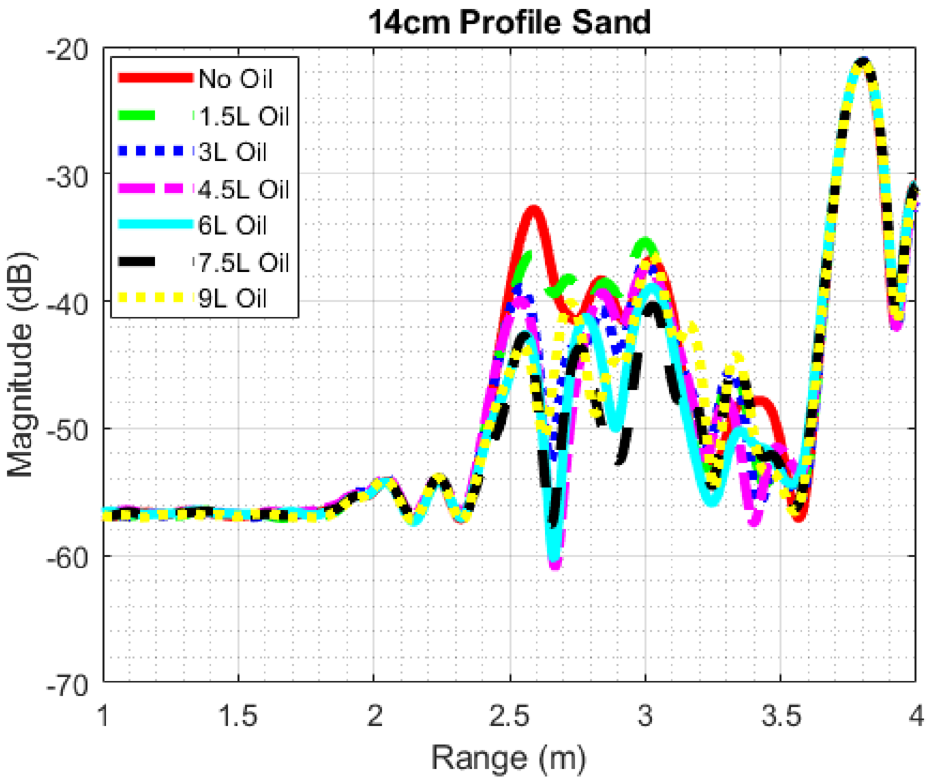

Figure 5.57: Reflectivity results from the varied application of oil on a 14cm rough surface

An average of the magnitudes between 2.5 m and 3.15 m for each of the scenarios i.e. No Oil to 9L oil is shown in Figure 5.58. This is done so that we could analyse the differences in reflectivity between each stage of the application of oil within the area of interest. From the figure, we can see that the reflectivity decreases as the application of oil also increases. There is about a 9 dB decrease in reflectivity between the 14 cm rough surface when there is no oil and the same rough surface that has been soaked by 7.5L of oil, probably emanating from oil leaks/spills. This 9 dB difference in reflectivity is quite significant and if the quantity of oil continues to increase, it is envisaged that the difference in reflectivity will also continue to increase more than the 9 dB obtained for 7.5L oil. The implication of this is that, if we have a 14 cm rough surface and oil spills onto it from say our pipeline infrastructure, then our radar system will be able to detect a 9 dB difference in reflectivity for that rough surface. On the average, it implies every dB difference in reflectivity equates to about 1L of oil leaks for a 14 cm rough surface. This makes sense because every parameter for 7cm earlier considered is either halved or doubled as appropriate depending on the parameter.

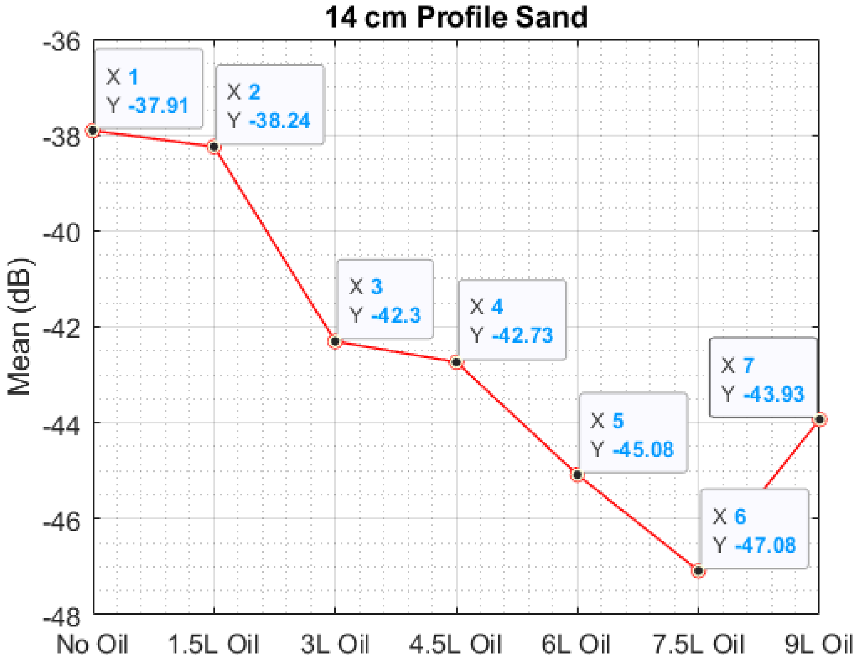

Figure 5.58: Average reflectivities of the varied applications of oil on the 14 cm rough surface

Furthermore, and following on from the previous discussions, a comparative evaluation of radar backscatter magnitudes is measured across flat, 7cm, and 14 cm sand profiles both without oil and with varying oil volumes (1.5L to 9L). The 7 cm surface profile offers optimal dielectric discrimination, showing significant variation in waveform structure with oil application. The 14 cm profile demonstrates reduced sensitivity to oil level variations, likely due to internal multiple scattering or roughness-induced noise. Flat sand provides limited utility for classification, with sharp but isolated reflections. This research confirms the nonlinear interplay between surface geometry and dielectric loading, supporting the development of more accurate radar-based classification tools in environmental and geotechnical applications. Table 5.5 shows a comparative evaluation of radar backscatter magnitudes measured across flat, 7cm and 14cm sand profiles, both without oil and varying oil volumes.

Table 5.5: Comparative evaluation of radar backscatter magnitudes across flat, 7cm and 14cm sand profiles with varying oil volumes and without oil

Profile Type	Peak Amplitude Range (dB)	Backscatter Pattern	Oil Sensitivity	Key Insight
Flat Sand (No Oil)	-55 to -25	Sharp late peak near 3.8 m; fewer oscillations before peak	Not applicable	Flat profile gives clean return but lacks surface texture detail
7cm Profile (No Oil)	-55 to -30	Multiple strong peaks across 2.5–3.5 m; visible ripple structure	High; 3L–6L oil affects mid-range peaks strongly	7cm is highly sensitive to surface and dielectric changes
14cm Profile (No Oil)	-55 to -30	Similar to 7 cm but more chaotic; peak broadening in 2.5–3.5 m	Moderate; differences exist but curves cluster more tightly	14cm may enter a multiple scattering regime with less clarity
7cm Profile (1.5–9L Oil)	-55 to -30	Amplitude decreases with more oil; pattern still structured	1.5L–6L shows gradual suppression; higher oil more damped	7cm profile provides optimal resolution for oil classification
14cm Profile (1.5–9L Oil)	-65 to -30	Heavier oil dampens mid-range peaks; waveform becomes dense	1.5L–9L shows tighter clustering; oil levels harder to differentiate	Beyond 6L oil, detection resolution decreases significantly

In conclusion, Table 5.6 presents a comparison of the mean reflectivity (in dB) for sand surfaces with varying roughness (flat, 7 cm, and 14 cm profiles) under different levels of oil application.

Table 5.6: Effect of Increasing Oil Quantity on Mean Reflectivity (dB) for Different Surface Roughness Profiles

Dielectric	Flat sand (mean mag dB)	7 cm (mean mag dB)	14 cm (mean mag dB)
No Oil	- 51.39	- 38.62	- 37.91
1.5 L		- 41.54	- 38.24
3 L		-39.99	- 42.30
4.5 L		- 40.27	- 42.73
6 L		- 40.74	- 45.08
7.5 L		- 41.14	- 47.08
9 L		- 42.25	- 43.93

5.7. Summary

In this chapter, we have looked at the experimental plan and set up for our measurements as well as the methodology for these measurements. The methodology for a smooth conduct of the experiments have been extensively discussed and considered. The calibration of the experimental set up was also thoroughly investigated and the results also analysed in detail. The three rough surface profiles were used in the measurement to ascertain the reflectivity of oil from the varied rough surfaces. The results were also compared to the simulation results, and both results i.e. experimental, and simulation showed a trend or relationship between the roughness of a lossy surface and the reflectivity from a rough surface. The rougher the surface, the higher the reflectivity and vice versa. This implies that oil spills and leaks can be easily detected from a rough surface than from a smooth surface. Furthermore, as the quantity of oil increases on the rough surface, the reflectivity reduces, and this same trend was noticed both for the simulations and the experiments. It is noteworthy to also mention here that the experimental results were also verified theoretically, and the results aligned with each other. In the final reflectivity measurements, the results obtained were clearer and better and aligned more with what was expected. The 14 cm rough surface profile had about a 10 dB difference between the rough surface without oil and the rough surface with 7.5L of oil. This 10 dB difference is significant because it shows us how easy it is to differentiate between both dielectrics. In the same vein, the 7 cm rough surface profile had about a 4 dB difference between the rough surface without oil and the rough surface with 9L of oil. This 4 dB difference is significant because it is about half the difference obtained for the 14cm rough surface profile and the 14 cm rough surface profile is double the 7 cm rough surface profile. Finally, the implications and interpretations of the RCS results of various dielectric materials was extensively analysed and discussed. As envisaged, the RCS for larger surface areas was higher compared to smaller surface areas. The results in this section also indicate that as we fill up the surface with oil, the reflectivity decreases by a lot i.e. about 4 dB for a 7 cm rough surface and about 10 dB for a 14 cm rough surface.

Furthermore, like we have seen, the experimental models use structured shapes to the surfaces and ridges while the theoretical models use random surfaces as seen in Chapter 4. The differences in the structure of the rough surfaces between the experimental model and the theoretical model arise primarily from practical fabrication constraints and the nature of numerical modelling approaches. In the experimental setup, a structured, periodic rough surface was used because manufacturing truly random surfaces with precise statistical properties – such as a defined rms height and correlation length – is highly challenging. Instead, a simplified, repeatable and well-characterised surface was created to maintain experimental control and ensure consistency across different measurements. The structured shape allows for easier fabrication and reproducibility while still capturing key scattering behaviours relevant to rough surface interactions.

In contrast, the theoretical model used in simulations employs a randomly generated surface profile that more closely follows the statistical nature of natural rough surfaces. This approach is standard in numerical simulations, where a stochastic surface generation method (e.g. a Gaussian algorithm) ensures that the surface meets the desired rms height and correlation properties without the physical limitations imposed by fabrication processes. The randomness in the model allows for more generalisable insights into how waves interact with naturally occurring rough surfaces. The key takeaway is that while both models aim to represent surfaces with similar heights (3.5 cm, 7 cm, and 14 cm), the experimental design prioritises practical fabrication feasibility and measurement repeatability, whereas the theoretical model is free from such constraints and can represent a more statistically accurate random rough surface.

Chapter 6. CONCLUSIONS AND FUTURE WORKS

In this chapter, we shall look at the conclusions from this PhD research work as well as discuss and elaborate on the findings from this PhD thesis. The limitations encountered during the conduct of this research shall be analysed and we shall take a look at the new frontiers as well as the future work that can be extended from this work.

6.1. Conclusions and Findings

This thesis focused on the remote monitoring of pipeline infrastructure for the detection of oil leaks using radar sensors. The main goal of this research was to investigate the methods and potential in using radar sensors as enabling technologies to remotely monitor oil and gas pipeline networks in real time. As oil pipeline networks span hundreds of thousands of kilometres, it is expedient to have a system with reduced complexity and which also rely on minimal signal processing to be able to be used efficiently and at scale.

Specifically, the research assessed the feasibility and performance of using radar sensors to detect temporal changes in an area at both small and large scales. These temporal changes were as a result of change in the roughness parameters, as well as the dielectric properties of the area due to oil leaks from pipeline infrastructure etc. we built an efficient system with reduced complexity and the simplest measurable parameter was the surface reflectivity.

First, a background and literature review were conducted to assess the challenge that would serve as the foundation for the investigation. The actual objectives as well as the novel contributions of this project were outlined and highlighted after careful research of the problem statement.

Next, the fundamentals of radar including a brief history of radar was discussed. The types of radar as well as a thorough description of the radar sensors and waveforms was extensively analysed. A through description of the propagation and target RCS as well as its implications in my experimental setup and simulations was thoroughly analysed. The results verified the theoretical findings. In terms of the experimental work, the experimental results also agreed with the simulation results and verified that our system works perfectly.

Following this, a rough surface model was developed with a thorough analysis of the propagation of electromagnetic waves in varied dielectric materials. The scattering effects and its problems in rough surfaces was extensively discussed and analysed. The implications of scattering in our developed rough surface model were also investigated including the implications of the reflectivity of oil from these varied degrees of surface roughness. The implications in varied dielectrics like dry sandy soil, wet sandy soil, PEC as well as sand soaked with oil was also investigated and the results analysed.

The simulation-based investigation highlights the combined effects of surface roughness and material condition on RCS behaviour. Key conclusions include:

- ✓ Surface roughness is a dominant factor in increasing radar backscatter under dry and oil-contaminated conditions
- ✓ Moisture content suppresses RCS even at higher surface roughness, likely due to dielectric matching and absorption
- ✓ Oil contamination enhances RCS especially at moderate to high surface roughness and larger incident angles – an important insight for remote sensing applications
- ✓ The 14 cm profile consistently demonstrates peak sensitivity across both dry and oil-contaminated simulations, suggesting it is a critical roughness threshold for enhanced detectability

In terms of novelty and contribution, this study offers a comparative RCS analysis across dry, wet and oil-contaminated soils – a rarely combined set of variables in radar scattering research. In addition, the interaction between roughness-induced scattering and material dielectric alterations provides new perspectives for environmental sensing, oil spill detection and terrain classification using radar. The methodology and findings can inform design parameters for GPRs and SAR systems operating over diverse soil conditions.

Furthermore, for the various dielectrics that were combined for each rough surface profile (3.5cm, 7cm 14cm and 21cm) and analysed, the study reveals a clear nonlinear interaction between surface geometry and dielectric composition. Oil contamination not only modifies the dielectric constant but amplifies surface scattering effects, leading to significantly enhanced RCS. Wet conditions consistently attenuate radar backscatter, masking roughness effects and flattening angular response. At extreme roughness (21 cm), dry sandy soil shows comparable or superior radar visibility to PEC, indicating that real-world rough terrain may exceed ideal flat conductors in scattering efficiency under specific conditions. This research therefore also contributes to the design and calibration of remote sensing systems by quantifying how surface and material properties jointly influence radar backscatter.

Now when the various rough surface profiles were filled up with oil which made the rough surfaces smoother, the analyses showed that surface roughness plays a crucial role in radar signal backscatter, with rougher surfaces generally yielding stronger RCS. Oil contamination amplifies this effect, while wet conditions tend to suppress it across all angles indicating that moisture dampens the reflectivity advantage of increased roughness. PEC materials remain highly reflective, although extreme smoothing can reduce their scattering efficiency. This research therefore underlines the importance of surface geometry in EM wave interaction and supports its application in as well as contributes valuable insight for remote sensing, terrain classification, material identification and radar system calibration using radar technologies.

In addition, the surface reflectivity from surfaces with and without oil contamination as a function of surface roughness, aspect angle and frequency were investigated. Furthermore, an experimental campaign in a proof-of-concept environment was conducted to validate findings obtained through electromagnetic wave simulations of soil surfaces considering different parameters. The radar cross section of different dielectric materials with varied roughness parameters when they are contaminated with varying quantities of oil was extensively discussed and analysed as well as their implications in the remote monitoring of pipeline infrastructure for the detection of oil leaks. The results show that there is 10 dB difference in RCS from a 14 cm rough surface without oil and a similar surface that has been soaked with at least 7.5 L of oil. This implies that a litre of oil results in at least 1 dB change in RCS from a rough surface of 14 cm rms height. In addition, there is about a 4 dB difference for that of 7 cm surface roughness for a 9L oil that leaks onto the rough surface. This also implies that 2 L of oil results in a dB change in reflectivity from a rough surface of 7 cm rms height. The results obtained via experiment were also verified via simulations and both results tally and align with each other as have been extensively discussed and analysed. A performance analysis of the analytical and experimental models was also undertaken and compared to what is expected.

Furthermore, when the experimental results were compared with the simulation results for 3.5 cm rms height for a dry sandy soil that has been soaked with oil, the addition of oil on sandy surfaces enhanced radar reflectivity as confirmed by both experimental and simulation datasets. Spraying oil leads to more uniform dielectric enhancement than sequential application, offering more consistent backscatter. Experimental results reveal micro-variations and nonlinear responses likely tied to oil coverage uniformity and surface absorption. Despite some variability, simulation trends and experimental measurements broadly agree, reinforcing model validity. These findings support the development of detection algorithms for oil contamination and improve modelling approaches for complex natural surfaces. Table 6.1 shows 6.1 presents a comparative analysis between the experimental backscatter magnitude plots for a dry sandy soil that has been soaked with oil and the simulated RCS results for dry and oily sandy soil at a surface roughness of 3.5 cm rms height.

Table 6.1: Comparative analysis between experimental and simulation results for the presence of oil on a dry sandy soil with rms height 3.5 cm

Comparison Area	Observation	Key Metrics / Values	Implication / Insight
Backscatter Magnitude (Experimental)	Sprayed oil yields the strongest magnitude peaks; 3rd oil application aligns closely	Max ~ -60 dB (Sprayed Oil); Min ~ -95 dB (1st Oil)	Spraying may lead to more uniform dielectric coverage than layered application
RCS (Simulation)	Oily soil consistently shows higher RCS (~1–2 dB more) than dry soil across angles	Max RCS: ~ -6 dB (Oil), ~ -8 dB (Dry); Min ~ -13 dB	Simulation supports oil-induced backscatter enhancement
Consistency Across Oil Levels	Magnitude response is not linear with oil application—intermediate applications show dips	Best consistency with sprayed and 3rd oil application	Real-world oil distribution complexity influences reflectivity
Effect of Oil on RCS	Oil presence increases average RCS and shifts curve upward compared to dry soil	Oily soil curve consistently ~1.5 dB higher than dry	Useful for detection applications (e.g., spill monitoring)
Peak Locations	Major reflectivity peaks between 1.65 m and 1.8 m in range for experimental plot	Peak observed at ~1.7 m (range)	Critical detection zone in range imaging
Backscatter Clarity	Waveform complexity increases with oil; more distinct ripples and shoulders	More pronounced for later applications	Higher dielectric contrast sharpens backscatter features
RCS Angular Behaviour	Simulation shows smooth RCS progression with clear peak near 75°	Angle θ = 75° gives highest RCS	Supports angular RCS analysis for target identification
Agreement Between Experimental and Simulation	Both confirm oil enhances RCS, though experimental shows more variability	General trend tallies, but experimental has irregular fluctuations	Simulation and experiment reinforce each other, despite local variations

Also, the experimental results were compared with the simulation results for 7 cm rms height for a dry sandy soil that has been soaked with varying volumes of oil for both the simulation and the experimental results. This research provided a comparative analysis of radar simulation and experimental results for a 7 cm rms height sand profile. The goal was to evaluate the impact of physical and dielectric variation on radar backscatter and classification accuracy. From the results, the 7 cm rms height profile is ideal for radar-based surface and dielectric characterisation. Simulation emphasised structural and angular influences on RCS, while experimental tests highlight range-based dielectric response. Real-world complexity introduces ripple structures and minor deviations in experimental outputs. Collectively, these results validate the use of electromagnetic simulation for predictive modelling and enhance the effectiveness of radar in practical sensing applications. Table 6.2 shows comparative evaluation of both simulation and experimental results for a 7 cm rms height sand profile.

Table 6.2: Comparative analysis between experimental and simulation results for the presence of oil on a dry sandy soil with rms height 7 cm

Aspect	Simulation Results	Experimental Results
Surface Type	Dry and Oil-covered 7 cm profile	7 cm profile (Dry, with varying oil)
Tested Variables	Varying RMS heights (1.19 cm to 5.07 cm)	Oil volumes from 0 to 9L
Peak RCS Range (Simulation)	-2 dB to -19 dB depending on angle and surface	N/A (RCS not displayed)
Peak Magnitude Range (Experiment)	N/A (no voltage amplitude shown)	-55 dB to -25 dB depending on oil and range
Oil Sensitivity	Strong response: Original 7 cm gives highest RCS	Clear response to 1.5L–6L oil; 9L becomes dense
Waveform Consistency	RCS varies smoothly with angle	Consistent ripple patterns; structured
Effect of Roughness (RMS)	Higher RMS = higher RCS; clear distinction	Oil level affects signal strength and clarity
Key Agreement	Peak angle responses support experimental backscatter peaks	Backscatter location aligns with high-RCS angles
Key Difference	Angular vs range domain representation	Oil variation studied instead of RMS height
Key Insights	Simulation emphasizes structural change and angle-based variation	Experiment highlights dielectric variation and signal range

Finally, the experimental results were compared with the simulation results for 14 cm rms height for a dry sandy soil that has been soaked with varying volumes of oil for both the experimental and simulation results. This research provided a comparative analysis of radar backscatter responses for a 14 cm rms height sand profile evaluated through both EM simulations and experimental measurements. From the results, the 14 cm profile produced high radar reflectivity, but waveform compression and clustering limit its use for material classification. Simulations affirm the influence of surface geometry on RCS, while experimental results show that oil saturation reduces backscatter contrast. The combination of simulation and experimental domains (angle and range) delivers a holistic view of radar-surface interaction. This research supports the conclusion that the 14 cm rms height profile, while powerful in scattering is less ideal for distinguishing fine dielectric differences. Table 6.3 shows a comparative analysis between the experimental and simulation results for the presence of oil on a dry sandy soil with surface roughness of 14 cm.

Table 6.3: Comparative analysis between experimental and simulation results for the presence of oil on a dry sandy soil with rms height 14 cm

Aspect	**Simulation Results**	**Experimental Results**
Surface Type	Dry and Oil-covered 14 cm profile	14 cm profile with oil volumes from 0 to 9L
Tested Variables	Modified RMS heights (1.89–9.57 cm)	Dielectric variation only (oil volume)
Peak RCS Range (Simulation)	-2 dB to -20 dB depending on angle and height	N/A (RCS not directly plotted)
Peak Magnitude Range (Experiment)	N/A (dB magnitude not shown)	-65 dB to -30 dB across range domain
Oil Sensitivity	Original 14 cm gives strong RCS: peak rises with roughness	Smaller differences between oil levels beyond 3L
Waveform Consistency	High variability; less smooth than 7 cm	Waveforms densely packed; harder to distinguish by oil
Effect of Roughness (RMS)	More scattered angular returns as RMS increases	Oil level flattens response but elevates background signal

Key Agreement	Trends match experimental behaviour at high scatter angles	Magnitude peak ranges align with high-RCS angles in simulation
Key Difference	Simulation uses structural variation; experiment varies oil	Oil variation dampens contrast more than RMS structural change
Key Insights	14 cm enters more complex scatter regime: less ideal for oil classification	Oil dampens signal contrast; 14 cm roughness reduces classification accuracy

6.2. Limitations

In terms of limitations, computing requirements were the major drawback during this research. Most times, the high-performance computing HPC system we are using (BEAR) is scheduled for maintenance occasionally and even when it is not, some of the rough surface models that were meant to run and give a positive update normally crash after a couple of days. It was also difficult to run a couple of models for an extended time (over ten days at least). These computing requirements were escalated and managed as best as we possibly could. Also, the size of the models was also reduced to smaller sizes as best as we reasonably could, and several iterations of these reduced models were conducted to compensate for this and to ensure the same trends were maintained for each model. However, going forward, it would be ideal to perform simulations for an actual rough surface area with bigger dimensions (say 1m x 1m) and analyse the results and compare with the results from the smaller scale (20cm x 20cm).

One of the notable limitations encountered in this project is the difficulty in accurately detecting or distinguishing surfaces with very low roughness, such as the flat or minimally profiled sand scenarios. The reflectivity values for these surfaces often exhibit minimal variation across different oil levels, typically with a narrow dB range (e.g. 1 – 2 dB). This small difference falls within the margin of measurement noise or system sensitivity, making it challenging to classify or confidently detect surface conditions based solely on reflectivity. To mitigate this limitation, a comparative analysis approach would be employed. Instead of relying on single-point measurements or individual reflectivity values, results would be compared across multiple surface profiles (flat, 7 cm and 14 cm) under identical oil conditions. This will allow the identification of relative trends and subtle shifts in reflectivity patterns that would otherwise be indistinguishable in isolation. Additionally, incorporating multiple features – such as peak voltage, waveform shape, or time-domain characteristics – alongside mean reflectivity can improve classification performance and help differentiate between low-roughness scenarios with greater accuracy.

6.3. Outlook / Future Work

In this sub section, we shall look at various ways in which this work can be extended depending on what can be achieved. This work has therefore provided a solid foundation for the future work highlighted below to be executed.

- Analysis of the RCS of dry sandy soil surface with more samples (N = 1000 and above) as well as a larger surface area (1m x 1m and above) but with better and higher computational facilities as well as computing requirements.
- Analyse the experimental RCS indoors when a plant is over the soil sample (a la real-life) and see the difference this will make in the reflectivity measurements
- Incorporate the rough surface model with a chirp signal as part of a radar signal processing system and analyse as well as compare the parameters measured
- Investigate the possibility of introducing 2 antennas with varied polarisations on CST and BlueBEAR and explore as well as analyse both co and cross polarisations for transmit and receive channels. Also investigate the scattering mechanisms when different polarisations are applied to the TX and RX on the rough surface model
- Expanding to other frequency ranges (asides from the frequency ranges previously used) in other to ascertain if they are better suited for detection of oil leaks.
- Explore the use of SAR technique or technology in the remote monitoring of pipeline infrastructure for the detection of oil and gas leaks as well as utilise radar imaging for the detection and identification of oil spills and leaks in pipeline networks.

Typical Specification

Frequency	1 to 18 GHz
Connector type	SMA type jack
Power Handling	40 Watt c.w.
VSWR	Typically < 2:1
Gain	1.3 to 12.8 dBi
Antenna Factor	28.9 to 43.6 dB/m
3dB Beamwidth	23 to 300 degrees
10dB Beamwidth	40 to 300 degrees
Weight	0.7 kg
Size- max.	96 mm x 90 mm x 148 mm long (incl. connector)
Mounting	2 x M5 tapped holes, 38 mm centres
Construction	Aluminium and engineering plastics. Painted.

Typical Antenna Gain / Factor

This is calculated by reference to standard gain horn antennas, and cross checked with reference to the antenna beamwidth, with an estimated error of +/- 0.8dB.

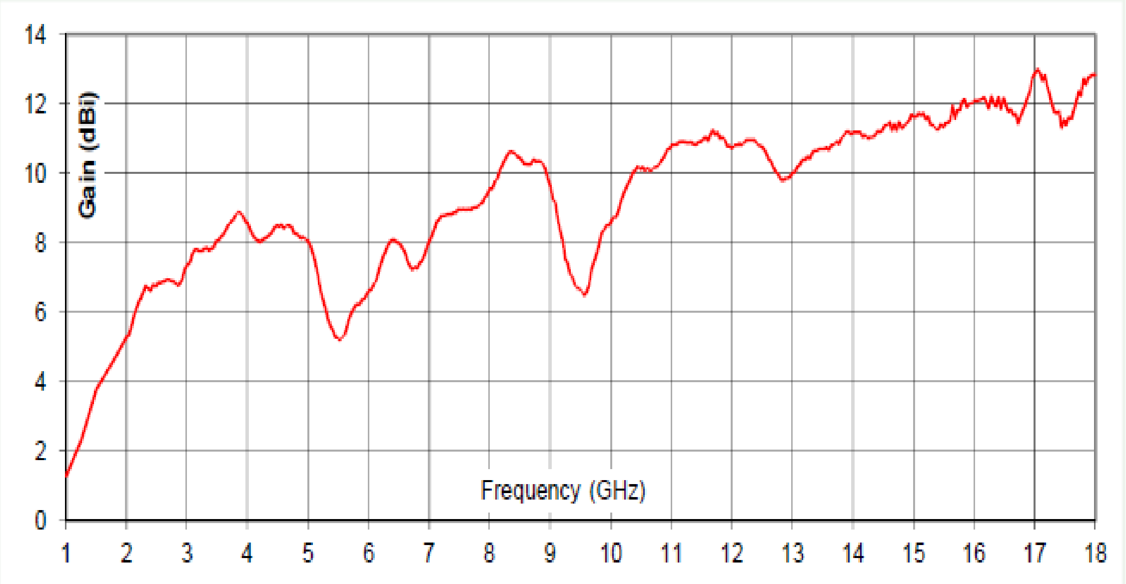

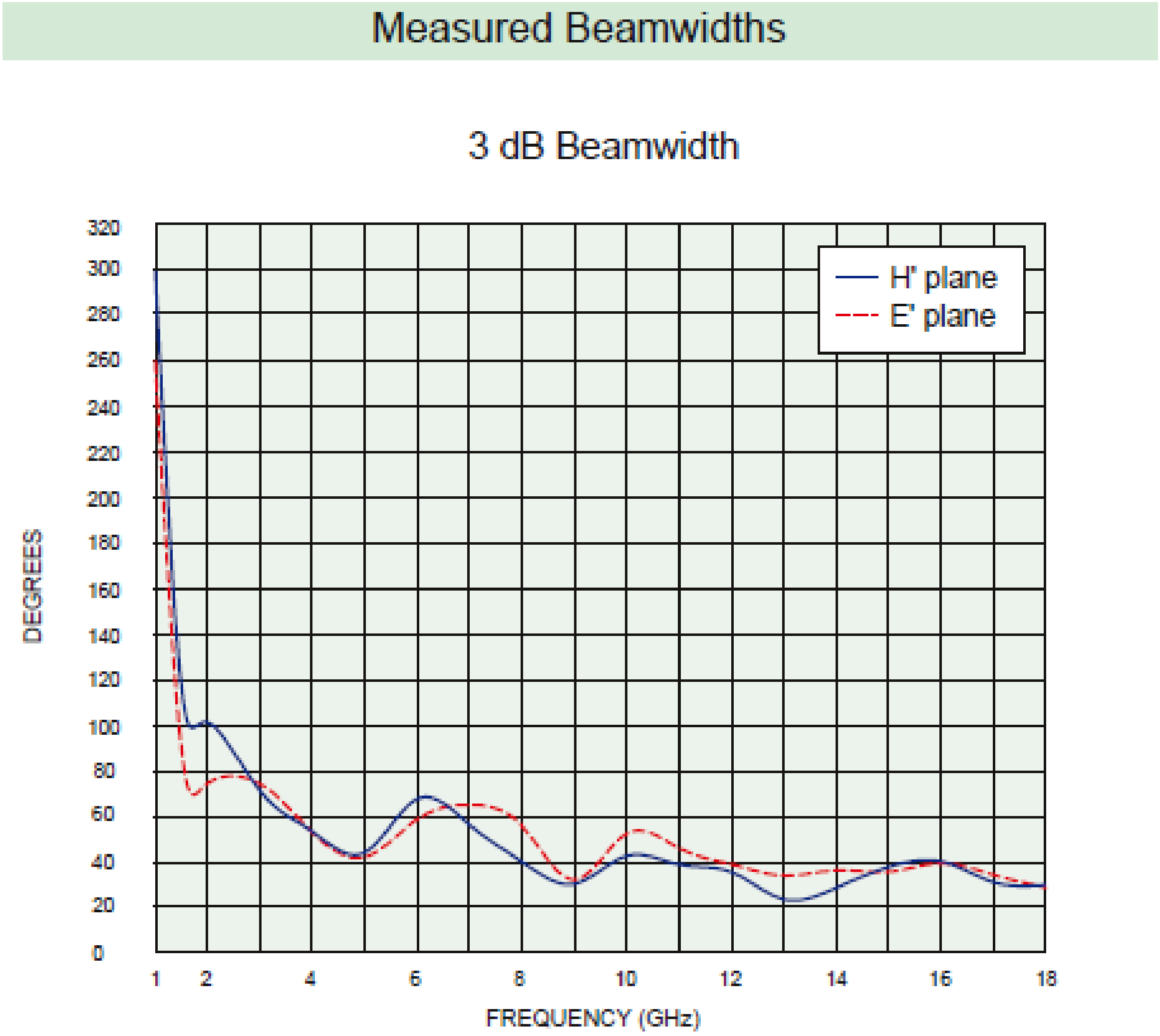

Specification of the white horn antennas as well as the frequency response of the white horn antennas across varied frequencies.

Simulation for different rough surfaces and comparison of the results

The dielectrics considered are dry sandy soil, wet sandy soil as well as the dry sandy soil mixed with oil. The following parameters were utilised in the simulation - ½ m by ½ m rough surface area, rms height of 14cm, with the number (N) of surface points as 20 x 20. The correlation lengths for the simulation were also given as 12.5 cm for one instance and 10cm for another instance.

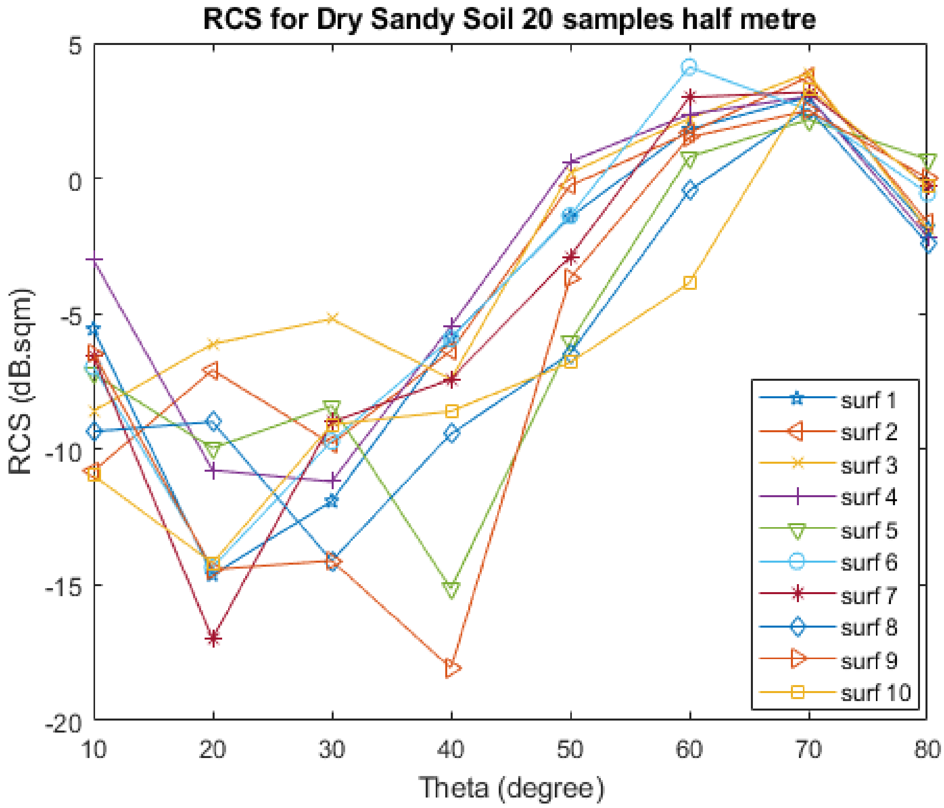

RCS analysis for dry sandy soil with cl 12.5cm and rms 14 cm

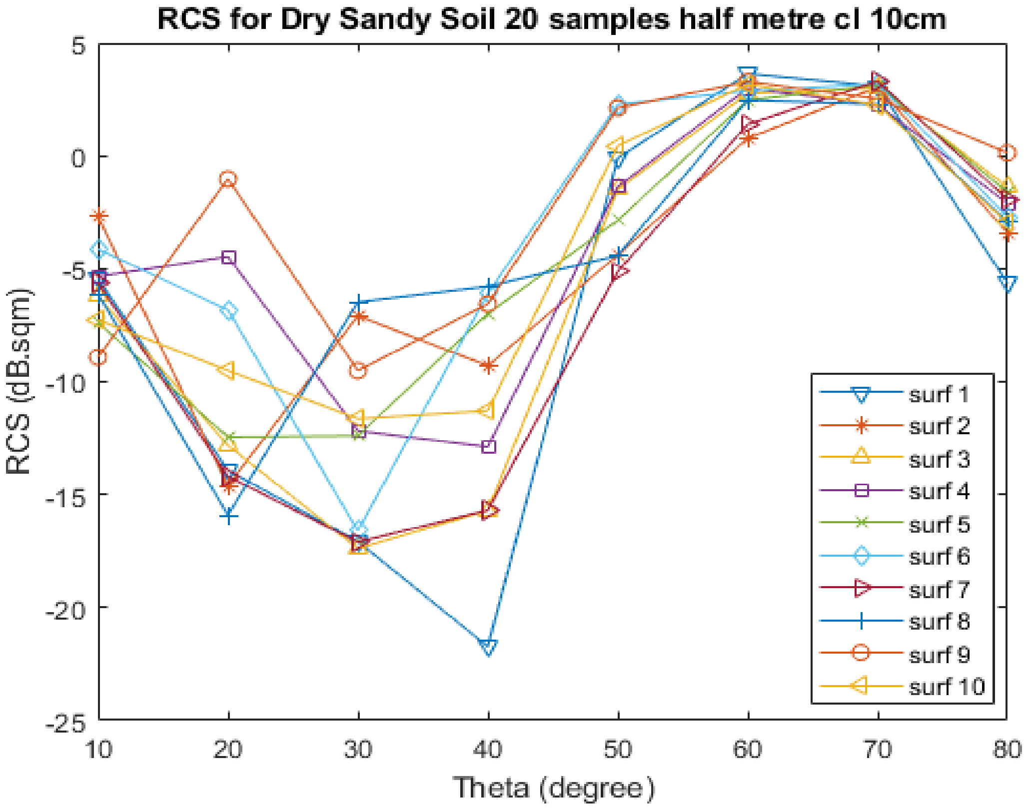

RCS analysis for dry sandy soil with cl 10 cm and rms 14 cm

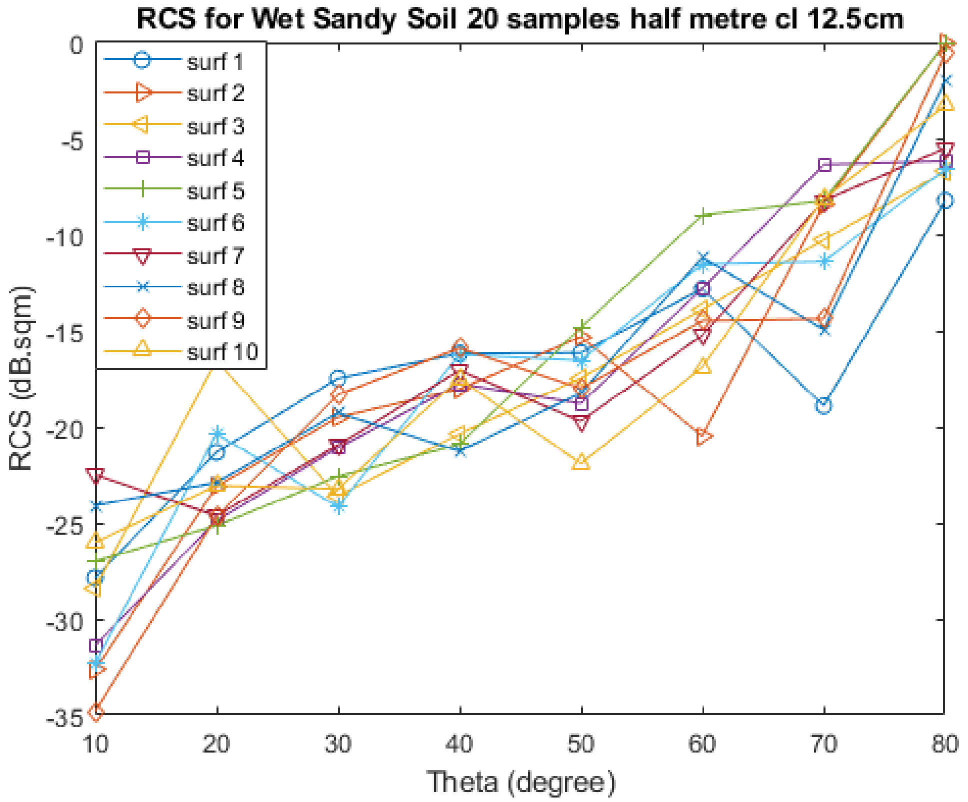

RCS analysis for wet sandy soil with cl 12.5cm and rms 14 cm

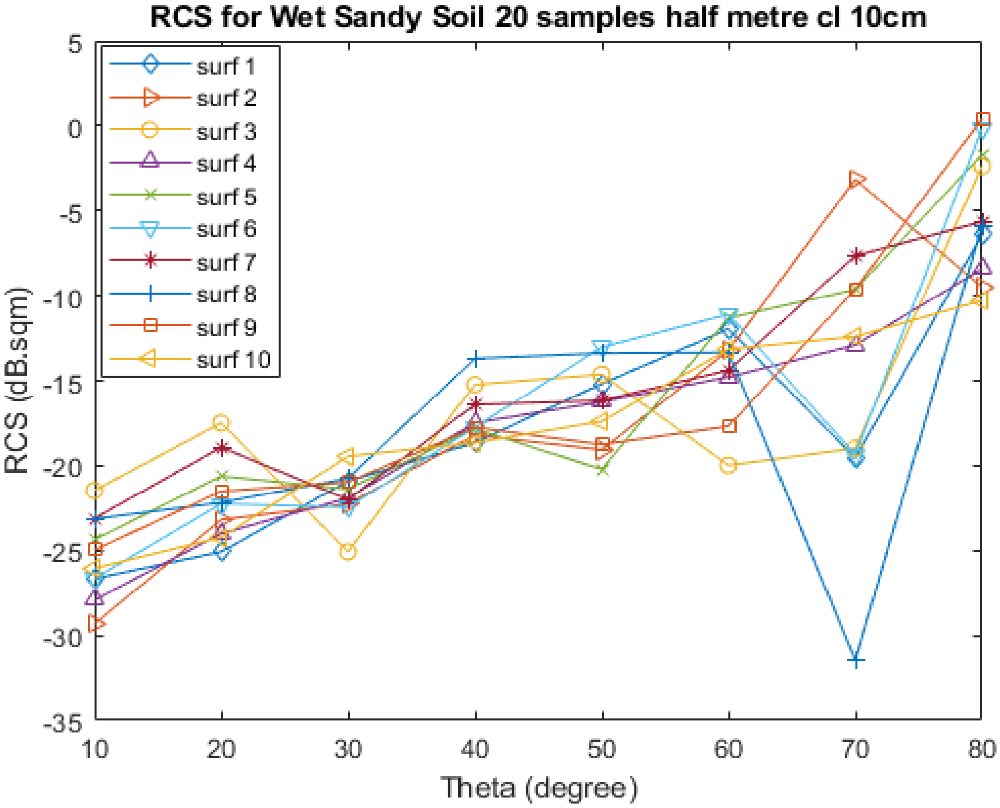

RCS analysis for wet sandy soil with cl 10cm and rms 14 cm

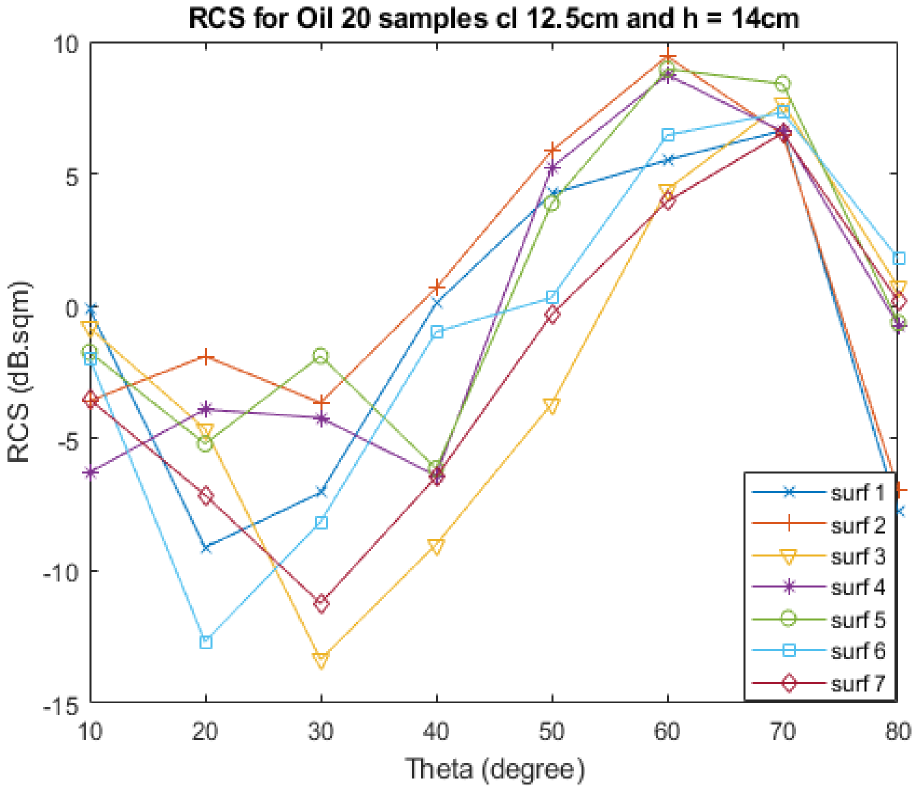

RCS for dry sandy soil mixed with oil cl 12.5cm and rms 14 cm

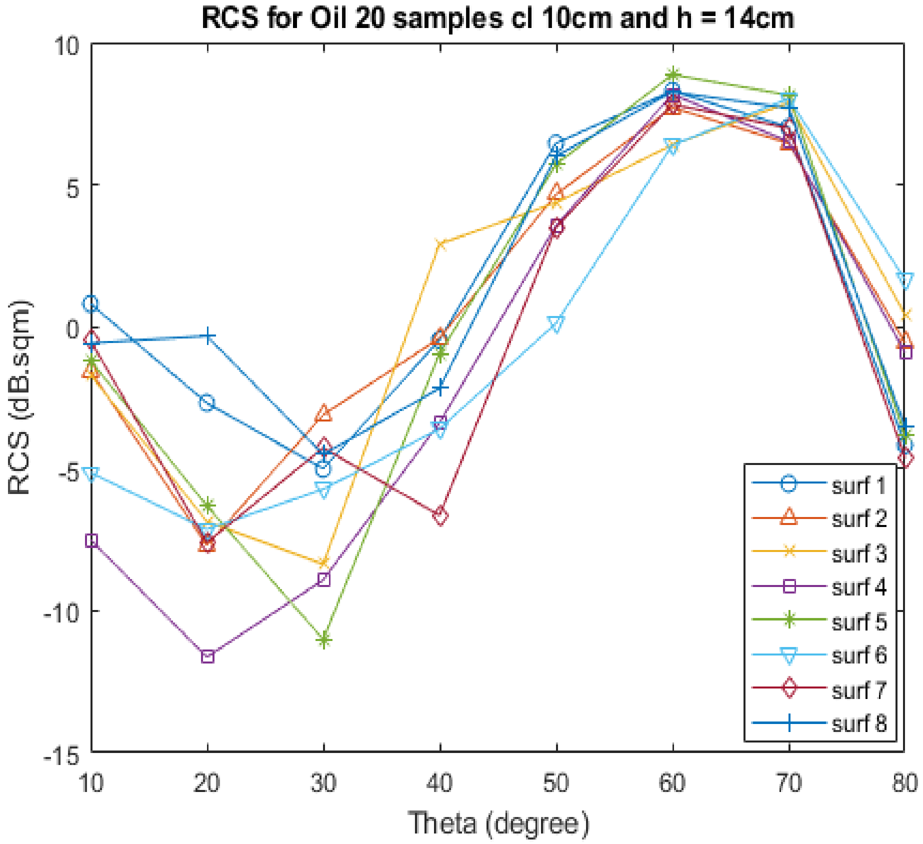

RCS for dry sandy soil mixed with oil with cl 10cm and rms 14 cm

It is also note-worthy to mention at this juncture that the results obtained from the plots for either a correlation length of 12.5 cm or 10 cm is not massively different from each other no matter the dielectric i.e. dry sandy soil, wet sandy soil and dry sandy oil filled with oil. The results tallied or aligned with themselves based on what's expected for each dielectric. Henceforth, we will only focus on correlation length of 12.5cm.

The figures below show the RCS for various rough surfaces – dry sandy soil, wet sandy soil and a dry sandy soil mixed with oil but for rms height of 7 cm.

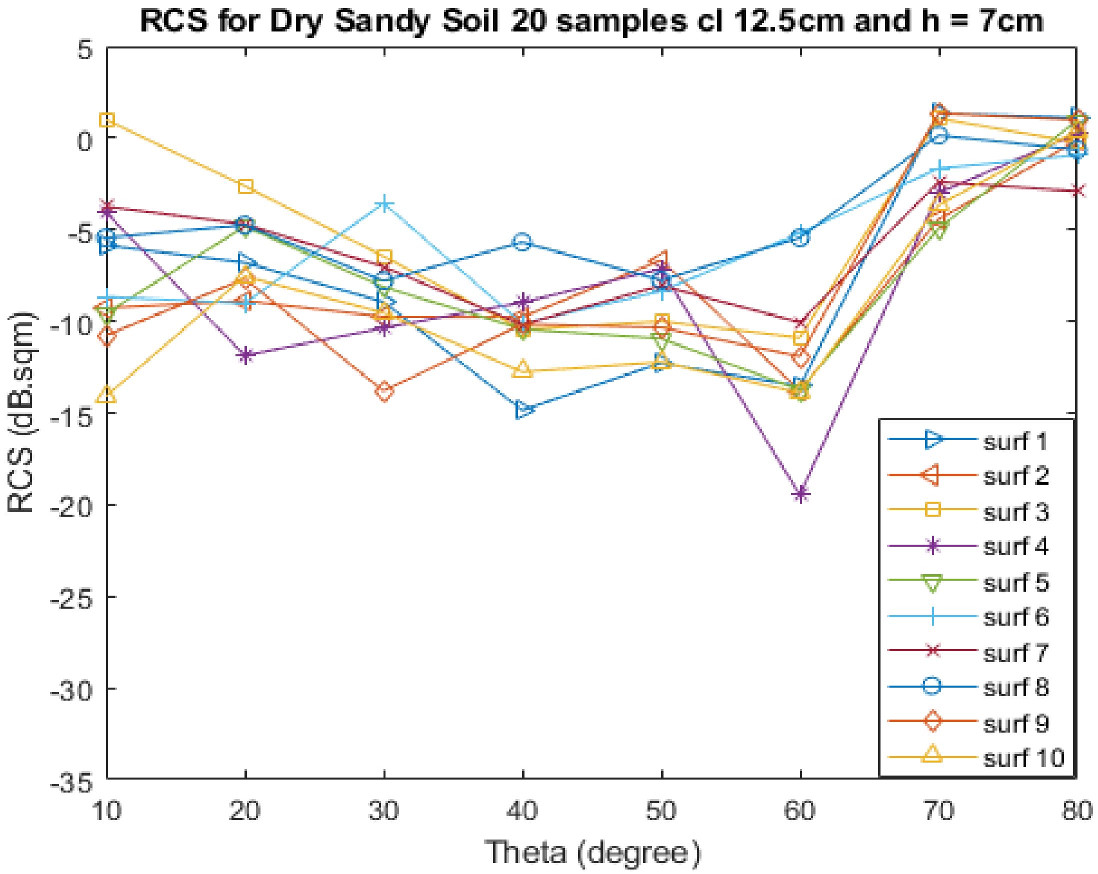

RCS analysis for dry sandy soil with cl 12.5cm and rms 7 cm

In the above figure, which is for the dry sandy soil, the range of the plot in terms of the RCS varied from about 1 dBsqm to about – 15 dBsqm as opposed to about 5 dB sqm to about -20 dB sqm for the previous figure of dry sandy soil with higher surface roughness of rms height 14 cm. Same analogy can be extended to the figures for both wet sandy soil and the dry sandy soil mixed with oil when also compared to previous figures at 14 cm rms height.

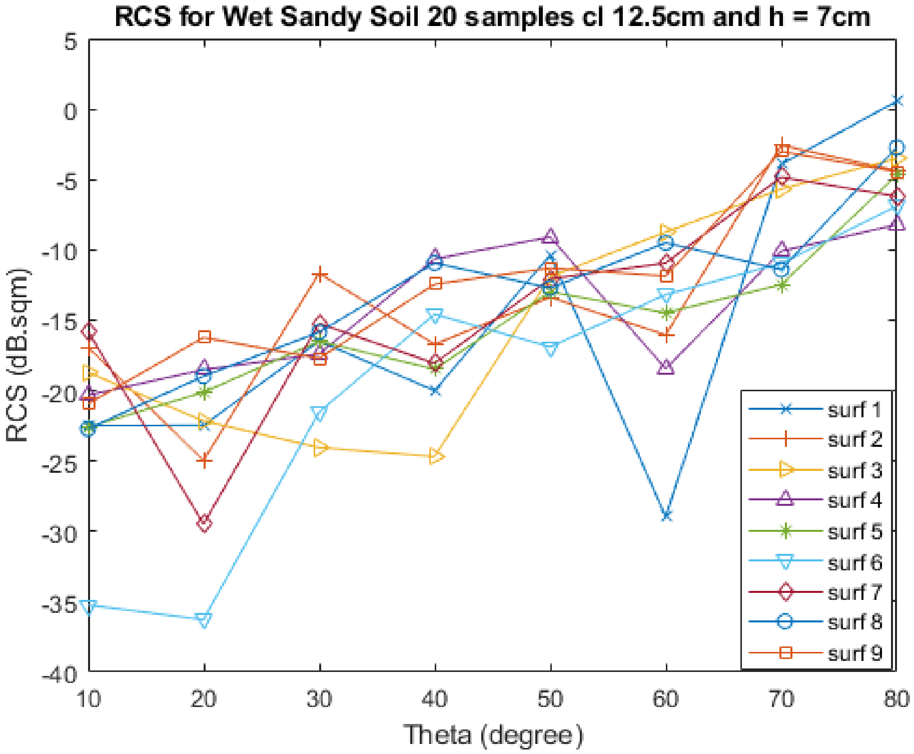

RCS analysis for wet sandy soil with cl 12.5cm and rms 7 cm

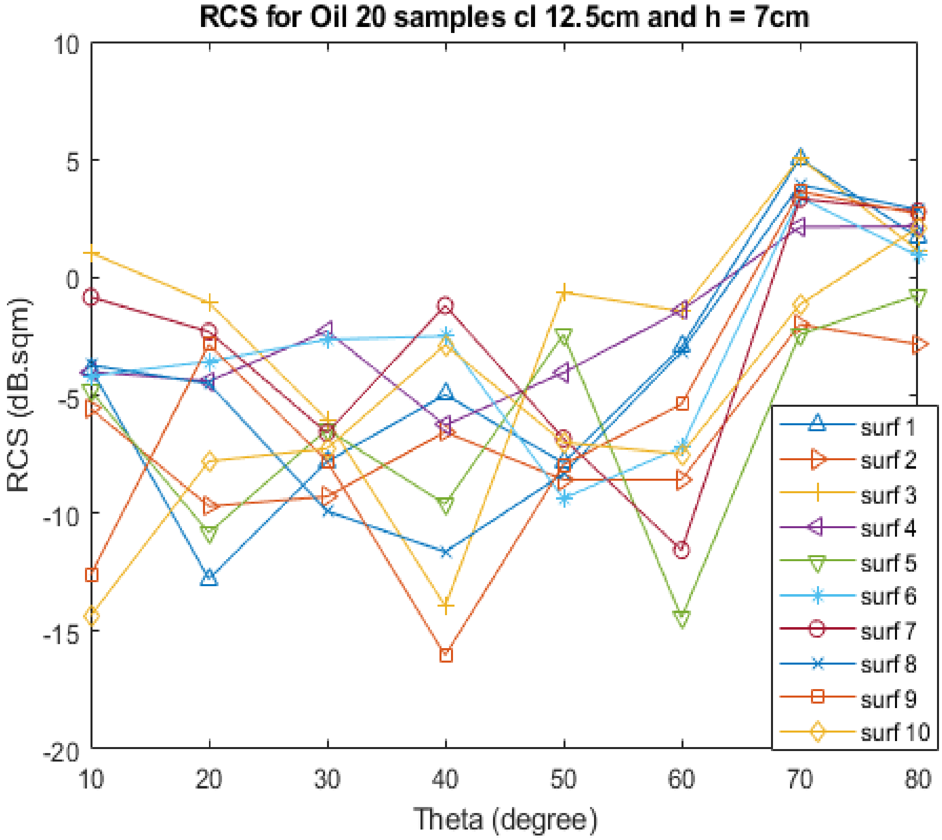

RCS for dry sandy soil mixed with oil with cl 12.5cm and rms 7 cm

Furthermore, the figures below show the three various rough surfaces under consideration but for a rms height of 3.5 cm. We have earlier posited that the reflectivity or RCS of our rough surfaces is also dependent on the roughness of the rough surface in a direct relationship. This invariably means the rougher the surface, the higher the reflectivity and this is further buttressed and analysed in these figures below. The implication of this is that when oil spills or leaks from our pipeline infrastructure, we are more likely to get a high return signal or echo if the surface upon which the oil leaks or spills onto is very rough compared to if it was just a smooth or a not-so rough surface. So, the higher the surface roughness, the higher the RCS of my rough surface and vice versa.

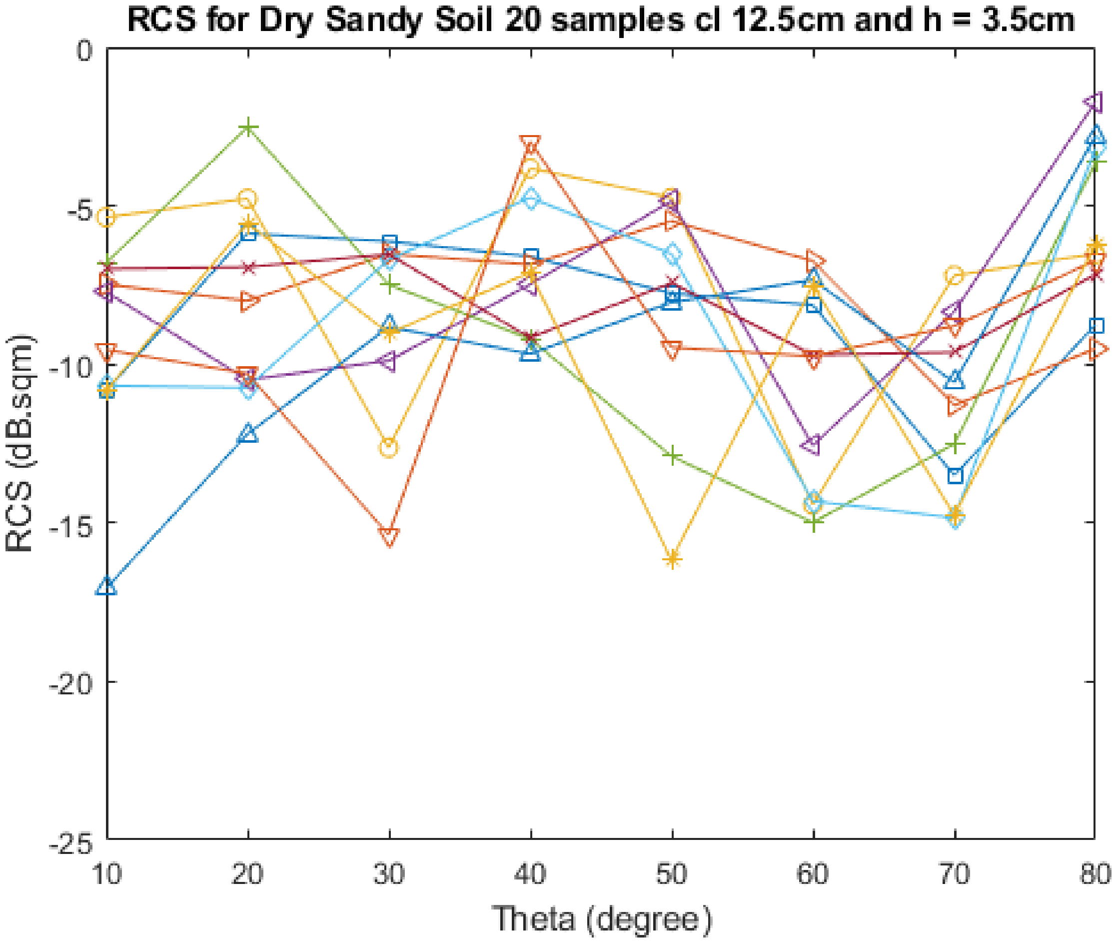

RCS analysis for dry sandy soil with cl 12.5cm and rms 3.5 cm

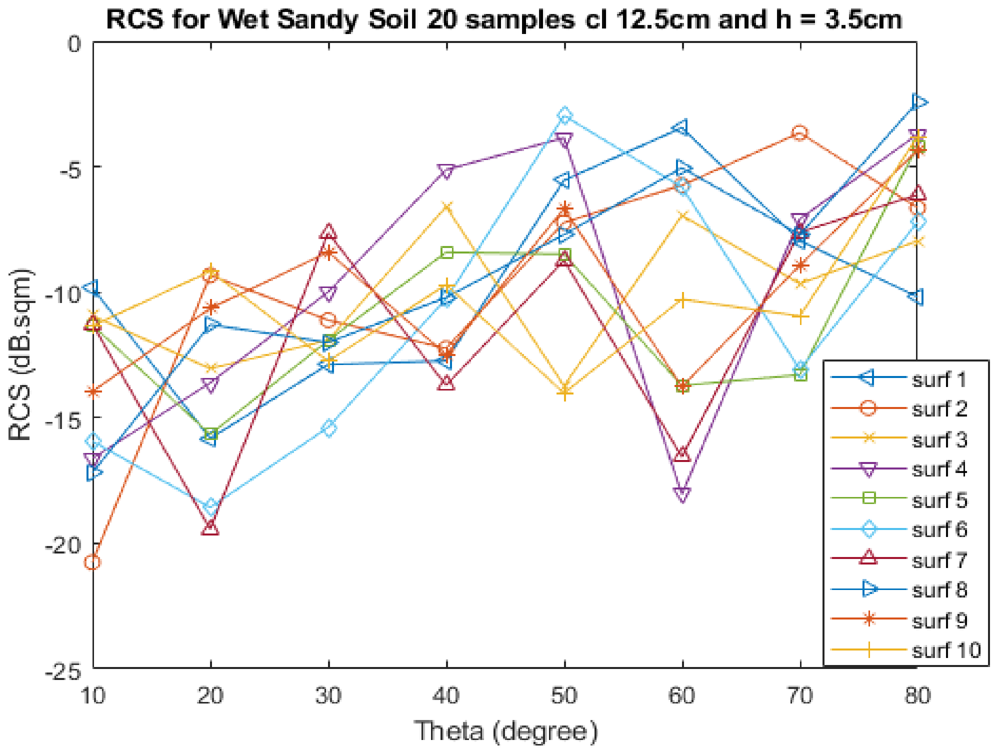

RCS analysis for wet sandy soil with cl 12.5cm and rms 3.5 cm

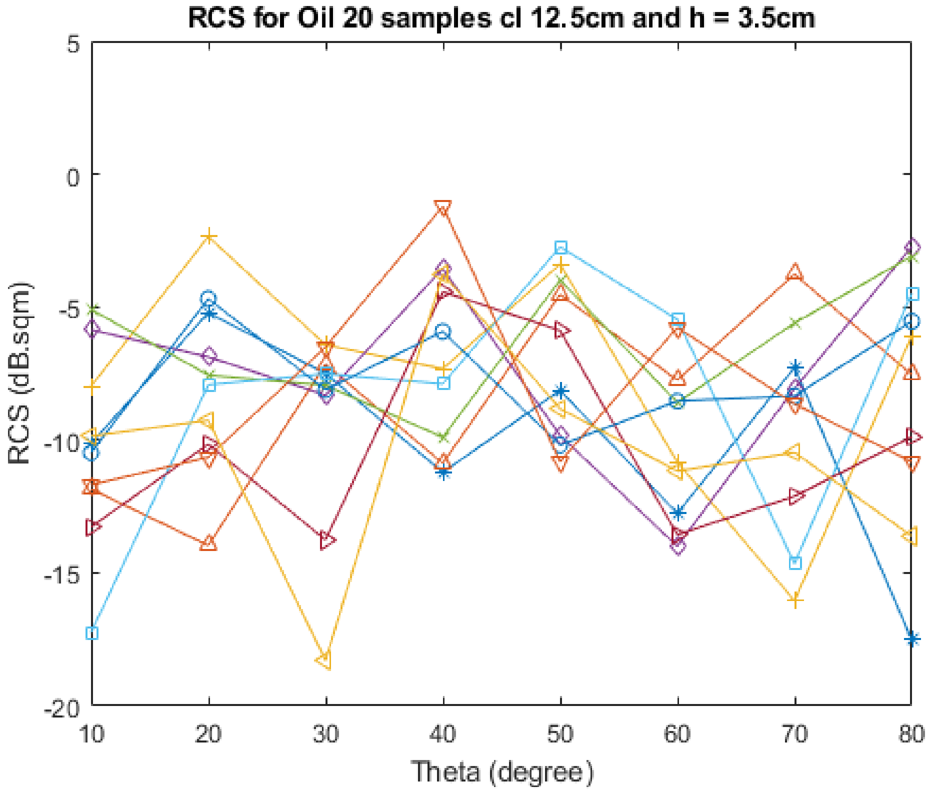

RCS for dry sandy soil mixed with oil with cl 12.5cm and rms 3.5 cm

The figure below shows the RCS measurements for 7 iterations for dry sandy soil with rms height as 21cm and with the same parameters earlier described – correlation length of 12.5 cm, for an area of ½ m by ½ m. Due to restrictions in computing facilities, only 7 plots were obtained for dry sandy soil, and we can extrapolate from these results obtained that the same trend was also maintained for these plots which lends accuracy and reliability to the results obtained. Unfortunately, due to computing restrictions, we could not perform this same simulation for 21cm for the dry sandy soil that has been soaked with oil, therefore analysis for 21cm is not part of the discussion for this dielectric.

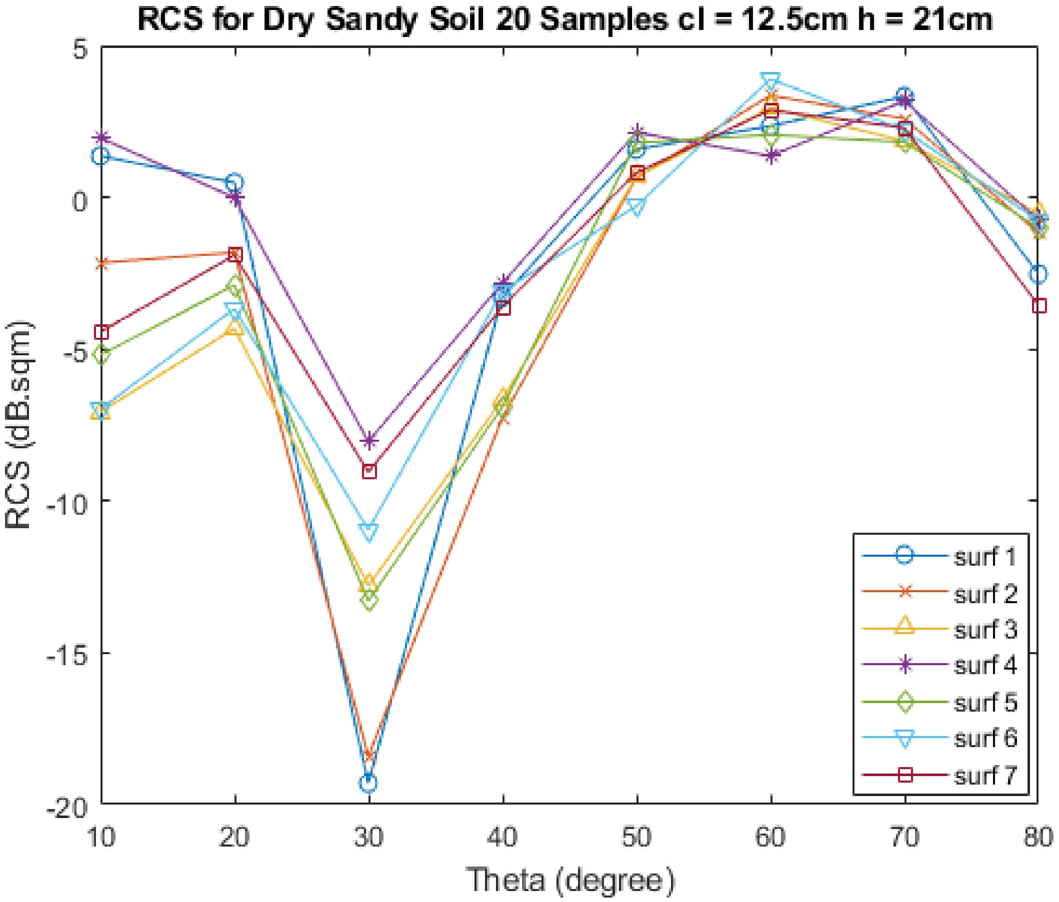

RCS analysis for dry sandy soil with cl 12.5cm and rms 21 cm

Bibliography

[1] K. Rehman and F. Nawaz, "Remote pipeline monitoring using Wireless Sensor Networks," *Proc. 2017 Int. Conf. Commun. Comput. Digit. Syst. C-CODE 2017*, pp. 32–37, 2017.

[2] M. A. Adegboye, W. K. Fung, and A. Karnik, "Recent advances in pipeline monitoring and oil leakage detection technologies: Principles and approaches," *Sensors (Switzerland)*, vol. 19, no. 11, 2019.

[3] L. Boaz, S. Kaijage, and R. Sinde, "An overview of pipeline leak detection and location systems," in *Proceedings of the 2nd Pan African International Conference on Science, Computing and Telecommunications (PACT 2014)*, 2014, pp. 133–137.

[4] Q. Xiao, J. Li, J. Sun, H. Feng, and S. Jin, "Natural-gas pipeline leak location using variational mode decomposition analysis and cross-time–frequency spectrum," *Meas. J. Int. Meas. Confed.*, vol. 124, no. April, pp. 163–172, 2018.

[5] R. Cramer, R. Tulalian, P. Angelo, M. Van Stuijvenberg, and D. Shaw, "Detecting and Correcting Pipeline Leaks Before They Become a Big Problem," *SPE Middle East Oil & Gas Show and Conference*. Society of Petroleum Engineers, Manama, Bahrain, p. 21, 2015.

[6] Z. Jia, Z. Wang, W. Sun, and Z. Li, "Pipeline leakage localization based on distributed FBG hoop strain measurements and support vector machine," *Optik (Stuttg).*, vol. 176, no. March 2018, pp. 1–13, 2019.

[7] A. Lukman, E. A. Adedokun, C. P. Nwishieyi, and M. A. Adegboye, "An Anti-Theft Oil Pipeline Vandalism Detection : Embedded System Development," vol. 2, no. June, 2018.

[8] B. Klaus and K. Rainer, *Compression Machinery for Oil and Gas*, 1st ed. Houston, Texas,: Gulf Professional Publishing, Houston, Texas, 2019.

[9] B. M. S. Arifin, Z. Li, S. L. Shah, G. A. Meyer, and A. Colin, "A novel data-driven leak detection and localization algorithm using the Kantorovich distance," *Comput. Chem. Eng.*, vol. 108, pp. 300–313, 2018.

[10] S. Mokhatab, W. Poe, and J. Mak, *Handbook of Natural Gas Transmission and Processing*, 3rd ed. Gulf Professional Publishing, Houston, Texas, 2015.

[11] M. Watts, "Resource curse? governmentality, oil and power in the Niger Delta, Nigeria," *Geopolitics*, vol. 9, no. 1, pp. 50–80, 2004.

[12] S. U. Ibeh and S. E. Nnakaihe, "Challenges and Prospects of the Use of Horizontal Directional Drilling Techniques for Laying Oil and Gas Pipelines in Nigeria," *SPE Nigeria Annual International Conference and Exhibition*. Society of Petroleum Engineers, Lagos, Nigeria, p. 14, 2016.

[13] J. Liu, J. Yao, M. P. Gallaher, J. Coburn, and R. Fernández, "Study on methane emission reduction potential in China's oil and natural gas industry," 2008.

[14] V. G. Lena, "Pipelines Explained: How Safe Are America's 2.5 Million Miles of Pipelines." [Online]. Available: https://www.propublica.org/article/pipelines-explained-how-safe-are-americas-2.5-million-miles-of-pipelines. [Accessed: 23-Dec-2019].

[15] I. Bolotina, V. Borikov, V. Ivanova, K. Mertins, and S. Uchaikin, “Application of phased antenna arrays for pipeline leak detection,” *J. Pet. Sci. Eng.*, vol. 161, no. October 2017, pp. 497–505, 2018.

[16] L. Meng, L. Yuxing, W. Wuchang, and F. Juntao, “Experimental study on leak detection and location for gas pipeline based on acoustic method,” *J. Loss Prev. Process Ind.*, vol. 25, no. 1, pp. 90–102, 2012.

[17] H. Jin, L. Zhang, W. Liang, and Q. Ding, “Integrated leakage detection and localization model for gas pipelines based on the acoustic wave method,” *J. Loss Prev. Process Ind.*, vol. 27, no. 1, pp. 74–88, 2014.

[18] Y. Mahmutoglu and K. Turk, “A passive acoustic based system to locate leak hole in underwater natural gas pipelines,” *Digit. Signal Process. A Rev. J.*, vol. 76, pp. 59–65, 2018.

[19] A. Martini, M. Troncossi, and A. Rivola, “Leak Detection in Water-Filled Small-Diameter Polyethylene Pipes by Means of Acoustic Emission Measurements,” *Appl. Sci.*, vol. 7, no. 1, 2017.

[20] K. Lim, L. Wong, W. K. Chiu, and J. Kodikara, “Distributed fiber optic sensors for monitoring pressure and stiffness changes in out-of-round pipes,” *Struct. Control Heal. Monit.*, vol. 23, no. 2, pp. 303–314, 2016.

[21] W. H. Png, H. S. Lin, C. H. Pua, and F. A. Rahman, “Pipeline monitoring and leak detection using Loop integrated Mach Zehnder Interferometer optical fiber sensor,” *Opt. Fiber Technol.*, vol. 46, no. October, pp. 221–225, 2018.

[22] Z. Jia, L. Ren, H. Li, and W. Sun, “Pipeline leak localization based on FBG hoop strain sensors combined with BP neural network,” *Appl. Sci.*, vol. 8, no. 2, 2018.

[23] S. H. Ni, Y. H. Huang, K. F. Lo, and D. C. Lin, “Buried pipe detection by ground penetrating radar using the discrete wavelet transform,” *Comput. Geotech.*, vol. 37, no. 4, pp. 440–448, 2010.

[24] Q. Hoarau, G. Ginolhac, A. M. Atto, J. M. Nicolas, and J. P. Ovarlez, “Robust adaptive detection of buried pipes using GPR,” in *2016 24th European Signal Processing Conference (EUSIPCO)*, 2016, pp. 533–537.

[25] H. Li, D. Y. Xiao, and X. Zhao, “Morphological filtering assisted field-pipeline small leakage detection,” *Conf. Proc. - IEEE Int. Conf. Syst. Man Cybern.*, no. October, pp. 3769–3774, 2009.

[26] M. R. Delgado and O. B. Mendoza, “A comparison between leak location methods based on the negative pressure wave,” in *2017 14th International Conference on Electrical Engineering, Computing Science and Automatic Control (CCE)*, 2017, pp. 1–6.

[27] Q. Chen *et al.*, “Effect of rubber washers on leak location for assembled pressurized liquid pipeline based on negative pressure wave method,” *Process Saf. Environ. Prot.*, vol. 119, pp. 181–190, 2018.

[28] S. I. Kam, “Mechanistic modeling of pipeline leak detection at fixed inlet rate,” *J. Pet. Sci. Eng.*, vol. 70, no. 3–4, pp. 145–156, 2010.

[29] S. Tian, J. Du, S. Shao, H. Xu, and C. Tian, “A study on a real-time leak detection method for pressurized liquid refrigerant pipeline based on pressure and flow rate,” *Appl. Therm. Eng.*, vol. 95, pp. 462–470, 2016.

[30] G. He *et al.*, “A method for simulating the entire leaking process and calculating the liquid leakage volume of a damaged pressurized pipeline,” *J. Hazard. Mater.*, vol. 332, pp. 19–32, 2017.

[31] Y. Zixuan, F. Shidong, and X. Ting, “Simulation and numerical calculation on pipeline leakage process,” *2010 2nd Int. Symp. Inf. Eng. Electron. Commer. IEEC 2010*, no. 1, pp. 375–379, 2010.

[32] L. Xinhong, C. Guoming, Z. Renren, Z. Hongwei, and F. Jianmin, “Simulation and assessment of underwater gas release and dispersion from subsea gas pipelines leak,” *Process Saf. Environ. Prot.*, vol. 119, pp. 46–57, 2018.

[33] J. Wan, Y. Yu, Y. Wu, R. Feng, and N. Yu, “Hierarchical leak detection and localization method in natural gas pipeline monitoring sensor networks,” *Sensors*, vol. 12, no. 1, pp. 189–214, 2012.

[34] M. H. Manekiya and P. Arulmozhivarman, “Leakage detection and estimation using IR thermography,” in *2016 International Conference on Communication and Signal Processing (ICCSP)*, 2016, pp. 1516–1519.

[35] J. Sun, Z. Peng, and J. Wen, “Leakage aperture recognition based on ensemble local mean decomposition and sparse representation for classification of natural gas pipeline,” *Meas. J. Int. Meas. Confed.*, vol. 108, pp. 91–100, 2017.

[36] Y. Gao, Y. Liu, Y. Ma, X. Cheng, and J. Yang, “Application of the differentiation process into the correlation-based leak detection in urban pipeline networks,” *Mech. Syst. Signal Process.*, vol. 112, pp. 251–264, 2018.

[37] S. Yin *et al.*, “Mass transfer characteristics of pipeline leak-before-break in a nuclear power station,” *Appl. Therm. Eng.*, vol. 142, no. April, pp. 194–202, 2018.

[38] N. C. Turner, “Hardware and Software Techniques for Pipeline Integrity and Leak Detection Monitoring,” *Offshore Europe*. Society of Petroleum Engineers, Aberdeen, United Kingdom, p. 10, 1991.

[39] P. S. Murvay and I. Silea, “A survey on gas leak detection and localization techniques,” *J. Loss Prev. Process Ind.*, vol. 25, no. 6, pp. 966–973, 2012.

[40] J. Zhang, “Designing a cost-effective and reliable pipeline leak-detection system,” 1997.

[41] G. Geiger, “State-of-the-art in leak detection and localization,” *Erdoel Erdgas Kohle*, vol. 122, no. 12, pp. 193–198, 2006.

[42] S. L. Scott and M. A. Baruffet, “Worldwide Assessment of Industry Leak Detection Capabailities for Single & Multiphase Pipelines,” *Offshore Technology Research Centre*, 2003. [Online]. Available: https://www.bsee.gov/sites/bsee.gov/files/tap-technical-assessment-program/409aa.pdf. [Accessed: 24-Dec-2019].

[43] S. Matos, D. Powell, R. Davies, X. Zhang, and P. Moore, “A Guideline Framework for the Integrity Assessment of Offshore Pipelines,” 2006. [Online]. Available:

https://www.bsee.gov/sites/bsee.gov/files/research-reports//565aa.pdf. [Accessed: 24-Dec-2019].

[44] S. M. Folga, “Natural Gas Pipeline Technology Overview,” *Argonne National Lab*, 2007. [Online]. Available: http://corridoreis.anl.gov/documents/docs/technical/APT_61034_EVS_TM_08_5.pdf. [Accessed: 24-Dec-2019].

[45] X.-J. Wang, M. Lambert, A. Simpson, and J. Vitkovsky, “Leak Detection in Pipelines and Pipe Networks: A Review,” in *6th Conference on Hydraulics in Civil Engineering: The State of Hydraulics*, 2001, pp. 391–400.

[46] A. A. Atojoko, “Design and Modelling of Passive UHF RFID Tags for Energy Efficient Liquid Level Detection Applications,” University of Bradford, UK, 2016.

[47] A. Mostafapour and S. Davoudi, “Analysis of leakage in high pressure pipe using acoustic emission method,” *Appl. Acoust.*, vol. 74, no. 3, pp. 335–342, 2013.

[48] S. W. Oh, D. B. Yoon, G. J. Kim, J. H. Bae, and H. S. Kim, “Acoustic data condensation to enhance pipeline leak detection,” *Nucl. Eng. Des.*, vol. 327, no. April 2017, pp. 198–211, 2018.

[49] S. Datta and S. Sarkar, “A review on different pipeline fault detection methods,” *J. Loss Prev. Process Ind.*, vol. 41, pp. 97–106, 2016.

[50] R. K. Miller, A. A. Pollock, D. J. Watts, J. M. Carlyle, A. N. Tafuri, and J. J. Yezzi, “A reference standard for the development of acoustic emission pipeline leak detection techniques,” *NDT E Int.*, vol. 32, no. 1, pp. 1–8, 1999.

[51] S. Li, Y. Song, and G. Zhou, “Leak detection of water distribution pipeline subject to failure of socket joint based on acoustic emission and pattern recognition,” *Meas. J. Int. Meas. Confed.*, vol. 115, no. July 2017, pp. 39–44, 2018.

[52] M. Ahadi and M. S. Bakhtiar, “Leak detection in water-filled plastic pipes through the application of tuned wavelet transforms to Acoustic Emission signals,” *Appl. Acoust.*, vol. 71, no. 7, pp. 634–639, 2010.

[53] K. Elandalibe, A. Jbari, and A. Bourouhou, “Application of cross-correlation technique for multi leakage detection,” *Proc. 2015 IEEE World Conf. Complex Syst. WCCS 2015*, vol. 2, pp. 1–4, 2016.

[54] S. El-Zahab, E. Mohammed Abdelkader, and T. Zayed, “An accelerometer-based leak detection system,” *Mech. Syst. Signal Process.*, vol. 108, pp. 58–72, 2018.

[55] S. Yazdekhasti, K. R. Piratla, S. Atamturktur, and A. Khan, “Experimental evaluation of a vibration-based leak detection technique for water pipelines,” *Struct. Infrastruct. Eng.*, vol. 14, no. 1, pp. 46–55, 2018.

[56] A. Martini, M. Troncossi, and A. Rivola, “Vibroacoustic measurements for detecting water leaks in buried small-diameter plastic pipes,” *J. Pipeline Syst. Eng. Pract.*, vol. 8, no. 4, pp. 1–10, 2017.

[57] A. Martini, A. Rivola, and M. Troncossi, “Autocorrelation analysis of vibro-acoustic signals measured in a test field for water leak detection,” *Appl. Sci.*, vol. 8, no. 12, 2018.

[58] A. A. Khan, V. Vrabie, J. I. Mars, A. Girard, and G. D'Urso, "A source separation technique for processing of thermometric data from fiber-optic DTS measurements for water leakage identification in dikes," *IEEE Sens. J.*, vol. 8, no. 7, pp. 1118–1129, 2008.

[59] A. Kroll, W. Baetz, and D. Peretzki, "On autonomous detection of pressured air and gas leaks using passive IR-thermography for mobile robot application," in *2009 IEEE International Conference on Robotics and Automation*, 2009, pp. 921–926.

[60] S. Zhang, B. Liu, and J. He, "Pipeline deformation monitoring using distributed fiber optical sensor," *Meas. J. Int. Meas. Confed.*, vol. 133, pp. 208–213, 2019.

[61] J. Du, L. Wang, C. Cai, C. Yin, and G. Zhao, "Study on distributed optical fiber heating pipeline network leak detection system," in *2017 IEEE 2nd Information Technology, Networking, Electronic and Automation Control Conference (ITNEC)*, 2017, pp. 137–140.

[62] F. Tanimola and D. Hill, "Distributed fibre optic sensors for pipeline protection," *J. Nat. Gas Sci. Eng.*, vol. 1, no. 4–5, pp. 134–143, 2009.

[63] K. S. Ong, W. H. Png, H. S. Lin, C. H. Pua, and F. A. Rahman, "Acoustic vibration sensor based on macro-bend coated fiber for pipeline leakage detection," *Int. Conf. Control. Autom. Syst.*, vol. 2017-Octob, no. Iccas, pp. 167–171, 2017.

[64] T. Zhang, Y. Tan, X. Zhang, and J. Zhao, "A novel hybrid technique for leak detection and location in straight pipelines," *J. Loss Prev. Process Ind.*, vol. 35, pp. 157–168, 2015.

[65] M. Bimpas, A. Amditis, and N. Uzunoglu, "Detection of water leaks in supply pipes using continuous wave sensor operating at 2.45 GHz," *J. Appl. Geophys.*, vol. 70, no. 3, pp. 226–236, 2010.

[66] C. Maas and J. Schmalzl, "Using pattern recognition to automatically localize reflection hyperbolas in data from ground penetrating radar," *Comput. Geosci.*, vol. 58, pp. 116–125, 2013.

[67] J. E. Patterson and F. A. Cook, "Successful application of ground-penetrating radar in the exploration of gem tourmaline pegmatites of Southern California," *Geophys. Prospect.*, vol. 50, no. 2, pp. 107–117, 2002.

[68] A. Simi, G. Manacorda, M. Miniati, S. Bracciali, and A. Buonaccorsi, "Underground asset mapping with dual-frequency dual-polarized GPR massive array," in *Proceedings of the XIII Internarional Conference on Ground Penetrating Radar*, 2010, pp. 1–5.

[69] J. H. Bradford, D. F. Dickins, and P. J. Brandvik, "Assessing the potential to detect oil spills in and under snow using airborne ground-penetrating radar," *Geophysics*, vol. 75, no. 2, 2010.

[70] A. Awwad, M. Yahyia, L. Albasha, M. M. Mortula, and T. Ali, "Communication Network for Ultrasonic Acoustic Water Leakage Detectors," *IEEE Access*, vol. 8, pp. 29954–29964, 2020.

[71] M. Elleuchi, R. Khelif, M. Kharrat, M. Aseeri, A. Obeid, and M. Abid, "Water Pipeline Monitoring and Leak Detection using soil moisture Sensors: IoT based solution," in

2019 16th International Multi-Conference on Systems, Signals & Devices (SSD), 2019, pp. 772–775.

[72] I. G. Cumming and F. H. Wong, *Digital Processing of Synthetic Aperture Radar Data*. Artech House, Inc., 2005.

[73] M. A. Richards, J. A. Scheer, and W. A. Holm, *Principles of Modern Radar*. Edison, New Jersey: Scitech Publishing, 2010.

[74] W. G. Carrara, R. S. Goodman, and R. M. Majewski, *Spotlight Synthetic Aperture Radar Signal Processing Algorithms*. Artech House, Inc., 1995.

[75] Y. K. Chan and V. C. Koo, “An introduction to Synthetic Aperture Radar (SAR),” *Prog. Electromagn. Res. B*, vol. 2, pp. 27–60, 2008.

[76] M. Antoniou, “Image Formation Algorithms for Space-Surface Bistatic SAR,” University of Birmingham, UK, 2007.

[77] G. W. Stimson, H. D. Griffiths, C. J. Baker, and D. Adamy, *Stimson’s Introduction to Airborne Radar*, 3rd. Edison, New Jersey: Scitech Publishing, 2014.

[78] Merrill Skolnik, *Introduction to Radar Systems*, 3rd ed. McGraw Hill, Inc, 2002.

[79] Merrill Skolnik, *Radar Handbook*. McGraw Hill, Inc, 1990.

[80] “Radar - History of Radar,” *Encyclopedia Britannica https://www.britannica.com/technology/radar*. .

[81] R. Kalyan, *System Modeling of Next Generation Digitally Modulated Automotive RADAR (DMR)*. .

[82] L. P. Goetz and J. D. Albright, “Airborne Pulse-Doppler Radar,” *IRE Trans. Mil. Electron.*, vol. MIL–5, no. 2, pp. 116–126, Apr. 1961.

[83] G. Gold and K. Helmreich, “A physical surface roughness model and its applications,” *IEEE Trans. Microw. Theory Tech.*, vol. 65, no. 10, pp. 3720–3732, 2017.

[84] N. Garcia and E. Stoll, “Monte Carlo Calculation for Electromagnetic-Wave Scattering from Random Rough Surfaces,” *Phys. Rev. Lett.*, vol. 52, no. 20, pp. 1798–1801, 1984.

[85] F. Ulaby *et al.*, *Microwave Radar and Radiometric Remote Sensing*. 2014.

[86] M. W. . Long, *Radar Reflectivity of Land and Sea*, 3rd ed. Boston: Artech House, Inc., 2001.

[87] A. K. FUNG and G. W. PAN, “A scattering model for perfectly conducting random surfaces I. Model development,” *Int. J. Remote Sens.*, vol. 8, no. 11, pp. 1579–1593, Nov. 1987.

[88] P. Spiga, G. Soriano, and M. Saillard, “Scattering of electromagnetic waves from rough surfaces: A boundary integral method for low-grazing angles,” *IEEE Trans. Antennas Propag.*, vol. 56, no. 7, pp. 2043–2050, 2008.

[89] F. Ticconi, L. Pulvirenti, and N. Pierdicc, “Models for Scattering from Rough Surfaces,” *Electromagn. Waves*, no. June, 2011.

[90] D. J. Daniels, “Ground Penetrating Radar,” *Encyclopedia of RF and Microwave Engineering*. 15-Apr-2005.

[91] M. G. Fernandez *et al.*, “Synthetic aperture radar imaging system for landmine detection using a ground penetrating radar on board a unmanned aerial vehicle,” *IEEE Access*, vol. 6, pp. 45100–45112, 2018.

[92] P. Beckmann and A. Spizzichino, *The Scattering of Electromagnetic Waves from rough Surfaces*. Oxford: Pergamon Press, 1963.

[93] H. R. Ward, “Radar reflectivity of land and sea,” *Proc. IEEE*, vol. 64, no. 6, pp. 1023–1023, 2008.

[94] D. H. Han, Y. L. Li, R. A. Vieweg, T. G. Ruttan, and L. A. Polka, “Dielectric material characterization using rough surface transmission lines,” *59th ARFTG Conf. Dig. Spring 2002 Test, Meas. Charact. High Speed Digit. Components Syst. ARFTG Spring 2002*, vol. 157, pp. 49–52, 2002.

[95] H. R. Ward, “Radar reflectivity of land and sea,” *Proc. IEEE*, vol. 64, no. 6, pp. 1023–1023, 2008.

[96] A. Chattopadhyay and S. Saha, “Reflection and refraction of P waves at the interface of two monoclinic media,” *Int. J. Eng. Sci.*, vol. 34, no. 11, pp. 1271–1284, 1996.

[97] F. E. Terman, *Radio Engineers’ Handbook*, 1st ed. New York, USA: McGraw Hill, Inc, 1943.

[98] D. J. Povejsil, R. S. Raven, and P. Waterman, *Airborne Radar*. Princeton, New Jersey: D. Van Nostrand Company Inc., 1961.

[99] E. S. Li and K. Sarabandi, “Low grazing incidence millimeter-wave scattering models and measurements for various road surfaces,” *IEEE Trans. Antennas Propag.*, vol. 47, no. 5, pp. 851–861, 1999.

[100] F. Ticconi, L. Pulvirenti, and N. Pierdicca, “Models for Scattering from Rough Surfaces,” in *Electromagn. Waves*, vol. 10, 2011.

[101] Q. Hoarau, G. Ginolhac, A. M. Atto, J. M. Nicolas, and J. P. Ovarlez, “Robust adaptive detection of buried pipes using GPR,” *Eur. Signal Process. Conf.*, vol. 2016-Novem, pp. 533–537, 2016.

[102] A. Darawankul and J. T. Johnson, “Band-Limited Exponential Correlation Function for Rough-Surface Scattering,” *IEEE Trans. Geosci. Remote Sens.*, vol. 45, no. 5, pp. 1198–1206, May 2007.

[103] M. Temiz, H. Griffiths, and M. A. Ritchie, “Improved Target Localization in Multiwaveform Multiband Hybrid Multistatic Radar Networks,” *IEEE Sens. J.*, vol. 22, no. 21, pp. 20785–20796, 2022.

[104] M. A. Richards, *Fundamentals of Radar Signal Processing*. McGraw-Hill Education, 2005.

[105] Y. Li, W. Li, L. Yuan, and L. Yang, “Research on RCS characteristic of three kinds of metal plate,” *Proc. - 2012 IEEE 2nd Int. Conf. Cloud Comput. Intell. Syst. IEEE CCIS 2012*, vol. 2, pp. 875–878, 2013.

[106] Merrill Skolnik, *Introduction to Radar Systems*, 2nd ed. Singapore: McGraw Hill, Inc, 1981.

[107] F. Norouzian *et al.*, “Low-THz Transmission Through Water-Containing Contaminants on Antenna Radome,” *IEEE Trans. Terahertz Sci. Technol.*, vol. 8, no. 1, pp. 63–75, 2018.